UNIVERSIDADE DE BRASÍLIA - UNB
INSTITUTO DE GEOCIÊNCIAS - IG
PROGRAMA DE PÓS-GRADUAÇÃO EM GEOLOGIA

EVOLUÇÃO CRUSTAL DA FAIXA SUNSÁS, SW DO CRÁTON AMAZÔNICO

Ingrid Moerschberger Nedel

TESE DE DOUTORADO Nº 169

Data da defesa: 18/12/2020

Área de Concentração: Geologia Regional

Orientador: Prof. Dr. Reinhardt Adolfo Fuck

BRASÍLIA, 2020

UNIVERSIDADE DE BRASÍLIA - UNB
INSTITUTO DE GEOCIÊNCIAS - IG
PÓS-GRADUAÇÃO EM GEOLOGIA

EVOLUÇÃO CRUSTAL DA FAIXA SUNSÁS, SW DO CRÁTON AMAZÔNICO

Tese de Doutorado

Ingrid Moerschberger Nedel

Área de Concentração: Geologia Regional

Orientador:
Prof. Dr. Reinhardt Adolfo Fuck

Banca Examinadora:

_____
Prof. Dr. Reinhardt Adolfo Fuck (IG – UNB)

_____
Prof. Dr. Nilson Francisquini Botelho (IG – UNB)

_____
Prof. Dr. Mauro Geraldes (UERJ)

_____
Prof. Dra. Eliza Inez Nunes Peixoto (suplente) (IG – UNB)

Brasília-DF, dezembro de 2020.

Nedel, Ingrid Moerschberger
NN371e Evolução Crustal da Faixa Sunsás, SW do Cráton Amazônico / Ingrid Moerschberger Nedel; orientador Reinhardt Adolfo Fuck; co-orientador Márcio Martins Pimentel (in memoriam). - Brasília, 2020.
196 p.

Tese (Doutorado - Doutorado em Geologia) -- Universidade de Brasília, 2020.

1. Cráton Amazônico. 2. Província Sunsas. 3. Faixa Sunsas. 4. Retrabalhamento crustal. 5. Supercontinente Rodinia. I. Fuck, Reinhardt Adolfo, orient. II. Pimentel (in memoriam), Márcio Martins, co-orient. III. Título.

Dedicado a todas as mulheres cientistas.

AGRADECIMENTOS

O presente trabalho foi realizado com apoio da Coordenação de Aperfeiçoamento de Pessoal de Nível Superior - Brasil (CAPES) - Código Financeiro 001.

Agradeço à minha família pelo apoio incondicional em transformar o ideal de um dia me tornar educadora um sonho possível. Em especial, agradeço ao meu colega, amigo e companheiro de várias batalhas Alanielson Ferreira, por ter confiado na minha capacidade e dedicado tanto do seu tempo no meu aprendizado. Aos meus orientadores e mentores, prof. Dr. Reinhardt Fuck, Dr. Amarildo Salina Ruiz e Dr. Gerardo Ramiro Matos, agradeço imensamente a confiança que me foi dada e à contribuição para minha formação. Agradeço também aos meus colegas de trabalho pelo ambiente de colaboração e amizade mantido até nos momentos mais difíceis. À Letícia Redes e Victor Chique, agradeço muitíssimo por terem sido os melhores companheiros de campo que eu poderia ter, pelas boas memórias, troca de experiênicas e bons momentos vividos na Bolívia.

SUMÁRIO

ÍNDICE DE FIGURAS

ÍNDICE DE TABELAS

RESUMO

A Faixa Sunsas, SW do Cráton Amazônico, apresenta evolução crustal do Paleo- ao Neoproterozoico e é área chave para o estudo dos múltiplos estágios e fases das orogenias grenvillianas que resultaram na formação do Supercontinente Rodínia. O magmatismo Paleoproterozoico registrado na faixa compreende complexos gnáissico-migmatíticos de 1,68 Ba no seu domínio norte cujas relações químicas apresentam baixo enriquecimento dos ETR's leves sobre os ETR's pesados, fortes anomalias negativas de Nb, Ta e Ti e altas razões iniciais $^{87}Sr/^{86}Sr$ (0.840). O embasamento do domínio sul da faixa é constituído por protólitos graníticos de 1,95–1,85 Ba, além de pequenas contribuições de magmatismo juvenil em 1,34 Ba, com padrões mais homogêneos dos elementos traços, fortes anomalias negativas de Nb, Ta e Ti e maior fracionamento dos ETR's pesados de oeste para leste do domínio. A integração de dados geocronológicos, geoquímicos, petrológicos e isotópicos demonstra intenso retrabalhamento crustal do embasamento Paleoproterozoico da Faixa Sunsas, com contribuição de fontes juvenis entre 1,42 e 1,35 Ba, associado à Orogenia San Ignácio em ambos os domínios. Novo período de retrabalhamento e diferenciação crustal é registrado entre 1,17 e 1,04 Ba, marcado pela pervasiva geração de leucossomas cálcio-alcalinos temporalmente relacionados às orogenias "grenvillianas", com pico da geração magmática em 1,08 Ba. O enriquecimento mineral progressivo em Na (plagioclásio rico em Ca-Na) e Fe + Mg (biotita) do protólito Paleoproterozoico até a formação do leocossoma granítico em 1,0 Ba também reflete os múltiplos processos de recristalização em ambos os domínios. Idades U-Pb em monazita, K-Ar em biotita e Rb-Sr sugerem um período de 1005 a ~935 Ma de atividade tectono-termal remanescente. Portanto, os protólitos paleoproterozoicos do domínio sul da faixa podem ser correlacionados ao Terreno Rio Apa, enquanto o embasamento de c. 1,68 Ba indica retrabalhamento dos complexos Lomas Manechis e Chiquitania no domínio norte. Além disso, a evolução geológica de 1,9 a 0,9 Ba documentada na Faixa Sunsas é similar às registradas na Província Grenville (Laurentia) e Província Sveconorwegian (Escudo Báltico). Logo, a Faixa Sunsas registra longo período de acresções de diferentes fragmentos continentais associados a múltiplos processos de diferenciação crustal. Além disso, representa importante elo geológico nas configurações e modelos propostos para o amálgama de Rodínia.

Palavras chave: Província Sunsas; Cráton Amazônico, Retrabalhamento crustal; Rodínia.

ABSTRACT

The Paleo to Neoproterozoic crustal evolution of the SW Amazonian Craton Sunsas belt is a key feature for the study of the multiple stages of grenvillian orogenies that resulted in the supercontinent Rodinia assembly. The Sunsas belt Paleoproterozoic magmatism comprises 1.68 Ga gneissic-migmatitic complexes in its northern domain with chemistry patterns of lower LREE/HREE ratios, stronger negative Nb, Ta and Ti anomalies and higher initial 87Sr/86Sr (0.840). The southern domain basement comprises 1.95–1.85 Ga granitic protoliths with higher fractionation HREE from west to east, strong negative anomalies of Nb, Ta and Ti, and evidence of lower 1.34 Ga juvenile contribution. The integration of geochronological, geochemical, petrological and isotopic data indicates intensive crustal reworking for the Paleoproterozoic Sunsas belt basement with 1.42 and 1.35 Ga juvenile contribution associated to the San Ignacio orogeny in northern and southern domains. A new crustal reworking and differentiation event is recorded between 1.17 and 1.04 Ga by pervasive calc-alkaline leocosomes generation associated to the “grenvillian” orogenies, with magmatic peaks in 1.08 Ga. Likewise, progressive mineral enrichment in Na (Ca- to Na-rich plagioclase) and Fe + Mg (biotite) from the Paleoproterozoic protolith to granitic 1.0 Ga leucosome also reflects the multiple recrystallization processes in the both domains. A last tectono-thermal activity between 1005 a ~935 Ma is registered by U-Pb ages in monazite, Rb-Sr, and K-Ar in biotite. Therefore, the Paleoproterozoic protoliths from the Sunsas belt southern domain can be correlate to the Rio Apa Terrane, whereas the 1.68 Ga basement from northern domain indicate crustal reworking of the Lomas Manechis and Chiquitania complexes. Besides that, the 1.9 to 0.9 Ga geological evolution of the Sunsas belt is similar to the Grenville Province (Laurentia) and Sveconorwegian Province (Baltic Shield). Thus, the Sunsas belt is associated to a long period of accretions from different continental fragments and multiple crustal differentiation processes. Also, represents an important link for the configuration and proposed models of Rodinia assembly.

Keywords: Sunsas Province; Amazonian Craton; Crustal reworking; Rodinia.

1. INTRODUÇÃO

1.1 Justificativa e importância do estudo

O Éon Proterozoico (2,5–0,54 Ba) marca um intervalo estratégico para a compreensão dos processos de diferenciação crustal na história evolutiva da Terra (e.g., Reddy e Evans, 2009; Brown et al., 2020). É responsável por expressiva atividade tectônica e processos acrescionários de crosta juvenil e retrabalhada, que resultaram no período de maior diferenciação da crosta continental (e.g., Condie, 2000; Evans e Mitchell, 2011; Cawood et al., 2013; Holder et al., 2019; Ferreira et al., 2020). Esse intervalo de tempo também inclui intenso retrabalhamento crustal, principalmente associado aos episódios de formação de supercontinentes como Nuna-Columbia (2,0–1,8 Ba), Rodinia (~0,9 Ba) e Gondwana (~0,55 Ba) (e.g., Condie, 2004; Hawkesworth et al., 2010; Nance et al., 2014; Ernst et al., 2016).

O início da Era Paleoproterozoica representa o período de consolidação da dinâmica terrestre em placas tectônicas (e.g., Brown et al., 2020). Com isso, a crosta continental passou a registrar uma variedade de processos de retrabalhamento gerados em função da dinâmica de placas análogas às do Fanerozoico, principalmente a partir de 2,2 Ga, o que resultou em mudanças significativas na composição da crosta (e.g., Cawood et al., 2013; Condie et al., 2012; Hawkesworth et al., 2017; Ferreira et al., 2020). O potencial de geração e preservação desses processos geodinâmicos é relacionado aos ciclos orogênicos responsáveis pelos mecanismos de acresção e diferenciação continental (e.g., Nance et al., 2014; Condie et al., 2012; Cawood et al., 2013; Ferreira et al., 2020). Compreender o papel da tectônica no crescimento continental leva a reconhecer que os processos que geraram a composição atual da crosta, bem como os mecanismos que culminaram na “destruição” (consumo) ou reciclagem nas margens convergentes (e.g., Armstrong, 1981; Cawood et al., 2013; Hawkesworth et al., 2020).

Nesse sentido, a montagem do supercontinente Rodínia é um importante estágio da evolução proterozoica (e.g., Meert, 2001; Li et al., 2008; Nance et al., 2014). Essa montagem é associada a amálgama de fragmentos crustais arqueanos e paleoproterozoicos durante o final do Mesoproterozoico e início do Neoproterozoico, em múltiplos espisódios colisionais, com intenso retrabalhamento crustal (e.g., Meert, 2001; Li et al., 2008; Nance et al., 2014). A porção leste de

Rodínia foi formada pela colisão entre Laurentia, Báltica, Amazônia e o oeste da África (e.g., Li et al., 2008; Merdith et al., 2017). De maneira secundária, ocorreu a colisão de fragmentos crustais menores, como o Cráton Río de La Plata, terrenos Arequipa-Antofalla e Escócia (e.g., Ramos et al., 2010; Cawood et al., 2013; Spencer et al., 2015). Os episódios magmáticos diacrônicos, com ampla distribuição espacial, são registrados na margem leste do Laurentia, sudoeste do Cráton Amazônico, sul da China, Austrália (N Queensland) e margem leste da Antártica (e.g., King Island-Transantarctic Mountains; McLelland et al., 1996; Fitzsimons et al., 2000; Li et al., 2002; Keppie et al., 2003; Hodych et al., 2004; Fioretti et al., 2005). No Cráton Amazônico a evolução das orogenias que culminaram na estabilização de Rodínia está registrada ao longo de três faixas móveis que formam a Província Sunsas em relação geodinâmica oposta à Província Grenville na Laurentia, com a qual teve relação direta durante a colisão (Hoffman, 1992; Li et al., 2008).

1.2 Relevância e objetivos da tese

A proposta central desta tese consiste em apresentar a evolução crustal proterozoica que resultou no desenvolvimento da Faixa Sunsas, e qual implicação para a formação do supercontinente Rodínia. Para tanto, foi realizada a caracterização petrológica, mineralógica, litogeoquímica, geocronológica e isotópica de rochas graníticas que a compõem. Assim, a tese contribui para a ampliação acerca do conhecimento geológico regional dos processos de acreção crustal e evolutivos do Pré-Cambriano da Província Sunsas. O maior desafio é definir o arranjo tectono-estratigráfico de uma área pouco estudada, na qual as relações de contato entre unidades distintas não são bem expostas em feições de campo, visto a superposição de distintos eventos deformacionais.

A proposta básica deste estudo consiste na geração de dados a partir do emprego de diferentes análises (mapeamento geológico, petrografia, geoquímica, geocronologia e dados isotópicos) a fim de contribuir com:

a) Identificação do retrabalhamento da crosta continental arqueana e paleoproterozoica durante a Orogenia Sunsas, bem como da geração de magmatismo granítico entre 1,1 e 1,0 Ba;
b) Comportamento dos sistemas isotópicos U-Pb e Sm-Nd em relação à superposição de eventos (ciclos) magmáticos-deformacionais;

c) Definição de limites durante evolução geodinâmica dos terrenos que formam a Faixa Sunsas;
d) Possíveis correlações das unidades proterozoicas em configurações (reconstruções) globais.

1.3 Contexto geológico

1.3.1 Província Sunsas

A Província Sunsas, localizada na porção sul/sudoeste do Cráton Amazônico, região da fronteira Bolívia-Brasil, é a mais jovem (1,20–0,95 Ba) das seis províncias geocronológicas que o constituem (Tassinari e Macambira, 2004). Compreende as unidades litoestratigráficas (e.g., grupos Sunsas, Aguapeí e Nova Brasilândia) geradas e retrabalhadas durante a Orogenia Sunsas (1,20 – 0,95 Ba; Litherland et al., 1986; Teixeira et al., 2010). Os registros do ciclo orogênico ocorrem nos limites das faixas Sunsas, no oriente da Bolívia, Aguapeí e Nova Brasilândia, estas últimas no extremo oeste do Brasil. O evento colisional esteve associado a baixo a médio grau de metamorfismo quase contemporâneo à intrusão granítica sin-tectônica entre 1,1 e 1,0 Ba (e.g., Litherland et al., 1989; Tassinari et al., 2000).

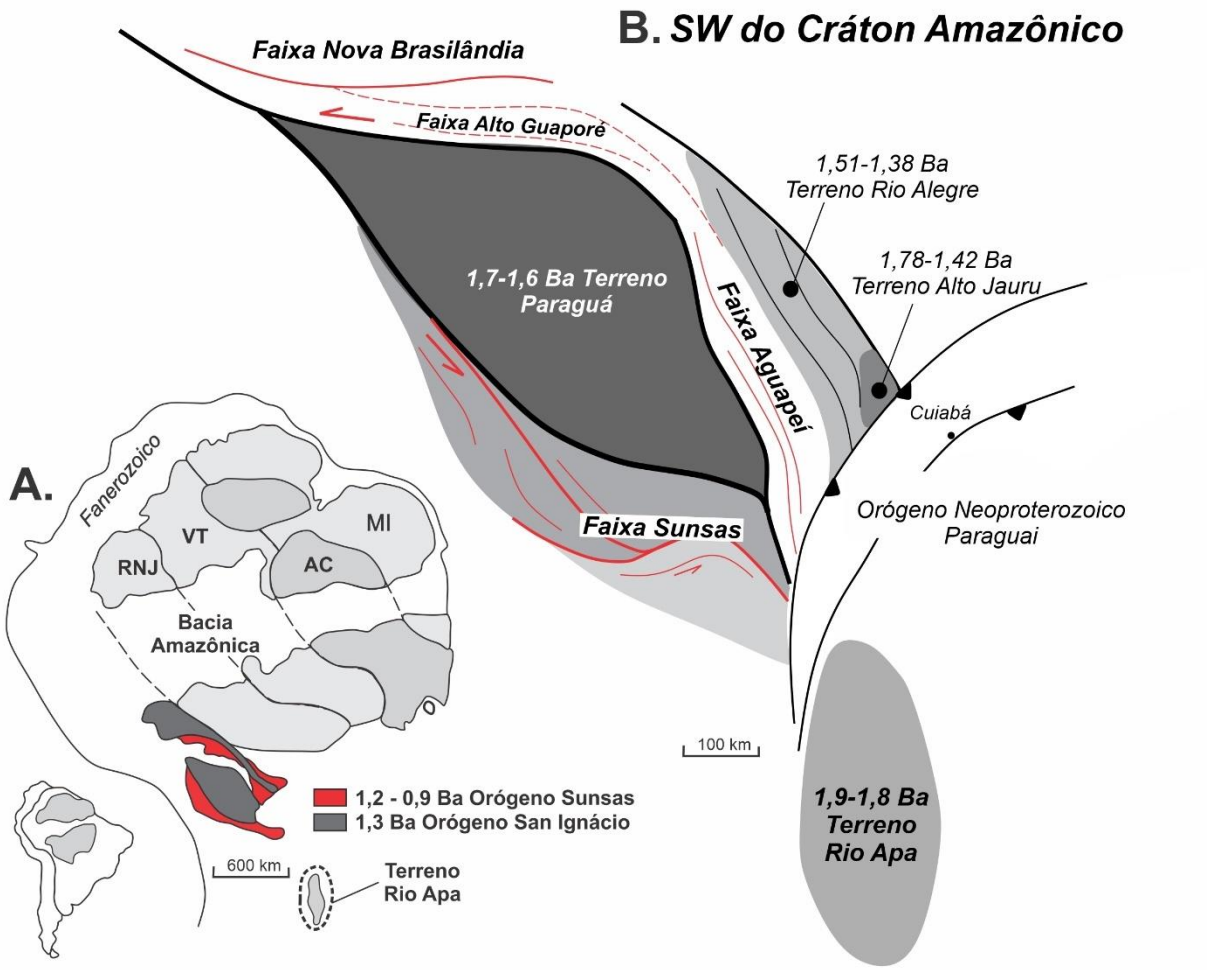

Figure 1.1. A) Cráton Amazônico e sua posição no continente Sul americano; B) Esquema tectono-estratigráfico da Província Sunsas na porção nordeste da Bolívia.

Correlações estruturais, litoestratigráficas e geocronológicas permitem compartimentar a evolução tectono-magmática da Orogenia Sunsas em três estágios (Tohver et al., 2004; Teixeira et al., 2010). O primeiro corresponde à fase de margem passiva: geração da bacia proto-ocêanica Nova Brasilândia (<1,21 Ba), deposição dos sedimentos do Grupo Sunsas-Vibosi e instalação do sistema de riftes abortados da Bacia Aguapeí-Huanchaca (1,17–1,15 Ba). O segundo estágio registra o processo colisional (1,1-1,0 Ba) desenvolvido nas margens do Terreno Paraguá e do Cratón Amazônico, representado por deformação transpressiva sinistral, sob condições de fácies anfibolito a granulito, e intrusões graníticas sin- a pós-tectônicas na Faixa Sunsas e sin-tectônicas na Faixa Nova Brasilândia (1,13–1,0 Ba). O último estágio, formação da Faixa Aguapeí (1,0 e 0,95 Ba), corresponde à deformação intracontinental do Cratón Amazônico, com metamorfismo na fácies xisto verde, correlato às etapas tardias da Orogenia Grenvilliana, e magmatismo pós-tectônico (granitos intra-placa, pegmatitos, diques e sills máficos de 730 Ma).

1.3.2 Faixa Sunsas

A Faixa Sunsas localiza-se na borda oeste do terreno Paraguá, extendendo-se por aproximadamente 600 km na direção NW-SE. Além do embasamento retrabalhado, que compreende os complexos Lomas Manechis e Chiquitania, é composta pelas sequências metassedimentares dos grupos Sunsas-Vibosi, pelo complexo máfico-ultramáfico Rincón del Tigre e por suítes intrusivas graníticas sin a pós-tectônicas. A faixa é interpretada como uma zona de sutura entre o continente Laurentia e o Cráton Amazônico (Sadowski & Bettencourt, 1996; Tohver et al., 2002, 2005; Loewy et al., 2004; Boger et al., 2005; Teixeira et al., 2010; Brito Neves & Fuck, 2014; Rizzotto et al., 2014) ou como faixa intracontinental contígua ao Orógeno Grenville (Santos et al., 2000, 2008). Sua deformação é controlada por quatro extensos lineamentos regionais, dominantemente transcorrentes, os fronts San Diablo (FSD), Rio Negro (FRN), Santa Catalina (FSC) e Concepción (FC) (Litherland et al., 1986).

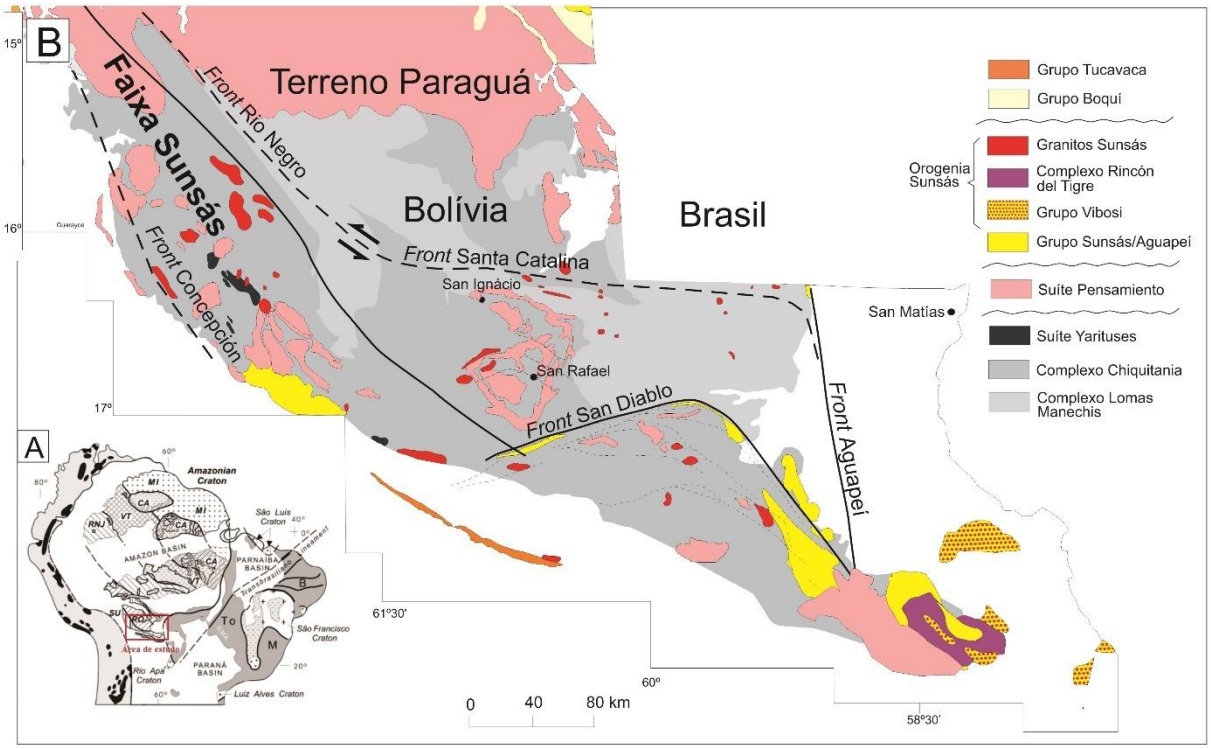

Figure 1.2 A) Cráton Amazônico e B) Província Sunsas (Adaptado de Matos et al., 2009).

Apesar da intensidade e do retrabalhamento provocado pela Orogenia Sunsas, em áreas afastadas das zonas mais deformadas é possível encontrar vestígios da deformação não-penetrativa interna pré-Sunsas, com pouca ou nenhuma sobreposição metamórfica (Litherland et al., 1986; Sadowski & Bettencourt, 1996;

Boger et al., 2005), bem como as estruturas mais antigas da Orogenia San Ignácio (Boger et al., 2005).

A granitogênese meso- a neoproterozoica engloba número significativo de intrusões compostas sobretudo por granitos sin- e tardi- a pós-cinemáticos (Litherland et al., 1986; Boger et al., 2005; Vargas-Mattos, 2006; Vargas-Mattos et al., 2010). Os corpos graníticos sin-tectônicos estão inseridos, preferencialmente, nas extensas zonas de cisalhamento miloníticas, ou fronts tectônicos, que compõem a Faixa Sunsas (Litherland et al., 1989) e cujo controle estrutural demonstra cinemática essencialmente sinistral. Considerados em conjunto, os granitos apresentam características químicas que sugerem contaminação crustal das fontes magmáticas, de acordo com o controle isotópico de Nd (Santos et al., 2000; Boger et al., 2005), razão pela qual Teixeira et al. (2010) assumem que essa granitogênese provavelmente se deu em ambiente de arco continental.

Os plútons graníticos mais antigos, como El Carmen, são quartzo monzonitos, monzonitos, sienogranitos e pequenos segmentos de granitos rapakivi. Os mais jovens, como os maciços Primavera e Señoritas, são formados por sienitos e granitos peraluminosos e peralcalinos, além de uma série de diques e pegmatitos. Os granitos Taperas, Naranjito e Casa de Piedra possuem composição monzogranítica, caráter metaluminoso a peraluminoso e assinatura geoquímica de ambiente crustal (Litherland et al., 1986; Boger, 2005; Isla-Moreno, 2009; Vargas-Mattos, 2010).

1.4 Localização e vias de acessos

A área de estudo localiza-se na porção leste da Bolívia (Fig. 1.1), abrangendo parte dos municípios de San Ramón, San Juan e San Javier. Os acessos principais são por meio da BR-262 de Corumbá no Estado de Mato Grosso do Sul ou BR-070 de Cáceres, no Estado de Mato Grosso. Se a rota de acesso for Corumbá, a partir da divisa com a Bolívia, segue-se pela Rota 4 até Roboré, em seguida pelas Rota 17, 10 e 9 até os municípios citados. Com acesso via Cáceres, segue-se pela BR-070 até a divisa dos países, depois pela Rota 10 até San Ignácio de Velasco, e em seguida pelas Rotas 10, 9 e 17 até os municípios citados.

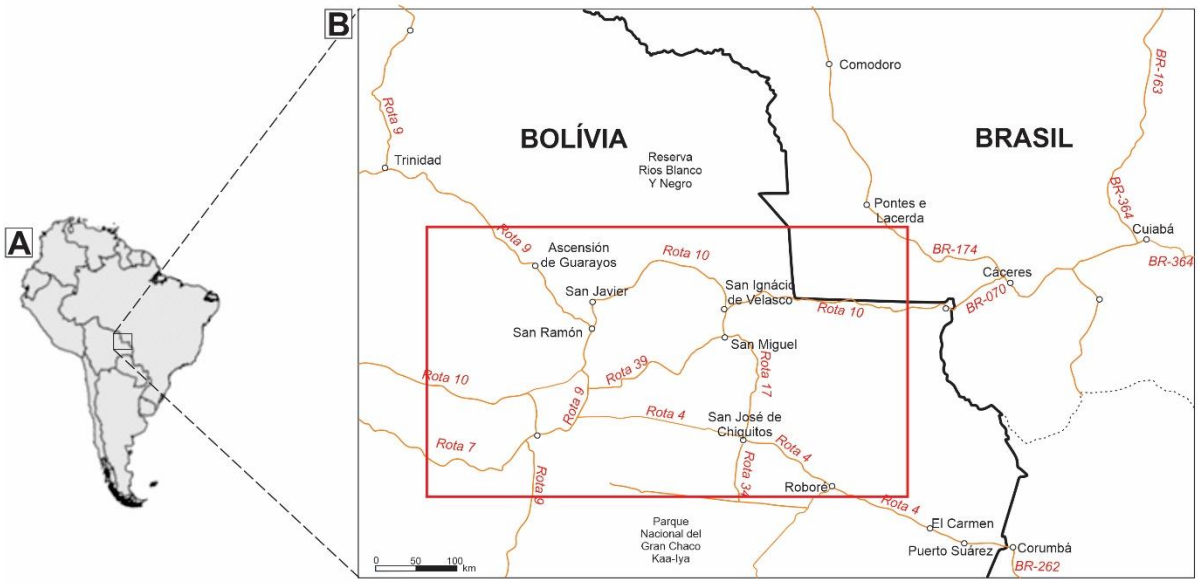

Figura 1.3. Mapa de localização e acesso à área de estudo. (A) Mapa da América do Sul; (B) Mapa da região leste da Bolívia, em divisa com o Estado de Mato Grosso, Brazil.

1.5 Escopo da tese

A tese apresenta-se estruturada na forma de capítulos. O Capítulo 1 apresenta as informações gerais da pesquisa: importância do estudo, seleção e histórico da área, relevância e objetivos, localização e este sub-tópico, “Escopo da tese”.

O Capítulo 2 traz o primeiro artigo publicado no Journal of South American Earth Sciences, intitulado “U-Pb geochronology and geochemistry of Grenville-age plutons in the Sunsas belt - Bolivia, SW Amazonian Craton: Tectonic and magmatic implications”. Nele são abordados dados geocronológicos e químicos de três intrusões graníticas da Faixa Sunsas, amostradas na primeira etapa de campo.

O Capítulo 3 contém o artigo “Long-lived Proterozoic magmatism in the Bolivian Precambrian Sunsas belt, SW Amazonian Craton”, submetido à revista Geoscience Frontiers. Nesse artigo são apresentados todos os 11 dados U-Pb em zircão e monazita produzidos durante o doutorado.

O Capítulo 4 contém o artigo que aborda dados químicos e isotópicos das intrusões graníticas datadas. Intitulado “The essential role of continental reworking processes in the Precambrian Sunsas belt, SW Amazonian Craton”, foi submetido a Lithos.

O Capítulo 5 contém uma síntese conclusiva da tese em formato de artigo curto, a partir dos dados apresentados nos três artigos, destacando a história evolutiva integrada a partir dos diferentes registros preservados nas rochas que compõem a Faixa Sunsas.

2. ARTIGO CIENTÍFICO 1: U–PB GEOCHRONOLOGY AND GEOCHEMISTRY OF GRENVILLE-AGE PLUTONS IN THE SUNSAS BELT - BOLIVIA, SW AMAZONIAN CRATON: TECTONIC AND MAGMATIC IMPLICATIONS

Ingrid Moerschberger Nedel[a], Reinhardt A. Fuck[a], Amarildo Salina Ruiz[b], Ramiro Matos[c], Alanielson da Câmara Dantas Ferreira[d]

[a]Instituto de Geociências, Universidade de Brasília (UnB), 70910-900, Brasília, DF, Brazil

[b]Faculdade de Geociências, Universidade Federal de Mato Grosso, Cuiabá, (MT), Brazil

[c]Instituto de Investigaciones Geológicas y del Medio Ambiente, Universidad Mayor de San Andrés (UMSA), Pabellón Geología, Calle 27, Campus Universitario Cota Cota, La Paz, Bolivia

[d]Laboratório de Geoquímica e Petrologia Experimental (LAGEPE), Universidade Federal do Rio Grande do Sul (UFRGS), 91501-970, Porto Alegre, RS, Brazil

Corresponding author: Ingrid Moerschberger Nedel (Ingrid_mn@hotmail.com)

2.1 Abstract

The Sunsas syn- to post-orogenic high-K calc-alkaline magmatism is crucial to understand the tectonic and thermodynamic history of the Sunsas Orogeny in the southwestern part of the Amazonian Craton. This orogeny is correlated with the Grenville orogenic cycle (c. 1.3 to 0.95 Ga) of Laurentia. Three granitic intrusions from Sunsas belt were classified as fractionated I-type and hybrid A-type granites. The first, the Nomoca granodiorite presents calc-alkaline affinity with peraluminous-magnesian composition (MgO=1.61 wt.%), and typical characteristics of intermediate magmas (SiO^2=67.3 w%). The La Asunta and Nocemano syenogranites have calc-alkaline affinity with peraluminous-ferrous composition (FeO=2.26-3.31 wt.%) and characteristics of silica-rich magmas (SiO^2=70.4-74.9 w%). Geochemical fractionation patterns suggest that the granites were derived from the reworking of two crustal protolith sources in the same tectonic environment. The Nomoca, La Asunta and Nocemano intrusions yield crystallization ages between 1.17 and 1.08 Ga. Inherited zircon cores with 3.63 and 2.91 Ga Archean ages from Nomoca and Nocemano intrusions may be correlated to the Superior Province evolution, which is located in the south-central part of the Canadian Shield. These U-Pb ages strengthen

the geotectonic model for the Rodinia supercontinent with Laurentia-Baltica-Amazonia configuration. Paleoproterozoic (2.12 to 1.69 Ga) and Mesoproterozoic (1.4 to 1.3 Ga) U–Pb inherited zircon ages from these intrusions support intensive reworking of the Paraguá basement. A concordant age of 555 Ma for zircon rims suggests reworking of the Sunsas Province during the Neoproterozoic Brasiliano Orogeny.

Keywords: Sunsas magmatism; Amazonian Craton; Rodinia supercontinent; Bolivia

2.2 Introduction

The study of calc-alkaline magmatism generated during orogenies plays a significant role to understand the tectonic and thermodynamic history of orogenic systems from pre-collision to post-tectonic magma generation (Wyllie, 1981; Wilson, 1991; Winter, 2010; Gill, 2010; Bucher and Grapes, 2011; Best, 2013). The determination of igneous rocks crystallization conditions and geodynamic setting is central to unravel the evolution of continental crust growth.

The Grenvillian magmatism shows diachronic evolution between 1.35 and 0.95 Ga and presents a wide spatial distribution recorded in the western margin of Laurentia, Southwest Amazonian Craton, Southern China, Australia (N Queensland) and Eastern Antarctica (King Island-Transantarctic Mountains; McLelland et al., 1996; Fitzsimons et al., 2000; Li et al., 2002; Keppie et al., 2003; Hodych et al., 2004; Fioretti et al., 2005). The Grenville Province was stabilized by orogens that represent the closing of distinct Mesoproterozoic oceans developed between Laurentia, Baltica, and Amazonia continents, and the continental collisions that led to the establishment of the Rodinia Supercontinent (Fig.2.1). The oldest magmatic records (1.2 Ga) are recognized from calc-alkaline plutonic and volcanic rocks in the southeast of Laurentia (Windley, 1989, 1993). The 1.18-1.15 Ga intraplate magmatism is documented in the northeast of Laurentia (Li et al., 2008). These ages are synchronic to the installation of calc-alkaline magmatic arcs in its southern portion (Li et al., 2008). The arcs remained active up to 1.07 Ga in the central-east portion of the Laurentia continent (Fitzsimons, 2000). The geological complexity of blocks and terrains assigned to the orogenic events between 1.3 and 0.9 Ga does not allow to formulate a unique tectonic model that supports the diversity of magma sources and

geodynamic processes that contributed to the formation of Rodinia (e.g., Cordani et al., 2009).

The Sunsas Province (Teixeira et al., 1989; Tassinari and Macambira, 2004; Ruiz, 2005; Cordani and Teixeira, 2007) represents an orogen developed between 1.2 and 0.95 Ga due to the collision between Laurentia and southwest Amazonian Craton (Sadowski and Bettencourt, 1996; Tohver et al., 2002, 2006; Loewy et al., 2004; Boger et al., 2005; Li et al., 2008; Fuck et al., 2008; Teixeira et al., 2010; Rizzotto et al., 2014). The province comprises syn- to post-tectonic igneous rocks (Table 2.1) and metasedimentary units present in the Sunsas Belt, exposed only in Bolivia, and Aguapeí and Nova Brasilândia belts in west Brazil (Teixeira et al., 2010; Rizzotto et al., 2013; Brito Neves and Fuck, 2014).

The Sunsas Orogen evolution is marked by transcurrent tectonic fronts developed under a sinistral transpressive regime along the western boundary of the Paraguá Terrane, active between 1.08 to 1.05 Ga (Litherland et al., 1986; Teixeira et al., 2010). This tectonic event was the last prominent tectonic record in the cratonic margin (Litherland et al., 1986; Teixeira et al., 2010). The fronts development was coeval to crustal transpression, shortening, and magmatism in the Nova Brasilândia Belt (1.13-1.0 Ga; Teixeira et al., 2010). The Aguapeí Belt and closely related shear zones represent the last ramifications of the Sunsas orogen.

Despite a large number of publications (Litherland et al., 1986, 1989; Darbyshire et al., 2000; Rizzotto, 2001; Boger et al., 2005; Santos et al., 2008; Isla-Moreno, 2009; Teixeira et al., 2010; Vargas-Mattos, 2010; Matos et al., 2009; Siqueira, 2015; Nedel et al., 2017) there is a gap on petrographic, geochemical and isotopic data of the rocks that form the Sunsas Province. Thus, the focus of this paper is the petrographic, geochemical, and geochronological description of the La Asunta, Nocemano, and Nomoca granites. These granitic intrusions occur in a strategic geographic position, still without basic geological mapping. The results obtained in this work represent the first step for further investigations and provide a better understanding of the magmatic evolution of the Sunsas Belt in the Southwest Amazonian Craton.

Table 2-1. Geochronological and isotopic data of the Sunsas Belt granitic plutons. Analysis on (b) biotite, (m) muscovite, (z) zircon and (rt) total rock.

SUNSAS BELT									
Granitoids	**Classification**	**References**	**U-Pb**	**Rb-Sr**	**Sm-Nd**			**K-Ar (Ma)**	
			Ages (Ma)	**Ages (Ma)**	**Tdm (Ga)**	**eNd(0)**	**eNd(T)**	**Ages (b)**	**Ages (m)**
Tasseoro	monzogranite	Litherland et al. (1986)						991 ± 27	
Taperas								935 ± 21	
		Boger et al. (2005)	1076 ± 18 (zr)						
		Vargas-Mattos (2010)	1047 ± 24 (zr)		1.71		-4.74 and -5.82		
Casa de Piedra		Litherland et al. (1986)		1005 ± 12				958 ± 27	911 ± 20
Casa de Piedra (dyke)									884 ± 20
Casa de Piedra		Darbyshire et al. (2000)			1.92		-4		
	monzogranite	Vargas-Mattos (2010)	1089 a 1030				-4.94 e -3.56		
San Pedro (pegmatite)		Litherland et al. (1986)						730 ± 21	1008 ± 22
San Javier (dyke)								948 ± 21	

SUNSAS BELT									
Granitoids	**Classification**	**References**	**U-Pb**	**Rb-Sr**	**Sm-Nd**			**K-Ar (Ma)**	
			Ages (Ma)	**Ages (Ma)**	**Tdm (Ga)**	**eNd(0)**	**eNd(T)**	**Ages (b)**	**Ages (m)**
Orobayaya (aplite dyke)								1078 ± 23	
El Carmem (pegmatite)									972 ± 21
El Carmem	monzogranite	Vargas-Mattos (2010)	1071 ± 34 (zr)		1.80		-5.03		
Naranjito			1048 ± 19 (zr)		1.75		-3.17 e -4.77		
Primavera	syenogranite		1.08 (zr)		1.66		-0.59 e 8.52		
Señoritas		Isla-Moreno (2009)	1004 ± 1						

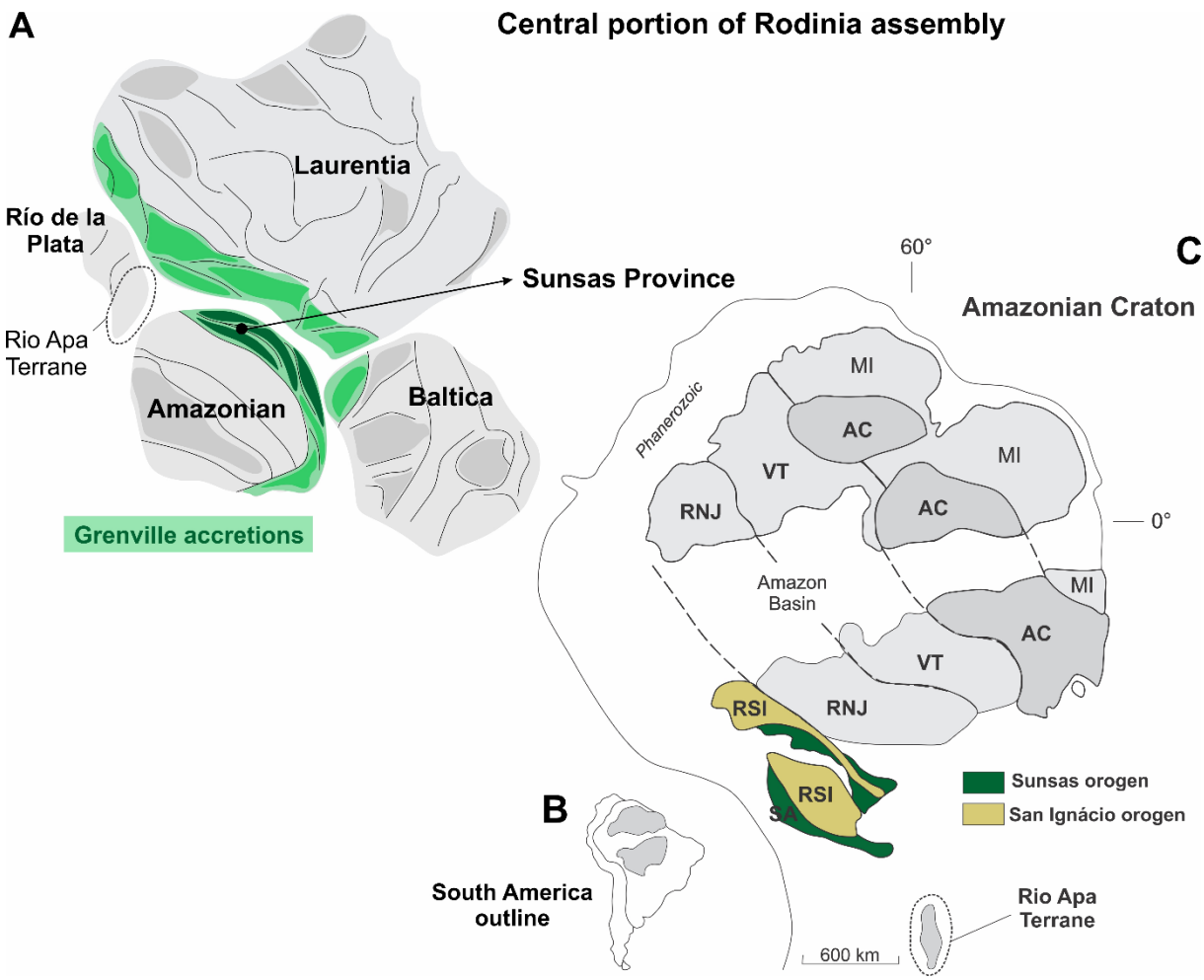

Figure 2.1. (A) Schematic model of central portion of Rodinia supercontinent assembly (modified from Li et al., 2008). The Rio Apa Block integration with the Rìo de La Plata Craton follow the model proposed by Dragone et al. (2017), based on geophysical gravity data; (B) Amazonian Craton position in the South America; (C) Geotectonic compartmentation of the Amazonian Craton, detaching the SW portion and respective provinces (modified from Cordani and Teixeira, 2007). Inset: CA = Central Amazonian province; MI = Maroni-Itaicaiunas province; VT = Ventuari–Tapajós, RNJ = Rio Negro–Juruena, RSI = Rondonian–San Ignacio, SA = Sunsas–Aguapeí.

2.3 Geological setting

2.3.1 Amazonian Craton

The Amazonian Craton, located in the northern part of the South American continent, represents one of the main Precambrian geotectonic entities of the world. It is an important component in many supercontinent reconstructions, such as Rodinia configuration.

According to Cordani et al. (1979), Tassinari (1981), Cordani and Brito Neves (1982), Teixeira et al. (1989), Tassinari (1996), Tassinari and Macambira (1999, 2004),

Tassinari et al. (2000), Ruiz (2005), and Santos et al. (2000, 2008), the craton evolution consisted of progressive microcontinents accretion to a crustal Archean core amid the formation of juvenile magmatism and crustal reworking of the increased terrains during the Paleoproterozoic and Mesoproterozoic. Teixeira et al. (1989), Tassinari and Macambira (1999, 2004) and Tassinari et al. (2000) suggested a geotectonic compartmentation in six major geochronological provinces: Amazônia Central (2.5 Ga), Maroni-Itacaiúnas (2.2–1.95 Ga), Ventuari-Tapajós (1.95–1.8 Ga), Rio Negro-Juruena (1.8–1.55 Ga), Rondoniana-San Ignácio (1.55–1.3 Ga) and Sunsas (1.3–1.0 Ga).

Also, it is important to highlight the tectonic compartmentation proposal by Santos et al. (2000, 2008) although not used in this work. Based on field control and integration of U-Pb and Sm-Nd isotopic data, these outhors subdivided the Amazonian Craton into eight different geological provinces: Amazônia Central, Carajás, Itamaca, Transamazônica, Tapajós-Parima, Rio Negro, Rondônia-Juruena, K'Mudku and Sunsas.

2.3.1.1 Sunsas Province

The Sunsas Province was originated during the last tectonic accretion of the Amazonian Craton (e.g., Tassinari and Macambira, 2004; Cordani and Teixeira, 2007; Teixeira et al., 2010). It is marked by transpressive boundaries to the west and east of the Paraguá Terrane (Ruiz, 2009) and the Rondoniana-San Ignácio Province (1.56-1.30 Ga), with prolongation to the Nova Brasilândia Belt (Teixeira et al., 2010). The Sunsas Province comprises three different mobile belts dated between 1.1 and 1.0 Ga: the Sunsas, Aguapeí, and Nova Brasilândia belts (Fig. 2.2). These belts were installed on Paleo- to Mesoproterozoic basement, comprising the Chiquitania Gneiss Complex (1,76-1.68 Ga) and Lomas Manechis Complex (1.81–1.65 Ga), the San Ignácio Group (<1.69 Ga) and the Pensamiento Suite (1.37-1.28 Ga; Teixeira et al., 2010). The basement behaved as host for the Sunsas high-K calc-alkaline magmatism, developed between 1.1 and 0.95 Ga in the craton southwestern portion (Litherland and Bloomfield, 1981; Litherland et al., 1986; Ruiz et al., 2006).

The Sunsas Province integrated interpretation of available data supports the hypothesis that the SW Amazonian Craton terrains and most of the Grenville margin of Laurentia were amalgamated to the Rodinia supercontinent as the result of two

independent collisional events (e.g., Teixeira et al., 2010). Comparing the Nd isotopic data reveals the different histories of these two cratons before the Grenville episode (e.g., Tohver et al., 2002, 2004). Parts of the Amazonian Craton were transferred towards the Superior Craton in Laurentia over extensive thrust sheets during the Grenvillian orogenesis after ~1.15 Ga ago (Rivers et al., 1989; Sadowski and Bettencourt, 1996; Tohver et al., 2002, 2004). The left-lateral transpressional character of the collision is consistent with the regional structural organization of both cratons as well as the indentation origin of the broad Grenvillian Orogenic System (e.g., Hoffman, 1992; Sadowski and Bettencourt, 1996). On the other hand, it is understood that the Sunsas Province is a Grenville Orogen continuation on the Laurentia eastern margin (Santos et al., 2000, 2008). The 1.3 Ga so called Alto Candeias orogen and the Santa Helena orogen at the southern portion of the Rondonian-San Ignácio Province can be correlated to the Pinwarian Orogeny of 1.4-1.3 Ga in Laurentia (Santos et al., 2008). This correlation indicates that the Rondoniana-San Ignacio Province and Laurentia connection began at ca. 1.45 Ga and culminated in the Sunsas collision and magmatism at 1.1-0.92 Ga, during the Amazonian Craton stabilization (Santos et al., 2008).

2.3.1.1.1 Magmatism

The Sunsas magmatism was generated during the collisional phase at the final stage of the Amazonian Craton stabilization (Litherland et al., 1989; Boger et al., 2005; Cordani and Teixeira, 2007; Teixeira et al., 2010). The final stage was marked by low- to medium-grade metamorphism in the Sunsas Belt basement, 1.1-1.0 Ga syn-tectonic granite intrusions along secondary shear zones (Litherland et al., 1989), and the installation of rift basins (Aguapeí aulacogen of 1.16 Ga; Saes, 1999; Geraldes et al., 2001; Ruiz, 2005, 2007; Teixeira et al., 2010). The 1.0 to 0.92 Ga post-tectonic magmatism, represented by the Rincón del Tigre Complex and the Guapé Suite, is associated with the crustal exhumation stage and consequent regional cooling after the orogenic collapse (Litherland et al., 1986; Teixeira et al., 2010, 2015; Siqueira, 2015).

The Aguapeí Belt granitic intrusions are mostly syn- to post-collisional, interpreted as a result of extensive intraplate magmatism (Ruiz, 2005; Cordani et al., 2010; Teixeira et al., 2015; Lima et al., 2016). The Stenian intracontinental large igneous province

(LIP; Ruiz et al., 2009; 2010; Lima, 2016; Lima et al., 2012, 2019; Teixeira et al., 2015), at the Brazil-Bolivia border, restricted to the Paraguá and Rio Apa terrains is represented by the Huanchaca, Rio Perdido, and Rincón del Tigre suites. This LIP resulted from an attempted continental break-up likely associated with the setting-up of the Aguapeí Aulacogen (Lima et al., 2019).

Studies estimate that in the Nova Brasilândia Belt (1215-910 Ma), the Sunsas orogeny developed continental extension with rift formation, intraplate plutonism, and turbidite sedimentation, followed by crustal transpression and thickening (Rizzotto, 2001). Detailed metamorphic petrology and structural data revealed that the Nova Brasilândia belt is characterized by heterogeneous metamorphic grades that increase from north to south (Luft et al., 2000; Tohver et al., 2004; Teixeira et al., 2010). The bimodal magmatism was accommodated in transcurrent zones (Rizzotto, 2001; Rizzotto and Hartmann, 2012; Rizzotto et al., 2013, 2014; Quadros et al., 2020).

2.3.1.1.2 Sunsas Belt

The NW-SE trending Sunsas Belt is approximately 600 km long (Fig. 2.2), compartmentalized by transpressive shear zones: the Rio Negro Front (RNF), Santa Catalina Straight Zone (SC), Concepción Front (CF) and San Diablo Front (SDF) (Litherland el a., 1986; Teixeira et al., 2010). The Rio Negro and Santa Catalina fronts define the tectonic transport of the Sunsas Belt from southwest to the northeast. The CF represents the northeastern boundary between high-grade metamorphic and metavolcanic-sedimentary sequence terrains (Litherland el a., 1986). Furthermore, this network of shear zones compartmentalized the Sunsas Province and acted as channels for the emplacement of syn- to late-tectonic granites (Sunsas granitic suite – Litherland et al., 1989; Teixeira et al., 2010; 2020).

The granitic plutons comprise syn-tectonic intrusions represented by the Limonal (1330 Ma; Matos, 2009), La Cruz (1673 Ma; Matos, 2009), San Miguel, Espiritu, Las Palmas, La Palca, San Pablo (1621 Ma; Matos, 2009), El Carmen and Nomoca granites, and post-tectonic intrusions, represented by the Talcoso, Casa de Piedra, Taperas, Cachuela, Lucma, and Tasseoro granites (Litherland et al., 1986). Interpretation of the Primavera and Naranjito granites suggest formation in a post-

tectonic setting (Litherland et al., 1986; Adamek et al., 1996). Isotopic and geochronological data (U-Pb in zircon) of the Talcoso and Cachuela granites reveal crystallization age of 1333±36 Ma and 1307±07 Ma, respectively (Vargas-Mattos, 2010), related to the San Ignácio Orogen (1.37-1.28 Ga) and not post-tectonic in relation to the Sunsas Orogen as previously inferred by Litherland et al. (1986).

Based on lithostratigraphic correlations and tectono-magmatic evolution, the Sunsas Orogen can be divided into three main stages (Ruiz, 2005; Teixeira et al., 2010). The first is defined by extensional tectonics when the passive margin was installed on the Paraguá Terrane western border, allowing for the Sunsas and Vibosi groups deposition. An internal rift was filled by intracontinental sediments of the Aguapeí Group, correlated to the Sunsas Group. The Sunsas Group comprises a 6500 m thick sequence with basal conglomerates, superposed by arkoses, sandstones, argillites, siltstones, and arkoses at the top. The Vibosi Group, formed of 2600 m of arkoses and sandstones, was deposited after a depositional hiatus (Litherland et al., 1986). The second stage is represented by tectonic inversion during an orogenic phase, which is characterized by maximum continental thickness, syn-tectonic magmatism, deformation, and medium grade metamorphism. At this stage, several syn- to late-granitic intrusions took place, along and across the previously formed second stage Sunsas and basement structures (Litherland et al., 1986; Adamek et al., 1996; Boger et al., 2005; Vargas-Mattos, 2006; Vargas-Mattos et al., 2009; Teixeira et al., 2010). The third and last stage is marked by decompression and post-tectonic granitic magmatism due to the extensional collapse of the orogen.

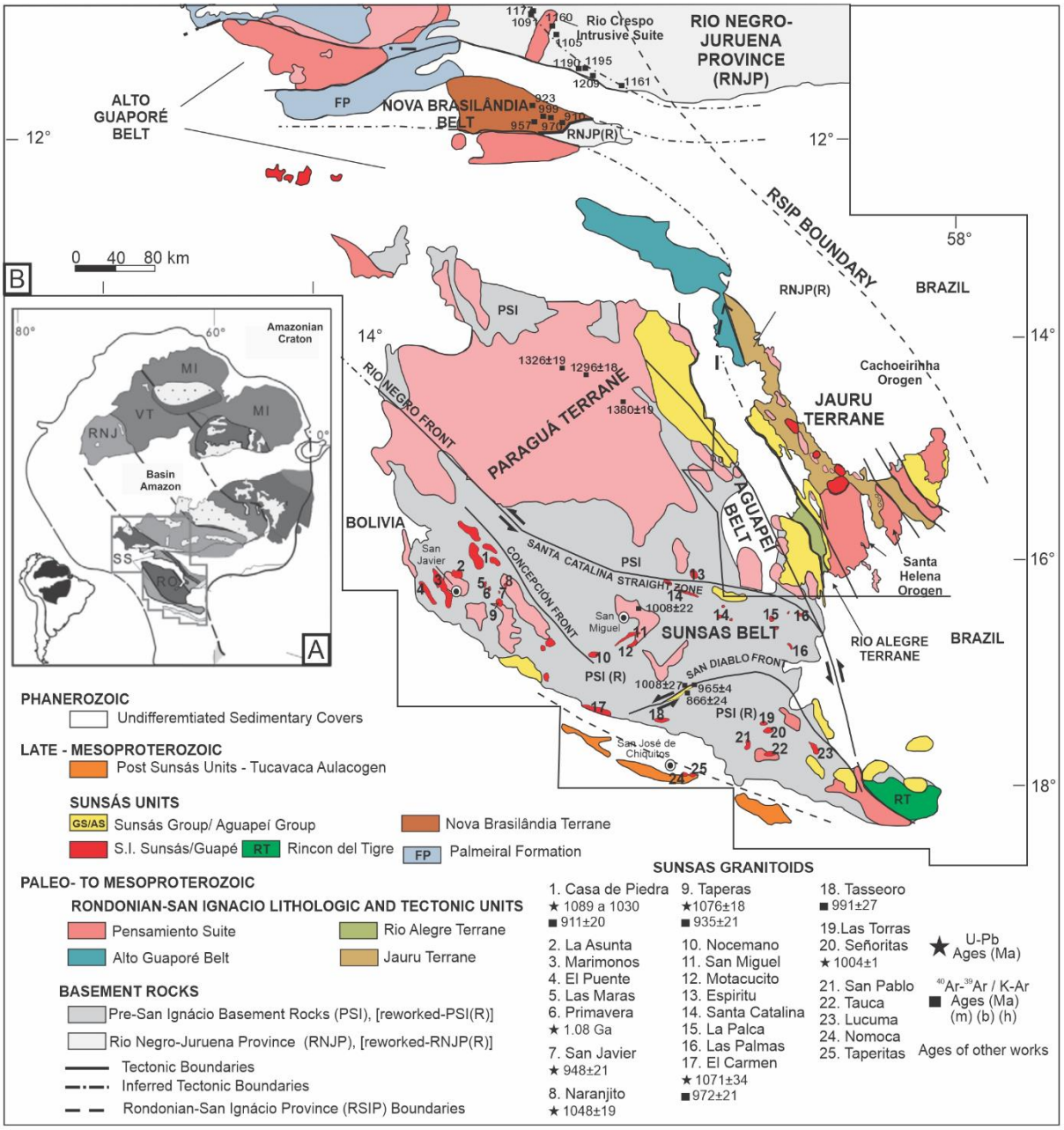

Figure 2.2. (A) Amazonian Craton tectonic compartmentalization (Cordani et al., 2010); (B) Schematic map of the Southwest Amazonian Craton with distribution of the main provinces, major orogens, terranes and belts, tectonic elements, and lithologic units in eastern Bolivia and western Brazil. Extracted and modified from Bettencourt et al. (2010).

2.4 Analytical methods and procedures

2.4.1 Geological Sampling

Sampling campaigns were performed in the San José de Chiquitos, San Miguel, and San Javier regions, northeastern Bolivia. The main petrographic units were recognized, and representative samples of the La Asunta, Nocemano, and Nomoca

granite plutons were collected. Thin sections were made and described for mineralogical and textural characterization at the Laboratory of Microscopy, Universidade de Brasília.

2.4.2 Geochemistry

Geochemical analyses were performed on three representative samples of the La Asunta, Nocemano, and Nomoca granites. The samples were crushed and ground in the Laboratory of Geochronology and Isotope Geochemistry at Universidade de Brasília. Analyses of major, minor, and trace elements were carried out by ALS Global Analytical Laboratories Ltd (Vancouver, Canadá). Major and minor elements were obtained by X-ray fluorescence (XRF) after fusion of the samples with lithium tetraborate. Trace elements were determined from melting 0.2 g of the samples with lithium metaborate/tetraborate, diluted nitric acid digestion, and ICP-MS analysis. Loss on ignition (LOI) was given by weight difference after heating at 1000°C. Precious metals and base metals were determined after 0.5 g of sample digestion with Acqua Regia with ICP-AES analysis.

2.4.3 U-Pb Isotopes

U-Pb isotopic analyses were performed on zircon grains using a Thermo-Fisher Neptune HR-MC-ICP-MS coupled with an Nd:YAG UP213 New Wave laser ablation system, at the Laboratory of Geochronology and Isotope Geochemistry, Universidade de Brasilia. The U-Pb analyses on zircon grains were carried out by the standard-sample bracketing method (Albarède et al., 2004), using the GJ-1 standard zircon (Jackson et al., 2004) in order to quantify the amount of ICP-MS fractionation. The tuned masses were 238, 207, 206, 204, and 202. The integration time was 1 second and the ablation time was 40 seconds. A 30 µm spot size was used and the laser setting was 10 Hz and 2-3 J/cm2. Two to four unknown grains were analyzed between GJ-1 analyses. $^{206}Pb/^{207}Pb$ and $^{206}Pb/^{238}U$ ratios were time corrected. On smaller zircon grains (about 50 µm), single-spot laser-induced fractionation of the $^{206}Pb/^{238}U$ ratio was corrected using the linear regression method (Košler et al., 2002). The raw data were processed off-line and reduced using an Excel worksheet (Bühn et al., 2009). During the analytical sessions, the zircon standard 91500 (Wiedenbeck et al., 2004) was also analyzed as an external standard.

Common ^{204}Pb was monitored using the ^{202}Hg and (^{204}Hg+^{204}Pb) masses. Common Pb corrections were not done due to very low signals for ^{204}Pb (<30 cps) and high $^{206}Pb/^{204}Pb$ ratios. Reported errors are propagated by quadratic addition [$(2SD^2+2SE^2)1/2$] (SD=standard deviation; SE=standard error) of external reproducibility and within-run precision. External reproducibility is represented by the standard deviation obtained from repeated analyses (~1.1 % for $^{207}Pb/^{206}Pb$ and up to ~2 % for $^{206}Pb/^{238}U$) of the GJ-1 zircon standard during the analytical sessions, and the within-run precision is the standard error calculated for each analysis. Concordia diagrams (2σ error ellipses), probability density plots, and weighted average ages were calculated using the Isoplot-3/Ex software (Ludwig, 2008).

2.5 Results

2.5.1 Field Aspects and Petrography

The Nomoca, La Asunta, and Nocemano plutons are located in the Proterozoic shield of eastern Bolivia (See Fig. 2.2). The La Asunta and Nocemano were emplaced into the Chiquitania Gneissic Complex (Fig. 2.3) and exhibit incipient tectonic foliation. The Nomoca is isotropic, partially covered by the Neoproterozoic Murciélago and Tucavaca sedimentary groups.

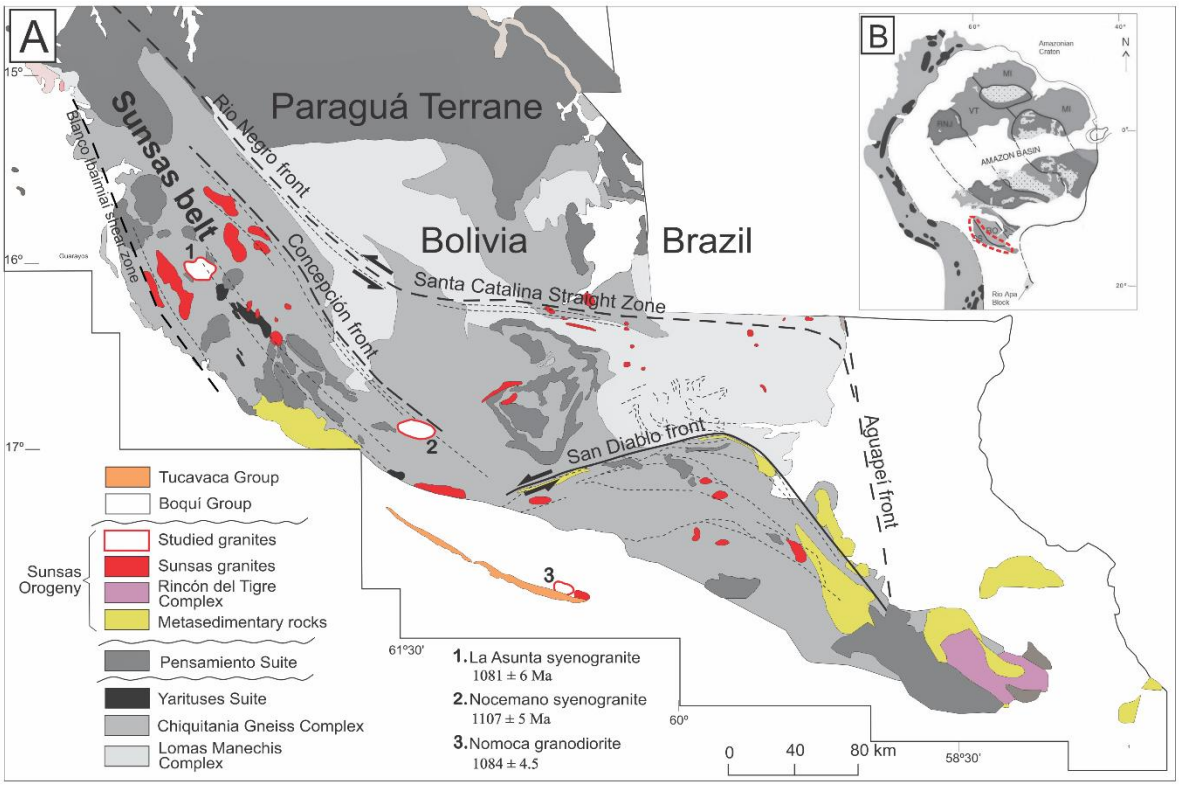

Figure 2.3. (A) Geological map of the Sunsas Belt showing the La Asunta (1), Nocemano (2) and Nomoca (3) plutons (modified from Matos et al., 2009); (B) tectonic compartmentalization of the Amazonian Craton (Cordani et al., 2010), showing the Sunsas Belt.

The Nomoca Granodiorite is mesocratic with massive internal structure. Plagioclase (60%), quartz (20%), biotite (10%) and megacrysts of K-feldspar (~10%; Fig. 2.4A) represent the mineral assemblage. Mineral proportions allow to classify the Nomoca intrusion as granodiorite of equigranular allotriomorphic texture, with a fine- to medium-grained matrix and K-feldspar phenocrysts. Titanite, apatite, zircon, sulfides, and Fe-Ti oxides occur as accessory minerals. Plagioclase exhibits albite-oligoclase composition (Fig. 2.4B, C) and occurs in anhedral crystals of 0.2 to 0.4 mm in size. Chlorite + epidote + clinozoisite inclusions indicate changes in central portions of the plagioclase crystals, typical of calcic compositions. Quartz is up to 0.2 mm in size and displays undulate extinction. Biotite occurs as subhedral and anhedral lamellae on the edges of feldspar crystals and in the interstices of quartz grains. In addition, biotite is also observed as euhedral inclusions in plagioclase, indicating coeval crystallization or assimilation processes. Titanite (~1%) presents rounded to angular forms, texturally associated with biotite lamellae (Fig. 2.4B, C). Hematite inclusions are commonly observed in titanite crystals. Magnetite subhedral crystals are observed in association with biotite and feldspars. Apatite and zircon (<1%) occur

preferably as inclusions within plagioclase and quartz. Sulfides are represented by subhedral crystals of chalcopyrite changing to covellite at the edges (Fig. 2.4B).

The La Asunta and Nocemano syenogranites are weakly foliated, leucocratic, and have porphyritic texture due to the presence of K-feldspar phenocrysts (Fig. 2.4F, H). In mesoscale, the Nocemano granite also presents equigranular textural facies and incipient foliation, marked by biotite orientation (Fig. 2.4I). Both granites present a similar mineral assemblage formed mainly of K-feldspar (40-50%), plagioclase (20-30%), quartz (~20%), and biotite (5-10%). These mineral proportions allow us to classify the La Asunta and Nocemano plutons as syenogranites of fine- to medium-grained inequigranular hypidiomorphic texture. Apatite, zircon, Fe-Ti oxides, magnetite, and hematite crystals complete the plutons mineralogy. La Asunta syenogranite also features monazite and epidote crystals.

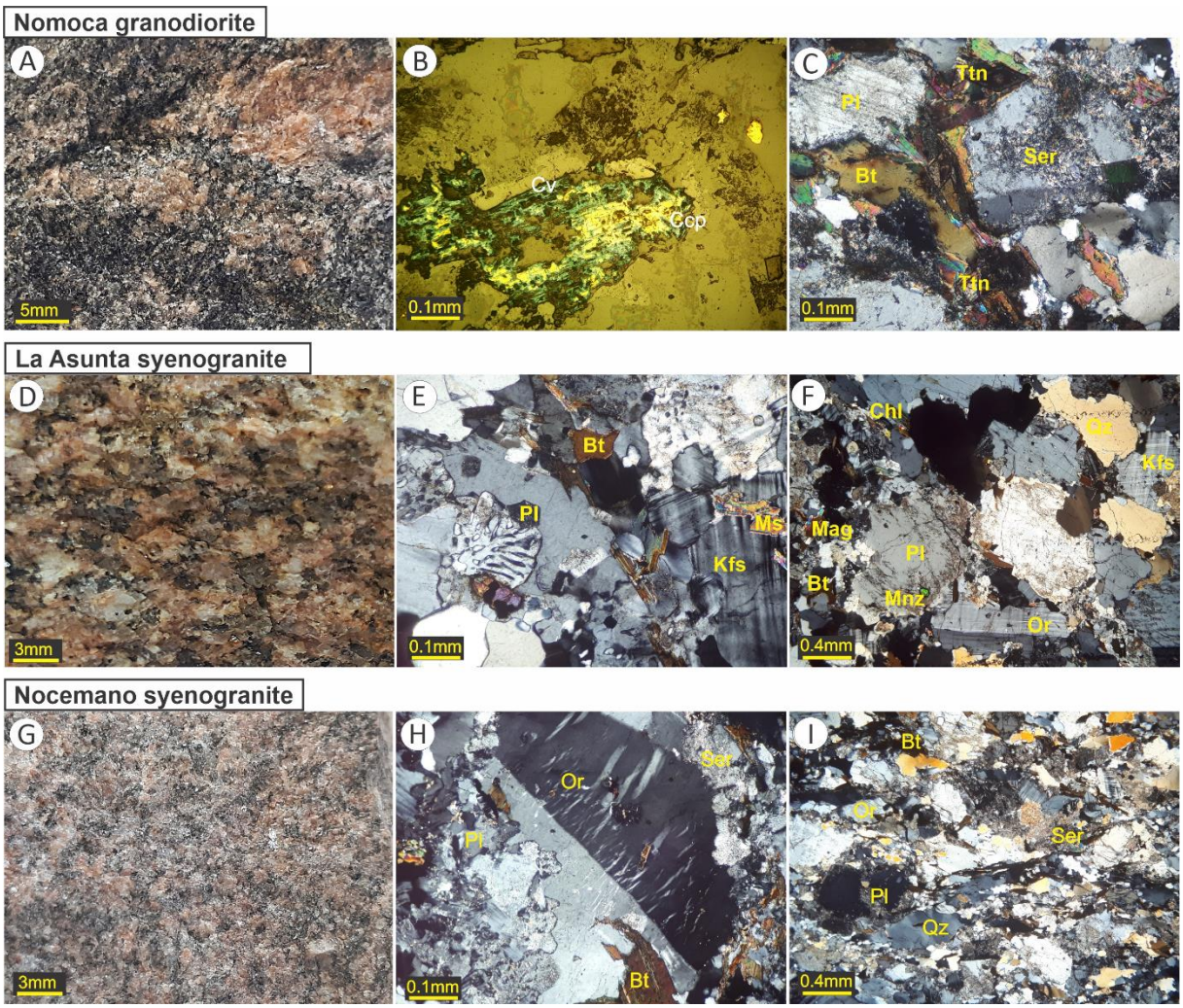

Figure 2.4. (A) Nomoca massive, mesocratic granodiorite hand specimen, with a centimetric phenocryst of K-feldspar; (B) photomicrography in reflected light of chalcopyrite crystal with alteration to covellite; (C) sericitized plagioclase and basal sections of titanite associated with biotite. Photomicrographs under natural light and with crossed nicols, respectively. (D) La Asunta granite macroscopic aspect showing porphyritic texture, marked by millimetric K-feldspar phenocrysts; (E) irregular contacts between feldspar crystals, plagioclase with myrmekite intergrowth texture and secondary muscovite associated with K-feldspar; (F) sericitized plagioclase, biotite altered to chlorite, orthoclase with combined Carlsbad and albite-pericline twinning, and rounded monazite crystal included in plagioclase. (G) leucocratic hand specimen of Nocemano granite, with K-feldspar phenocrysts; (H) perthitic orthoclase phenocryst; (I) stretched quartz crystals in the matrix, sericitized plagioclase and fine-grained alkali feldspar crystals. C, E, F, H and I, photomicrographs under crossed nicols. Mineral symbols according to Whitney and Evans (2010).

K-feldspar occurs as subhedral to anhedral crystals, with “tartan” and Carlsbad twinning. Occasionally, twinning can occur in combination (Fig. 2.4H). K-feldspar crystals exhibit dimensions between 0.1 and 0.4 mm in length, while phenocrysts reach 1 cm. Some phenocrysts exhibit perthitic intergrowth (Fig. 2.4H). Based on optical properties, plagioclase has a sodic composition between albite and oligoclase; it occurs as anhedral to subhedral crystals of 0.2 to 0.8 mm in length and

presents albite/pericline-type gemination. Myrmekite is locally observed (Fig. 2.4E). The La Asunta and Nocemano plagioclase crystals exhibit intense sericitization (Fig. 2.4F, I) like the Nomoca Granodiorite (Fig. 2.4C). The quartz grains are anhedral, rounded, with dimensions between 0.02 and 0.4mm. Biotite occurs as free subhedral lamellae and euhedral crystals included in the feldspar grains. In the La Asunta pluton, biotite is altered to chlorite and muscovite along cleavage planes. Quartz crystals exhibit strong undulate extinction. Quartz ribbons are reoriented according to the direction of biotite in the Nocemano syenogranite (Fig. 2.4I). Apatite and zircon occur within feldspars and biotite. Euhedral crystals of martitized magnetite and Fe-Ti oxides are recorded in the syenogranites.

2.5.2 Geochemistry

Chemical analyses were carried out on samples of Nomoca granodiorite and La Asunta and Nocemano syenogranites and later compiled and compared with compositions and patterns of Sunsas magmatism presented by Vargas-Mattos et al. (2009) (Table 2.2). The Nomoca granodiorite has a low content of SiO_2 (67.3 wt.%) and K_2O (2.88 wt.%) and high concentrations of Al_2O_3 (16.45 wt.%), Fe_2O_3 (3.81 wt.%), MgO (1.61 wt. %), CaO (2.88 wt. %) and Na_2O (4.21 wt. %) in relation to the Nocemano and La Asunta granites. The Nocemano syenogranite has a higher content of SiO_2 (70.4 wt.%) and K_2O (5.94 wt.%) and lower concentrations of Al_2O_3 (14 wt.%), Fe_2O_3 (3.31 wt.%), MgO (0.56 wt.%), CaO (1.3 wt.%) and Na_2O (2.68 wt.%) in relation to the Nomoca granodiorite. The La Asunta syenogranite shows high contents of SiO_2 (74.9 wt.%) and K_2O (5.14 wt.%) and concentrations of Al_2O_3 (13.85 wt.%), Fe_2O_3 (2.26 wt.%), MgO (0.34 wt.%), CaO (0.92 wt.%) and Na_2O (3.16 wt.%) close to those presented by the Nocemano granite.

Table 2-2. Geochemical data for the El Carmen, Naranjito, and Taperas monzogranites, Primavera granite (Vargas-Mattos, 2010), La Asunta and Nocemano syenogranites, and Nomoca granodiorite.

Sample	EC0601	EC0604a	EC0604b	NJ0725	NJ0726	NJ0727	NJ0728	NJ0729	BO0419	TP0711	TP0712	TP0714	TP0715	TP0716a	TP0716b	TP0717	BO0421	PV0719	PV0720	PV0721	PV0722	PV0723	PV0724	BO0420	LA14	SM-07A	TAP02
Petrograph	Monzogranite																	Granite							Sienogranite		Granodiorite
SiO_2	73.64	69.81	74.39	77.41	74.26	75.29	75.84	75.26	74.65	76.03	70.08	69.30	70.23	72.97	72.00	72.22	72.47	70.13	79.65	72.05	75.40	76.91	75.65	75.36	74.90	70.40	67.30
Al_2O_3	13.46	14.28	12.99	12.60	13.61	13.24	13.11	12.64	13.43	12.47	15.15	13.73	13.14	12.99	13.80	13.78	12.98	13.71	11.75	14.73	13.68	12.46	13.03	13.34	13.85	14.00	16.45
Fe_2O_3	2.14	2.54	1.21	0.64	0.71	0.93	0.80	0.70	1.49	1.09	1.61	3.50	2.84	2.13	2.44	2.35	2.97	4.09	0.61	2.04	0.80	1.01	0.75	1.12	2.26	3.31	3.81
MnO	0.04	0.04	0.02	0.09	0.08	0.06	0.04	0.05	0.04	0.03	0.03	0.06	0.05	0.05	0.05	0.05	0.06	0.08	0.06	0.05	0.07	0.06	0.05	0.09	0.03	0.03	0.06
MgO	0.34	0.59	0.22	0.05	0.04	0.11	0.09	0.07	0.15	0.13	0.34	0.76	0.59	0.42	0.51	0.53	0.60	1.34	0.01	0.46	0.02	0.04	0.03	< 0.01	0.34	0.56	1.61
CaO	1.15	1.72	1.13	0.60	0.88	0.84	0.77	0.54	1.07	0.39	1.17	1.97	1.63	1.09	1.36	1.72	1.94	3.62	0.22	1.77	0.33	0.37	0.16	0.52	0.92	1.30	2.88
Na_2O	3.07	3.23	2.79	3.86	4.02	3.73	3.64	3.81	3.89	3.64	3.64	3.81	3.61	3.34	3.25	3.50	3.49	2.72	3.58	3.72	4.13	3.59	3.53	3.91	3.16	2.68	4.21
K_2O	5.83	5.50	5.77	4.19	4.98	4.57	4.67	4.34	4.44	4.49	6.71	4.27	4.50	4.61	5.89	4.79	3.93	2.50	3.83	4.65	4.54	4.59	5.14	4.50	5.14	5.94	2.88
P_2O_5	0.08	0.16	0.05	0.02	0.02	0.03	0.03	0.02	0.04	0.06	0.10	0.19	0.15	0.13	0.14	0.14	0.15	0.16	0.02	0.12	0.03	0.03	0.02	0.02	0.05	0.15	0.21
TiO_2	0.28	0.47	0.19	0.05	0.04	0.10	0.08	0.07	0.13	0.14	0.27	0.62	0.53	0.42	0.50	0.49	0.54	0.56	0.02	0.32	0.03	0.06	0.04	0.03	0.24	0.50	0.54
Cr_2O_3	0.00	0.00	0.00	0.00	0.00	0.00	0.00	0.00	0.00	0.00	0.00	0.00	0.00	0.00	0.00	0.00	0.00	0.00	0.00	0.00	0.00	0.00	0.00	0.00	0.01	0.01	0.01
LOI	0.76	1.12	0.52	1.09	0.96	1.03	0.68	1.03	0.60	0.94	0.92	0.93	0.95	0.95	1.02	1.01	0.74	1.86	1.11	0.74	1.20	1.23	1.05	1.07	0.72	1.06	1.41
TOTAL	100.79	99.46	99.28	100.60	99.60	99.93	99.75	98.53	99.93	99.41	100.02	99.14	98.22	99.10	100.96	100.58	99.87	100.77	100.86	100.65	100.23	100.35	99.45	99.96	101.61	99.93	101.37
Mg#	22.07	29.28	24.48	12.22	9.13	17.41	16.70	15.13	15.21	17.53	27.35	27.91	27.02	26.01	27.14	28.67	26.48	36.87	2.84	28.67	4.27	6.59	6.66	<	21.15	23.17	42.96
Sc	6.00	3.00	0.00	5.00	3.00	5.00	3.00	6.00	5.00	3.00	3.00	7.00	6.00	5.00	5.00	5.00	5.00	11.00	1.00	4.00	2.00	2.00	2.00	2.00	4.00	5.00	7.00
V	14.00	32.00	8.00	0.00	0.00	5.00	0.00	0.00	9.00	6.00	20.00	38.00	31.00	24.00	30.00	29.00	29.00	75.00	0.00	18.00	0.00	5.00	0.00	0.00	16.00	33.00	80.00
Cr	0.00	0.00	0.00	0.00	0.00	0.00	0.00	0.00	0.00	0.00	0.00	0.00	0.00	0.00	0.00	0.00	30.00	60.00	0.00	0.00	0.00	0.00	0.00	20.00	10.00	10.00	90.00
Co	20.00	18.00	16.00	47.00	24.00	15.00	24.00	39.00	2.00	59.00	19.00	20.00	28.00	34.00	24.00	24.00	4.00	26.00	26.00	16.00	21.00	26.00	17.00	0.00	2.00	4.00	9.00
Ni	0.00	0.00	0.00	0.00	0.00	0.00	0.00	0.00	0.00	0.00	0.00	0.00	0.00	0.00	0.00	0.00	0.00	0.00	0.00	0.00	0.00	0.00	0.00	0.00	1.00	2.00	26.00
Cu	0.00	0.00	0.00	0.00	0.00	10.00	0.00	0.00	0.00	0.00	0.00	10.00	10.00	0.00	0.00	0.00	0.00	0.00	0.00	0.00	0.00	0.00	0.00	0.00	5.00	3.00	378.00
Zn	70.00	50.00	40.00	0.00	0.00	50.00	40.00	40.00	40.00	40.00	40.00	60.00	60.00	60.00	80.00	70.00	70.00	70.00	50.00	70.00	60.00	60.00	40.00	60.00	48.00	85.00	98.00

Sample	EC0601	EC0604a	EC0604b	NJ0725	NJ0726	NJ0727	NJ0728	NJ0729	BO0419	TP0711	TP0712	TP0714	TP0715	TP0716a	TP0716b	TP0717	BO0421	PV0719	PV0720	PV0721	PV0722	PV0723	PV0724	BO0420	LA14	SM-07A	TAP02
Petrograph	Monzogranite																				Granite				Sienogranite		Granodiorite
Ga	20.00	21.00	18.00	26.00	26.00	25.00	22.00	25.00	23.00	17.00	22.00	18.00	17.00	23.00	23.00	23.00	21.00	15.00	26.00	21.00	31.00	24.00	26.00	30.00	20.10	22.60	25.90
Rb	262.00	251.00	249.00	467.00	557.00	439.00	378.00	508.00	395.00	124.00	322.00	118.00	162.00	313.00	344.00	282.00	243.00	77.00	630.00	160.00	776.00	572.00	674.00	739.00	214.00	305.00	164.00
Sr	115.00	200.00	193.00	26.00	30.00	86.00	89.00	40.00	86.00	81.00	253.00	264.00	222.00	179.00	219.00	225.00	199.00	456.00	6.00	337.00	9.00	6.00	6.00	9.00	167.00	139.00	395.00
Y	26.00	70.00	20.00	29.00	21.00	57.00	19.00	15.00	24.00	27.00	10.00	37.00	37.00	18.00	32.00	34.00	27.00	24.00	114.00	12.00	109.00	133.00	87.00	168.00	15.70	22.20	17.90
Zr	0.00	0.00	0.00	0.00	0.00	0.00	0.00	0.00	0.00	145.00	140.00	303.00	277.00	246.00	290.00	284.00	298.00	196.00	45.00	212.00	57.00	97.00	72.00	77.00	267.00	447.00	383.00
Nb	15.00	19.00	8.00	19.00	12.00	25.00	20.00	27.00	27.00	11.00	10.00	13.00	13.00	16.00	20.00	18.00	23.00	7.00	27.00	11.00	43.00	38.00	33.00	37.00	12.70	14.70	12.50
Cs	0.90	1.40	0.70	9.00	11.20	10.40	5.30	12.00	7.90	0.00	4.30	4.30	6.30	6.70	8.80	5.90	5.80	2.30	10.20	4.20	7.80	12.20	9.80	10.90	3.09	1.34	2.78
Ba	574.00	924.00	894.00	103.00	115.00	369.00	324.00	112.00	329.00	774.00	996.00	1208.00	1140.00	656.00	1110.00	708.00	637.00	967.00	13.00	1146.00	10.00	54.00	33.00	12.00	733.00	784.00	542.00
Hf	8.90	8.00	4.90	5.70	3.80	4.60	3.90	4.80	5.10	5.10	4.40	8.10	7.60	7.80	8.60	8.10	8.40	5.20	4.10	5.80	5.60	5.60	5.20	6.10	8.10	13.40	9.40
Ta	0.50	2.20	1.10	2.30	1.30	3.10	2.50	3.40	2.30	1.10	1.10	1.20	1.30	1.60	2.10	2.00	2.20	0.70	6.40	1.00	11.50	5.60	8.00	6.60	0.60	0.30	1.30
Pb	42.00	21.00	34.00	37.00	66.00	48.00	46.00	49.00	47.00	15.00	31.00	12.00	14.00	37.00	49.00	21.00	35.00	10.00	36.00	26.00	27.00	26.00	10.00	41.00	29.00	38.00	19.00
Th	80.50	55.60	56.70	20.90	23.20	28.50	21.20	32.60	30.70	14.10	27.00	13.20	15.50	48.70	62.70	45.20	66.60	9.20	14.20	14.90	21.20	43.00	27.40	32.40	59.90	83.60	33.60
U	15.30	5.70	4.90	5.70	18.20	8.60	17.80	9.60	27.00	2.30	6.30	4.50	4.90	10.30	16.50	7.20	10.70	1.80	6.10	3.00	9.20	4.60	2.90	5.30	5.71	1.71	4.58
La	96.10	74.40	48.30	7.30	7.40	62.90	4.60	12.30	38.50	41.30	48.50	52.20	59.40	80.30	87.70	80.80	87.50	33.30	11.80	28.20	11.90	20.10	11.80	23.20	115.00	171.50	74.30
Ce	191.00	136.00	86.50	12.10	16.20	52.50	19.20	26.70	50.60	79.70	73.10	107.00	114.00	144.00	160.00	141.00	161.00	70.60	35.80	76.10	38.80	58.60	33.20	58.90	242.00	397.00	141.00
Pr	23.20	16.60	9.61	1.67	1.66	13.00	1.24	2.82	7.07	9.20	7.40	13.00	13.90	14.80	16.70	15.50	17.30	8.58	4.61	6.36	4.36	7.41	4.25	8.68	24.50	41.70	12.95
Nd	76.60	55.70	29.10	5.50	4.70	40.70	4.60	8.30	24.10	29.00	21.70	43.50	44.40	42.90	50.20	47.40	54.30	29.20	21.50	19.40	19.50	32.10	19.60	45.50	81.40	141.50	43.00
Sm	14.80	10.50	4.50	1.20	0.90	8.40	1.20	1.50	4.00	5.20	3.30	7.70	7.60	6.50	8.00	7.90	9.10	5.40	6.70	3.40	5.60	7.90	5.30	13.50	13.20	22.80	6.61
Eu	1.22	1.77	1.06	0.21	0.18	1.33	0.35	0.24	0.61	0.73	0.92	1.81	1.61	1.25	1.43	1.46	1.64	1.41	0.07	0.87	< 0.05	0.21	0.10	0.13	1.06	1.42	1.38
Gd	11.30	10.50	3.70	1.50	1.00	9.20	1.70	1.40	3.40	4.30	2.40	7.10	7.00	5.10	6.20	6.70	6.60	4.80	8.50	2.60	7.20	9.20	6.30	16.00	7.92	11.15	4.28
Tb	1.30	1.80	0.60	0.30	0.20	1.40	0.30	0.30	0.50	0.70	0.40	1.10	1.10	0.70	0.90	1.00	1.00	0.80	2.10	0.40	1.70	2.10	1.50	3.50	0.98	1.39	0.59

Sample	EC0601	EC0604a	EC0604b	NJ0725	NJ0726	NJ0727	NJ0728	NJ0729	BO0419	TP0711	TP0712	TP0714	TP0715	TP0716a	TP0716b	TP0717	BO0421	PV0719	PV0720	PV0721	PV0722	PV0723	PV0724	BO0420	LA14	SM-07A	TAP02
Petrograph	Monzogranite																	Granite							Sienogranite		Granodiorite
Dy	5.50	10.30	3.50	2.40	1.40	7.20	2.50	1.70	2.80	4.10	1.80	6.00	5.80	3.40	4.40	5.00	5.00	4.00	14.80	2.10	12.80	15.00	10.80	24.10	4.45	5.90	3.46
Ho	0.90	2.10	0.70	0.70	0.40	1.40	0.60	0.40	0.60	0.80	0.30	1.20	1.20	0.60	0.80	1.00	1.00	0.80	3.20	0.40	3.00	3.30	2.50	5.20	0.60	0.91	0.58
Er	2.60	6.60	2.20	2.90	1.50	4.30	2.10	1.60	2.00	2.50	1.00	3.80	3.70	1.90	2.50	3.10	2.80	2.40	11.50	1.10	11.40	11.60	8.70	17.90	1.34	2.01	1.77
Tm	0.37	0.98	0.34	0.72	0.34	0.76	0.40	0.34	0.37	0.40	0.15	0.58	0.56	0.28	0.37	0.46	0.42	0.36	2.22	0.15	2.31	2.01	1.51	3.33	0.17	0.23	0.23
Yb	2.20	6.10	2.10	6.30	2.80	5.40	3.00	2.80	2.70	2.50	1.00	3.60	3.50	1.80	2.30	2.80	2.70	2.20	15.80	1.00	17.10	13.60	11.00	23.20	1.04	1.30	1.65
Lu	0.34	0.87	0.31	1.28	0.57	0.92	0.53	0.52	0.47	0.37	0.16	0.55	0.56	0.29	0.34	0.43	0.42	0.34	2.31	0.14	2.65	2.02	1.62	3.57	0.22	0.20	0.25
(La/Yb)N	31.33	8.75	16.50	0.83	1.90	8.36	1.10	3.15	10.23	11.85	34.79	10.40	12.17	32.00	27.35	20.70	23.25	10.86	0.54	20.23	0.50	1.06	0.77	0.72	79.32	94.63	32.30
(La/Sm)N	4.19	4.57	6.93	3.93	5.31	4.83	2.47	5.29	6.21	5.13	9.49	4.38	5.05	7.98	7.08	6.60	6.21	3.98	1.14	5.35	1.37	1.64	1.44	1.11	5.62	4.86	7.26
(Tb/Yb)N	2.69	1.34	1.30	0.22	0.32	1.18	0.45	0.49	0.84	1.27	1.82	1.39	1.43	1.77	1.78	1.62	1.68	1.65	0.60	1.82	0.45	0.70	0.62	0.69	4.28	4.86	1.63
(La/Lu)N	30.29	9.17	16.70	0.61	1.39	7.33	0.93	2.54	8.78	11.96	32.49	10.17	11.37	29.68	27.64	20.14	22.33	10.50	0.55	21.59	0.48	1.07	0.78	0.70	56.02	91.90	31.85
Eu/Eu*	0.29	0.52	0.79	0.48	0.58	0.46	0.75	0.51	0.51	0.47	1.00	0.75	0.67	0.66	0.62	0.61	0.65	0.85	0.03	0.89	#VALOR!	0.08	0.05	0.03	0.32	0.27	0.79

Harker diagrams of major elements, taking the SiO_2 as fractionation factor (Fig. 2.5), show ferromagnesian compositions (3.8-4.0 Fe_2O_3 and 1.31-1.81 wt% MgO) with high Ca (2.88-3.62 wt.%) and Al (13.75-16.45 wt.%) for the Nomoca granodiorite and Primavera granite, in their mesocratic portions. La Asunta and Nocemano syenogranites show compatibility of major elements concentrations with those presented by the Naranjito, Taperas and El Carmen monzogranites and leucocratic portions of the Primavera granite, that is, high content of SiO_2 (69-79 wt.%) and low concentrations of Al_2O_3 (11-13 wt.%), Fe_2O_3 (0.6-3 wt.%), MgO (<0.7 wt.%) and CaO (<1.9 wt.%). SiO_2 versus oxides diagrams show a fractionation trend between the granites of 79 to 67 wt.% (Fig. 2.5). Na_2O (2-3 wt.%) and K_2O (4-6 wt.%) contents show a flat trend with increasing SiO_2 content (Fig. 2.5E, F). The immobile behavior of P_2O_3 and TiO_2 better discriminates the less fractionated Nomoca granodiorite from the more evolved Nocemano and La Asunta granites (Fig. 2.5G, H).

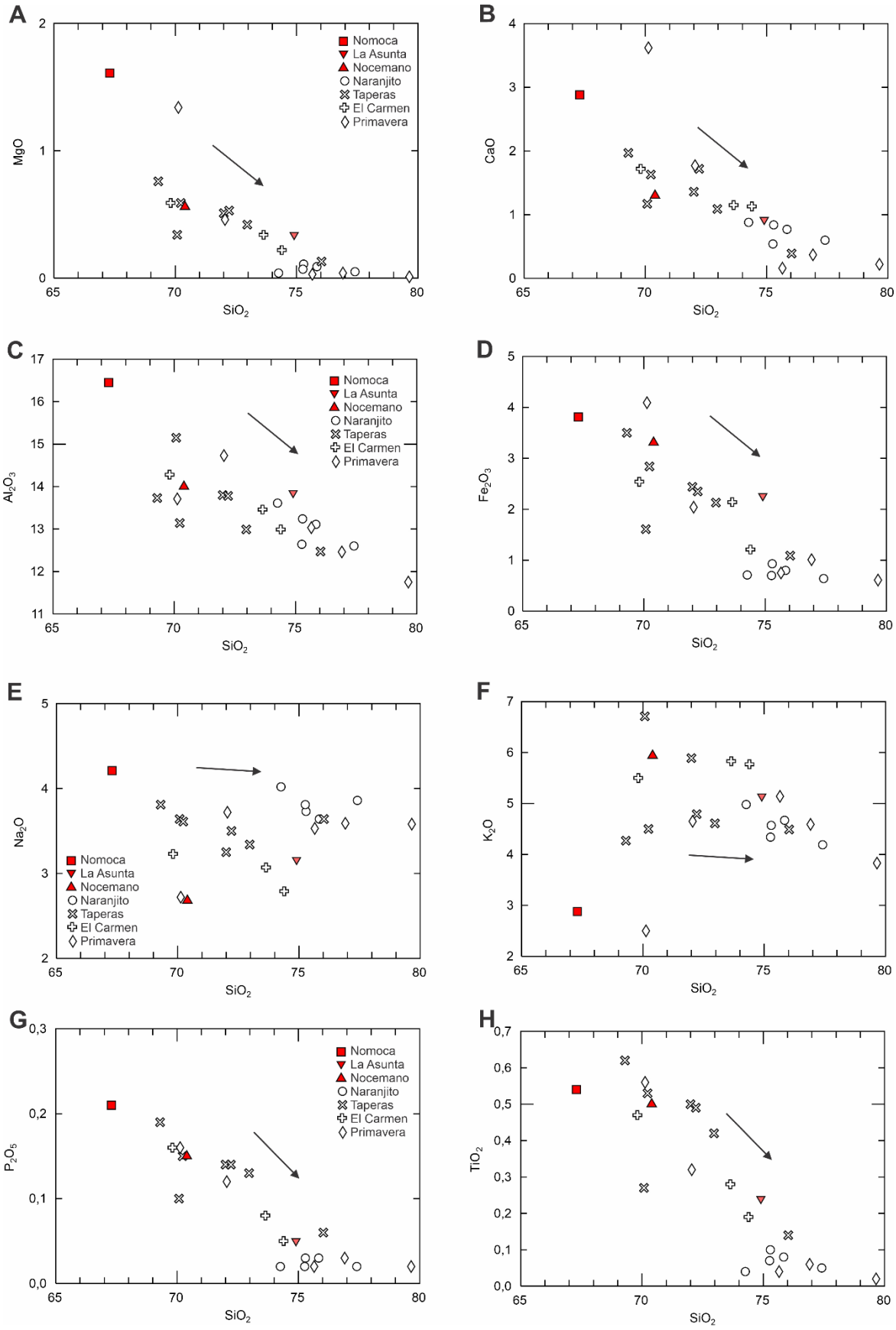

Figure 2.5. Harker diagrams of major elements versus Si02 of the Sunsas magmatism in Bolivia.

In the AFM diagram (Irvine and Baragar, 1971), the studied plutons show calc-alkaline geochemical affinity, with a well-defined alkali enrichment trend from the Nomoca granodiorite to the La Asunta syenogranite (Fig. 2.6A). The Na_2O+K_2O-CaO diagram versus SiO_2 (Frost et al., 2001) shows the fractionation of the Nomoca granodiorite in relation to the La Asunta syenogranite. The Nocemano syenogranite presents a pattern compatible with more fractionated alkali-calcium (K_2O ~6 wt.%) evolution, although the calc-alkaline series is the main evolutionary trend recorded in the studied rocks (Fig. 2.6B). In the Al/(Na+K) versus Al/(Ca+Na+ K) diagram (Shand, 1943), the granitic bodies show metaluminous to peraluminous character (Fig. 2.6C), recording the fractionation of the Nomoca granodiorite compared to La Asunta granite in both depletion of aluminum (16 to 13 wt.%) and calcium (2.8 to 0.9 wt.%). The compositional transition from magnesian to ferrous magma in Harker diagrams is also evident in the FeOt/(FeOt+MgO) versus SiO_2 diagram (Frost et al., 2001), in which the FeOt/(FeOt+MgO) ratio ranges from 0.6 to 1 (Fig. 2.6D), reflecting the decrease of MgO contents from 1.61 wt.% (Nomoca granodiorite) to only 300 ppm (Primavera granite).

The Rb versus Y/Nb ratios are used as discriminant factors of tectonic setting (Pearce et al., 1984, 2008). The diagram shows that the studied magmatism has a typical signature of post-collisional granitogenesis (Fig. 2.6E). In the R1-R2 diagram (Batchelor and Bowden, 1985), the granitic intrusions define a magmatic trend in syn- to post-collisional stages.

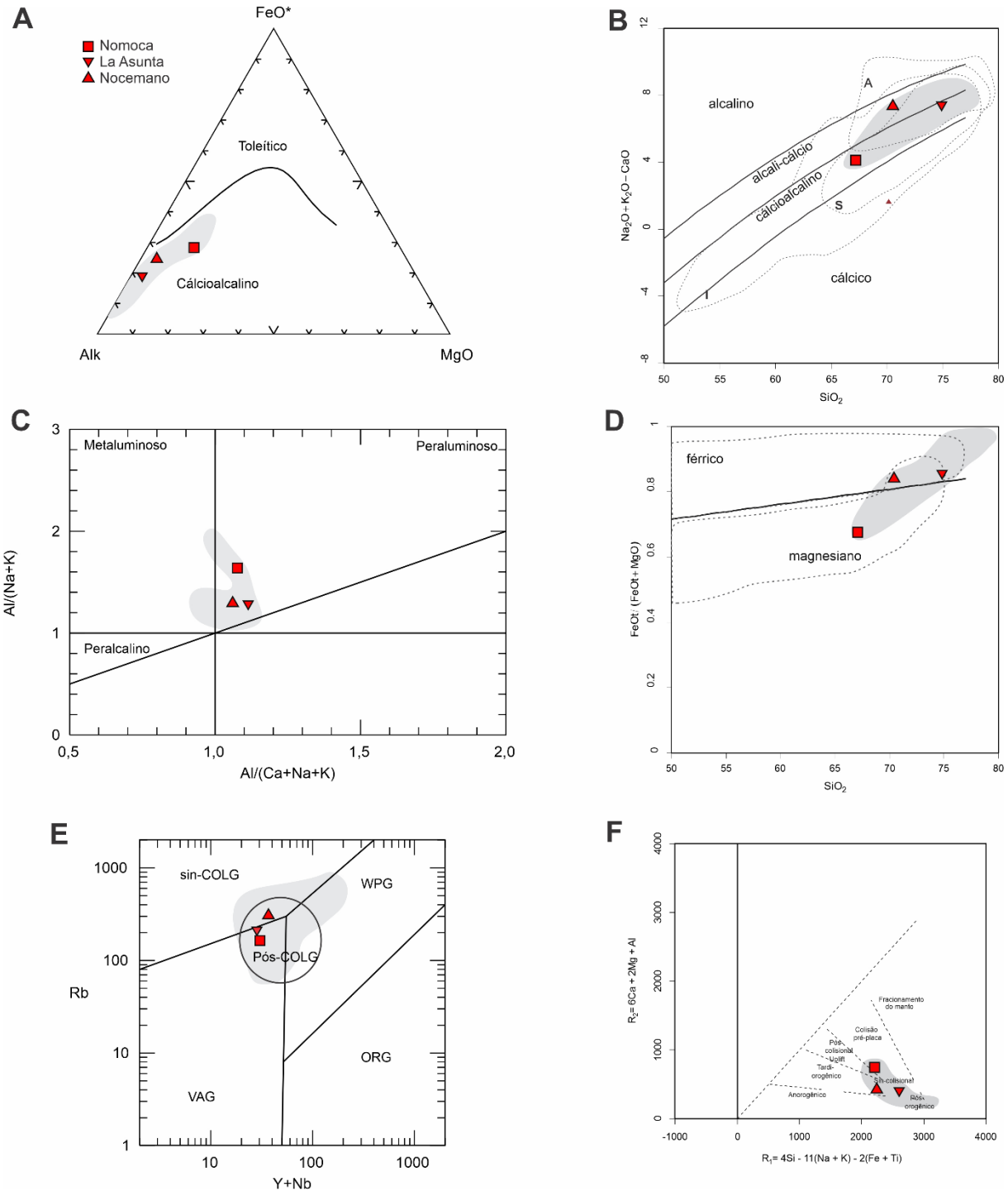

Figure 2.6. Discriminant diagrams of the studied Sunsas granitoids. (A) AFM diagram from Irvine and Baragar (1971); (B) Na2O+K2O-CaO versus SiO2 (Frost et al., 2001); (C) A/NK [= (Al/Na+K)] versus A/CNK [= (Al+Na+K)] (Shand, 1943); (D) FeOt/(FeOt-MgO) versus SiO2 (Frost et al., 2001); (E) Y+Nb versus Rb (Pearce et al., 2008); (F) R1 [4Si–11(Na+K)–2(Fe+Ti)] versus R2 [6Ca+2Mg+Al] (Batchelor and Bowden, 1985); The compositional field of the Naranjito, Taperas, El Carmen and Primavera granites is evidenced in gray (Vargas-Mattos, 2010).

The REE chondrite-normalized discriminant diagrams (Sun and McDonough, 1989) define the slight enrichment of the heavy REE in the Nomoca granodiorite,

(Tb/Yb)N=1.63, and higher fractionation of the light rare earth elements (LREE), (La/Sm)N=7.26, with a discrete Eu anomaly (Eu/Eu*=~0.79) (Fig. 2.7A). La Asunta and Nocemano syenogranites show LREE enrichment, (Tb/Yb)N of 4.28 to 4.68, but smaller fractionation of HREE, (La/Sm)N=5.62 to 4.86, with negative Eu anomaly values, between 0.27 and 0.31 (Fig. 2.7A). The primitive mantle-normalized multielement diagram (McDonough and Sun, 1995) shows all analyses with significant negative anomalies of Ti, P, Sr, Nb, Ta, and Ba and positive anomalies of Nd, Sm, Pb, Th and Rb (Fig. 2.7B). In the Figure 6C diagram, the samples display two different fractionation patterns for the studied rocks. The first pattern is sub-horizontal, with (La/Lu)N ratios between 1.07 and 0.55 and stronger negative Eu anomalies. Chemical analyses of the second group show high fractionation ratios, with (La/Lu)N ratio up to 91, but with weak negative Eu anomalies. Both groups have the same geochemical signature in the multielement diagrams (Fig. 2.7D). The Primavera granite is the best example of the two distinct geochemical patterns (Fig. 2.7E): samples with (La/Lu)N ratios between 0.55 and 1, with prominent Eu anomaly (0.08 and 0.03) (subhorizontal black lines; Fig. 2.7E), and analyses with (La/Lu)N ratios between 10.5 and 20.5 and discrete negative Eu anomalies (0.89) (inclined gray lines in Fig. 2.7E). Although they preserve the same geochemical signature pattern, in the multielement diagram the less fractionated samples (black lines) present depletion of Ti, Eu, P, Sr, La, and Ba, besides being more enriched in ETRP, Pb, Rb, and Cs. On the other hand, samples with high (La/Lu)N ratios (gray lines) exhibit more positive anomalies of Sr and Ba and more negative anomalies of Nb and Ta than the first group samples.

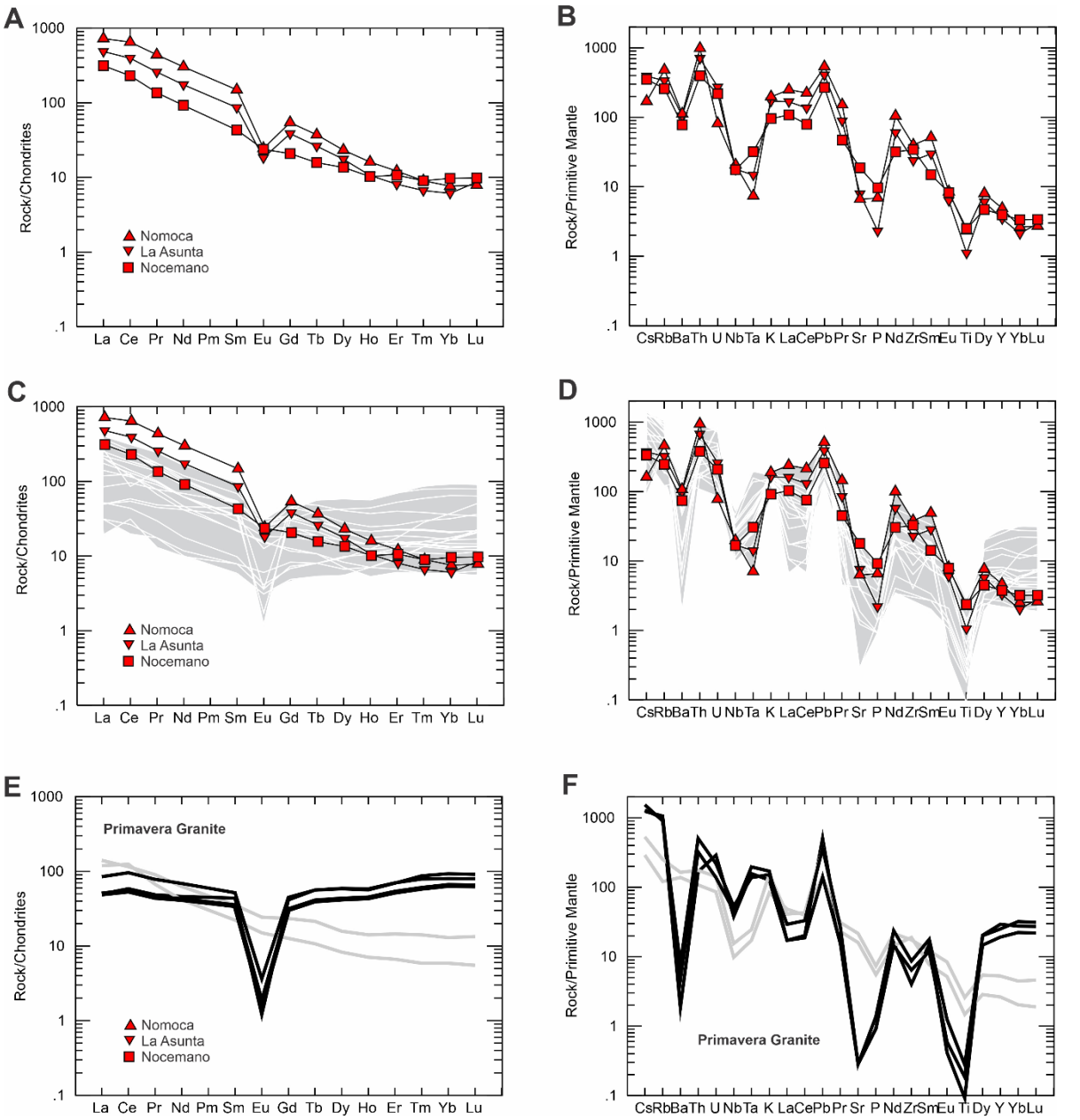

Figure 2.7. (A, C, E) Chondrite-normalized REE fractionation diagrams from Sun and McDonough (1989); (B, D, F) Primitive mantle-normalized multielement diagrams according to McDonough and Sun (1995). A and B present the fractionation pattern of the La Asunta, Nocemano, and Nomoca plutons. C and D show the data pattern compiled from the Taperas, El Carmen, Naranjito, and Primavera plutons. E and F diagrams show the Primavera granite fractionation pattern from Vargas-Mattos (2010).

2.5.3 Geochronology

U-Pb analyses were performed on zircon crystals from the Nomoca, La Asunta, and Nocemano plutons (Table 2.3). The spots for the analyses were preferably performed on crystal cores. Analyses were also performed at the edges of grains with well-developed rims observed in backscattered electron images. Inclusions, fractures, or metamictic zircon domains were avoided for U-Pb analyses.

The Nomoca granodiorite displays prismatic zircon crystals between 200 and 300 μm long. Backscattered electron images (BSE) show internal structuring of crystals, well-delimited zonation between core and rim, and commonly lighter rims than cores (Fig. 2.8E). Zircon cores record Archean, Paleoproterozoic, and Mesoproterozoic ages (Table 2.3; Fig. 2.8A, E). The oldest zircon cores produced two discordia ages, one Rhyacian age of 2122±196 Ma and another discordia of 1761±160 Ma (Fig. 2.8B). These zircon cores have rims of 1445-1332 Ma and 1169-968 Ma. Zircon crystals yield a third discordia age of 1109±22 Ma (Fig. 2.8B), from which was obtained a concordia age of 1083±5 Ma (Fig. 2.8C). Prismatic zircon rims record age of 504±7 Ma ($^{206}Pb/^{238}U$ age) with a core age of 1001±19 Ma. Zircon crystals with cores and rims analyses show a reduction of Th/U ratios from older cores to younger rims (Table 2.3). However, it is not possible to establish a trend of Th/U ratio decreasing from older to younger ages in a unified form for all the samples due to the heterogeneity of the initial zircon sources and compositions. The histogram of $^{207}Pb/^{206}Pb$ ages displays the large amplitude of zircon sources present in the Nomoca granodiorite (Fig. 2.8A, D).

Table 2-3. U-Pb data on zircon for the Nomoca, La Asunta and Nocemano plutons.

Nomoca	^{204}Pb cps	^{206}Pb mV[1]	Th/U	^{206}Pb/^{204}Pb	1σ%	^{207}Pb/^{206}Pb	1σ %	^{207}Pb/^{235}U	1σ %	^{206}Pb/^{238}U	1σ %	Rho	^{207}Pb/^{206}Pb	2σ abs	^{206}Pb/^{238}U	2σ abs	^{207}Pb/^{235}U	2σ abs	% U-Pb disc[4]
056-ZR30B	84	0.0222	0.411	22356	14.08	0.07581	0.53	1.918	0.96	0.1835	0.70	0.74	1090	21	1086	14	1087	13	0.35
048-ZR26N	35	0.0058	1.196	119641	30.41	0.07577	0.64	1.911	1.05	0.1829	0.75	0.71	1089	26	1083	15	1085	14	0.59
038-ZR21B	3799	0.0508	0.258	861	6.70	0.08575	2.15	1.668	3.55	0.1411	2.80	0.79	1332	82	851	45	996	45	36.16
036-ZR20	4871	0.0351	0.452	467	3.25	0.10819	2.18	2.562	3.38	0.1717	2.56	0.76	1769	79	1021	48	1290	49	42.26
033-ZR18	878	0.0130	0.622	938	2.64	0.12432	1.01	5.215	1.76	0.3042	1.39	0.79	2019	35	1712	42	1855	30	15.20
024-ZR12	1787	0.0149	1.098	534	2.99	0.10226	1.31	2.137	2.19	0.1516	1.71	0.78	1666	48	910	29	1161	30	45.39
023-ZR11	3604	0.0401	0.565	664	5.96	0.09214	2.22	1.919	2.98	0.1511	1.95	0.66	1470	83	907	33	1088	39	38.31
009-ZR4B	850	0.0143	0.329	1164	4.30	0.10592	0.88	3.637	3.72	0.2490	3.60	0.97	1730	32	1433	92	1558	58	17.16
004-ZR1N	1177	0.0115	0.435	625	4.95	0.12692	1.20	4.711	2.66	0.2692	2.35	0.88	2056	42	1537	64	1769	44	25.25
014-ZR6	14	0.0105	0.619	310175	25.26	0.10490	0.40	4.210	1.14	0.2911	1.00	0.88	1713	15	1647	29	1676	19	3.84
029-ZR16	33	0.0048	0.827	75835	27.21	0.07757	0.60	2.137	1.10	0.1998	0.84	0.77	1136	24	1174	18	1161	15	-3.37
057-ZR30N	77	0.0238	0.330	62556	58.17	0.07536	0.38	1.807	1.24	0.1739	1.13	0.90	1078	15	1034	21	1048	16	4.11
053-ZR28	46	0.0146	0.715	264534	36.43	0.07626	0.29	1.904	0.90	0.1811	0.77	0.85	1102	12	1073	15	1083	12	2.63
055-ZR29B	1453	0.0245	0.223	1022	4.26	0.08658	1.01	2.095	1.32	0.1755	0.77	0.58	1351	39	1042	15	1147	18	22.86
050-ZR27N	97	0.0082	0.221	6068	14.49	0.07884	0.64	1.835	1.15	0.1688	0.88	0.76	1168	25	1005	16	1058	15	13.94
049-ZR27B	232	0.0081	0.560	11930	68.02	0.09453	1.23	2.472	1.45	0.1897	0.68	0.47	1519	46	1120	14	1264	21	26.28
047-ZR26B	82	0.0082	0.887	121796	34.90	0.07899	0.52	2.028	0.89	0.1862	0.63	0.70	1172	20	1101	13	1125	12	6.09
044-ZR24N	11299	0.0503	0.029	282	1.44	0.13320	0.95	1.504	7.33	0.0819	7.26	0.99	2141	33	507	71	932	88	76.30
037-ZR21N	120	0.0060	0.561	72787	42.76	0.07794	3.62	2.023	3.74	0.1882	0.88	0.24	1145	141	1112	18	1123	50	2.93
035-ZR19	320	0.0130	0.674	5587	12.14	0.09100	2.55	1.998	2.67	0.1592	0.71	0.27	1447	96	953	13	1115	36	34.16
034-ZR18B	3619	0.0536	0.202	993	5.74	0.08431	2.25	1.723	2.62	0.1482	1.30	0.50	1300	86	891	22	1017	33	31.45
018-ZR9	1605	0.0291	0.435	1707	21.88	0.07375	1.92	1.906	2.19	0.1874	0.98	0.45	1035	77	1107	20	1083	29	-7.05
017-ZR8	177	0.0106	0.584	6385	15.50	0.07354	3.13	1.984	3.26	0.1957	0.83	0.25	1029	124	1152	17	1110	43	-11.97
016-ZR7N	77	0.0089	0.903	76300	53.91	0.07889	0.86	2.041	1.31	0.1876	0.92	0.70	1169	34	1108	19	1129	18	5.22
015-ZR7B	2313	0.0221	0.260	609	11.56	0.07775	3.87	1.779	4.37	0.1660	2.01	0.46	1140	150	990	37	1038	56	13.21
010-ZR4N	476	0.0101	0.434	1414	7.75	0.11035	1.62	4.554	2.22	0.2993	1.47	0.66	1805	58	1688	44	1741	37	6.50
008-ZR3N	16	0.0070	0.822	189356	37.90	0.07552	0.46	2.014	1.35	0.1934	1.21	0.90	1082	19	1140	25	1120	18	-5.33
007-ZR3B	165	0.0059	0.652	90118	29.09	0.09372	2.25	2.429	2.44	0.1879	0.88	0.36	1502	84	1110	18	1251	35	26.11
006-ZR2N	7425	0.0460	0.075	404	4.84	0.11228	3.25	1.948	6.29	0.1258	5.37	0.85	1837	116	764	77	1098	83	58.40
005-ZR2B	1528	0.0533	0.047	3310	9.55	0.07139	6.65	1.979	6.88	0.2011	1.71	0.25	969	260	1181	37	1108	91	-21.94

Nomoca	^{204}Pb cps	^{206}Pb mV[1]	Th/U	^{206}Pb/^{204}Pb	1σ%	^{207}Pb/^{206}Pb	1σ %	^{207}Pb/^{235}U	1σ %	^{206}Pb/^{238}U	1σ %	Rho	^{207}Pb/^{206}Pb	2σ abs	^{206}Pb/^{238}U	2σ abs	^{207}Pb/^{235}U	2σ abs	% U-Pb disc[4]
003-ZR1B	1114	0.0316	0.136	1743	6.17	0.07238	0.96	1.327	4.15	0.1330	4.03	0.97	997	39	805	61	858	48	19.26
040-ZR22B	19	0.0026	0.496	69558	23.94	0.05867	0.44	0.658	0.94	0.0813	0.74	0.79	555	19	504	7	513	8	9.17
030-ZR17	296	0.0413	0.428	10188	8.02	0.08613	0.34	2.612	0.78	0.2200	0.60	0.77	1341	13	1282	14	1304	11	4.43
039-ZR22N	17	0.0094	0.126	221426	34.09	0.07255	0.47	1.455	1.04	0.1454	0.86	0.82	1001	19	875	14	912	13	12.60
025-ZR13	3776	0.0114	0.924	219	8.59	0.21052	3.78	4.363	4.15	0.1503	1.68	0.40	2910	120	903	28	1705	67	68.97
019-ZR10N	17571	0.0182	0.362	66	2.41	0.29815	3.61	9.603	4.74	0.2336	3.05	0.64	3461	110	1353	74	2397	85	60.90
043-ZR23	48959	0.0571	0.402	73	3.62	0.33289	3.82	15.321	4.39	0.3338	2.13	0.49	3630	114	1857	69	2835	82	48.86
La Asunta	**^{204}Pb cps**	**^{206}Pb mV[1]**	**Th/U**	**^{206}Pb/^{204}Pb**	**1σ%**	**^{207}Pb/^{206}Pb**	**1σ %**	**^{207}Pb/^{235}U**	**1σ %**	**^{206}Pb/^{238}U**	**1σ %**	**Rho**	**^{207}Pb/^{206}Pb**	**2σ abs**	**^{206}Pb/^{238}U**	**2σ abs**	**^{207}Pb/^{235}U**	**2σ abs**	**% U-Pb disc[4]**
024-ZR14	890	0.0270	0.275	2051	8.27	0.08990	1.48	2.184	2.75	0.1762	2.29	0.83	1423	56	1046	44	1176	38	26.50
017-ZR10	99	0.0273	0.045	58292	29.50	0.07492	0.36	1.901	1.19	0.1840	1.07	0.90	1066	14	1089	21	1081	16	-2.09
040-ZR27	2997	0.0291	0.112	622	3.01	0.09802	1.96	1.600	2.47	0.1184	1.47	0.59	1587	72	721	20	970	31	54.54
013-ZR7	887	0.0383	0.045	2806	16.57	0.07789	0.75	1.707	2.48	0.1590	2.33	0.94	1144	30	951	41	1011	31	16.89
020-ZR12	7404	0.0393	0.065	356	2.85	0.11631	2.38	2.520	2.99	0.1571	1.77	0.59	1900	84	941	31	1278	43	50.49
038-ZR25	867	0.0398	0.312	3240	10.64	0.07821	1.10	2.062	2.21	0.1912	1.87	0.85	1152	44	1128	39	1136	30	2.10
036-ZR23	369	0.0399	0.263	7470	6.40	0.07735	0.28	1.948	1.09	0.1826	0.99	0.91	1130	11	1081	20	1098	15	4.32
034-ZR21	687	0.0400	0.392	5022	11.47	0.08109	0.83	2.239	1.12	0.2002	0.65	0.58	1224	32	1176	14	1193	16	3.85
016-ZR9	1009	0.0413	0.185	5034	21.84	0.07251	0.83	1.810	1.42	0.1810	1.09	0.77	1000	33	1072	21	1049	18	-7.23
008-ZR4	256	0.0430	0.029	11035	16.21	0.07278	0.36	1.911	1.55	0.1904	1.46	0.94	1008	14	1124	30	1085	21	-11.49
044-ZR29	1514	0.0436	0.144	1815	2.76	0.08211	0.91	1.059	4.54	0.0935	4.43	0.98	1248	36	576	49	733	47	53.82
009-ZR5	461	0.0452	0.123	14273	53.18	0.07709	1.09	2.080	1.71	0.1956	1.26	0.74	1124	43	1152	27	1142	23	-2.51
043-ZR28	1127	0.0465	0.059	2384	14.24	0.07701	0.84	1.541	3.85	0.1451	3.74	0.97	1121	33	873	61	947	47	22.12
007-ZR3B	87	0.0506	0.033	39687	11.32	0.07335	0.28	1.852	0.84	0.1832	0.69	0.83	1024	11	1084	14	1064	11	-5.93
026-ZR15N	1082	0.0539	0.340	3495	8.37	0.07557	1.82	1.537	3.35	0.1475	2.79	0.83	1084	72	887	46	945	41	18.14
010-ZR6	125	0.0539	0.039	635234	49.14	0.07313	0.41	2.005	1.16	0.1988	1.02	0.88	1018	17	1169	22	1117	16	-14.88
023-ZR13	49	0.0543	0.253	1035075	26.79	0.07475	0.33	2.092	1.52	0.2030	1.44	0.95	1062	13	1191	31	1146	21	-12.19
035-ZR22	76	0.0556	0.081	68735	19.34	0.07469	1.95	1.614	4.03	0.1567	3.51	0.87	1060	77	939	61	976	50	11.47
039-ZR26	3723	0.0591	0.231	5146	28.06	0.06842	3.11	1.523	3.74	0.1614	2.05	0.55	881	126	965	37	940	45	-9.47
028-ZR17	1800	0.0601	0.061	5372	38.94	0.07174	0.89	1.785	1.47	0.1805	1.10	0.75	979	36	1069	22	1040	19	-9.29
025-ZR15B	204	0.0605	0.213	25780	10.34	0.07562	0.48	1.915	1.46	0.1836	1.33	0.91	1085	19	1087	27	1086	19	-0.15
037-ZR24	2210	0.0605	0.123	2188	9.67	0.07243	1.66	1.432	3.21	0.1434	2.72	0.85	998	67	864	44	902	38	13.44
030-ZR19	109	0.0672	0.054	467640	54.54	0.07524	0.35	1.969	0.76	0.1898	0.56	0.74	1075	14	1120	11	1105	10	-4.25

Nomoca	^{204}Pb cps	^{206}Pb mV[1]	Th/U	^{206}Pb/^{204}Pb	1σ%	^{207}Pb/^{206}Pb	1σ %	^{207}Pb/^{235}U	1σ %	^{206}Pb/^{238}U	1σ %	Rho	^{207}Pb/^{206}Pb	2σ abs	^{206}Pb/^{238}U	2σ abs	^{207}Pb/^{235}U	2σ abs	% U-Pb disc[4]
029-ZR18	195	0.0682	0.153	25126	10.13	0.07504	0.32	2.002	1.78	0.1934	1.71	0.96	1070	13	1140	36	1116	24	-6.59
006-ZR3N	20	0.0687	0.067	1392676	30.05	0.07332	0.24	2.002	0.84	0.1980	0.71	0.85	1023	10	1165	15	1116	11	-13.88
046-ZR31	381	0.0707	0.274	14580	10.45	0.07353	0.46	1.152	3.02	0.1136	2.96	0.98	1029	18	694	39	778	33	32.56
045-ZR30	125	0.0713	0.054	862383	46.19	0.07357	0.48	1.916	0.81	0.1888	0.54	0.67	1030	19	1115	11	1087	11	-8.30
015-ZR8B	230	0.0754	0.217	26348	16.26	0.07285	0.35	1.721	0.87	0.1713	0.70	0.81	1010	14	1019	13	1016	11	-0.94
019-ZR11N	516	0.0779	0.235	32721	27.86	0.07530	0.84	1.734	1.58	0.1670	1.28	0.81	1077	33	996	24	1021	20	7.51
004-ZR1B	766	0.0877	0.215	8110	9.70	0.07232	0.43	1.627	1.38	0.1631	1.26	0.91	995	18	974	23	981	17	2.10
033-ZR20	43	0.1015	0.239	1755953	28.02	0.07334	0.28	1.923	0.68	0.1901	0.50	0.73	1023	11	1122	10	1089	9	-9.64
003-ZR1N	1850	0.1139	0.030	7492	39.75	0.07626	1.10	2.410	1.80	0.2292	1.38	0.77	1102	44	1330	33	1246	26	-20.72
014-ZR8N	706	0.1664	0.190	15070	3.85	0.06994	0.31	1.102	1.41	0.1142	1.33	0.94	927	13	697	18	754	15	24.75
Nocemano	**^{204}Pb cps**	**^{206}Pb mV[1]**	**Th/U**	**^{206}Pb/^{204}Pb**	**1σ%**	**^{207}Pb/^{206}Pb**	**1σ %**	**^{207}Pb/^{235}U**	**1σ %**	**^{206}Pb/^{238}U**	**1σ %**	**Rho**	**^{207}Pb/^{206}Pb**	**2σ abs**	**^{206}Pb/^{238}U**	**2σ abs**	**^{207}Pb/^{235}U**	**2σ abs**	**% U-Pb disc[4]**
006-ZR4	422	0.0145	0.655	12491	29.09	0.09712	2.49	3.561	2.67	0.2659	0.89	0.33	1570	92	1520	24	1541	42	3.16
029-ZR21	121	0.0084	0.330	9501	27.62	0.10404	1.61	4.420	1.97	0.3081	1.08	0.55	1697	59	1731	33	1716	32	-2.00
025-ZR17	333	0.0118	0.536	3711	32.35	0.08125	3.08	2.162	4.20	0.1930	2.84	0.68	1228	119	1137	59	1169	58	7.35
016-ZR11	333	0.0206	0.806	5902	14.18	0.07801	0.65	2.230	2.52	0.2073	2.41	0.95	1147	26	1214	53	1190	35	-5.87
005-ZR3	1446	0.0328	0.141	3506	31.38	0.07781	3.74	2.133	6.87	0.1988	5.75	0.84	1142	145	1169	122	1160	93	-2.36
035-ZR24	344	0.0268	0.704	8183	35.07	0.07581	0.59	1.989	1.38	0.1903	1.20	0.86	1090	24	1123	25	1112	19	-3.01
033-ZR22B	499	0.0220	0.237	4573	24.15	0.07600	1.03	1.935	1.61	0.1847	1.18	0.73	1095	41	1092	24	1093	21	0.24
020-ZR14	233	0.0249	0.548	9727	15.80	0.07798	0.73	2.010	1.21	0.1870	0.89	0.73	1146	29	1105	18	1119	16	3.60
027-ZR19	606	0.0176	0.593	2078	10.84	0.07917	1.22	2.089	1.92	0.1914	1.44	0.75	1176	48	1129	30	1145	26	4.04
023-ZR15	251	0.0185	0.396	13490	34.27	0.07543	0.74	1.740	4.56	0.1672	4.49	0.98	1080	29	997	83	1023	58	7.69
034-ZR23	726	0.0321	0.294	3191	8.87	0.07816	1.10	2.189	2.56	0.2031	2.28	0.89	1151	43	1192	50	1177	35	-3.54
030-ZR22	73	0.0049	0.486	194402	91.94	0.10364	1.31	4.003	1.55	0.2801	0.74	0.48	1690	48	1592	21	1635	25	5.82
007-ZR5	117	0.0197	0.365	14815	17.01	0.08769	0.56	3.127	2.57	0.2586	2.48	0.97	1376	21	1483	65	1439	39	-7.78
028-ZR20	1161	0.0240	0.281	1455	13.46	0.08516	1.49	2.000	1.92	0.1704	1.15	0.60	1319	57	1014	22	1116	26	23.13
019-ZR13	712	0.0141	0.491	2809	24.68	0.08903	1.69	2.353	3.64	0.1917	3.21	0.88	1405	64	1131	66	1229	51	19.51
018-ZR12	469	0.0144	0.456	3515	39.53	0.08467	0.87	2.264	2.59	0.1939	2.41	0.93	1308	33	1142	50	1201	36	12.67
017-ZR11B	877	0.0173	0.864	1314	4.91	0.08947	0.74	2.488	2.67	0.2017	2.54	0.95	1414	28	1184	55	1269	38	16.25
015-ZR10	1396	0.0271	0.643	1404	6.55	0.08852	1.22	2.254	1.89	0.1847	1.40	0.74	1394	46	1092	28	1198	26	21.63
014-ZR9	658	0.0160	0.250	1890	9.99	0.08726	1.25	2.264	1.69	0.1881	1.07	0.63	1366	48	1111	22	1201	24	18.66
003-ZR1	2559	0.0417	0.401	1230	10.65	0.08742	2.35	2.030	2.75	0.1684	1.39	0.51	1370	89	1003	26	1125	37	26.77

Nomoca	^{204}Pb cps	^{206}Pb mV[1]	Th/U	^{206}Pb/^{204}Pb	1σ%	^{207}Pb/^{206}Pb	1σ %	^{207}Pb/^{235}U	1σ %	^{206}Pb/^{238}U	1σ %	Rho	^{207}Pb/^{206}Pb	2σ abs	^{206}Pb/^{238}U	2σ abs	^{207}Pb/^{235}U	2σ abs	% U-Pb disc[4]
026-ZR18	2767	0.0199	0.927	452	3.36	0.10815	2.24	2.066	3.31	0.1386	2.40	0.73	1768	81	836	38	1138	45	52.70
024-ZR16	11395	0.0247	2.944	232	8.56	0.27164	3.41	6.084	3.80	0.1624	1.64	0.43	3316	105	970	29	1988	65	70.74
013-ZR8	2228	0.0101	0.828	1178	42.94	0.14276	5.84	4.104	6.42	0.2085	2.63	0.41	2261	195	1221	58	1655	102	46.01
008-ZR6	8731	0.0177	0.905	187	7.59	0.25960	2.84	6.436	3.99	0.1798	2.77	0.69	3244	88	1066	54	2037	69	67.15
004-ZR2	5266	0.0516	0.105	1071	16.58	0.10247	4.51	3.143	4.59	0.2224	0.77	0.17	1669	162	1295	18	1443	69	22.45
010-ZR7B	623	0.0153	0.579	1861	11.12	0.08431	1.85	2.120	2.85	0.1824	2.14	0.75	1300	71	1080	42	1155	39	16.89

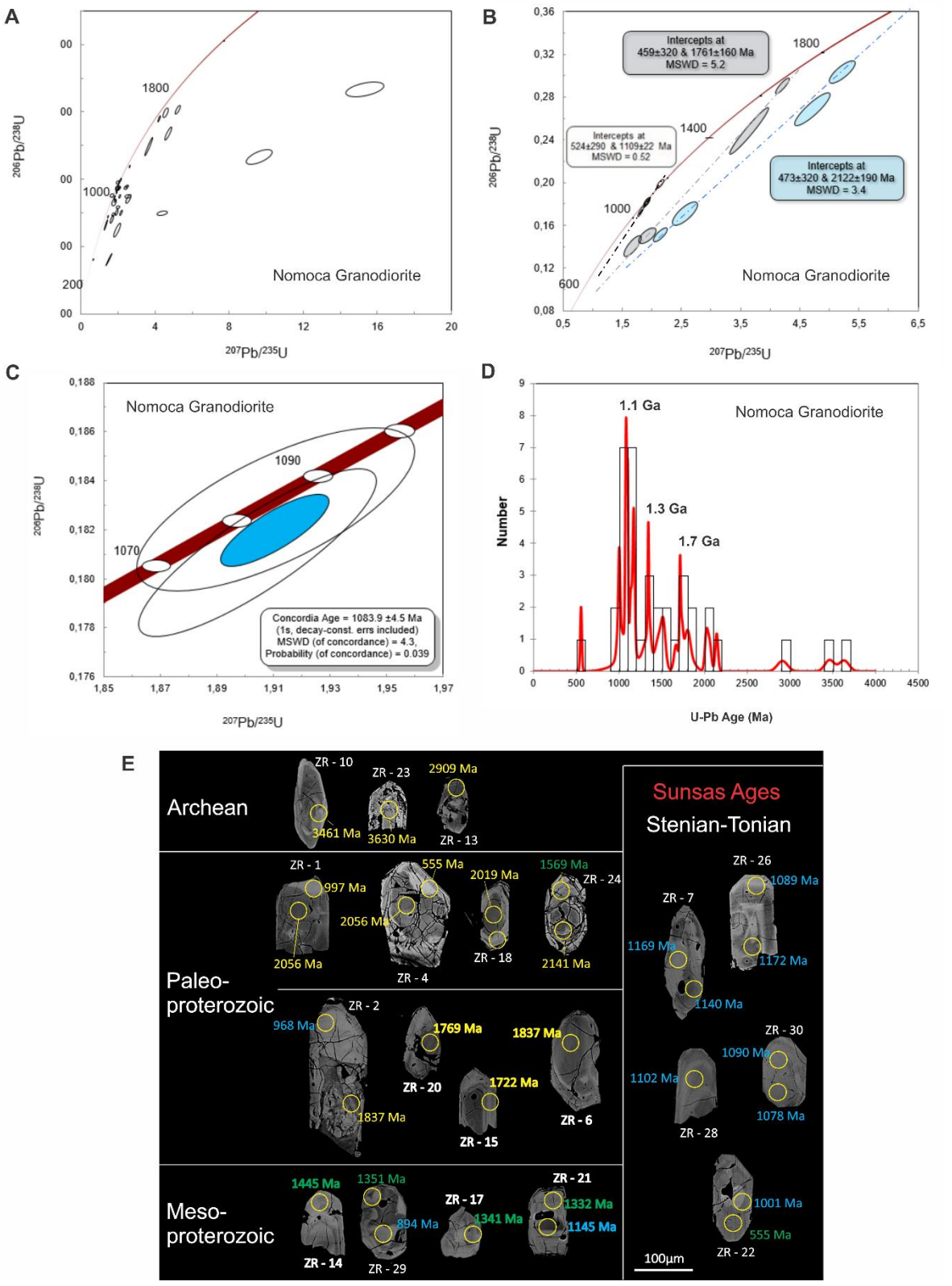

Figure 2.8. (A) Concordia diagram with ages recorded in the Nomoca granodiorite; (B) Concordia diagram with three upper intercept age groups, 2122±190 Ma, 1761±160 Ma and 1109±22 Ma; (C) Concordia age of 1084±4.5 Ma; (D) Histogram of 207Pb/206Pb average ages showing peaks at 1730, 1350 and 1140 Ma; (E) Back-scattering (BSE) image of zircon crystals of the Nomoca granodiorite, sample TAP2.

The La Asunta syenogranite presents prismatic, elongated (3:1) zircon crystals, measuring between 150 and 200 µm, with internal structuring and well-defined zonation, in which some layers are up to 20 µm thick (Fig. 2.9D). A second morphological group of subhedral crystals, measuring between 100 and 150 µm, with ratio of 2:1, is also observed. The La Asunta sample includes crystals with ^{207}U-^{206}Pb ages between 1900 and 965 Ma (Fig. 2.9B), and exhibits an upper intercept of 1022±100 Ma (Fig. 2.9A), with a concordia age of 1081±6 Ma (Fig. 2.9C). Th/U ratios range from 0.02 to 0.39 in crystals with core and rim analyses; reduction of ratios is observed from the center to the rim.

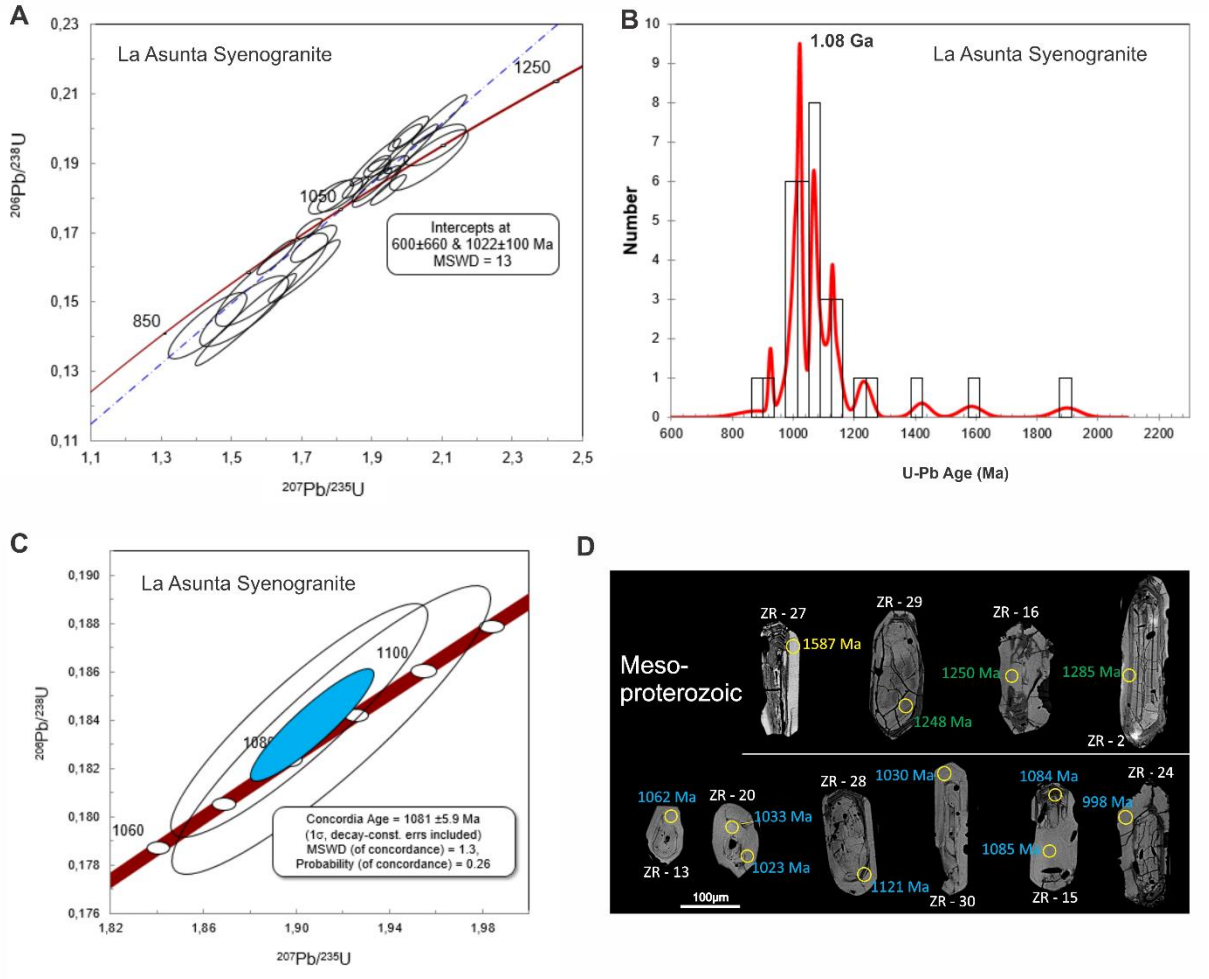

Figure 2.9. (A) Concordia diagram of 46 analyzed crystals of the La Asunta sample displaying upper intercept at 1022±100 Ma; (B) Histogram of 207Pb/206Pb average ages with peak at 1008 Ma; (C) Concordia age of 1081±5.9 Ma; (D) Back-scattering image (BSE) of La Asunta syenogranite zircon crystals, sample LA-14.

The Nocemano syenogranite shows elongated (1:3), prismatic zircon crystals from 200 to 250 µm, with internal structuring and well-defined core and rim zonation.

Subhedral crystals (2:1) with dimensions up to 300 µm are also observed. Three discordia ages are obtained in this syenogranite sample (Fig. 2.10A). The first age is 1699±37 Ma in zircon cores with Th/U ratios between 0.33 and 0.92. The second discordia age is 1386±18 Ma, obtained mainly on prismatic zircon rims, and the third upper intercept is 1196±99 Ma, both obtained on zircon core and rim. The last intercept shows a concordia age of 1102±14 Ma (Fig. 2.10B) in homogeneous zircon crystals and in zircon rims with core of 1.69 Ga. Paleoproterozoic (2261 Ma) and Archean (3244 and 3316 Ma) zircon crystals with high Th/U ratios of 0.8 to 2.9 were also recorded in the Nocemano syenogranite analyzed sample.

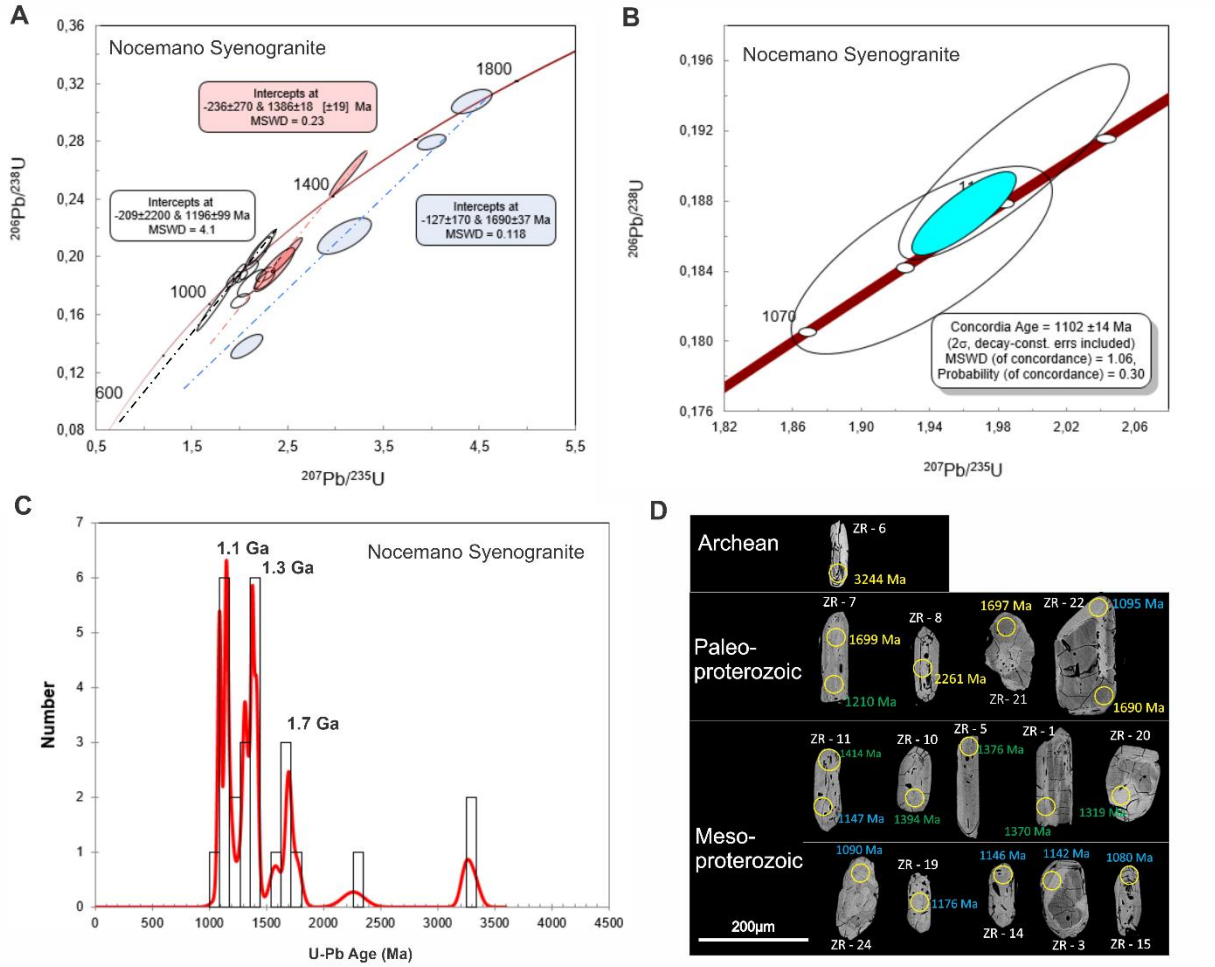

Figure 2.10. (A) Concordia diagram of the Nocemano granite sample, with three upper intercept age groups, 1690±37 Ma, 1386±18 Ma and 1196±99 Ma; (B) Concordia age of 1102±14 Ma; (C) Histogram of $^{207}Pb/^{206}Pb$ average age with peak at 1.7, 1.3 and 1.1 Ga; (D) Back-scattering image (BSE) of zircon crystals of the Nocemano syenogranite, sample SM-7A.

2.6 Discussion

2.6.1 Nocemano, Nomoca and La Asunta Sources and Tectonic Setting

The studied intrusions record part of the several and heterogeneous geochemical features of the complex Sunsas magmatism. The La Asunta and Nocemano syenogranites have a ferric composition with peraluminous affinity and calc-alkaline to alkali-calcic nature. They crystallized from acid magmas (SiO_2=70.4-74.9 w%; Fig. 2.6) and are more fractionated and enriched in alkalis than the Nomoca Granodiorite (Fig. 2.7), with concentrations close to the Naranjito, Taperas and El Carmen monzogranites and leucocratic portions of the Primavera Granite (Table 2.2). The Nomoca granodiorite is magnesian, has a peraluminous affinity and calc-alkaline signature, with a typical silica content of intermediate magmas (SiO_2=67.3 w%, Fig. 2.6). It has high alkali contents, compatible with the mesocratic portion of the Primavera Granite (Table 2.2).

The granite classification based on magmatic series and their typology, A-, I-, M- and S-types, has been applied since the 1980s (e.g., Pitcher, 1982; Whalen et al., 1987; Chappell and White, 1992; Eby, 1992; Barbarin, 1999). The classification takes into account the magmatic source characteristics and the geotectonic context of intrusion. A-type granites have high contents of SiO_2 (>70 %), FeO_t/MgO, K_2O/ Na_2O, Ga/Al, Zr, Nb, Y, Ta, and REE (except Eu), and low contents of CaO, Al_2O_3, MgO, Ba, Sr, and Ti (Whalen et al., 1987; Eby, 1992). The studied plutons present characteristics between fractionated I-type granites and hybrid A-type granites (Barbarin, 1990; Castro et al., 1991; Murphy et al., 2017). The presence of magnetite in the La Asunta and Nocemano syenogranites and the presence of titanite in the Nomoca granodiorite (Fig. 2.4) are compatible with I-type granites classification of Chappell and White (1974) and Ishihara (1977), formed after reworking of igneous and metamorphic rocks. However, classification as hybrid A-type granites, crystallized from magmas derived of partial melting, can also be made due to the ferric composition of the syenogranites (Fig. 2.6D), the lower fractionation index of the Nomoca granodiorite (Fig. 2.6, 2.7), the post-collisional granitic affinity (Fig. 2.6E), the calc-alkaline to alkali-calcic character, and the high contents of REE, together with the negative anomalies of Ba, Sr and Eu (Fig. 2.7; Collins et al., 1982; Whalen et al., 1987; Bonin, 1990; Eby, 1992; Barbarin, 1996; Patiño Douce, 1997). These

factors support a mature continental magmatic arc scenario or the transition to a post-collisional setting for the Sunsas magmatism emplacement (Bonin, 1990; Barbarin, 1999; Frost et al., 2001; Pearce, 2008).

The REE diagrams for the studied plutons show lower enrichment of LREE, high fractionation of HREE, discrete Eu anomaly for the Nomoca granodiorite, and enrichment of LREE with lower fractionation of HREE, and negative Eu anomalies for the La Asunta and Nocemano syenogranites (Fig. 2.7A, B). All analyses show strong negative anomalies of Ti, P, Sr, Nb, Ta, and Ba and positive anomalies of Nd, Sm, Pb, Th, and Rb (Fig. 2.7C, D). The Nb and Ta negative anomalies indicate a magmatic arc signature (Hugh, 1993) since Nb and Ta behave as refractory elements during the subduction process (Baier et al., 2008). Thus, derived-melts that ascend to the continental crust are depleted in Nb and Ta. When a late partial melting takes place in this Nb and Ta depleted crustal source, essentially generates Nb- and Ta-poor magma with high Y/Nb ratios such as A-type granites (Eby, 1992; Baier et al., 2008). On the other hand, Ba, Sr, and Eu negative anomalies reflect felsic minerals as feldspar in the parental magma (Baier et al., 2008). Therefore, the geochemical patterns from the studied intrusions indicate that they were generated in a mature arc environment likely during the transition of orogenic to post-orogenic crustal anatexis (Bonin 1990; Barbarin 1999; Baier et al., 2008). The compilation of geochemical results of this work with Vargas-Mattos (2010) geochemical data shows two distinct fractionation patterns for the Sunsas magmatism (Fig. 2.7C), which suggests at least two magmatic sources for the same tectonic environment.

The calc-alkaline magmatism is developed from pre- to post-collision stage of an orogeny. Besides, it records the interaction characteristics of its protolith sources, as well as the change of pre- to post-collision of the thermodynamic regime during orogen evolution (Pearce, 1996; Barbarin, 1999). The crustal thickness is controlled by the rheological and compositional characteristics of the calc-alkaline magmatism source (e.g., He et al., 2011; Chapman et al., 2015). For the Sunsas magmatic sources, this is evidenced by the restrict partial melting with protolith signature preserved in the chemical patterns, inherited structures, and zircon cores. Therefore, in the Sunsas Province, the continental crust architecture is important to explore the relationship between anatexis, segregation by partial melting and granitic bodies formation during orogeny as observed in other orogens (e.g., Zeng et al., 2011; Gao

and Zeng, 2014; Zhang et al., 2018). Thus, geochemical results suggest a transitional tectonic setting from magmatic arc with within-plate signatures to post-collisional setting for the Sunsas granites.

2.6.2 Geochronology and Sunsas Belt Magmatism: implications for assembly of Rodinia

The Meso- to Neoproterozoic granitogenesis developed during the Sunsas Orogeny includes a significant number of intrusions (Litherland et al., 1986; Boger et al., 2005; Vargas-Mattos, 2006, 2010). U-Pb zircon geochronology allows proposing that the lithostratigraphic units of the SW Amazonian Craton, as the Chiquitania gneissic Complex, Lomas Manechis granulitic complex, Rondoniana-San Ignácio Province, Pensamiento intrusive suite and Sunsas-Aguapeí Province, present diachronic and more complex evolution than the models presented in the literature (Table 2.1).

The concordia ages between 1.17 and 1.08 Ga, obtained in cores of newly formed zircon of the three investigated intrusions, support their crystallization during the collision phase of the Sunsas orogeny (e.g., Litherland et al., 1986; Adamek et al., 1996; Boger et al., 2005; Isla-Moreno, 2009; Vargas-Mattos, 2010). The granitic bodies location south of the Concepcion Front, which marks a deformed zone limit, may indicate that the granitic emplacement was controlled by structures in a transcurrent setting. A zircon rim concordant age of 555 Ma obtained in the Nomoca Granodiorite (Table 2.3) may indicate reworking of the Sunsas basement during the development of the Neoproterozoic Tucavaca aulacogen, whose metamorphism is recorded in K-Ar ages of the Chiquitania Complex (Litherland et al., 1986; Trompette et al., 1998; Ramos et al., 2010; Walde et al., 2015).

The older inherited or captured ages in zircon cores obtained in the La Asunta, Nocemano and Nomoca plutons confirm the reworking of Archean and Paleoproterozoic crust (Table 2.3; Cordani et al., 2000; Cordani and Teixeira, 2007) during Sunsas magmatism. Zircon cores of the Nomoca granodiorite and the Nocemano syenogranite record Paleoarchean to Mesoarchean ages, between 3630 and 2910 Ma (Fig. 2.8E, 2.10D). These Archean ages are the first recognized in the study area. They may represent inherited zircon grains with preserved cores, during the recycling of older crust along with the development of arc magmatism or preserved during the older crust melting (A-type granites) in collisional processes. In

the Amazonian Craton, the Archean crust is restricted to the Central Amazonian province, including the Carajás, Rio Maria and Santana do Araguaia domains, and to the reworked Archean terrains within the Maroni-Itacaiunas province, whose rocks yielded radiometric ages between 2600 and 3200 Ma (Cordani et al., 2000; Cordani and Teixeira, 2007). Paleo- to Mesoarchean ages are registered in inherited zircon from magmatic or sedimentary sources in the Grenville Province of Laurentia, taken as related to the Superior Province (3.4–3.3 Ga; Davis et al., 2005; Bickford et al., 2006; Chiarenzelli et al., 2015), located to the west of the central part of Grenville. Therefore, two hypotheses for zircon sources can be suggested for crystals with Archean ages between 3.6 and 3.2 Ga, obtained in the Nocemano and Nomoca plutons. The first hypothesis is that there was a link of crustal fragments that today form the basement of the Paraguá Terrane (~1.7 Ga) to an Archean Amazonian Craton crustal fragment during the Statherian. Repeated cycles of convergence and separation between Laurentia and Amazonia during the Mesoproterozoic produced a complex arrangement of allochthonous blocks. The intense tectonic reworking in the region may have erased or masked the records of this link, which weakens the proposition. The second hypothesis is that the zircon crystals with Paleoarchean cores are inherited from the basement of the Grenville Province (Superior Province). The collision between the Amazonian Craton and Laurentia at ca. 1.0 Ga allowed the reworking of crystals along the Sunsas Belt. This link is recorded through sinistral transpressive structures and sin- to post-collisional magmatism in the Sunsas, Aguapeí, and Nova Brasilândia belts (e.g., Litherland et al., 1986; Geraldes et al., 2001; Rizzotto et al., 2002; Boger et al., 2005; Teixeira et al., 2010).

The Nomoca and Nocemano intrusions also have inherited zircon crystals with Paleo- and Mesoproterozoic cores with ca. 1.0-0.9 Ga rims, which record the reworking of the Paraguá Terrane basement and older crustal fragments. For the Rhyacian age of 2.12 Ga, there are two possible correlations, since such ages were not recorded in the Lomas Manechis and Chiquitania complexes. The Rio Apa Terrane (Teixeira et al., 2020) is taken as a possible source for the older crystals. The block is located in the extreme south of the Amazonian Craton, at the Brazil-Paraguay border, and has been recognized in the extreme southeast of Bolivia, in the Santo Corazón region (Vargas-Mattos, 2010; Redes et al., 2016, 2018; Plens, 2018). The Correreca granite (1925±32 Ma and 1894±13 Ma; Vargas-Mattos, 2010),

age-correlated to the Alumiador Suite, marks the relation between the craton and the Rio Apa Terrane in the region. The Rio Apa Terrane is formed of terrains with different tectonic histories, divided into the western and eastern domains (Lacerda Filho et al., 2006; Cordani et al., 2010; Faleiros et al., 2016; Lacerda Filho, 2016), with some authors pointing out the existence of a third smaller crustal fragment, the southeast domain (Faleiros et al., 2016). In this scenario, the Porto Murtinho Complex, basement of the western domain, formed of gneisses with U-Pb ages between 2074±7 and 1892±31, could be the source of the Rhyacian zircon crystals.

The second hypothesis is the correlation of Rhyacian zircon grains with the Rio Negro-Juruena Province, formed of rocks dated between 1.80 and 1.60 Ga (e.g., Cordani and Teixeira, 2007; Bettencourt et al., 2010; Teixeira et al., 2010). The Paraguá Terrane has been considered as a crustal fragment probably displaced from the Rio Negro-Juruena crustal counterpart between 1.50 and 1.40 Ga (Sadowski and Bettencourt, 1996; Bettencourt et al., 2010). This relation is based on magmatic zircon from the Lomas Manechis Granulitic Complex that yielded an age of 1818 Ma, suggesting an older crust in eastern Bolivia, comparable to the basement ages of the Juruena region (Santos et al., 2008; Bettencourt et al., 2010). In this way, zircon of Rhyacian age may have been assimilated from the oldest crust during the Orosirian continental accretion phase. However, the distance between these terrains and the new studies in the Rio Apa Terrane proposing its extension to the east of Bolivia (Cordani et al., 2010; Lacerda-Filho et al., 2016; Faleiros et al., 2016; Teixeira et al., 2018), indicate that the latter is a better candidate as a possible source for inherited or captured Rhyacian zircon crystals in the Sunsas belt granites.

The Chiquitania Complex reworking (Litherland et al., 1986; Boger et al., 2005; Santos et al., 2008; Vargas-Mattos, 2010; Faria et al., 2014) during formation of the granites associated to Sunsas magmatism emplacement is evidenced by the ages of 1.76 to 1.69 Ga in inherited or captured zircon cores from different melt in the course of magma mixing or rapid disaggregation of solid fallen roof material (e.g. Bacon & Lowenstern, 2005; Beard et al., 2005; Acosta-Vigil et al., 2010; Simakin & Bindeman, 2012) leading to rapid zircon contact with melts (Journal of Petrology, Bindeman 2016, Zircon Survival, Rebirth and Recycling during Crustal Melting, Magma Crystallization, and Mixing Based on Numerical Modelling. The zircon crystals of regional basement occasionally present ages of 1.3 Ga in zircon rims with low Th/U

ratios, indicating reworking of the same during the San Ignácio Orogeny, between 1.40 and 1.28 Ga (Litherland et al., 1986; Darbyshire, 2000; Geraldes, 2000; Boger et al., 2005; Ruiz, 2005; Santos et al., 2008; Bettencourt et al., 2010; Matos et al., 2009).

2.7 Conclusions

The petrological, geochemical, and U-Pb isotope data from the La Asunta, Nocemano, and Nomoca granitic intrusions performed in this research highlight the following main contributions:

1. The three granitic plutons of the Sunsas suite have metaluminous to peraluminous composition with calc-alkaline signature, and can be classified as I-type fractionated granite and (hybrid) A-type granite.
2. Two geochemical trends are recognized in the Sunsas granitic intrusions: the first with Mg-rich pattern and less fractionated, and the second Fe-rich and more REE enriched, suggesting at least two precursor sources for the Sunsas granitic magmatism.
3. The 1.17 to 1.0 Ga Sunsas granitic magmatism may have been generated by the reworking of Archean and Paleoproterozoic continental crust sources.
4. The 3.6 to 2.9 Ga inherited zircon cores can be correlated to the Superior Province, Laurentia. These ages strengthen the geotectonic model for Rodinia supercontinent with Laurentia-Baltica-Amazonia configuration
5. The 2.2 to 2.0 Ga Paleoproterozoic ages yielded by inherited zircon cores from the studied granites may be related to the Porto Murtinho Complex, the basement of the Rio Apa Terrane that extends to the extreme south of Bolívia. Similarly, ages of 1.7 to 1.6 Ga and 1.3 Ga could represent the reworking of the Chiquitania and Lomas Manechis complexes and San Ignácio Orogeny rocks, respectively.
6. The concordant age of 555 Ma obtained in zircon overgrowth suggests some restrict thermal reactivation during the Late Neoproterozoic.

2.8 Acknowledgements

This study was financed in part by the Coordenação de Aperfeiçoamento de Pessoal de Nível Superior - Brasil (CAPES) - Finance Code 001. The authors acknowledge

the support of the Laboratório de Geocronologia (Universidade de Brasília) and the Grupo de Pesquisa em Evolução Crustal e Tectônica (Guaporé). The authors also acknowledge Fundação de Apoio à Pesquisa do Distrito Federal (FAPDF) and INCT Estudos Tectônicos (CNPq-CAPES-FAPDF) for financial support. IMN thanks CAPES and Programa de Excelência Acadêmica (PROEX, Edital - 0487) for granting the Doctorate scholarship. RAF and ASR acknowledge CNPq for research fellowship.

3. ARTIGO CIENTÍFICO 2: LONG-LIVED PROTEROZOIC MAGMATISM IN THE BOLIVIAN PRECAMBRIAN SUNSAS BELT, SW AMAZONIAN CRATON

Ingrid Moerschberger Nedel[1], Reinhardt A. Fuck[1], Amarildo Salina Ruiz[2], Gerardo Ramiro Matos-Salinas[3], Alanielson da Câmara Dantas Ferreira[4]

[1]Instituto de Geociências, Universidade de Brasília (UnB), Brasília-DF, Brazil.

[2]Faculdade de Geociências, Universidade Federal de Mato Grosso, Cuiabá-MT, Brazil.

[3]Instituto de Investigaciones Geológicas y del Medio Ambiente, Universidad Mayor de San Andrés (UMSA), Pabellón Geología, Calle 27, Campus Universitario Cota Cota, La Paz, Bolivia.

[4]Instituto de Geociências, Universidade Federal do Rio Grande do Sul, Porto Alegre - RS, Brazil

Author's correspondence: Ingrid Moerschberger Nedel (ingrid_mn@hotmail.com)

3.1 Abstract

We present the systematic U-Pb zircon and monazite ages from granitic magmatism of the Sunsas belt in Bolivia, SW Amazonian Craton. The geochronological results revealed four magmatic events in the Sunsas belt: the first formed a granitic basement related to the Rio Apa Terrane at 1.95–1.85 Ga in its southern part; the second magmatism is represented by c. 1.68 Ga granites associated with the Mesoproterozoic Paraguá Terrane; the third event at 1.42–1.35 Ga refers to granitic intrusions generated during the San Ignacio orogeny; lastly, the 1.1–1.04 Ga Sunsas orogeny magmatism related to south Laurentia and SW Amazonian Craton collision. Therefore, the Sunsas belt shows a complex magmatic history with multiple crustal reworking processes from 1.95 to 1.04 Ga. Furthermore, the 1000±9.8 Ma and 992±41 Ma monazite ages can be related to lower temperature melt pulses in the post-collision setting. Thus, the Sunsas belt was built by heterogeneous 1.95–1.85 and c. 1.68 Ga crustal fragments that were reworked at c. 1.42–1.35 Ga and 1.1–1.0 Ga during the orogenic collage. In addition, ~1.0 Ga monazite ages suggest that some granites dated by zircon can bear evidence of a younger thermal history.

These results support that the c. 1.0 Ga Sunsas Orogeny may have been more pervasive than previously thought.

Keywords: SW Amazonian Craton, Sunsas belt, Grenville Orogeny, Bolivia

3.2 Introduction

The Proterozoic eon represents the most significant time of continental growth produced by magmatic arcs and successive terrane accretions (e.g., Cawood et al., 2013; Holder et al., 2019; Ferreira et al., 2020). This time interval included strong reworking processes during episodic supercontinent assemblies (1.7 to 1.3 Ga and 1.1 to 0.7 Ga) and later breakup induced by dispersal movement of the lithosphere driven by plate tectonics (e.g., Condie, 2004; Hawkesworth et al., 2010; Nance et al., 2014; Ernst et al., 2016). In this geodynamic context, the Rodinia supercontinent is the significant stage for Proterozoic evolution (e.g., Meert, 2001; Li et al., 2008; Nance et al., 2014). The Rodinia assembly marks the amalgamation of Archean to early Proterozoic continental fragments during late Mesoproterozoic to Neoproterozoic times, leading to maximum crustal thickness and magmatism during the Grenville orogenic collage (e.g., Meert, 2001; Li et al., 2008; Nance et al., 2014). The magmatism associated with Rodinia formation shows diachronic episodes and presents a wide spatial distribution. It is recorded in the eastern margin of Laurentia, southwestern portion of the Amazonian Craton, Southern China Craton, Australia (N Queensland) and eastern margin of Antarctica (e.g., King Island-Transantarctic Mountains; McLelland et al., 1996; Fitzsimons et al., 2000; Li et al., 2002; Keppie et al., 2003; Hodych et al., 2004; Fioretti et al., 2005).

The Sunsas orogeny was responsible for the continental accretion developed in the SW Amazonian Craton related to Rodinia stabilization (e.g., Sadowski and Bettencourt, 1996; Tohver et al., 2002, 2006; Loewy et al., 2004; Boger et al., 2005; Li et al., 2008; Fuck et al., 2008; Teixeira et al., 2010). The Sunsas belt is the southwestern component of the Sunsas province, built during the Sunsas orogeny (e.g., Boger et al., 2005). Heterogeneous Archaean and Paleoproterozoic basement rocks were major sources for the 1.10 to 1.04 Ga granitic magmatism recorded in the Sunsas belt (Nedel et al., 2020). Here we present U-Pb zircon and monazite ages of magmatic rocks exposed in the Sunsas belt – Bolivia. The U-Pb monazite ages suggest that the previously dated zircon can be inherited, i.e., reworked from older

sources. This paper aims to (1) confirm magmatic episodes recorded in the Precambrian Sunsas belt; (2) compare the geochronological results with magmatic and metamorphic ages of the Aguapeí and Nova Brasilândia belts inserted in the Sunsas Province, and (3) compare the Bolivian basement evolution with the Rio Apa terrane.

3.3 Geological setting

In north-central South America, the Amazonian Craton represents continent-scale terrain accretion processes from Archean to Mesoproterozoic times (e.g., Tassinari and Macambira, 2004; Cordani and Teixeira, 2007). It consists of the central 3.0-2.5 Ga Archean Carajás-Amapá and Imataca blocks surrounded by 2.2–2.0 Ga Paleoproterozoic juvenile and reworked terrains related to the Transamazonian orogenic collage (e.g., Cordani et al., 2000; Tassinari and Macambira, 2004). The late Paleo- to early Mesoproterozoic transition recorded progressively younger magmatic accretions as evidenced by the 1.95–1.8 Ga Ventuari-Tapajós, 1.8–1.55 Ga Rio Negro-Juruena, 1.55–1.3 Ga Rondonian-San Ignacio and 1.3–1.0 Ga Sunsas provinces (e.g., Teixeira et al., 1989; Tassinari and Macambira, 1999, 2004). The latter includes rift stages, such as the Aguapeí aulacogen, and deposition of metasedimentary rocks related to the Mesoproterozoic Sunsas Group (Litherland et al., 1986; Saes et al., 1993; Geraldes et al., 2001). A different proposal divides the craton into eight geochronological provinces (Santos et al., 2000, 2008): Carajás (3-2.5 Ga), Central Amazonian (~2.6 Ga), Transamazonas (2.26-2.01 Ga), Tapajós-Parima (2.03-1.88 Ga), Rio Negro (1.82-1.52 Ga), Rondônia-Juruena (!.82-1.54 Ga), Sunsas (1.45-1.0 Ga) and K'Mudku (~1.2 Ga). Despite of the difference, there is consensus that the Grenvillian-Sunsas orogeny closed the Amazonian Craton assembly at c. 1.0 Ga (e.g., Teixeira et al., 1989; Tassinari and Macambira, 2004; Cordani and Teixeira, 2007; Santos et al., 2008).

3.3.1 Late Mesoproterozoic to Tonian Sunsas Province

The Sunsas Province comprises the supracrustal and magmatic rocks generated and affected by the Sunsas Orogeny (1.1–1.0 Ga), the last continental accretion recorded in the Amazonian Craton before its final tectonic stabilization (e.g., Tassinari and Macambira, 2004; Cordani and Teixeira, 2007; Teixeira et al., 2010). The collisional-type event was confined in the Sunsas, Aguapeí, and Nova Brasilândia mobile belts,

generated along the Paraguá Terrane and Rondonian-San Ignacio basement margins (Fig. 3.1; Table 3.1) (e.g., Teixeira et al., 2010). Litherland et al. (1986, 1989) undertook the initial lithostratigraphic studies of the Sunsas Orogen in eastern Bolivia. Soon after, Hoffman et al. (1991) suggested the most significant petrogenetic link between the Sunsas and Grenville provinces. Several geotectonic models were designed to take account of structural, igneous, and metamorphic features of igneous and supracrustal sequences that built the Sunsas belt (e.g., Santos et al., 2000; Tohver et al., 2004; Boger et al., 2005).

3.3.1.1 Sunsas belt

The Sunsas belt is an NW-SE trending, 600 km long belt that comprises the rock assemblage exposed in the western portion of the Sunsas Province. Its final structuring occurred during the Sunsas orogeny (Litherland et al., 1986, 1989; Tassinari and Macambira, 2004; Cordani and Teixeira, 2007; Teixeira et al., 2010).

The Sunsas belt is compartmentalized by transpressive shear zones, namely the Rio Negro, Santa Catalina, Concepción, and San Diablo fronts (Fig. 3.1). The Rio Negro and Santa Catalina fronts record the tectonic transport from southwest to northeast of the Sunsas belt. The San Diablo front is a curvilinear dextral shear zone related to tectonic northward stress whereas the Rio Negro front resulted from the near frontal, tangential, SW–NE directed collage (Litherland et al., 1986; Nedel et al., 2017). The Concepción front separates a pervasively deformed domain in the SW to a non-pervasive deformation domain in the NE (Litherland et al., 1986). These continental-scale shear zones were developed at c. 1.08–1.04 Ga along the southern margin of the Paraguá Terrane (Litherland el a., 1986; Teixeira et al., 2010). The shear zones acted as channels for the Sunsas high-K granitic intrusions into the Paleo- to Mesoproterozoic basement, which comprises the 1.76-1.68 Ga Chiquitania and 1.81-1.65 Ga Lomas Maneches complexes, <1.69 Ga San Ignacio Group, and the 1.37-1.28 Ga Pensamiento Suite (Litherland and Bloomfield, 1981; Litherland et al., 1986; Teixeira et al., 2010). That is, the network of shear zones allowed the emplacement of syn- to late-tectonic granites (e.g., Litherland et al., 1986, 1989; Teixeira et al., 2010). Thus, these structures control occurrences of gold in Mato Grosso, Brazil (e.g., Fernandes et al., 2006) and in the Don Mario mineral district in Bolivia (Teixeira et al., 2010).

Table 3-1. Magmatic and metamorphic ages for the Sunsas orogeny, West Amazonian Craton (Teixeira et al., 2010; Quadros, 2020).

Tectonic Unit	Granite	References	U-Pb	Rb-Sr	Sm-Nd			Tectonic setting
			Ages (Ma)	Ages (Ma)	Tdm (Ga)	eNd(0)	eNd(T)	
SUNSAS BELT	Tasseoro	Litherland et al. (1986)						Magmatic arc
	Taperas							
		Boger et al. (2005)	1076±18 (zr)					
		Vargas-Mattos (2010)	1047±24 (zr)		1,71		-4,74 e -5,82	
	Casa de Piedra	Litherland et al. (1986)		1005±12				
	Casa de Piedra (dyke)							
	Casa de Piedra	Darbyshire et al. (2000)			1,92		-4	
		Vargas-Mattos (2010)	1089 a 1030				-4,94 e -3,56	
	San Pedro (pegmatite)	Litherland et al. (1986)						
	San Javier (dyke)							
	Orobayaya (aplite dyke)							
	El Carmem (pegmatite)							
	El Carmem	Vargas-Mattos (2010)	1071±34 (zr)		1,80		-5,03	
	Naranjito		1048±19 (zr)		1,75		-3,17 e -4,77	
	Primavera		1.08 (zr)		1,66		-0,59 e 8,52	
	Señoritas	Isla-Moreno (2009)	1004±1					
AGUAPEÍ BELT	Guapé	Teixeira e Tassinari (1984)		835 e 900 (rt)				Aulacogen setting
	Guapé	Menezes et al. (1993)		950 ± 40 (rt)				
	São Domingos	Geraldes et al. (2000)	936±26 (z)		2.21		-7,1 e -7,6	
	São Domingos		930±12 (z)					
	Sararé	Araújo-Ruiz (2003)	907±18 (z)					

Tectonic Unit	Granite	References	U-Pb Ages (Ma)	Rb-Sr Ages (Ma)	Sm-Nd Tdm (Ga)	Sm-Nd eNd(0)	Sm-Nd eNd(T)	Tectonic setting
	Sararé	Ruiz (2005)			2.9	-8.1	-4.97	
	Guapé e São Domingos					-14		
	São Domingos	De Paulo (2005)						
NOVA BRASILÂNDIA BELT	Rio Branco suite	Quadros (2020)	1113±7 1112±2 1119±3 1106±3					Magmatic emplacement arc - back-arc system formation
	São Domingos	Siqueira (2015)	928±5 (z)		1.58	-13	-2.9	Collision and crustal thickening (High-grade metamorphic and migmatization)
	Granito Rio Branco	Rizzotto (1999)	1113 ± 53					
	Granitos sin-tectônicos		1110 ± 8					
	Metagabro		1110 ± 10					
	Granito Rio Pardo		1005 ± 41					

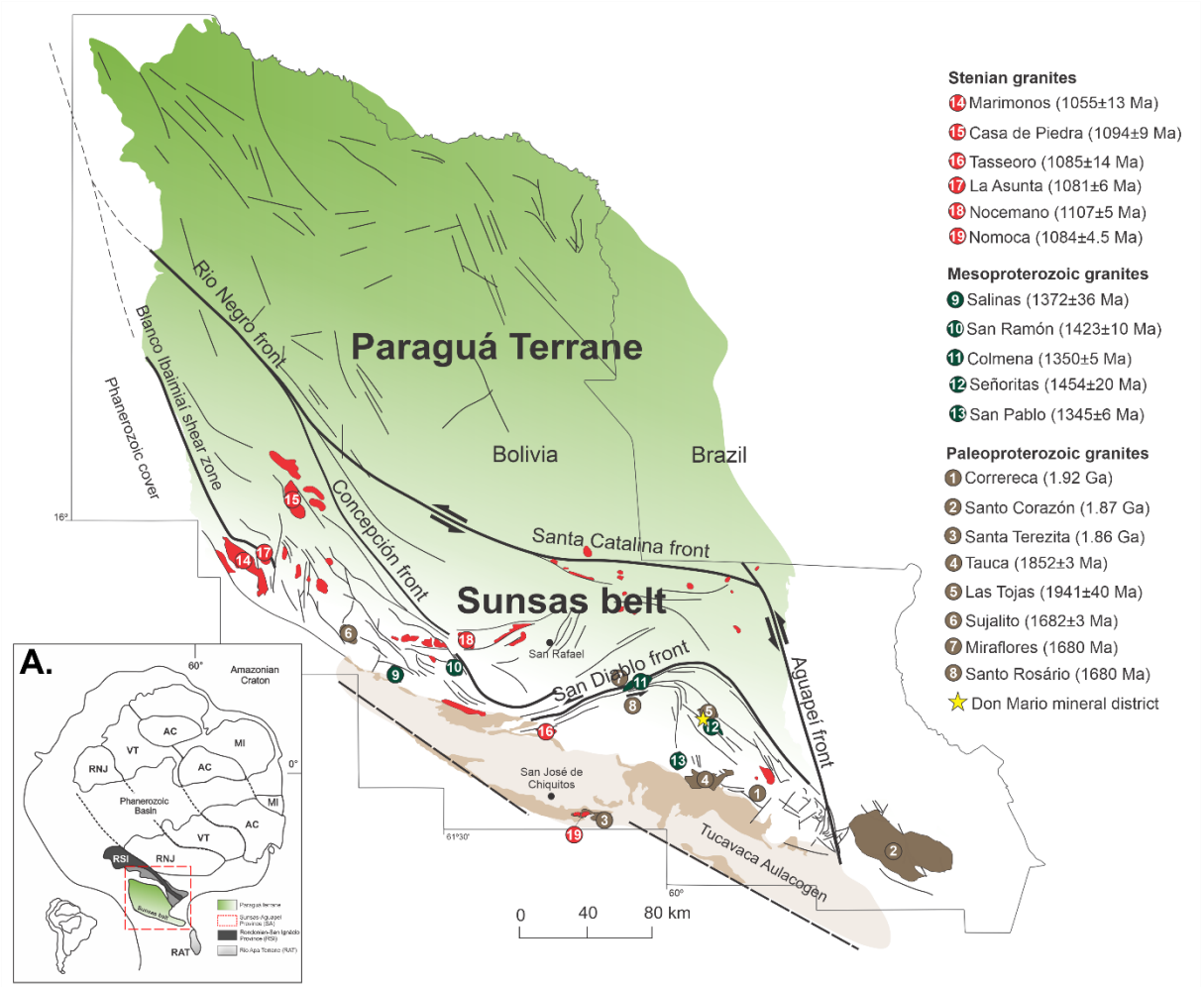

Figure 3.1. (A) Schematic geotectonic compartment for the Amazonian Craton detaching the SW portion and Sunsas Province (after Teixeira et al., 1989; Tassinari and Macambira, 1999, 2004; Tassinari et al., 2000) (modified from Cordani et al., 2000). AC - Amazônia Central (2.5 Ga), MI - Maroni-Itacaiúnas (2.2–1.95 Ga), VT - Ventuari-Tapajós (1.95–1.8 Ga), RNJ - Rio Negro-Juruena (1.8–1.55 Ga), RAT – Rio Apa Terrane (2.0-1.5); RSI - Rondonian-San Ignácio (1.55–1.3 Ga) and SA - Sunsas (1.3–1.0 Ga); (B) Schematic geological map for the West Amazonian Craton with focus in the Sunsas belt and the studied plutons location.

3.4 Analytical methods and procedures

3.4.1 Geological Sampling and Petrography

A total of eleven granitic plutons from the Sunsas belt in Southeastern Bolivia were sampled and dated (Fig. 3.1; Table 3.2). The plutons were chosen based on geological mapping of eastern Bolivia performed by Servicio Geologico de Bolivia during the development of the Proyecto Precambrico, in the 1970s and 1980s (Litherland et al., 1986). Rock outcrops are scarce in the study region due to intense chemical weathering, thickness of soil layers and forest cover. Systematic thin sections cut relative to foliation were obtained from the granite samples. Petrographic

descriptions were done at the Microscopy Laboratory of the Institute of Geosciences of Universidade de Brasília (Brazil).

Table 3-2. Studied granitic from the Sunsas Belt in northeast Bolivia.

Pluton	Sample	Classification	Area 1:250.000	Location	
Marimonos	MR11	Granite	Concepcion CUAD, SE 20-3/SE 20-2	514849	8197726
San Ramón	ID11	Granite		536428	8176968
Sujalito	SR20	Granite		568896	8161116
Tasseoro	TAS 15	Granite	San José de Chiquitos CUAD, SE 20-8/SE20-7	734892	8075813
Colmena	IM34	Granite		772148	8101574
Salinas	SM10	Monzogranite		622464	8120572
San Pablo	ID02	Monzogranite	Santo Corazón CUAD, SE 21-5/SE 21-9	193169	8058223
Señoritas	ID06	Two-mica granite		213825	8081030
Las Tojas	ID08	Two-mica granite		210690	8090872
Tauca	ID09	Granodiorite		217672	8038242
Casa de Piedra	ID18	Monzogranite	Monte Verde CUAD SD 20-15	554208	8243651

3.4.2 Zircon and Monazite U-Pb isotopes

U-Pb isotopic analyses were performed on zircon from eleven granite samples (LA14, TAP02, SM10, ID02, ID06, ID08, ID09, ID11, ID18, SR20, SM07) and monazite grains from two samples (ID06, ID08) conducted on a Thermo Finnigan Neptune MC-ICP-MS, coupled with a New Wave UP213 Nd: YAG laser (λ=213 nm) at the Laboratory of Geochronology of University of Brasília, following the procedures described by Bühn et al. (2009). Measurements consisted of point analyses.

In order to extract zircon and monazite grains, samples were first processed in a rock crusher, producing chips roughly 3–5 cm in size. Samples were then processed in a Selfrag high voltage laboratory equipment, with a voltage of 130 kV and a frequency of 3 Hz. Zircon and monazite grains were concentrated using a pan to separate the heavy mineral fraction and a Franz was then used to remove the magnetic fraction. Zircon and monazite grains were handpicked using a binocular microscope. Grains were mounted in epoxy mounts and polished to create a smooth surface. HNO3 (ca. 2%) was used to clean the surface of the mounts. Backscatter electron images (BSE) of the zircon grains were taken with a FEI-Quanta 450 scanning electron microscope, working at 20–25 kV, at the University of Brasília, in order to characterize grain zonation.

U-Pb analyses on zircon grains were carried out by the standard-sample bracketing method (Albarède et al., 2004), using the GJ-1 standard zircon (Jackson et al., 2004) in order to quantify the amount of ICP-MS fractionation. The tuned masses were ^{238}U, ^{207}Pb, ^{206}Pb, ^{204}Pb and ^{202}Hg. The integration time was 1 second, and the ablation time was 40 seconds. A 30 µm spot size was used, and the laser setting was 10 Hz and 2-3 J/cm2. For monazite, a laser beam diameter of 25 µm at 10 Hz and ~ 2.4 J/cm2 was implemented. Two to four unknown grains were analyzed between GJ-1 analyses. $^{206}Pb/^{207}Pb$ and $^{206}Pb/^{238}U$ ratios were time corrected. The raw data were processed off-line and reduced using an Excel worksheet (Bühn et al., 2009) with the aid of "Chronus" software (Oliveira, 2015). During the analytical sessions, zircon standard 91500 (Wiedenbeck et al., 2004) was also analyzed as an external standard. Zircon ages were calculated using ISOPLOT v.3 (Ludwig, 2003), with isotopic ratio errors presented at the 1σ level. The internal laboratory monazite (Chaves et al., 2010) and 44,069 monazites (424.86±0.36 Ma; Aleinikoff et al., 2006) were used as the primary and external standard for monazite analyses.

Common ^{204}Pb was monitored using the ^{202}Hg and ($^{204}Hg+^{204}Pb$) masses. Common Pb corrections were done due to weak signals of ^{204}Pb (< 30cps) and high $^{206}Pb/^{204}Pb$ ratios. Reported errors are propagated by quadratic addition [(2SD2+2SE2)1/2] (SD=standard deviation; SE=standard error) of external reproducibility and within-run precision. External reproducibility is represented by the standard deviation obtained from repeated analyses (~1.1 % for $^{207}Pb/^{206}Pb$ and up to ~2 % for $^{206}Pb/^{238}U$) of the GJ-1 zircon standard during the analytical sessions and the within-run precision is the standard error calculated for each analysis. Concordia diagrams (2σ error ellipses), probability density plots and weighted average ages were calculated using the Isoplot-3/Ex software (Ludwig, 2008).

3.5 Results of U-Pb dating

3.5.1 Paleoproterozoic granites

The older magmatism is represented by granodiorite and granite emplaced in the southern part of the Sunsas belt (Fig. 3.1 and tables 3.3 and 3.4). The Las Tojas two-mica granite (30-39% plagioclase, 25-31% K-feldspar, 20-30% quartz and 8-15% mica) presents incipient foliation that reflects the host NW-SE tectonic transcurrent shear zone. The Tauca granodiorite (38-42% plagioclase; 29-32%

quartz; 15-18% K-feldspar; and 10-15% biotite) and Sujalito granite (33-35% quartz; 29-35% K-feldspar; 25-33% plagioclase; and 3-5% biotite) exposures are very weathered, making it difficult to recognize deformation structures. However, the primary mineral assemblage remains partially preserved.

All zircon grains from the Las Tojas, Tauca, and Sujalito samples are prismatic crystals with lengths of 100–300 μm, length/width ratio of 2:1 and 3:1 (Fig. 3.2). The backscattered electron (BSE) images show magmatic zoning with recrystallization fronts and zones (Fig. 3.2) (e.g., Corfu et al., 2003).

Table 3-3. U-Pb zircon data from the granitic plutons of the Sunsas Belt in northeast Bolivia.

Sujalito Sample	Spot	^{204}Pb cps	^{206}Pb mV[1]	Th/U	^{206}Pb/^{204}Pb	1s%	^{207}Pb/^{206}Pb	1s %	^{207}Pb/^{235}U	1s %	^{206}Pb/^{238}U	1s %	Rho	^{207}Pb/^{206}Pb	±2s	^{206}Pb/^{238}U	±2s	^{207}Pb/^{235}U	±2s	% U-Pb disc[2]
SR20	003-ZR1	11	0.0113	0.399	568820	27.74	0.10349	0.45	4.233	0.80	0.2967	0.54	0.68	1688	17	1675	16	1681	13	0.76
SR20	007-ZR5	92	0.0115	0.347	96403	44.36	0.10304	0.49	4.255	0.90	0.2995	0.67	0.74	1680	18	1689	20	1685	15	-0.55
SR20	010-ZR8	17	0.0244	0.326	606676	23.99	0.10336	0.54	4.227	0.90	0.2966	0.62	0.69	1685	20	1674	18	1679	15	0.65
SR20	015-ZR11	8	0.0086	0.408	358983	12.03	0.10336	0.50	4.099	0.87	0.2876	0.60	0.70	1685	19	1629	17	1654	14	3.32
SR20	017-ZR13	5	0.0064	0.337	249282	12.27	0.10354	0.42	4.170	0.89	0.2921	0.68	0.77	1688	16	1652	20	1668	14	2.16
SR20	018-ZR14	6	0.0080	0.452	302834	12.56	0.10338	0.43	4.276	0.82	0.2999	0.59	0.72	1686	16	1691	17	1689	13	-0.32
SR20	024-ZR20	17	0.0188	0.419	451051	26.44	0.10335	0.54	4.314	0.84	0.3028	0.52	0.62	1685	20	1705	16	1696	14	-1.18
SR20	028-ZR22	11	0.0123	0.390	399527	14.19	0.10284	0.46	4.222	0.85	0.2977	0.62	0.72	1676	17	1680	18	1678	14	-0.24
SR20	032-ZR26	9	0.0076	0.298	293830	14.61	0.10292	0.40	4.371	0.83	0.3080	0.63	0.75	1677	15	1731	19	1707	14	-3.18
SR20	033-ZR27	15	0.0081	0.378	171510	21.21	0.10359	0.46	4.251	0.81	0.2976	0.55	0.68	1689	17	1679	16	1684	13	0.60
SR20	034-ZR28	197	0.0172	0.452	5646	5.24	0.10377	0.48	4.380	0.89	0.3061	0.65	0.73	1693	18	1722	20	1709	15	-1.71
SR20	035-ZR29	123	0.0141	0.287	14930	15.74	0.10372	0.88	4.270	1.15	0.2986	0.65	0.56	1692	32	1684	19	1688	19	0.45
Tauca **Sample**	**Spot**	**^{204}Pb cps**	**^{206}Pb mV[1]**	**Th/U**	**^{206}Pb/^{204}Pb**	**1s%**	**^{207}Pb/^{206}Pb**	**1s %**	**^{207}Pb/^{235}U**	**1s %**	**^{206}Pb/^{238}U**	**1s %**	**Rho**	**^{207}Pb/^{206}Pb**	**±2s**	**^{206}Pb/^{238}U**	**±2s**	**^{207}Pb/^{235}U**	**±2s**	**% U-Pb disc[2]**
ID09	003-ZR1N	16	0.0080	0.485	226545	21.30	0.11313	0.42	5.321	0.80	0.3411	0.57	0.71	1850	15	1892	19	1872	14	-2.25
ID09	004-ZR1B	60	0.0128	0.605	61305	62.27	0.11400	0.36	4.763	0.85	0.3030	0.67	0.79	1864	13	1706	20	1778	14	8.48
ID09	005-ZR2N	13	0.0055	0.585	152658	18.36	0.11376	0.46	5.030	0.80	0.3207	0.54	0.68	1860	16	1793	17	1824	14	3.61
ID09	006-ZR2B	18	0.0067	0.458	169041	24.67	0.11236	0.38	5.447	0.83	0.3516	0.63	0.77	1838	14	1942	21	1892	14	-5.67
ID09	007-ZR3N	20	0.0051	0.442	128189	21.35	0.11300	0.41	5.005	0.75	0.3212	0.51	0.68	1848	15	1796	16	1820	13	2.85
ID09	008-ZR3B	16	0.0058	0.551	147728	22.24	0.11296	0.50	5.178	0.86	0.3325	0.60	0.70	1848	18	1850	19	1849	15	-0.15
ID09	009-ZR4	24	0.0067	0.670	193914	23.19	0.11309	0.60	5.132	0.93	0.3291	0.60	0.65	1850	22	1834	19	1841	16	0.85
ID09	010-ZR5	15	0.0059	0.496	208110	21.74	0.11341	0.67	5.180	1.05	0.3313	0.72	0.69	1855	24	1845	23	1849	18	0.54
ID09	011-ZR6	10	0.0059	0.326	286116	17.92	0.11304	0.69	5.041	0.97	0.3234	0.57	0.59	1849	25	1806	18	1826	16	2.29
ID09	015-ZR8N	19	0.0058	0.492	129676	21.77	0.11430	0.67	5.242	0.99	0.3326	0.63	0.64	1869	24	1851	20	1859	17	0.95
ID09	016-ZR8B	23	0.0047	0.457	73153	28.20	0.11470	0.59	5.187	0.94	0.3280	0.64	0.68	1875	21	1828	20	1851	16	2.50

Paleoproterozoic magmatism

ID09	017-ZR9	23	0.0032	1.377	60626	25.93	0.11335	0.71	5.137	1.05	0.3287	0.68	0.65	1854	25	1832	22	1842	18	1.18
ID09	020-ZR12N	17	0.0041	0.496	147547	27.51	0.11308	0.51	4.850	0.86	0.3110	0.59	0.68	1849	18	1746	18	1794	15	5.60
ID09	022-ZR13	11	0.0054	0.498	188908	17.65	0.11372	0.60	5.230	0.90	0.3336	0.57	0.63	1860	22	1856	18	1858	15	0.22
ID09	023-ZR14N	10	0.0036	0.539	157520	11.92	0.11381	0.65	5.210	0.97	0.3320	0.61	0.63	1861	24	1848	19	1854	16	0.70
ID09	028-ZR16	22	0.0058	0.478	107350	24.48	0.11350	0.47	5.244	0.79	0.3351	0.51	0.65	1856	17	1863	17	1860	13	-0.36
ID09	029-ZR17N	16	0.0058	0.583	134956	24.96	0.11268	0.42	5.243	0.87	0.3375	0.67	0.77	1843	15	1874	22	1860	15	-1.70
ID09	030-ZR17B	18	0.0080	0.454	257414	25.88	0.11302	0.46	5.236	0.99	0.3360	0.80	0.80	1848	16	1867	26	1858	17	-1.02
ID09	031-ZR18	16	0.0048	0.530	104578	21.46	0.11344	0.43	4.939	0.83	0.3157	0.60	0.73	1855	16	1769	19	1809	14	4.65
ID09	032-ZR19	15	0.0085	0.450	250298	22.13	0.11408	0.48	5.275	0.79	0.3353	0.50	0.63	1865	17	1864	16	1865	13	0.06
ID09	033-ZR20N	19	0.0039	0.515	114324	19.13	0.11323	0.58	5.007	0.91	0.3207	0.60	0.65	1852	21	1793	19	1820	15	3.18
ID09	036-ZR22	20	0.0030	1.021	85054	19.97	0.11338	0.59	5.101	0.97	0.3263	0.68	0.70	1854	21	1820	22	1836	16	1.82
ID09	041-ZR25	19	0.0060	0.621	174211	18.61	0.11425	0.34	5.040	0.75	0.3199	0.55	0.74	1868	12	1789	17	1826	13	4.22
ID09	042-ZR26	77	0.0112	0.796	81781	48.71	0.11425	0.38	5.250	0.77	0.3333	0.56	0.72	1868	14	1854	18	1861	13	0.74
ID09	043-ZR27	24	0.0063	0.519	92003	28.29	0.11411	0.31	5.137	0.73	0.3265	0.55	0.75	1866	11	1821	17	1842	12	2.40
ID09	044-ZR28	17	0.0077	0.463	254021	17.72	0.11408	0.35	5.153	0.78	0.3275	0.59	0.75	1865	13	1826	19	1845	13	2.09
ID09	045-ZR29	15	0.0048	0.480	141317	17.58	0.11390	0.51	5.161	0.91	0.3286	0.66	0.72	1862	18	1832	21	1846	15	1.66
ID09	046-ZR30	18	0.0074	0.826	180950	25.23	0.11405	0.50	5.174	0.95	0.3290	0.71	0.75	1865	18	1833	23	1848	16	1.68

Las Tojas																				
Sample	**Spot**	**^{204}Pb cps**	**^{206}Pb mV[1]**	**Th/U**	**^{206}Pb/^{204}Pb**	**1s%**	**^{207}Pb/^{206}Pb**	**1s %**	**^{207}Pb/^{235}U**	**1s %**	**^{206}Pb/^{238}U**	**1s %**	**Rho**	**^{207}Pb/^{206}Pb**	**±2 s**	**^{206}Pb/^{238}U**	**±2 s**	**^{207}Pb/^{235}U**	**±2 s**	**% U-Pb disc[2]**
ID08	019-ZR13	43	0.0063	0.590	14019	17.55	0.11440	0.79	4.948	1.11	0.3136	0.69	0.62	1871	28	1759	21	1810	19	5.98
ID08	021-ZR15	606	0.0265	0.233	2714	8.73	0.11699	0.93	5.650	1.64	0.3502	1.30	0.79	1911	33	1936	44	1924	28	-1.31
ID08	025-ZR17	180	0.0182	0.496	6909	4.28	0.10870	0.72	4.466	1.16	0.2980	0.84	0.72	1778	26	1681	25	1725	19	5.43
ID08	030-ZR22	249	0.0109	0.465	2847	4.50	0.11664	0.57	5.383	1.02	0.3347	0.76	0.75	1905	21	1861	25	1882	17	2.32
ID08	032-ZR24	398	0.0517	0.480	10040	8.60	0.10975	0.66	4.539	1.11	0.2999	0.81	0.73	1795	24	1691	24	1738	18	5.81
ID08	038-ZR28	676	0.0137	0.310	29971	74.01	0.12018	1.26	6.099	1.97	0.3680	1.46	0.74	1959	45	2020	51	1990	34	-3.13
ID08	039-ZR29	463	0.0125	0.272	2419	19.85	0.11522	0.68	5.025	1.36	0.3162	1.12	0.82	1883	25	1771	35	1823	23	5.95
ID08	004-ZR2	550	0.0170	0.323	2116	6.61	0.10132	1.02	2.935	1.56	0.2101	1.12	0.72	1648	38	1229	25	1391	23	25.42
ID08	013-ZR8	416	0.0081	0.550	1197	3.54	0.11949	0.66	5.066	1.25	0.3075	1.00	0.80	1949	24	1728	30	1830	21	11.30

ID08	022-ZR16	376	0.0162	0.060	3020	5.73	0.11042	0.85	4.058	1.45	0.2665	1.11	0.77	1806	31	1523	30	1646	23	15.68
ID08	026-ZR18	718	0.0954	0.091	8197	2.55	0.12653	0.58	6.031	1.06	0.3457	0.81	0.76	2050	21	1914	27	1980	18	6.66

San Pablo

Sample	Spot	^{204}Pb cps	^{206}Pb mV[1]	Th/U	^{206}Pb/^{204}Pb	1s%	^{207}Pb/^{206}Pb	1s %	^{207}Pb/^{235}U	1s %	^{206}Pb/^{238}U	1s %	Rho	^{207}Pb/^{206}Pb	±2 s	^{206}Pb/^{238}U	±2 s	^{207}Pb/^{235}U	±2 s	% U-Pb disc[2]
ID02	004-ZR2	18	0.0037	0.552	116924	18.47	0.08655	0.51	2.930	1.05	0.2455	0.84	0.80	1350	20	1415	21	1390	16	-4.81
ID02	007-ZR4	7	0.0032	0.477	130482	12.43	0.08683	0.50	2.735	0.91	0.2284	0.66	0.73	1357	19	1326	16	1338	14	2.27
ID02	008-ZR5	12	0.0092	0.719	332398	18.18	0.08633	0.39	2.753	0.74	0.2313	0.51	0.69	1346	15	1341	12	1343	11	0.33
ID02	009-ZR6	15	0.0027	0.440	72487	21.42	0.08620	0.98	2.728	1.44	0.2295	0.98	0.68	1343	38	1332	24	1336	21	0.79
ID02	010-ZR7N	15	0.0028	0.665	55163	24.40	0.08591	0.61	2.682	0.97	0.2264	0.66	0.68	1336	23	1315	16	1323	14	1.56
ID02	012-ZR8	12	0.0105	0.307	294852	26.70	0.08602	0.90	2.887	1.31	0.2434	0.87	0.67	1339	35	1404	22	1378	20	-4.92
ID02	015-ZR9	17	0.0021	0.433	63361	18.49	0.08592	0.80	2.710	1.21	0.2287	0.82	0.68	1336	31	1328	20	1331	18	0.64
ID02	018-ZR12	17	0.0026	0.482	78233	18.95	0.08607	0.70	2.721	1.13	0.2293	0.80	0.71	1340	27	1331	19	1334	17	0.66
ID02	020-ZR14	16	0.0039	0.539	99667	20.73	0.08644	0.40	2.803	0.78	0.2351	0.55	0.71	1348	15	1361	14	1356	12	-0.98
ID02	023-ZR17	12	0.0033	0.712	113181	40.16	0.08632	0.74	2.784	1.06	0.2339	0.66	0.62	1345	28	1355	16	1351	16	-0.71
ID02	024-ZR18	20	0.0050	0.581	97856	29.33	0.08663	0.57	2.747	0.87	0.2299	0.54	0.62	1352	22	1334	13	1341	13	1.34
ID02	027-ZR19	20	0.0063	0.435	230857	32.77	0.08652	0.60	2.817	0.98	0.2362	0.68	0.70	1350	23	1367	17	1360	15	-1.25
ID02	028-ZR20	21	0.0035	0.507	84832	22.21	0.08684	0.61	2.835	1.00	0.2367	0.70	0.70	1357	24	1370	17	1365	15	-0.94
ID02	029-ZR21N	15	0.0073	0.438	254621	18.97	0.11300	0.69	5.243	1.02	0.3365	0.66	0.64	1848	25	1870	21	1860	17	-1.16
ID02	030-ZR21B	5	0.0036	0.421	156920	12.07	0.08628	0.50	2.789	0.84	0.2345	0.57	0.68	1345	19	1358	14	1353	13	-0.99
ID02	031-ZR22	20	0.0062	0.639	138619	28.10	0.08600	0.50	2.735	0.84	0.2306	0.57	0.68	1338	19	1338	14	1338	12	0.04
ID02	033-ZR24	17	0.0027	0.467	87371	18.74	0.08586	0.51	2.837	0.99	0.2396	0.76	0.77	1335	20	1385	19	1365	15	-3.72
ID02	034-ZR25	17	0.0019	0.464	53430	21.02	0.08649	0.73	2.848	1.10	0.2388	0.74	0.67	1349	28	1380	18	1368	16	-2.30
ID02	036-ZR27	15	0.0030	0.618	61861	20.71	0.08653	0.62	2.770	0.98	0.2321	0.66	0.68	1350	24	1346	16	1347	15	0.32
ID02	037-ZR28	13	0.0033	0.457	133152	14.33	0.08682	0.60	2.822	0.93	0.2357	0.60	0.65	1356	23	1364	15	1361	14	-0.59
ID02	039-ZR30	11	0.0046	0.554	144173	16.34	0.08576	0.64	2.768	0.94	0.2341	0.58	0.62	1333	25	1356	14	1347	14	-1.75

Salinas

Sample	Spot	^{204}Pb cps	^{206}Pb mV[1]	Th/U	^{206}Pb/^{204}Pb	1s%	^{207}Pb/^{206}Pb	1s %	^{207}Pb/^{235}U	1s %	^{206}Pb/^{238}U	1s %	Rho	^{207}Pb/^{206}Pb	±2 s	^{206}Pb/^{238}U	±2 s	^{207}Pb/^{235}U	±2 s	% U-Pb disc[2]
SM10	003-ZR1	243	0.0165	0.778	7630	24.44	0.08798	1.03	2.424	3.35	0.1999	3.16	0.94	1382	39	1175	68	1250	48	15.01
SM10	006-ZR3	2483	0.0336	0.304	863	2.84	0.09907	2.55	1.831	4.56	0.1340	3.76	0.83	1607	94	811	57	1057	59	49.53

Mesoproterozoic magmatism

SM10	007-ZR4N	1453	0.0166	0.330	757	3.26	0.10392	1.10	1.709	2.33	0.1192	2.02	0.87	1695	40	726	28	1012	30	57.17
SM10	013-ZR17	528	0.0271	0.350	3159	4.06	0.08680	0.92	1.429	3.53	0.1194	3.38	0.96	1356	35	727	46	901	42	46.39
SM10	014-ZR8	655	0.0153	0.420	1502	7.61	0.08903	0.90	1.602	6.69	0.1305	6.62	0.99	1405	34	791	98	971	82	43.70
SM10	018-ZR11N	191	0.0142	0.656	6071	14.03	0.08972	0.61	2.945	1.75	0.2381	1.60	0.91	1419	23	1377	40	1394	26	3.02
SM10	019-ZR12	165	0.0176	0.383	7181	12.09	0.08480	0.67	2.256	1.73	0.1929	1.55	0.90	1311	26	1137	32	1199	24	13.26
SM10	020-ZR13B	871	0.0287	0.525	2153	4.14	0.09228	0.48	2.024	3.26	0.1591	3.21	0.98	1473	18	952	57	1124	44	35.40
SM10	024-ZR14N	243	0.0065	0.565	3466	23.69	0.08788	0.81	2.791	1.41	0.2303	1.09	0.77	1380	31	1336	26	1353	21	3.17
SM10	025-ZR14B	24	0.0163	0.376	351359	36.43	0.08652	0.43	2.932	1.76	0.2458	1.66	0.95	1350	17	1417	42	1390	26	-4.94
SM10	026-ZR15	514	0.0156	0.714	6466	25.91	0.08425	1.09	2.551	3.16	0.2196	2.94	0.93	1298	42	1280	68	1287	46	1.42
SM10	027-ZR16	895	0.0214	0.579	1746	12.47	0.08609	1.76	2.705	2.63	0.2279	1.92	0.73	1340	67	1323	46	1330	39	1.26
SM10	028-ZR17	343	0.0150	0.329	2442	15.55	0.08333	1.40	1.926	2.27	0.1676	1.75	0.77	1277	54	999	32	1090	30	21.77
SM10	029-ZR18N	180	0.0134	0.688	22912	54.17	0.09048	1.09	3.194	2.59	0.2560	2.32	0.90	1436	41	1469	61	1456	40	-2.34
SM10	030-ZR18B	39	0.0115	0.611	293294	20.99	0.08608	0.51	2.873	1.64	0.2420	1.52	0.92	1340	20	1397	38	1375	25	-4.28
SM10	033-ZR19B	40	0.0149	0.330	124158	34.74	0.09869	1.05	3.703	3.76	0.2721	3.59	0.95	1600	39	1552	99	1572	59	2.99
SM10	034-ZR19N	87	0.0126	0.399	146212	32.49	0.10546	1.29	4.968	3.21	0.3416	2.91	0.91	1722	47	1895	95	1814	54	-9.99
SM10	035-ZR20B	943	0.0130	0.684	886	3.64	0.10451	1.11	2.747	2.30	0.1906	1.98	0.86	1706	40	1125	41	1341	34	34.06
SM10	036-ZR20N	237	0.0139	0.585	4176	8.19	0.08782	0.62	2.665	1.74	0.2201	1.58	0.91	1379	24	1282	37	1319	25	6.99

San Ramón		^{204}Pb cps	^{206}Pb mV[1]	Th/U	^{206}Pb/^{204}Pb	1s%	^{207}Pb/^{206}Pb	1s %	^{207}Pb/^{235}U	1s %	^{206}Pb/^{238}U	1s %	Rho	^{207}Pb/^{206}Pb	±2 s	^{206}Pb/^{238}U	±2 s	^{207}Pb/^{235}U	±2 s	% U-Pb disc[2]
Sample	**Spot**																			
ID11	004-ZR2	21	0.0097	0.393	128215	28.80	0.08956	0.48	3.166	0.81	0.2564	0.54	0.66	1416	18	1471	14	1449	12	-3.90
ID11	007-ZR5	54	0.0039	0.588	5933	18.29	0.09213	0.95	2.763	1.42	0.2175	0.99	0.70	1470	36	1269	23	1346	21	13.70
ID11	032-ZR26	28	0.0027	0.350	70324	45.33	0.08979	0.70	2.996	1.04	0.2420	0.67	0.65	1421	27	1397	17	1407	16	1.70
ID11	047-ZR38B	11	0.0030	0.285	116708	17.67	0.08903	0.72	3.010	1.02	0.2452	0.62	0.61	1405	28	1414	16	1410	15	-0.64
ID11	055-ZR44	144	0.0111	0.439	8906	48.15	0.09264	0.42	3.118	0.82	0.2441	0.60	0.73	1481	16	1408	15	1437	13	4.90
ID11	057-ZR46	25	0.0034	0.448	78898	36.03	0.08996	0.70	2.950	1.51	0.2378	1.28	0.85	1425	27	1375	32	1395	23	3.46
ID11	067-ZR52B	15	0.0020	0.338	62515	21.08	0.08951	0.78	2.950	1.25	0.2390	0.91	0.73	1415	30	1382	23	1395	19	2.36
ID11	071-ZR56	150	0.0127	0.161	5492	3.92	0.09269	0.43	2.908	0.79	0.2276	0.55	0.70	1481	16	1322	13	1384	12	10.78
ID11	078-ZR61N	47	0.0158	0.291	297594	43.72	0.08947	0.48	3.059	0.83	0.2479	0.56	0.68	1414	18	1428	14	1422	13	-0.96
ID11	084-ZR66	56	0.0031	0.235	9993	54.23	0.08953	1.31	2.667	1.79	0.2160	1.16	0.65	1416	50	1261	26	1319	26	10.95

ID11	085-ZR67N	39	0.0066	0.488	78162	37.28	0.09184	0.64	3.165	0.99	0.2500	0.66	0.67	1464	24	1438	17	1449	15	1.76
ID11	086-ZR67B	10	0.0045	0.229	126205	19.45	0.09000	0.61	3.112	1.01	0.2508	0.72	0.71	1425	23	1443	19	1436	16	-1.20
Colmena																				
Sample	**Spot**	**^{204}Pb cps**	**^{206}Pb mV[1]**	**Th/U**	**^{206}Pb/^{204}Pb**	**1s%**	**^{207}Pb/^{206}Pb**	**1s %**	**^{207}Pb/^{235}U**	**1s %**	**^{206}Pb/^{238}U**	**1s %**	**Rho**	**^{207}Pb/^{206}Pb**	**±2 s**	**^{206}Pb/^{238}U**	**±2 s**	**^{207}Pb/^{235}U**	**±2 s**	**% U-Pb disc[2]**
IM34	006-ZR3	32	0.0083	0.415	149861	24.86	0.08623	0.41	2.933	1.25	0.2467	1.13	0.90	1343	16	1421	29	1390	19	-5.81
IM34	007-ZR4	10	0.0061	0.318	221148	13.52	0.08659	0.38	2.729	0.87	0.2286	0.69	0.79	1351	15	1327	17	1336	13	1.80
IM34	008-ZR5	27	0.0099	0.332	465520	48.70	0.08659	0.73	2.766	1.91	0.2317	1.73	0.90	1351	28	1343	42	1346	28	0.60
IM34	009-ZR6	54	0.0103	0.393	162860	34.35	0.08505	0.50	2.932	1.35	0.2501	1.20	0.89	1317	19	1439	31	1390	20	-9.27
IM34	010-ZR7	41	0.0090	0.416	173694	26.59	0.08641	0.46	2.961	1.82	0.2485	1.72	0.95	1347	18	1431	44	1398	27	-6.18
IM34	013-ZR8	26	0.0136	0.322	224440	35.18	0.08652	0.60	3.065	2.64	0.2569	2.54	0.96	1350	23	1474	67	1424	40	-9.21
IM34	014-ZR9	105	0.0300	0.213	20876	10.87	0.08624	0.34	2.604	1.49	0.2190	1.41	0.94	1344	13	1276	33	1302	22	5.00
IM34	015-ZR10	63	0.0293	0.158	181003	44.15	0.08580	1.33	2.676	2.87	0.2261	2.52	0.88	1334	51	1314	60	1322	42	1.46
IM34	016-ZR11	16	0.0130	0.237	286324	21.76	0.08650	0.35	2.834	0.85	0.2376	0.68	0.80	1349	14	1374	17	1365	13	-1.84
IM34	017-ZR12	16	0.0080	0.680	203770	18.55	0.08699	0.36	2.863	0.97	0.2387	0.82	0.85	1360	14	1380	20	1372	15	-1.44
IM34	018-ZR13	15	0.0157	0.282	521859	15.34	0.08698	0.79	2.904	1.65	0.2421	1.40	0.85	1360	30	1398	35	1383	25	-2.75
IM34	019-ZR14	21	0.0083	0.333	158153	23.49	0.08635	0.38	2.986	3.67	0.2508	3.63	0.99	1346	15	1443	93	1404	55	-7.17
IM34	020-ZR15	15	0.0053	0.491	190995	18.15	0.08739	0.49	2.771	1.04	0.2300	0.84	0.81	1369	19	1334	20	1348	15	2.53
IM34	026-ZR18N	19	0.0092	0.317	907341	66.01	0.08596	0.33	2.899	2.88	0.2446	2.84	0.99	1337	13	1411	72	1382	43	-5.48
IM34	028-ZR20	12	0.0127	0.294	444965	19.87	0.08693	0.44	3.086	2.36	0.2574	2.29	0.97	1359	17	1477	60	1429	36	-8.66
IM34	034-ZR24	208	0.0238	0.299	8055	11.48	0.08633	0.50	2.082	4.40	0.1749	4.35	0.99	1346	19	1039	83	1143	59	22.79
IM34	035-ZR25	54	0.0107	0.590	69196	47.97	0.08744	0.35	3.126	2.01	0.2593	1.95	0.97	1370	13	1486	52	1439	31	-8.47
IM34	036-ZR26	27	0.0117	0.229	364011	20.20	0.08700	0.38	3.001	1.30	0.2501	1.19	0.91	1360	15	1439	31	1408	20	-5.79
IM34	037-ZR27	40	0.0130	0.289	291753	27.82	0.08672	0.34	3.070	1.12	0.2568	1.00	0.89	1354	13	1473	26	1425	17	-8.80
IM34	039-ZR29	193	0.0150	0.293	7504	31.86	0.08615	0.69	3.019	2.49	0.2542	2.36	0.95	1342	27	1460	62	1413	38	-8.82
IM34	044-ZR30	507	0.0133	0.668	1636	5.17	0.08457	1.04	1.068	2.81	0.0916	2.58	0.92	1306	40	565	28	738	29	56.74
IM34	046-ZR7B	386	0.0119	0.043	1717	5.69	0.08382	0.80	0.673	2.59	0.0582	2.44	0.94	1288	31	365	17	522	21	71.70
Señoritas																				
Sample	**Spot**	**^{204}Pb cps**	**^{206}Pb mV[1]**	**Th/U**	**^{206}Pb/^{204}Pb**	**1s%**	**^{207}Pb/^{206}Pb**	**1s %**	**^{207}Pb/^{235}U**	**1s %**	**^{206}Pb/^{238}U**	**1s %**	**Rho**	**^{207}Pb/^{206}Pb**	**±2 s**	**^{206}Pb/^{238}U**	**±2 s**	**^{207}Pb/^{235}U**	**±2 s**	**% U-Pb disc[2]**
ID06	005-ZR2	63	0.0139	0.636	19186	17.45	0.11473	0.45	4.956	0.83	0.3133	0.59	0.72	1876	16	1757	18	1812	14	6.33

ID06	011-ZR8	3478	0.0467	0.305	841	1.11	0.08814	0.63	1.035	1.55	0.0852	1.36	0.88	1386	24	527	14	721	16	61.97
ID06	020-ZR14	5692	0.0534	0.310	601	4.27	0.08951	0.79	1.824	1.64	0.1478	1.38	0.84	1415	30	888	23	1054	21	37.21
ID06	023-ZR17	1999	0.0258	0.364	808	1.12	0.09161	0.54	2.470	1.03	0.1955	0.79	0.77	1459	21	1151	17	1263	15	21.12
ID06	027-ZR19	480	0.0086	0.229	1159	2.97	0.09030	0.83	1.777	1.46	0.1427	1.14	0.78	1432	32	860	18	1037	19	39.93
ID06	030-ZR22	130	0.0214	0.393	35558	64.47	0.12213	0.40	5.445	1.47	0.3234	1.37	0.93	1988	14	1806	43	1892	25	9.13
ID06	035-ZR24	629	0.0299	0.156	2908	5.96	0.10659	0.63	3.845	1.13	0.2616	0.87	0.77	1742	23	1498	23	1602	18	14.01
ID06	036-ZR25N	687	0.0266	0.610	3210	9.89	0.08949	1.05	2.919	1.79	0.2365	1.41	0.79	1415	40	1369	35	1387	27	3.24
ID06	042-ZR29	24	0.0119	0.812	127645	41.13	0.12270	0.76	6.323	1.18	0.3737	0.82	0.70	1996	27	2047	29	2022	21	-2.56
ID06	043-ZR30N	156	0.0144	0.487	7397	9.71	0.11381	0.57	4.655	1.04	0.2967	0.78	0.75	1861	21	1675	23	1759	17	10.01
ID06	068-ZR48	19	0.0103	0.690	225387	35.12	0.12151	0.88	6.102	1.18	0.3642	0.68	0.58	1978	31	2002	23	1990	20	-1.19
ID06	074-ZR52	62	0.0076	0.516	14158	26.23	0.12179	0.77	6.934	1.75	0.4129	1.53	0.87	1983	27	2228	57	2103	31	-12.39
ID06	075-ZR53	46	0.0301	0.660	365516	33.14	0.11345	0.48	4.832	1.03	0.3089	0.84	0.81	1855	17	1735	25	1790	17	6.48
ID06	076-ZR54	1954	0.0362	0.703	1618	9.35	0.09097	0.80	2.199	1.15	0.1753	0.75	0.65	1446	30	1041	14	1181	16	27.99

Tonian-Stenian magmatism

Tasseoro																				
Sample	**Spot**	**^{204}Pb cps**	**^{206}Pb mV[1]**	**Th/U**	**^{206}Pb/^{204}Pb**	**1s%**	**^{207}Pb/^{206}Pb**	**1s %**	**^{207}Pb/^{235}U**	**1s %**	**^{206}Pb/^{238}U**	**1s %**	**Rho**	**^{207}Pb/^{206}Pb**	**±2 s**	**^{206}Pb/^{238}U**	**±2 s**	**^{207}Pb/^{235}U**	**±2 s**	**% U-Pb disc[2]**
TAS15	030-ZR22	8	0.0030	0.731	103570	15.28	0.07642	1.01	1.841	1.35	0.1747	0.81	0.60	1106	40	1038	16	1060	18	6.15
TAS15	031-ZR23	6	0.0018	1.118	76305	12.04	0.07573	0.79	1.781	1.21	0.1705	0.83	0.69	1088	32	1015	16	1038	16	6.69
TAS15	032-ZR24N	9	0.0054	0.674	184978	16.17	0.07541	0.53	1.983	1.00	0.1907	0.76	0.76	1079	21	1125	16	1110	13	-4.24
TAS15	033-ZR24B	5	0.0038	0.641	167165	11.58	0.07582	0.56	1.867	1.07	0.1786	0.83	0.78	1090	22	1059	16	1070	14	2.85
TAS15	036-ZR26	15	0.0039	1.539	125537	20.24	0.07590	0.74	1.786	1.26	0.1706	0.95	0.76	1093	29	1016	18	1040	16	7.05
TAS15	041-ZR29	6	0.0020	1.542	86774	14.25	0.07546	0.92	1.782	1.31	0.1713	0.86	0.65	1081	37	1019	16	1039	17	5.70
TAS15	044-ZR31	8	0.0018	1.224	76410	13.48	0.07582	0.72	1.750	1.17	0.1674	0.84	0.72	1090	29	998	15	1027	15	8.49
Casa de Piedra																				
Sample	**Spot**	**^{204}Pb cps**	**^{206}Pb mV[1]**	**Th/U**	**^{206}Pb/^{204}Pb**	**1s%**	**^{207}Pb/^{206}Pb**	**1s %**	**^{207}Pb/^{235}U**	**1s %**	**^{206}Pb/^{238}U**	**1s %**	**Rho**	**^{207}Pb/^{206}Pb**	**±2 s**	**^{206}Pb/^{238}U**	**±2 s**	**^{207}Pb/^{235}U**	**±2 s**	**% U-Pb disc[2]**
ID18	008-ZR5B	1549	0.0322	0.139	2441	13.25	0.09718	1.11	2.015	1.88	0.1504	1.47	0.78	1571	41	903	25	1121	25	42.51
ID18	009-ZR6	124	0.0394	0.101	24072	9.52	0.07630	0.46	2.109	1.12	0.2005	0.95	0.85	1103	18	1178	20	1152	15	-6.79
ID18	012-ZR9	484	0.0235	0.060	4142	11.89	0.08028	1.39	2.020	1.52	0.1825	0.48	0.32	1204	54	1080	10	1122	20	10.25
ID18	018-ZR13	346	0.0139	0.043	2803	6.72	0.08052	1.23	2.009	1.38	0.1810	0.51	0.37	1210	48	1072	10	1119	19	11.36
ID18	021-ZR15	148	0.0187	1.060	342570	75.74	0.08092	0.98	2.030	1.23	0.1820	0.65	0.53	1220	38	1078	13	1126	17	11.64

ID18	036-ZR27B	13	0.0288	0.047	770112	29.48	0.07563	0.57	1.988	0.83	0.1906	0.47	0.57	1085	23	1125	10	1111	11	-3.61
ID18	038-ZR29	191	0.0437	0.233	76176	73.70	0.10642	0.66	4.034	1.25	0.2749	0.99	0.80	1739	24	1565	28	1641	20	9.98
ID18	045-ZR33	1110	0.0232	1.121	4282	18.38	0.09944	1.31	2.277	1.68	0.1661	0.99	0.59	1614	48	991	18	1205	24	38.62
ID18	049-ZR37	27	0.0815	0.060	640223	31.16	0.07572	1.03	1.967	1.24	0.1884	0.58	0.47	1088	41	1113	12	1104	17	-2.28
ID18	061-ZR45	35	0.0352	0.287	218308	60.91	0.07523	0.42	1.909	0.75	0.1840	0.49	0.66	1075	17	1089	10	1084	10	-1.33
ID18	062-ZR46	522	0.0113	0.728	1363	5.57	0.08297	1.22	2.080	1.41	0.1818	0.60	0.42	1269	47	1077	12	1142	19	15.12
ID18	067-ZR49N	394	0.0173	0.279	3202	10.18	0.07639	1.06	1.964	1.26	0.1864	0.57	0.46	1105	42	1102	12	1103	17	0.29
ID18	068-ZR49B	68	0.0132	0.860	159075	40.86	0.07665	0.42	1.886	0.83	0.1784	0.61	0.73	1112	17	1058	12	1076	11	4.83
ID18	069-ZR50	30	0.0098	1.347	62636	46.79	0.07527	0.56	1.929	0.88	0.1859	0.57	0.64	1076	23	1099	11	1091	12	-2.17
ID18	076-ZR56	368	0.0119	0.090	2061	3.45	0.08232	0.92	2.033	1.14	0.1791	0.57	0.50	1253	36	1062	11	1127	15	15.25
ID18	080-ZR58	8	0.0034	0.834	137865	19.10	0.07573	1.02	1.864	1.36	0.1785	0.82	0.60	1088	41	1059	16	1068	18	2.71
ID18	084-ZR61	243	0.0143	0.902	3775	15.62	0.07672	0.57	1.938	0.91	0.1832	0.61	0.67	1114	23	1085	12	1094	12	2.62
ID18	087-ZR64	482	0.0099	0.455	1620	9.12	0.08343	1.81	2.458	2.08	0.2137	0.95	0.46	1279	70	1248	22	1260	30	2.40

Marimonos		^{204}Pb cps	^{206}Pb mV[1]	Th/U	^{206}Pb/^{204}Pb	1s%	^{207}Pb/^{206}Pb	1s %	^{207}Pb/^{235}U	1s %	^{206}Pb/^{238}U	1s %	Rho	^{207}Pb/^{206}Pb	±2 s	^{206}Pb/^{238}U	±2 s	^{207}Pb/^{235}U	±2 s	% U-Pb disc[2]
Sample	Spot																			
MR10	003-ZR1N	6	0.0023	0.713	97344	11.39	0.08637	0.64	2.561	1.13	0.2150	0.86	0.76	1346	25	1255	20	1289	16	6.76
MR10	004-ZR1B	28	0.0390	0.042	302472	38.17	0.07532	0.36	2.051	0.93	0.1975	0.78	0.83	1077	14	1162	17	1133	13	-7.86
MR10	009-ZR4B	17	0.0428	0.028	922323	23.25	0.07508	0.46	1.881	0.87	0.1817	0.64	0.73	1071	19	1076	13	1074	11	-0.53
MR10	011-ZR6	87	0.0502	0.025	607019	47.20	0.07512	0.64	1.842	1.27	0.1779	1.03	0.81	1072	26	1055	20	1061	17	1.52
MR10	012-ZR7N	598	0.0262	0.289	2774	4.19	0.07536	1.19	1.271	2.14	0.1223	1.75	0.82	1078	47	744	25	833	24	30.99
MR10	019-ZR8B	28	0.0502	0.027	845029	29.59	0.07492	0.37	1.887	0.74	0.1827	0.52	0.71	1066	15	1082	10	1077	10	-1.43
MR10	021-ZR9B	781	0.0321	0.221	2937	6.27	0.07966	0.71	1.615	1.17	0.1470	0.86	0.73	1188	28	884	14	976	15	25.61
MR10	022-ZR10N	340	0.0276	0.493	5782	8.20	0.07773	0.50	1.897	0.99	0.1770	0.78	0.78	1140	20	1051	15	1080	13	7.83
MR10	023-ZR10B	34	0.0327	0.057	593603	30.90	0.07485	0.37	1.977	0.76	0.1916	0.55	0.73	1064	15	1130	11	1108	10	-6.15
MR10	024-ZR11	62	0.0282	0.045	165726	42.89	0.07496	0.44	2.014	0.84	0.1949	0.62	0.73	1067	18	1148	13	1120	11	-7.52
MR10	026-ZR13	59	0.0567	0.138	82394	25.02	0.07522	0.52	1.872	0.81	0.1805	0.49	0.61	1074	21	1070	10	1071	11	0.44
MR10	030-ZR15	381	0.0410	0.036	145676	48.49	0.07865	0.78	1.969	1.09	0.1816	0.67	0.61	1163	31	1076	13	1105	15	7.54
MR10	036-ZR19B	185	0.0425	0.036	14569	6.32	0.07426	0.56	1.777	1.47	0.1735	1.31	0.89	1049	23	1031	25	1037	19	1.66
MR10	037-ZR20N	7	0.0098	0.285	359695	17.10	0.08799	0.63	2.806	0.96	0.2313	0.62	0.64	1382	24	1341	15	1357	14	2.99

MR10	042-ZR21B	11	0.0482	0.030	1322232	19.14	0.07492	0.38	1.967	0.99	0.1904	0.83	0.84	1066	15	1124	17	1104	13	-5.38
MR10	045-ZR24	1572	0.0474	0.066	5054	21.31	0.07443	1.17	1.907	1.42	0.1858	0.71	0.50	1053	47	1099	14	1084	19	-4.30
MR10	046-ZR25	12	0.0055	0.634	150431	15.25	0.07533	0.51	1.977	0.87	0.1903	0.61	0.70	1077	20	1123	13	1108	12	-4.24
MR10	048-ZR26B	28	0.0455	0.026	943232	27.62	0.07478	0.47	1.819	1.26	0.1764	1.11	0.88	1063	19	1047	21	1052	16	1.45
MR10	049-ZR27N	189	0.0362	0.381	12174	6.85	0.07412	0.56	1.690	1.50	0.1653	1.34	0.89	1045	23	986	24	1005	19	5.60
MR10	050-ZR27B	187	0.0414	0.108	14774	10.06	0.07409	0.71	1.762	1.34	0.1725	1.08	0.80	1044	28	1026	20	1032	17	1.73
MR10	055-ZR29	49	0.0334	0.053	430914	55.28	0.07449	0.37	1.934	0.85	0.1883	0.67	0.79	1055	15	1112	14	1093	11	-5.44
MR10	056-ZR30N	8	0.0056	0.224	252500	19.63	0.09993	0.40	3.913	0.82	0.2840	0.61	0.74	1623	15	1611	17	1616	13	0.70

Data report template (with modifications) from http://www.plasmage.org/recommendations

[1] Convertion factor from mV to CPS is 62500000

[2] Discordance calculated as (1-($^{206}Pb/^{238}U$ age/$^{207}Pb/^{206}Pb$ age))*100

Decay constants of Jaffey et al. (1971) used

Table 3-4. U-Pb monazite data from the granitic plutons of the Sunsas Belt in northeast Bolivia.

Las Tojas granite		^{204}Pb	^{206}Pb		^{206}Pb/^{204}Pb		^{207}Pb/^{206}Pb		^{207}Pb/^{235}U		^{206}Pb/^{238}U			^{207}Pb/^{206}Pb		^{206}Pb/^{238}U		^{207}Pb/^{235}U		
Sample	Spot	cps	mV[1]	Th/U		1s%		1s %		1s %		1s %	Rho		2s abs		2s abs		2s abs	% U-Pb disc[2]
ID08	003-MZ1	173	0.0378	25.242	16411	9.27	0.07501	0.47	1.781	1.02	0.1772	0.91	0.89	1069	19	1052	18	1038	13	1.59
ID08	005-MZ3	128	0.0227	28.684	61734	80.06	0.07557	0.41	1.835	1.00	0.1812	0.91	0.91	1084	17	1074	18	1058	13	0.92
ID08	006-MZ4	156	0.0414	20.706	17893	6.03	0.07514	0.46	1.859	1.04	0.1846	0.93	0.90	1072	18	1092	19	1066	14	-1.86
ID08	008-MZ6	133	0.0269	28.996	15933	17.44	0.07488	0.57	1.834	1.20	0.1828	1.06	0.88	1065	23	1082	21	1058	16	-1.61
ID08	009-MZ7	134	0.0300	21.310	57388	67.84	0.07478	0.66	1.871	1.39	0.1868	1.22	0.88	1063	26	1104	25	1071	18	-3.90
ID08	012-MZ10	509	0.0370	24.781	4780	6.41	0.07577	0.79	1.908	1.52	0.1880	1.30	0.86	1089	31	1110	27	1084	20	-1.96
ID08	015-MZ11	188	0.0369	25.906	13175	5.50	0.07522	0.62	1.920	1.34	0.1905	1.19	0.89	1074	25	1124	25	1088	18	-4.64
ID08	016-MZ12	154	0.0257	32.397	12041	9.51	0.07621	0.57	1.929	1.24	0.1890	1.10	0.89	1101	23	1116	23	1091	17	-1.37
ID08	017-MZ13	123	0.0208	29.263	12737	10.35	0.07588	0.56	1.980	1.18	0.1948	1.03	0.88	1092	22	1147	22	1109	16	-5.06
ID08	018-MZ14	161	0.0299	27.016	12333	6.17	0.07534	0.54	1.853	1.09	0.1836	0.94	0.87	1078	22	1087	19	1065	14	-0.85
ID08	020-MZ16	151	0.0313	23.718	13368	4.46	0.07621	0.66	1.974	1.28	0.1933	1.09	0.86	1101	26	1139	23	1107	17	-3.51
ID08	028-MZ22	144	0.0330	25.126	15828	6.59	0.07549	0.94	1.989	1.69	0.1966	1.41	0.83	1082	37	1157	30	1112	23	-6.99

Señoritas granite		^{204}Pb	^{206}Pb		^{206}Pb/^{204}Pb		^{207}Pb/^{206}Pb		^{207}Pb/^{235}U		^{206}Pb/^{238}U			^{207}Pb/^{206}Pb		^{206}Pb/^{238}U		^{207}Pb/^{235}U		
Sample	Spot	cps	mV[1]	Th/U		1s%		1s %		1s %		1s %	Rho		2s abs		2s abs		2s abs	% U-Pb disc[2]
ID06	018-MZ14	474	0.0959	12.488	12970	3.38	0.07469	0.32	1.784	0.52	0.1783	0.40	0.78	1060	13	1058	8	1040	7	0.25
ID06	022-MZ18	422	0.1357	8.482	20178	2.77	0.07471	0.48	1.714	0.65	0.1712	0.44	0.68	1061	19	1019	8	1014	8	3.95
ID06	032-MZ26	257	0.0543	20.353	14542	5.34	0.07496	0.35	1.730	0.55	0.1723	0.43	0.77	1067	14	1025	8	1020	7	4.00
ID06	033-MZ27	315	0.0697	13.191	14621	4.92	0.07526	0.42	1.722	0.62	0.1707	0.46	0.74	1076	17	1016	9	1017	8	5.52
ID06	034-MZ28	242	0.0740	9.469	19902	4.62	0.07463	0.41	1.672	0.66	0.1672	0.52	0.78	1059	17	997	10	998	8	5.85
ID06	035-MZ29	352	0.0665	16.806	12284	3.40	0.07484	0.46	1.709	0.80	0.1704	0.66	0.82	1064	18	1015	12	1012	10	4.68
ID06	036-MZ30	229	0.0531	18.095	15723	4.69	0.07455	0.45	1.703	0.76	0.1705	0.61	0.80	1056	18	1015	11	1010	10	3.93

Data report template (with modifications) from http://www.plasmage.org/recommendations

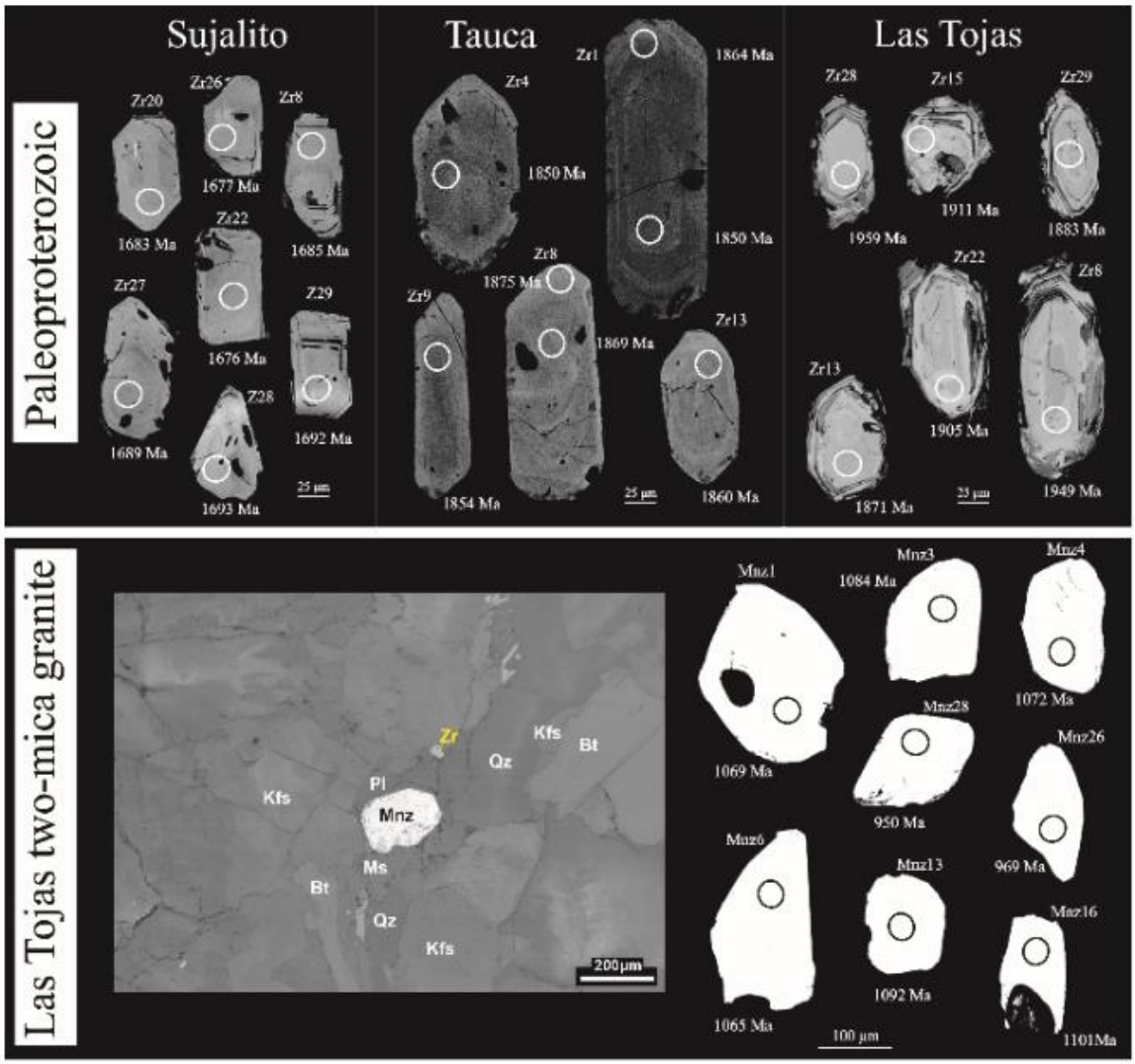

Figure 3.2. Representative cathodoluminescence (CL) and backscattered electron (BSE) images for zircon and monazite grains from the Sunsas belt Paleoproterozoic granitic plutons. The Sujalito sample displays two morphological populations; 1- rounded zircon crystals, lengths of 100–300 µm, length/width ratio of 2:1; 2- prismatic elongated crystals, lengths of 200–300 µm, length/width ratio of 3:1. Both populations show internal structures with faint concentric oscillatory zoning or unzoned crystals. Many inclusions and fractures are also observed. The Tauca sample shows two morphological populations: 1- rounded zircon, lengths of 100–300 µm, ratio of 2:1; 2- prismatic elongated crystals, lengths of 200–300 µm, ratio of 3:1. Both populations display faint concentric oscillatory zoning or unzoned crystals. Many inclusions and fractures are also observed. The Las Tojas sample contains fractured subhedral rounded and prismatic zircon. Prismatic grains have lengths of 100–200 µm, ratio of 1:1 and rounded crystals 90-190 µm, ratio of 2:1. In BSE images, all crystals have xenoscrystic internal structures, cores present faint oscillatory zoning truncated by growth of zoned rims, up to 20 µm. In general, cores are lighter than rims and have not well marked limits. There is evidence of resorption and recrystallization.

The Sujalito granite yielded a Discordia age of 1685±6 Ma (Fig. 3.3A). Seven concordant zircon grains with high Th/U ratios between 0.287 and 0.452 yielded a

Concordia age of 1682±3 Ma (Fig. 3.3B), interpreted as the crystallization age. The Las Tojas two-mica granite shows an upper intercept of 1941±40 Ma (Fig. 3.3C) obtained from zircon cores with high Th/U ratios of 0.233 to 0.590. The zircon rims with Th/U values of 0.165 and 0.262 have younger $^{207}Pb/^{206}Pb$ ages of 1271 and 1215 Ma (Table 3.3). These Mesoproterozoic ages suggest a subsequent recrystallization event. However, the Th/U values of rims are high and not so typical of common metamorphic rims (often <0.1) unless resulting from high-T metamorphism. Thirty monazite crystals from the Las Tojas two-mica granite were also dated. They yielded a Neoproterozoic Discordia age of 992±41 Ma (Fig. 3.3D). Monazite has morphological features of igneous crystals and occurs as inclusions in feldspar and white mica, indicating equilibrium with later melt (Fig. 3.2) (Ondrejka et al., 2012). The 1.2 Ga zircon rims likely mean an intermediary recrystallization event between 1.94 and 0.99 Ga. In turn, the Tauca granodiorite displays a discordant upper intercept age of 1856±4 Ma (Fig. 3.3E) with Concordia Age of 1856±4.4 Ma (Fig. 3.3F), interpreted as the zircon crystallization age.

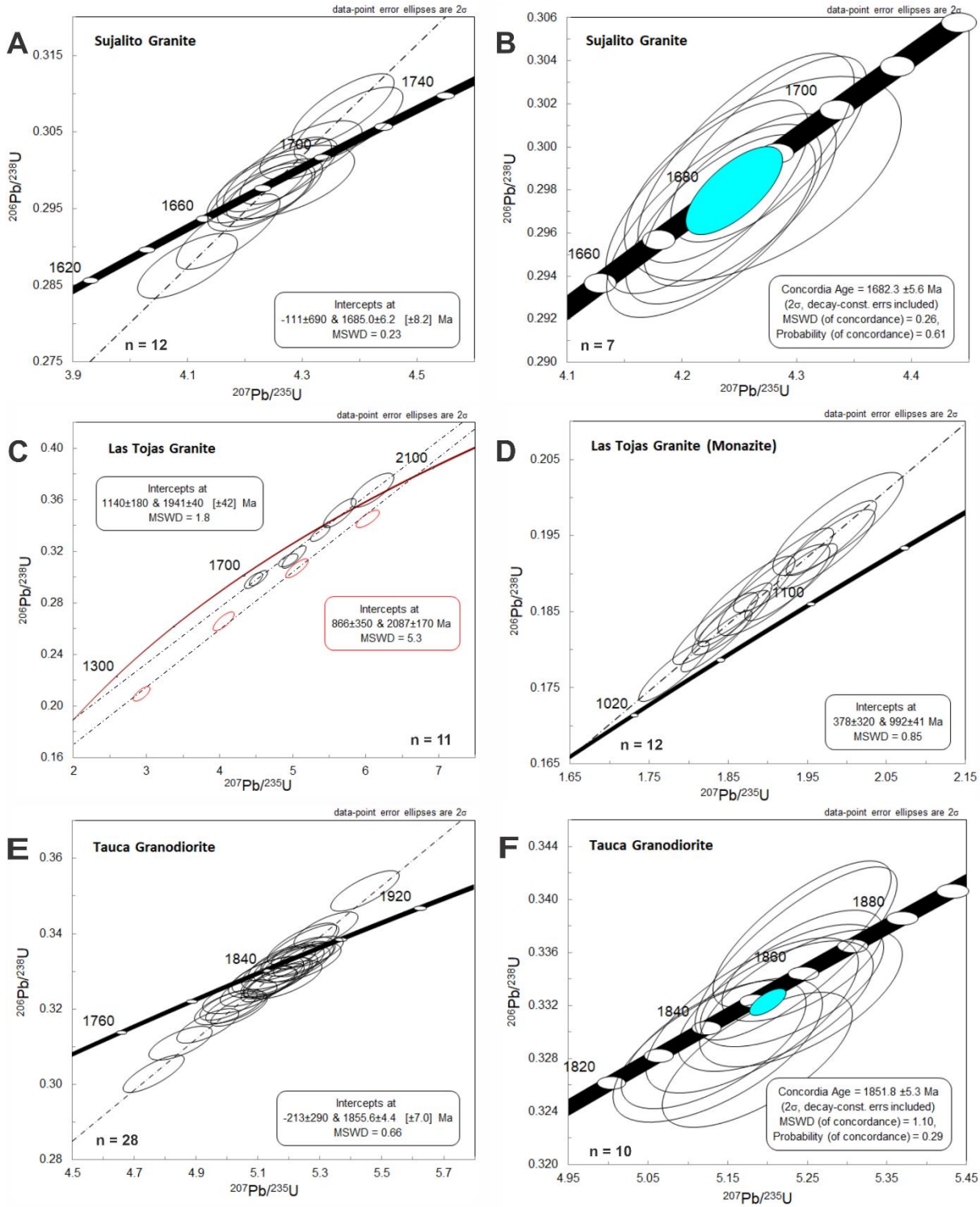

Figure 3.3. A) Concordia diagram and (B) concordia age for U-Pb zircon data from the Sujalito pluton; C) Concordia diagram for U-Pb zircon and (D) monazite data from the Las Tojas granitic pluton; E) Concordia diagram and (F) concordia age for U-Pb zircon data from the Tauca pluton. Data from tables 3.3 and 3.4.

3.5.2 Mesoproterozoic granites

The Colmena granite is hosted along the San Diablo shear zone within the Chiquitania Gneissic Complex. It is strongly deformed, displaying E-W lineation

compatible with the San Diablo shear zone trace. The Colmena pluton is formed of K-feldspar (30-35%) + plagioclase (20-25%) + quartz (20-25%) + biotite (10-15%). The San Ramón granite exhibits incipient foliation marked by the biotite orientation. The Señoritas two-mica granite occurs as parallel lenses hosted in the WNW-ESE-trending mica-schist sequence related to a gold mineralized shear zone in the Don Mario mineral district (e.g., Litherland et al., 1986). White mica and K-feldspar grains present monazite inclusions, indicating cogenetic generation. The Salinas and San Pablo monzogranites have massive structure and present hornblende and pyroxene in their mineral assemblage mainly composed of plagioclase (40-44%) + K-feldspar (24-29%) + quartz (20-27%) + biotite (3%). The mafic minerals display adcumulatic texture, sometimes producing a banded mineral structure.

The zircon grains from these samples are prismatic, measuring 50 to 300 μm, with length/width ratios of 2:1 and 3:1. The BSE images show unzoned to oscillatory and banded zircon internal texture. The zircon crystals usually have well-delimited zonation between core and rim and show disruption of concentric oscillatory zoning, typical of metamorphic recrystallization fronts and zones (see San Ramón, Fig. 3.4) (e.g., Corfu et al., 2003). The BSE images show unzoned grains with recrystallization zones mainly in the San Pablo and Colmena intrusions.

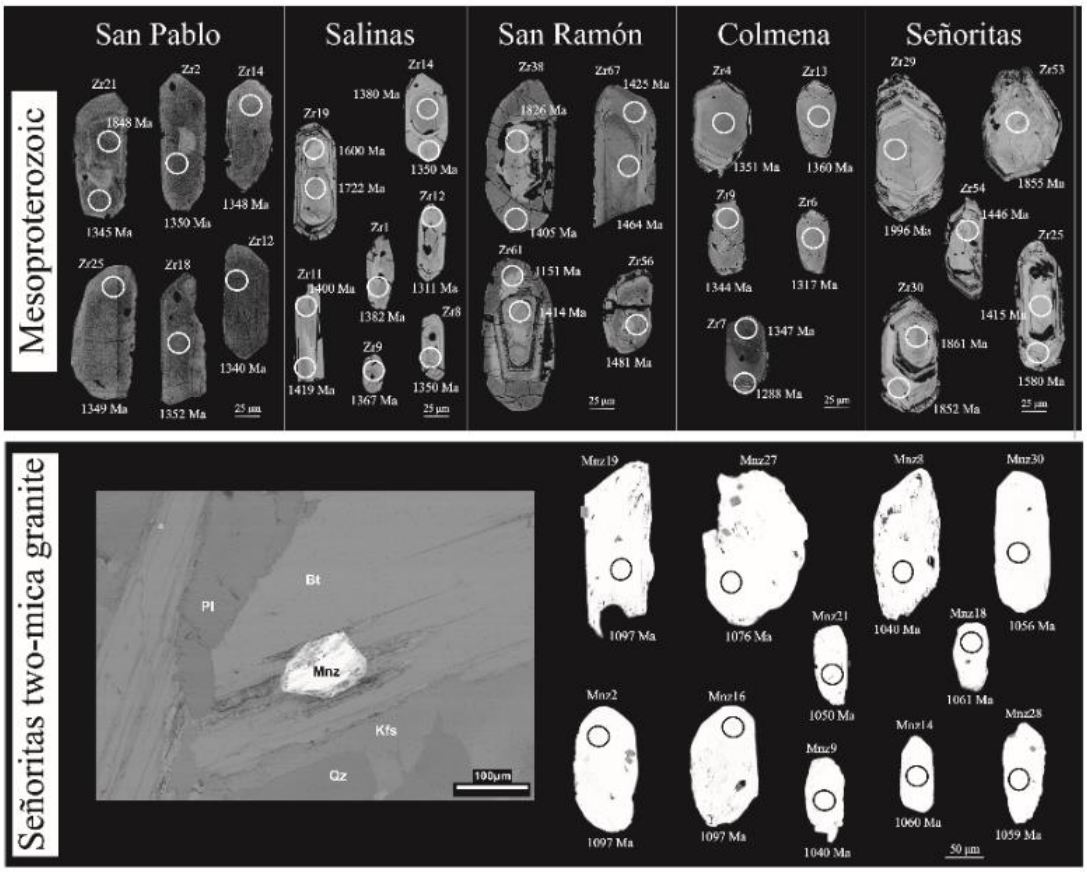

Figure 3.4. Representative cathodoluminescence (CL) and backscattered electron (BSE) images for the zircon and monazite grains from Mesoproterozoic granitic plutons in the Sunsas belt. The San Pablo pluton sample shows rounded and elongated crystals with subhedral shapes measuring between 80 and 320 µm. BSE images show unzoned internal structures. Some crystals have light-colored cores without age variation. The Salinas intrusion sample presents prismatic and elongated zircon grains, measuring 50 to 200 µm, length/width ratio of 3:1. The crystals display some inclusions and fractures. BSE images show unzoned to faint oscillatory zoning internal structures with thin portions of oscillatory zoning. The San Ramón sample contains rounded grains with subhedral shapes, measuring between 80 and 300 µm, ratio of 2:1. Most crystals are very fractured and present inclusions. BSE images show complex internal structures with oscillatory and banded zonation, in which some layers are up to 10 µm thick, and BSE-dark zircon cores, indicating high Pb concentration. These crystals usually have well-delimited zonation between core and rim and show disruption of concentric oscillatory zoning, typical of late and post-magmatic cooling. Some crystals with unzoned internal structure are also observed. The Colmena intrusion sample displays two zircon populations, different in terms of external appearance and internal geometry: 1- prismatic zircon grains of 40 to 120 µm that preserve igneous internal zoning structures. 2- rounded zircon grains of 90 to 190 µm, ratios of 2:1 and 1:1. BSE images show uniform unzoned to faint zoning internal structures and evidence for resorption and recrystallization of the grains. Thin portions of rim overgrowth with oscillatory zoning indicate conditions of medium to high temperature metamorphism. The Señoritas pluton sample contains three morphological populations with different internal geometry: 1- rounded subhedral crystals, lengths of 100–150 µm, ratio of 1:1, with complex internal structures of xenocrystic cores with chaotic zoning and growth of zoned rims. Core and rim limits are not well defined. 2- prismatic subhedral crystals measuring 100 to 200 µm, ratio of 2:1, with faint oscillatory zoning commonly truncated by growth of thin zoned rims. 3- Less common, prismatic grains, 100–120 µm, ratio of 2:1. Regular oscillatory zoning and evidence for resorption.

The zircon cores from the San Pablo monzogranite have high Th/U values, from 0.421 to 0.712, and yielded a Concordia age of 1345±6 (Fig. 3.5A), interpreted as the crystallization age. The Salinas monzogranite displays an upper intercept age of 1372±36 Ma (MSWD=11), interpreted as the crystallization age. In contrast, six inherited zircon grains from Salinas yielded an upper intercept age of 1684±110 Ma (Fig. 3.5B). The San Ramón granite shows a discordant upper intercept age of 1423±10 Ma (Fig. 3.5C) on unzoned grains and zircon rims with Th/U ratios between 0.22 and 0.48. Inherited zircon cores present $^{207}Pb/^{206}Pb$ ages between 1815 and 1876 Ma, with Th/U ratios varying from 0.070 to 0.361. For instance, zircon 38 (see Fig. 3.4) from San Ramón has a core dated at 1826 Ma, with Th/U ratio of 0.07, while its overgrowth rim is dated at 1405 Ma, with Th/U ratio of 0.285. It indicates that isolated Th/U ratios can lead to bias.

The Colmena granite shows a Discordia age of 1350±5 Ma (Fig. 3.5D) obtained from zircon cores with Th/U ratios between 0.158 and 0.680, interpreted as the crystallization age. 1635 and 1761 Ma old inherited zircon grains were also found in the Colmena granite. The Señoritas two-mica granite displays two Discordia ages (Fig. 3.4, 3.5E). Zircon grains with length/width ratio of 2:1 yielded an older discordant upper intercept age of 1954±51 Ma. Zircon grains with length/width ratio of 3:1 yielded a younger upper intercept age of 1454±20 Ma, with a concordant age of 1415±30 Ma. Th/U ratios overlap for both age groups. Monazite from the Señoritas granite was also dated (Table 3.4). BSE images show small and faceted monazite, typical of igneous crystals (Fig. 3.4) (Ondrejka et al., 2012). U-Pb monazite results show a Discordia age of 1006±8 Ma (Fig. 3.5F). Thus, the Señoritas granite records a complex evolution, with zircon generated at 1.95 and 1.45 Ga, and a monazite formation event at 1006±8 Ma.

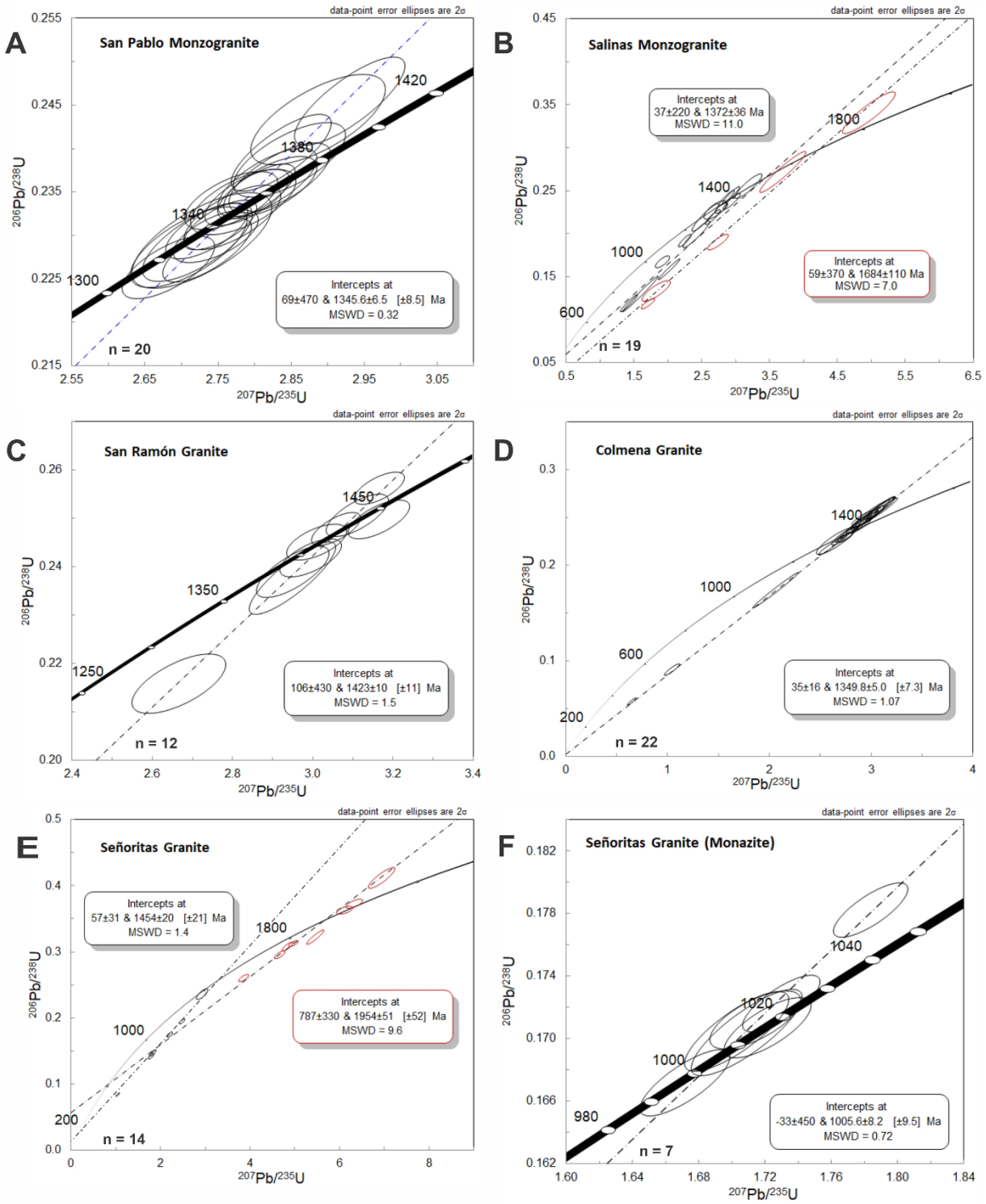

Figure 3.5. Concordia diagram for U-Pb zircon data from the (A) San Pablo, (B) Salinas, (C) San Ramón, (D) Colmena, and (E) Señoritas granitic plutons; F) U-Pb monazite data from the Señoritas granite. Data from tables 3.3 and 3.4.

3.5.3 Stenian granites

The Tasseoro, Casa de Piedra, and Marimonos granodioritic to monzogranitic intrusions emplaced in the western and southern limit of the Paraguá Terrane represent the younger studied igneous rocks. These granitic plutons mainly occur as massive lenses controlled by NW-SE structures, often with deformed borders and incipient foliation marked by biotite orientation. The mineral assemblage is formed of plagioclase (20-30%) + K-feldspar (25-35%) + quartz (30-40%) + biotite (5-15%). Amphibolite and pyroxenite xenoliths are found in the Casa de Piedra intrusion.

The zircon grains from the Tasseoro, Casa de Piedra, and Marimonos granites are prismatic, 100 and 400 µm long with length/width of 3:1 and 4:1. The zircon crystals from Casa de Piedra and Marimonos show cores with internal zoning surrounded by a thick homogeneous rim (Fig. 3.6). Zircon grains from Tasseoro have prismatic morphology but their unzoned internal texture likely indicates later recrystallization (Fig. 3.6) (e.g., Corfu et al., 2003).

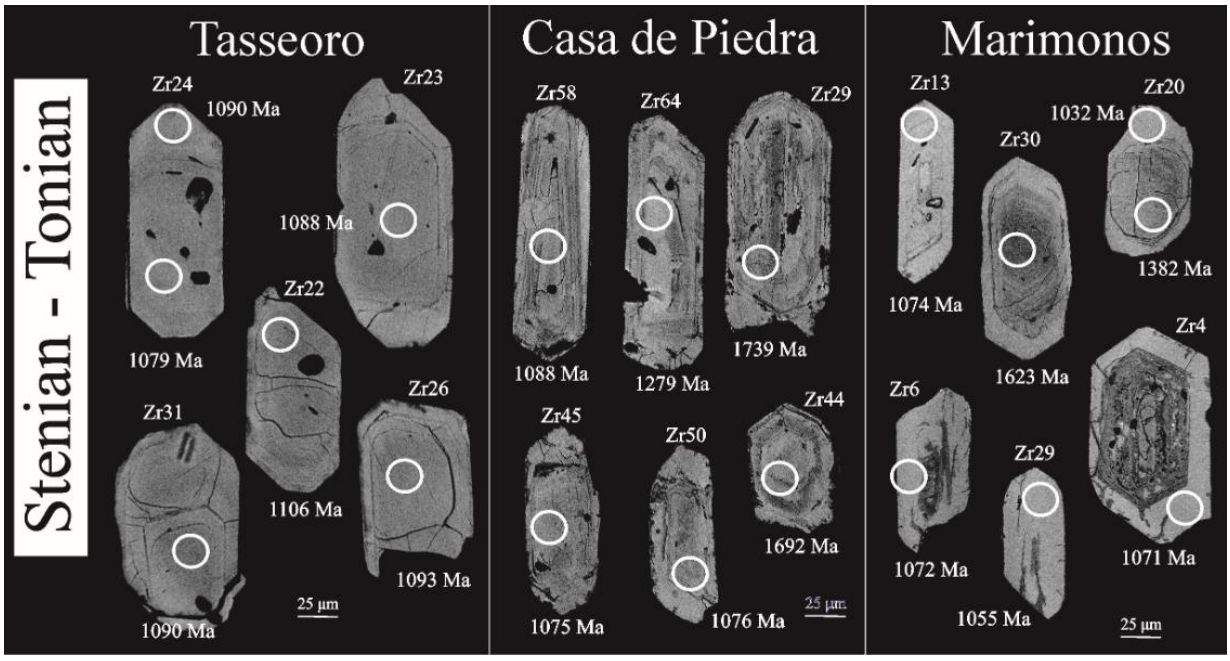

Figure 3.6. Representative cathodoluminescence (CL) and backscattered electron (BSE) images for zircon grains from Stenian granitic plutons in the Sunsas belt. The Tasseoro intrusion sample presents zircon crystals with prismatic shapes, lengths between 100 and 300 µm and 2:1 length/width. BSE images show faint regular oscillatory zoning or unzoned crystals with many inclusions. The Casa de Piedra sample contains two morphological zircon groups. The most representative group is of prismatic elongated crystals, measuring 100-400 µm, ratio of 4:1. The other group is of rounded zircon crystals with subhedral shapes, lengths 100 to 300 µm, ratio 2:1; they show faint oscillatory zoning and zircon with homogeneous and xenocrystic cores truncated by growth of lighter rims. Zonation between core and rim is not well defined. Also, some crystals present dark cores, indicating high trace-element contents, and many inclusions of rounded and prismatic minerals. The Marimonos granitic

pluton sample shows zircon grains with subhedral shapes, lengths of 120-350 μm, length/width 2:1, and elongated prismatic crystals with lengths of 200-300 μm, length/width 3:1, with complex internal structures. In general, crystals present homogeneous cores, oscillatory zoning and growth of unzoned rims with well delimited zonation between core and rim. Also, chaotically zoned cores in xenocrystic crystals with evidence for resorption and recrystallization are observed.

The Tasseoro granite yielded a Discordia age of 1085±14 Ma (Fig. 3.7A), interpreted as the crystallization age. However, an older Discordia age of 1168±34 Ma (Fig. 3.7A) from the Tasseoro intrusion suggest a major period of c. 60-80 Ma for magmatic activity. The Casa de Piedra monzogranite shows three upper intercept ages: 1763±35 Ma (Fig. 3.7C) yielded by zircon cores with Th/U ratios between 0.14 and 1.12. Prismatic zircon grains (2:1) with relatively low Th/U ratios (0.04 and 1.06), yielded a Discordia age of 1278±96 Ma (Fig. 3.7C), with one concordant zircon crystal of 1279±70 Ma. A group of prismatic zircon grains yielded a Discordia age of 1094±9 Ma (Fig. 3.7D). Fifteen homogenous zircon cores and overgrowth rims from the Marimonos granite yielded an upper intercept of 1055±13 Ma (Fig. 3.7F). Four zircon cores with internal zoning yielded an upper intercept of 1388±28 Ma (Fig. 3.7E), with one concordant zircon core of 1382±24 Ma. Three zircon cores obtained in Marimonos with magmatic zoning display an upper intercept age of 1633±41 Ma (Fig. 3.7E). One zoned zircon core shows a concordant age of 1623±15 Ma. Thus, the Marimonos granite records three magmatic episodes at around 1.62, 1.38, and 1.05 Ga.

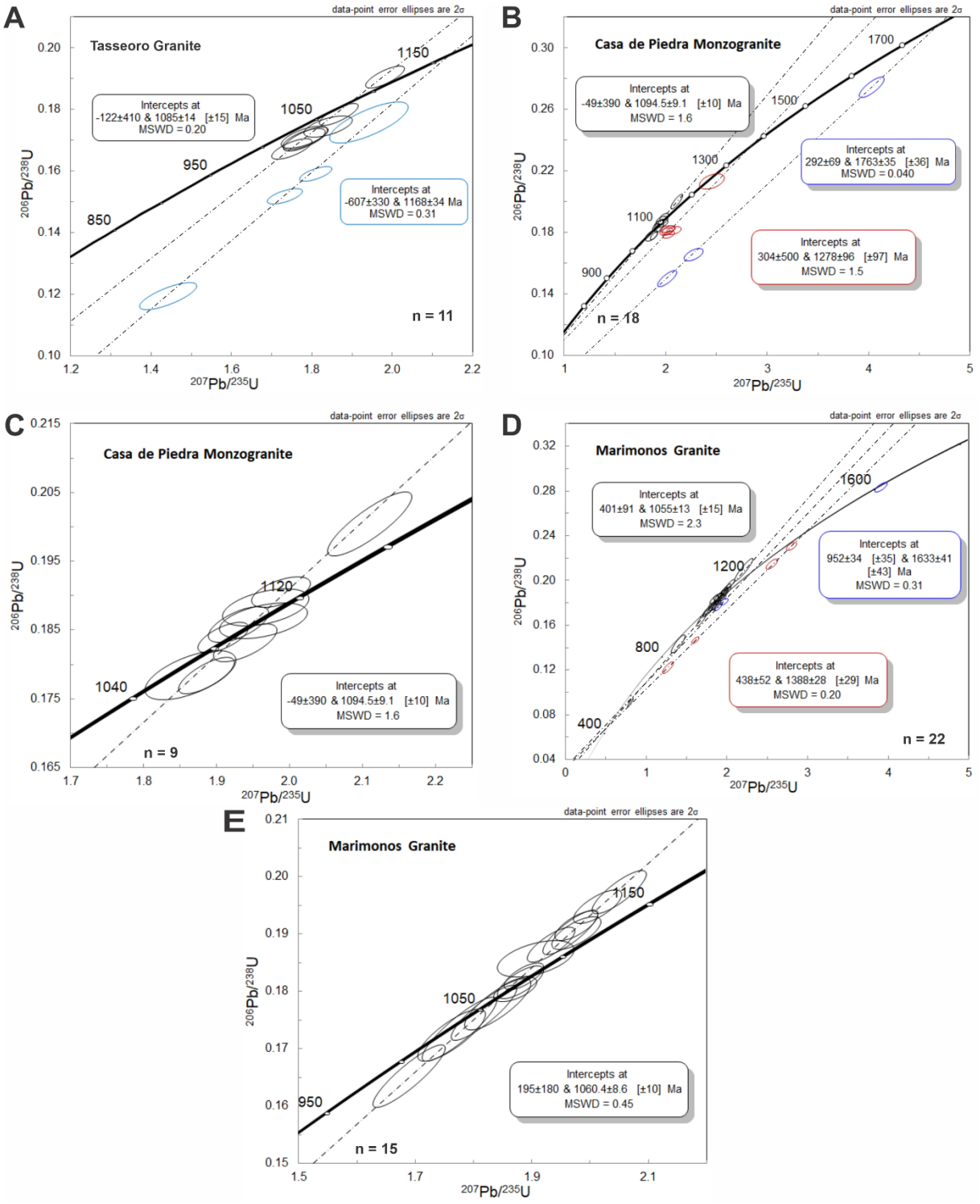

Figure 3.7. U-Pb zircon diagrams for the (A) Tasseoro, (B-C) Casa de Piedra and (D-E) Marimonos granitic plutons from the Sunsas belt. Data from Table 3.3.

3.6 Discussion

3.6.1 Paleoproterozoic source correlations

The Paleoproterozoic Las Tojas granite (1918±22 Ma) and Tauca granodiorite (1855±4 Ma) are exposed in the southwestern portion of the San Diablo front. This geographical position indicates transport of 1.9-1.8 Ga felsic crust from southwest to northeast in the Sunsas belt. It should be noted that the 1941±40 Ma Las Tojas (Nedel et al., 2020), 1925±32 Ma Correreca (Vargas-Mattos, 2010), 1874 Ma Santo Corazón (Redes et al., 2020) and 1861±8 Ma Santa Terezita (Redes et al., 2018) granites are exposed in the southern domain, corroborating an Orosirian basement (Fig. 3.1). Thus, the Paleoproterozoic ages in the Sunsas belt can result from inherited zircon. This Orosirian calc-alkaline magmatism documented in the Sunsas belt added to the geological configuration (Fig. 3.1) suggests a 1.9-1.8 Ga petrogenetic link with the western domain of the Rio Apa Terrane (Cordani et al., 2010; Faleiros et al., 2016; Redes et al., 2016, 2018; Plens, 2018; Nedel et al., 2020; Teixeira et al., 2020). However, Faleiros et al. (2015) do not endorse the correlation between the Paraguá and Rio Apa terranes due to Nd isotope evidence of distinct signatures (Lacerda-Filho et al., 2006; Santos et al., 2008; Matos et al., 2009; Cordani et al., 2010).

The 1682±3 Ma Sujalito granite represents the oldest igneous rock exposed northeastwards of the San Diablo front. This Statherian magmatic age correlates with the Chiquitania Complex (Litherland et al., 1986; Teixeira et al., 2010). Thus, the geochronological results suggest crustal reworking from distinct sources in the Sunsas belt, an older (1.9-1.8 Ga) to the south of the San Diablo front and a younger (1.6 Ga) to the north.

3.6.2 Mesoproterozoic correlations

The Ectasian to Calymmian transition records the main magmatic rocks generation in the central portion of the Sunsas belt (Fig. 3.3). Five granitic intrusions were emplaced between 1.45 and 1.35 Ga (Fig. 3.8A). Specifically, the 1.37-1.34 Ga granites can be related to the Mesoproterozoic Pensamiento Complex that represents the final stage of the Rondonian-San Ignacio orogeny (Matos et al., 2009). Furthermore, the 1350±5 Ma Colmena granite was emplaced along the San

Diablo front, indicating a possible collision between the 1.8-1.9 Ga southern and the 1.6 Ga northern Paleoproterozoic basement during the San Ignacio orogeny. Thus, the San Diablo shear zone was an active structure at 1.35 Ga, later reactivated during the 1.0 Ga Sunsas orogeny. Likewise, the 1.9-1.8 Ga and 1.6 Ga inherited zircon cores present in 1.4-1.3 Ga granitic intrusions also indicate crustal reworking of the Paleoproterozoic basement during the San Ignacio orogeny. The older 1.45-1.42 Ga San Ramón and Señoritas granites may be related to the Santa Helena Orogen recorded eastwards in the Jauru Terrane (Santos et al., 2000; Matos et al., 2009; Bettencourt et al., 2010).

3.6.3 The Sunsas orogen

The 1094±9 Ma Casa de Piedra and 1055±13 Ma Marimonos intrusions represent the younger magmatism episodes in the northwestern domain of the Sunsas belt (Fig. 3.3). The Casa de Piedra and Marimonos granites are controlled by the NNW-SSE Blanco Ibiaimiai and Concepción shear zones. The 1.76 Ga, 1.62 Ga, and 1.38 Ga inherited zircon cores found in 1.09-1.04 Ga old granitoids suggest crustal reworking of the Chiquitania and Lomas Maneches complexes and relation to San Ignacio magmatic rocks in the northern domain. Moreover, they may be indicating a younger age progression from 1.09 Ga westwards to 1.05 Ga eastwards. Such geochronological patterns and time intervals (c. 60-80 Ma) are commonly related to continental accretion by magmatic arcs (e.g., Condie, 2004; Hawkesworth et al., 2010; Nance et al., 2014; Ernst et al., 2016). However, Nd isotopic studies and geochemistry data are necessary to support the magmatic arc hypothesis. On the other hand, the Tasseoro granite was emplaced parallel to the east-west San Diablo front and records two zircon crystallization ages of 1168±34 Ma and 1085±14 Ma. Like the 1.35 Ga Colmena granite, the Tasseoro intrusion may have been generated by melts derived from northern and southern protoliths. Thus, the San Diablo front shows a diachronic evolution which was activated at 1.35 and ~1.08 Ga.

3.6.4 U-Pb monazite ages

Monazite crystals contain considerable amounts of U (ppm) and mainly Th (% wt.) (e.g., Parrish 1990; Rubatto et al., 2013). Radiogenic Pb is dominant in the monoclinic structure of monazite due to high closure temperature (>700ºC) for diffusive Pb loss, allowing younger ages to be measured (e.g., Parrish, 1990; Smith

and Gilletti, 1997). Therefore, monazite is the mineral of choice for magmatism, metamorphism, and timescale related to an orogenic cycle, particularly the timing of tectonic collision and post-collision heating (e.g., Vance & Harris 1999; Rubatto et al., 2013).

In this study, monazite crystals from two granitic plutons were dated by the U-Pb method. The analyzed Las Tojas granite sample displays monazite grains included in K-feldspar and mica crystals. The monazite analyses yielded an upper intercept age of 992±41 Ma (Fig. 3.5D), interpreted as the Las Tojas recrystallization event. For the Señoritas granite, the monazite analyses yielded an upper intercept age of 1006±8 Ma (Fig. 3.7F). These monazite ages are coeval with Rb-Sr (1005 ± 12 Ma) and K-Ar (1008 ± 22 to 935 ± 21 Ma) ages in biotite from Sunsas belt (Litherland et al., 1986). It confirms the biotite + monazite mineral equilibrium observed for the granitic melt (Fig. 3.4). The 1006±8 and 992±41 Ma monazite crystallization ages may represent a partial melting event in a late- to post-collision setting in the Sunsas belt (Fig. 3.8B, Table 3.4). Likewise, U-Pb monazite ages indicate that the 1.9 Ga and 1.4 Ga protolith sources were reworked during Rodinia assembly. Thus, the monazite results are relevant and can contribute to unravel a complex tectonic history for igneous rocks dated only by U-Pb zircon (e.g., Ondrejka et al., 2012; Piechocka et al., 2017).

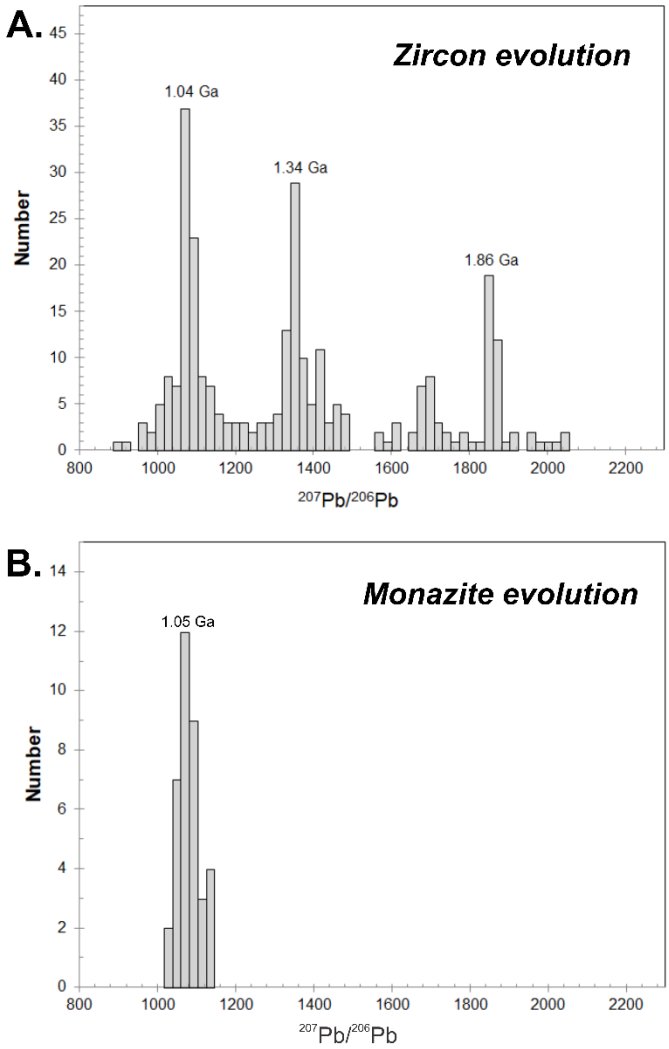

Figure 3.8. (A) Histogram of 207Pb/206Pb zircon ages from the Sunsas Belt. Compiled data from Table 3.3 and Nedel et al. (2020); (B) Histogram of 207Pb/206Pb monazite ages from the Sunsas Belt. Data from Table 3.4.

3.6.5 Constraints for the SW Amazonian Craton

The geochronological results support a 1.9-1.8 Ga old felsic basement for the southern portion of the Sunsas belt, similar to the Rio Apa Terrane (Fig. 3.8A). Therefore, this terrane appears to extend up to the southern part of the Paraguá Terrane. In contrast, 1.7-1.6 Ga old rocks represent the basement of the northern domain, related to the Chiquitania and Lomas Maneches complexes (Litherland et al., 1989; Teixeira et al., 2010). The Paleoproterozoic basement was reworked during the 1.4-1.3 Ga San Ignacio orogeny (Matos et al., 2009; Bettencourt et al., 2010). The E-W San Diablo shear zone may be a structure inherited from the San Ignacio orogeny. The Archean and Paleoproterozoic inherited zircon cores and grains suggest a possible correlation between Sunsas belt protoliths and 2.2 to 1.8 Ga

orogenies that resulted in the Nuna-Columbia assembly (Nedel et al., 2020). The 1.87–1.85 Ga, 1.76–1.75 Ga, 1.35 Ga, and 1.0 Ga magmatic episodes are recorded in northern Laurentia and also support a long-lived connection among different blocks and terrains in the Proterozoic (e.g., Ernst et al., 2016). In this context, the Sunsas belt reveals a geochronological evolution similar to eastern Laurentia when taking into account that the Sunsas magmatism was generated between 1.1 and 1.04 Ga, with a magmatic peak at 1.08 Ga, by reworking Paleoproterozoic and Mesoproterozoic protoliths (Fig. 3.8A). It indicates a time interval of c. 60 Ma for the complete magmatic episode.

The Sunsas belt displays 1.9-1.8 Ga felsic protoliths in the southern domain, whereas in the northwestern domain, the basement is formed of 1.7-1.6 Ga protoliths (Fig. 3.9). These Paleoproterozoic fragments were reworked and accreted to the Amazonian Craton during the 1.4-1.3 Ga San Ignacio orogeny (Nedel et al., 2020). The 1.1-1.0 Ga Sunsas orogeny promoted a new partial melting of Paleo- and early Mesoproterozoic felsic crust. Our geochronological data confirm previous geodynamic correlations (e.g., Rizzotto et al., 2001; Tohver et al., 2006; Boger et al., 2005; Fernandes et al., 2006; Teixeira et al., 2010; Nedel et al., 2020) and open new hypotheses for the evolution of the Sunsas Belt. Moreover, the monazite ages can indicate that some previous ages based solely on zircon should be reconsidered. Lastly, the protracted reworking of the older basement by the younger orogenies is the major petrogenesis processes in the Sunsas belt.

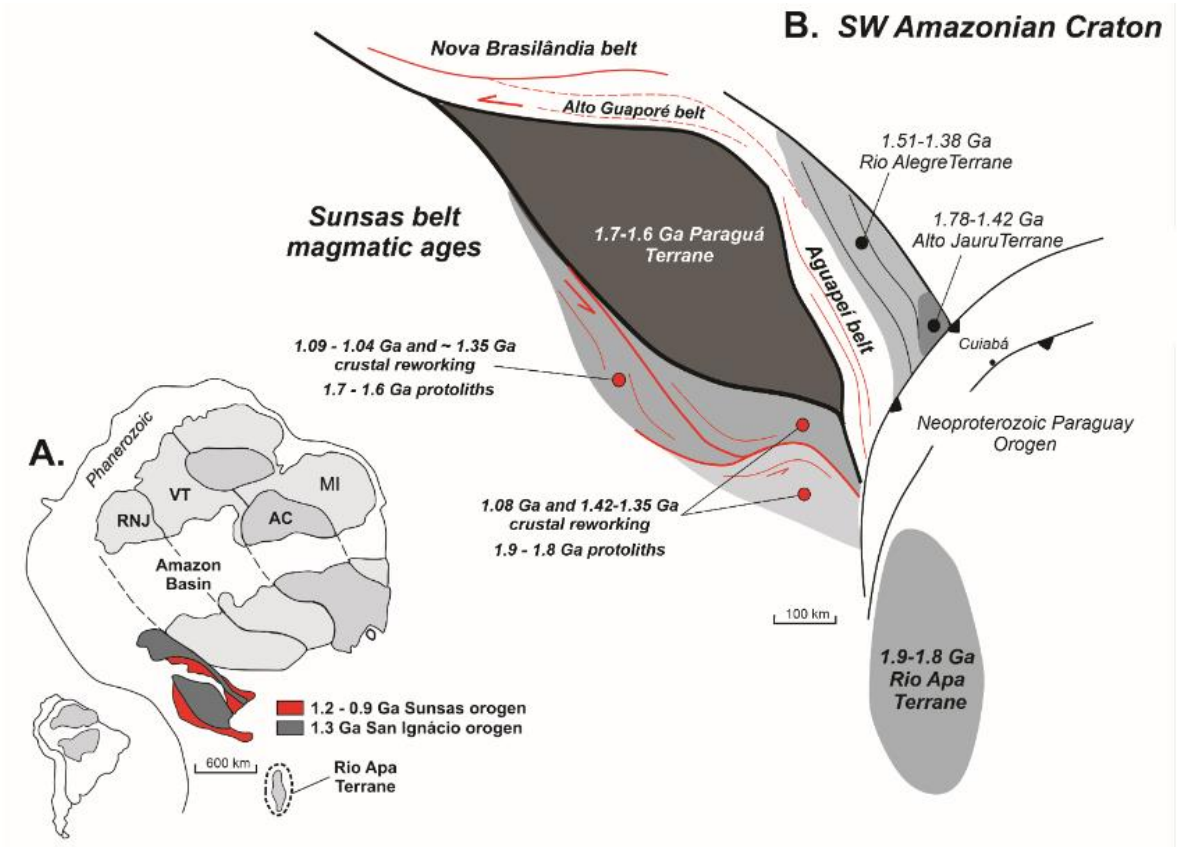

Figure 3.9. (A) Schematic geotectonic compartment of the Amazonian Craton with emphasis on the SW portion; (B) Tectonic evolution model for the Sunsas Province, SW Amazonian Craton. Correlated ages of inherited zircons and protholite sources for the Sunsas belt magmatism.

3.7 Conclusion

Combined U-Pb zircon and monazite geochronological data reveal that the Sunsas belt was generated by several crustal reworking events from Paleoproterozoic sources. Specifically, the main contributions are:

1. The southern basement of the Sunsas belt is formed of 1.9-1.8 Ga granitic magmatism similar to the Rio Apa Terrane, whereas the 1.7 to 1.6 Ga magmatic rocks are related to the Chiquitania and Lomas Maneches complexes that make up the northern basement.
2. The 1.37-1.34 Ga granites related to the Pensamiento Granitoid Complex suggest a previous collision and reworking of the southern and northern basements during the San Ignacio orogeny.
3. The Sunsas belt records significant granitic magmatism between 1.10 and 1.04 Ga related to the last partial melting of the Paleoproterozoic sources.

4. The 1000±9 Ma and 992±41 Ma U-Pb monazite ages can be associated with the late- to post-collision stage of the Sunsas belt not registered in zircon dating.

3.8 Acknowledgements

This study was financed in part by the Coordenação de Aperfeiçoamento de Pessoal de Nível Superior - Brasil (CAPES) - Finance Code 001. The authors acknowledge the support of the Laboratório de Geocronologia (Universidade de Brasília) and the Grupo de Pesquisa em Evolução Crustal e Tectônica (Guaporé). The authors also acknowledge Fundação de Apoio à Pesquisa do Distrito Federal (FAPDF) and INCT Estudos Tectônicos (CNPq-CAPES-FAPDF) for financial support. IMN thanks CAPES and Programa de Excelência Acadêmica (PROEX, Edital - 0487) for granting the Doctorate scholarship. RAF and ASR acknowledge CNPq for research fellowship.

4. ARTIGO CIENTÍFICO 3: THE ESSENTIAL ROLE OF CONTINENTAL REWORKING PROCESSES IN THE PRECAMBRIAN SUNSAS BELT, SW AMAZONIAN CRATON

Ingrid M. Nedel[1], Reinhardt A. Fuck[1], Alanielson C. D. Ferreira[2], Amarildo S. Ruiz[3], Gerardo R. Matos-Salinas[4]

[1]Instituto de Geociências, Universidade de Brasília (UnB), Brasília-DF, Brazil.

[2]Instituto de Geociências, Universidade Federal do Rio Grande do Sul, Porto Alegre - RS, Brazil

[3]Faculdade de Geociências, Universidade Federal de Mato Grosso, Cuiabá-MT, Brazil.

[4]Instituto de Investigaciones Geológicas y del Medio Ambiente, Universidad Mayor de San Andrés (UMSA), Pabellón Geología, Calle 27, Campus Universitario Cota Cota, La Paz, Bolivia.

Author's correspondence: Ingrid M. Nedel (ingrid_mn@hotmail.com)

4.1 Abstract

We present the first integrated geochemical, Nd and Sr isotopes, and mineral chemistry data for the magmatic evolution in the Sunsas belt, SW Amazonian Craton. Our results support that the multiple crustal reworking processes were the main mechanism for continental differentiation. For the Sunsas northern domain, the sources are represented by 1.68 Ga felsic protoliths with lower LREE/HREE ratios, stronger negative Nb, Ta and Ti anomalies and higher initial 87Sr/86Sr (0.840). Moreover, 1.42 Ga mafic magmas show positive εNd(t), lower initial 87Sr/86Sr (0.696) and lower HREE contents with positive Eu anomalies indicate juvenile sources. It suggests a mixing of felsic crust and plagioclase-garnet-bearing sources during the c. 1.35 and c. 1.0 Ga orogenies in the northern domain. In contrast, for the southern domain of the Sunsas belt, the 1.95 and 1.85 Ga granitic crust with minor 1.34 Ga juvenile melt represents the main sources. Likewise, progressive mineral enrichment in Na (Ca- to Na-rich plagioclase) and Fe + Mg (biotite) from protolith to granitic leucosome also reflects the multiple recrystallization processes in the both domains. Therefore, the Sunsas belt was formed from multiple crustal reworking

processes of 1.95 – 1.68 Ga crustal protoliths with 1.42 – 1.35 Ga mantle-derived sources during the 1.35 Ga Rondonian-San Ignacio and 1.0 Ga Sunsas orogenies.

Keywords: Sunsas belt; Crustal reworking; Amazonian Craton

4.2 Introduction

Granitoids define temporal changes in the composition of Earth's continental crust and reflect a variety of crustal and mantle sources in a wide range of tectonic settings (Martin et al., 2005; Bonin et al., 2019; Moyen, 2020). Analytical data such as Pb-Nd-Hf isotopes, whole-rock and mineral composition support the research of granitic magmatism that took place during continental orogenic collages (Condie and Kröner, 2013; Hawkesworth et al., 2020; Brown et al., 2020). Enriched Sr and Nd isotopes and incompatible trace element compositions in granitoids may be interpreted as a record of significant crustal components (e.g., Condie and Kröner, 2013; Hagen-Peter and Cottle, 2018; Brown et al., 2020). Moreover, geochronological ages of inherited zircon cores and metamorphic rims can provide further evidence of reworked crust in the unexposed basement (e.g., Hagen-Peter and Cottle, 2018). Combined geochemical and isotopic analyses indicate assimilation-fractionation processes and discriminate the crustal and juvenile sources in the calc-alkaline magmatism (e.g., Condie and Kröner, 2013; Hagen-Peter and Cottle, 2018; Ferreira et al., 2020).

Global-scale granitic episodes are mainly related to orogenic collages that built the supercontinents (e.g., Hawkesworth et al., 2009, 2020; Brown et al., 2020). For instance, in the Rodinia (1.0-0.9 Ga) assembly, the major magmatism in southern Laurentia was generated from crustal reworking of different felsic components during the 1.2-0.9 Ga Grenvillian orogenies (e.g., Roberts and Slagstad, 2014; Spencer et al., 2019). Similarly, the SW Amazonian Craton records multiple collisional episodes with intense crustal reworking at 1.9-1.8 Ga, 1.6 Ga, 1.4-1.3 Ga, and 1.1-1.0 Ga, the latter related to the Sunsas-Grenville orogenies (Boger et al., 2005; Teixeira et al., 2010, 2020; Nedel et al., 2020a, b). Thus, Nd and Sr isotopes and chemical patterns of granitoids emplaced in the Sunsas belt may expand the knowledge of the juvenile and reworked protoliths during the Sunsas orogeny along the SW Amazonian Craton from late Mesoproterozoic and early Neoproterozoic, that lead to Rodinia assembly.

This paper aims to characterize the sources and Proterozoic evolution of the igneous rocks that constitute the Precambrian Sunsas belt, Northeastern Bolivia.

4.3 Geological setting

The Amazonian Craton represents continent-scale terrain accretion processes from Archean to Mesoproterozoic times (e.g., Tassinari and Macambira, 2004; Cordani and Teixeira, 2007) (Fig. 4.1A). It consists of the central 3.0–2.5 Ga Archean Carajás-Amapá and Imataca blocks surrounded by 2.2–2.0 Ga Paleoproterozoic juvenile and reworked terrains related to the Transamazonian orogenic collage (e.g., Cordani et al., 2000; Tassinari and Macambira, 2004). The late Paleo- to early Mesoproterozoic transition recorded progressively younger magmatic accretions as evidenced by the 1.95–1.85 Ga Ventuari-Tapajós, 1.81–1.55 Ga Rio Negro-Juruena, 1.55–1.32 Ga Rondonian-San Ignacio and 1.3–1.0 Ga Sunsas provinces (e.g., Teixeira et al., 1989; Tassinari and Macambira, 1999, 2004). The latter includes the rift stages, such as the Aguapeí aulogen, and deposition of metasedimentary rocks related to the Mesoproterozoic Sunsas Group (Litherland et al., 1986; Saes et al., 1993; Geraldes et al., 2001). A different proposal divides the craton into eight geochronological provinces (Santos et al., 2000, 2008): Carajás (3-2.5 Ga), Central Amazonian (~2.6 Ga), Transamazonas (2.26-2.01 Ga), Tapajós-Parima (2.03-1.88 Ga), Rio Negro (1.82-1.52 Ga), Rondônia-Juruena (1.82-1.54 Ga), Sunsas (1.45-1.0 Ga) and K'Mudku (~1.2 Ga). However, there is a consensus that the Grenvillian-Sunsas orogeny stabilized the Amazonian Craton assembly at c. 1.0 Ga (e.g., Teixeira et al., 1989; Tassinari and Macambira, 2004; Cordani and Teixeira, 2007; Santos et al. 2008).

4.3.1 Sunsas Province

The Sunsas Province corresponds to the last crustal accretion at the southwestern Amazonian Craton before the final tectonic stabilization (e.g., Tassinari and Macambira, 2004; Cordani and Teixeira, 2007) (Fig. 4.1B). It comprises igneous and supracrustal rocks affected by the Sunsas orogeny along the Sunsas, Nova Brasilândia and Aguapeí belts (Litherland et al., 1986, 1989; Tassinari and Macambira, 2004; Cordani and Teixeira, 2007; Teixeira et al., 2010). The collisional-type event was associated with low- to medium-grade metamorphism near-coeval

with 1.1–1.0 Ga syn-tectonic granite emplacement (e.g., Litherland et al., 1989; Tassinari et al., 2000).

The Nova Brasilândia belt evolution was marked by two cycles of crustal shortening and extension between 1120 and 980 Ma, with a contribution of bimodal magmatism (Rizzotto et al., 2002). It is estimated that the orogenic cycle lasted from 1122 to 1110 Ma (Rizzotto, 2001; Teixeira et al., 2010), generating different grades of metamorphism that increase from north to south (Luft et al., 2000; Tohver et al., 2004). The Rio Branco (1119-1106 Ma) and Rio Pardo suites represent two granitic pulses contemporary with the Sunsas magmatism in the Bolivian shield (Boger et al., 2005; Teixeira et al., 2010). According to Quadros et al. (2020), the Rio Branco suite evolved in an arc-back-arc system followed by younger intrusions at high-grade metamorphic conditions that generated an incipient 1110 Ma leucosome. The suture model contradicts an earlier proposal of Rizzotto (1999) that the Nova Brasilândia Group was formed in an intracontinental rift setting, followed by a proto-oceanic opening, synchronous to the development of the Grenville orogeny (Shawinigan phase) in Laurentia (Rizzotto et al., 2013).

The Aguapeí belt represents the intracontinental geotectonic setting related to the compressional orogenic structures of the Sunsas belt. The result was a narrow NNW–SSE strip of folded sedimentary rocks, structurally confined, extending discontinuously for more than 500 km (Teixeira et al., 2010). Peraluminous felsic plutonic rocks, mafic sills and dike swarms (1.1-0.9 Ga) and younger 930-907 Ma old bimodal magmatism comprise the magmatic rocks emplaced in the Aguapeí belt basement (Lima et al., 2012, 2019; Lima, 2016).

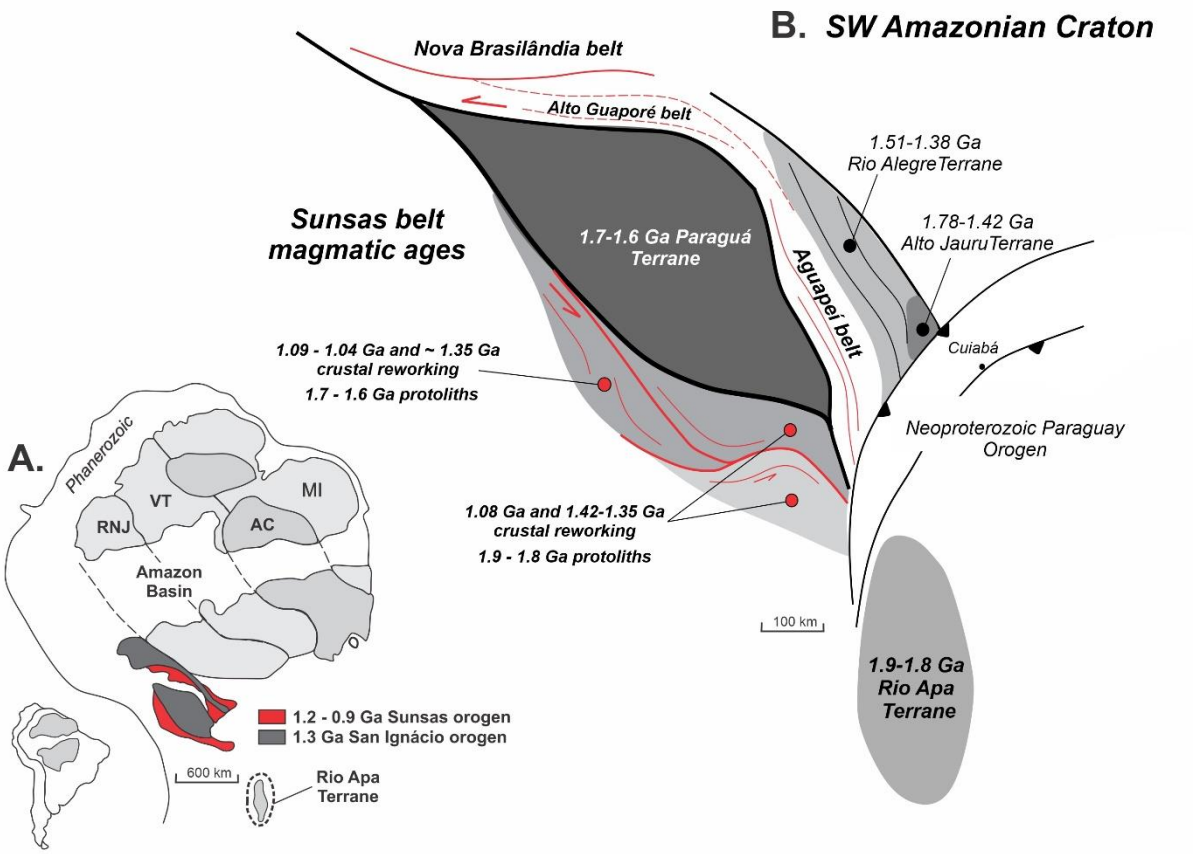

Figure 4.1. (A) Schematic geotectonic compartment for the Amazonian Craton detaching the SW portion and Sunsas Province (after Teixeira et al., 1989; Tassinari and Macambira, 1999, 2004; Tassinari et al., 2000) (modified from Cordani et al., 2000). AC - Amazônia Central (2.5 Ga), MI - Maroni-Itacaiúnas (2.2–1.95 Ga), VT - Ventuari-Tapajós (1.95–1.8 Ga), RNJ - Rio Negro-Juruena (1.8–1.55 Ga), RAB – Rio Apa Block (2.0-1.5); RSI - Rondoniana-San Ignácio (1.55–1.3 Ga) and SA - Sunsas (1.3–1.0 Ga); (B) Schematic model of Rodinia central portion assembly (modified from Li et al., 2008).

4.3.1.1 Sunsas belt

The Sunsas belt (Fig. 4.2) represents the rock assemblage exposed in the western portion of the Sunsas Province, whose final structuring occurred during the Sunsas orogeny (Litherland et al., 1986, 1989; Tassinari and Macambira, 2004; Cordani and Teixeira, 2007; Teixeira et al., 2010). The NW-SE-trending, 600 km long belt is compartmentalized by transpressive shear zones, namely the Rio Negro, Santa Catalina, Concepción, and San Diablo fronts (Fig. 4.2). The shear zones acted as channels for the Sunsas high-K granitic intrusions into the Paleo- to Mesoproterozoic basement (Litherland and Bloomfield, 1981; Litherland et al., 1986; Teixeira et al., 2010; Nedel et al., 2020a, b). South of the San Diablo front, the basement comprises 1.9-1.8 Ga granitic rocks, whereas the 1.7 to 1.6 Ga magmatic rocks related to the Chiquitania and Lomas Manechis complexes make up the basement north of the

front (Nedel et al., 2020a, b). The Sunsas belt also is marked by extensive 1.37-1.34 Ga magmatism related to the Pensamiento Granitoid Complex that reworks the southern and northern basements during the San Ignacio orogeny (1.37-1.28 Ga; Bettencourt et al., 2010)

The Sunsas magmatism (1.1-0.9 Ga) was generated during the collisional phase at the final stage of the Amazonian Craton stabilization (Litherland et al., 1989; Boger et al., 2005; Cordani and Teixeira, 2007; Teixeira et al., 2010). Recent studies regarding syn-tectonic granitic intrusions of 1.1-1.0 Ga in the Sunsas belt show that the Sunsas orogeny produced I-type fractionated granite and (hybrid) A-type granite with metalluminous to peraluminous composition and calc-alkaline signature (Vargas-Mattos, 2010; Nedel et al., 2020a, b). Furthermore, geochemical analyses indicate at least two precursor sources for the Sunsas granites, one Mg-rich and less fractionated, and another Fe-rich and more REE enriched (Nedel et al., 2020a, b). Late- to post-collision stages are recorded in monazite of 1000±9 Ma and 992±41 Ma U-Pb (Nedel et al., 2020a, b).

The results format presented in this work will take into account three previous studies of Nedel et al. (2017) and Nedel et al. (2020a, b) that present petrography, U-Pb geochronology and initial whole-rock geochemistry data of the Sunsas belt granitic magmatism. We aim to introduce the local geologic context of the analyzed samples, as well the previous results, that will underline the presentation of new isotopic data. Herein we will divide the Sunsas belt magmatism in northern and southern granites (Nedel et al., 2020a, b).

Northern granites domain

The Sunsas belt northern intrusions present granitic compositions with ages between 1.68 and 1.05 Ga (Table 4.1, Fig. 4.2) (Nedel et al., 2020a, b). All plutons, except the San Ramón (1423 Ma), display inheritance records of 1.76-1.60 Ga related to reworking processes of the Chiquitania and Lomas Manechis complexes. The Sujalito, Santo Rosário and Miraflores intrusions crystallized at c. 1.68 Ga (Nedel et al., 2017). The Salinas monzogranite, which is the only pluton in the north with hornblende and pyroxene in its mineral assemblage, crystallized at 1.37 Ga, corresponding to the Pensamiento Complex age. The younger magmatism is represented by the Casa de Piedra (1095 Ma), Nocemano (1102 Ma), La Asunta

(1081 Ma), and Marimonos (1060 Ma) intrusions. Casa de Piedra and Marimonos mainly occur as massive lenses controlled by NW-SE structures, often with deformed borders and incipient foliation marked by biotite orientation. Evidence of relationships between mafic enclaves and schlieren layering are found in the Casa de Piedra granite. The La Asunta and Nocemano syenogranites are weakly foliated, leucocratic, with porphyritic texture due to the presence of K-feldspar phenocrysts. The plutons have rounded shapes emplaced into the Chiquitania Gneissic Complex.

Southern granites domain

The older magmatism is represented by granodiorite, monzogranite and granite emplaced in the southern part of the Sunsas belt (Table 4.1, Fig. 4.2) (Nedel et al., 2020a, b). The Las Tojas two-mica granite (1941 Ma), exposed in the Don Mario mineral district (Fig. 4.2), shows a mineral assemblage formed of 30-39% plagioclase, 25-31% K-feldspar, 20-30% quartz and 8-15% mica. This granitic body presents incipient foliation that reflects an NW-SE tectonic transcurrent shear zone. The Tauca granodiorite (1852 Ma) exposures are very weathered, making it difficult to recognize deformation structures. However, the primary mineral assemblage remains partially preserved (38-42% plagioclase; 29-32% quartz; 15-18% K-feldspar; and 10-15% biotite). The Nomoca granodiorite (1084 Ma) is mesocratic with massive internal structure and presents K-feldspar megacrysts (~10%). The Tasseoro granite (1085 Ma) occurs as massive lenses controlled by NW-SE structures, often with deformed borders and incipient foliation marked by biotite orientation. The San Pablo (1345 Ma) monzogranite displays massive structure and presents hornblende and pyroxene in its mineral assemblage. The mafic minerals display adcumulatic texture, sometimes producing a banded mineral structure. The Señoritas two-mica granite (1454 Ma) occurs as parallel lenses hosted in the WNW-ESE-trending mica-schist sequence (e.g., Litherland et al., 1986).

Table 4-1. Data compilation from previous works of Sunsas belt magmatism. Data from Nedel et al. (2020 a, b).

Domain	Granitoid	Sample	U-Pb zircon ages (Ga)			
			Protolith	*Crustal reworking*		
North	Sujalito	SR 20	1.68			
	Santo Rosário	IM32	1.68			
	Casa de Piedra	ID 18	1.76		1.28	1.09
	Miraflores	IM11	1.68			
	Marimonos	MR11/10	1.63		1.38	1.06
	La Asunta	LA 14	1.60		1.28	1.08
	Salinas	SM10	1.68		1.37	
	Nocemano	SM 07	1.69	1.41	1.37	1.10
	San Ramón	ID 11		1.42		
South	Las Tojas	ID 08	1.94			0.99
	Tauca	ID 09	1.85			
	Señoritas	ID 06	1.95	1.45		1.00
	Nomoca	TAP 02	1.83	1.44	1.35	1.08
	San Pablo	ID 02(A)			1.34	
	San Pablo	ID 02(B)			1.34	
	Tasseoro	TAS 15				1.08
	Colmena	IM 34			1.34	

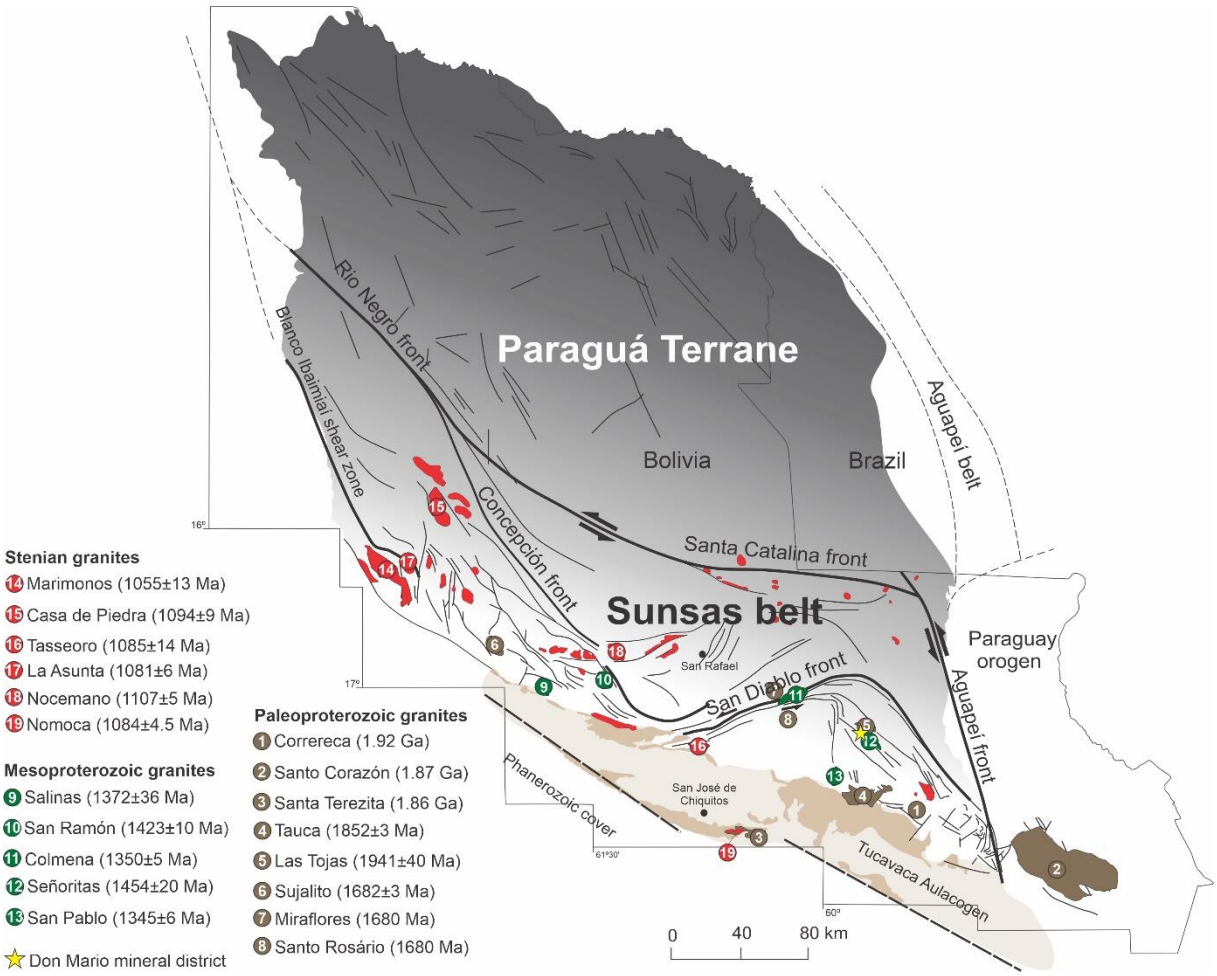

Figure 4.2. Schematic geological map for the Paraguá Terrane, SW Amazonian Craton, showing the Sunsas belt structures and studied plutons.

4.4 Analytical methods and procedures

4.4.1 Geological sampling and petrography

Geological sampling in the Northeastern Bolivia area was carried out with the purpose of investigating the Sunsas belt. Systematic thin sections cut relative to foliation were obtained from representative samples from nine outcrops of granitic plutons. The petrography was done at the Microscopy Laboratory of the Institute of Geosciences of Universidade de Brasília (Brazil).

4.4.2 Mineral Chemistry

Systematic analyses were obtained from 13 samples from outcrops of the Sunsas belt. Mineral analyses were performed on polished thin section using a JEOL JXA-8230 SuperProbe with 5 wavelengths dispersive (WDS) spectrometers at the Electron Microprobe Laboratory of the Universidade de Brasília (Brazil). WDS

analyses were obtained for pyroxene, plagioclase, K-feldspar, amphibole and biotite. Operating conditions for the WDS analyses were 15 kV accelerating voltage, with a beam current of 10 nA and probe diameters of 3 μm for all minerals except plagioclase (5 μm). Count times on peak and on background were 10s and 5s, respectively. Both synthetic and natural mineral standards were used for the analyses and the same standards and procedure were retained throughout. Fe^{3+} contents were estimated using site and charge balance calculations on cation-normalized analyses (Droop, 1987).

4.4.3 Geochemistry

Geochemical analyses were performed on 16 samples from granitic plutons. The samples were crushed and ground in the Laboratory of Geochronology at Universidade de Brasília. Analyses of major, minor and trace elements were carried out by ALS Global Analytical Laboratories Ltd (Vancouver, Canadá). Major and minor elements were obtained by X-ray fluorescence (XRF) after fusion of the sample with lithium tetraborate. Trace elements were determined from melting 0.2g of the sample with lithium metaborate/tetraborate, diluted nitric acid digestion and ICP-MS analysis. The loss on ignition (LOI) was given by weight difference after heating at 100°C. Precious metals and base metals were determined after 0.5 g of sample digestion with Acqua Regia with ICP-AES analysis.

4.4.4 Sm-Nd isotopes

Sm–Nd isotopic analyses followed the method described by Gioia and Pimentel (2000) and were carried out at the Geochronology Laboratory of Universidade de Brasília. Whole-rock powders (~50 mg) of 12 samples were mixed with ^{149}Sm–^{150}Nd spike solution and dissolved in Savillex Digestion Vessels. Sm and Nd extraction of whole-rock samples followed conventional cation exchange chromatography techniques, with Teflon columns containing LN-Spec resin (HDEHP – diethylhexil phosphoric acid supported on PTFE powder). Sm and Nd fractions were loaded on Re evaporation filaments of double filament assemblies, and the isotopic measurements were carried out on a multicollector TRITON thermal ionization mass spectrometer in static mode. Uncertainties of Sm/Nd and $^{143}Nd/^{144}Nd$ ratios were better than ±0.1% (2σ standard error) and ±0.0015% (1σ), respectively, according to repeated analyses of the international rock standard BHVO-1. $^{143}Nd/^{144}Nd$ ratios

were normalized to $^{146}Nd/^{144}Nd=0.7219$, and the decay constant used was $6.54x10^{-12}$. The T_{DM} values were calculated using the DePaolo (1981) model.

4.4.5 Sr isotopes

Sr isotopic ratios were determined for 12 whole-rock samples at the Geochronology Laboratory of Universidade de Brasília. The samples were processed by electrodynamic disaggregation using a SELFRAG® Lab 2.0 High Voltage Pulse Power Fragmentation at voltages of 100–140 kV. An aliquot of 0.5 ml of the solutions of each sample was directly loaded onto Teflon® columns containing approximately 83 mg of Eichrom® Sr-Spec resin (50–100 μm) to separate the Sr fraction from the matrix. Sr isotope measurements were performed using a Thermo Scientific TRITON™ Plus Thermal Ionization Mass Spectrometer (TIMS) operating in the static multi-collector mode. The average $^{87}Sr/^{86}Sr$ obtained for the NBS-987 standard was 0.710257±0.000007 (2SD; n=9) consistent with the recommended $^{87}Sr/^{86}Sr=0.71025$ of Thirlwall (1991). Initial ratios for the crystallization time of each sample were calculated using the ^{87}Rb decay constant of $1.393\times10^{-11}a^{-1}$ (Nebel et al., 2011).

4.5 Results

4.5.1 Petrography and mineral chemistry

The Sunsas belt comprises syenogranite to granodiorite intrusions (Table 4.1 and Fig. 4.3). Petrographic features and textures reveal the recrystallization processes (Fig. 4.4). To check these different mineral assemblage, systematic electron microprobe analyses of feldspar, biotite, amphibole and pyroxene were obtained in unweathered samples of granitic rocks with primary minerals and magmatic textures. Mineral chemistry analyzes reveal different compositions in mineral paragenesis of granites from the northern and southern portions of Sunsas belt.

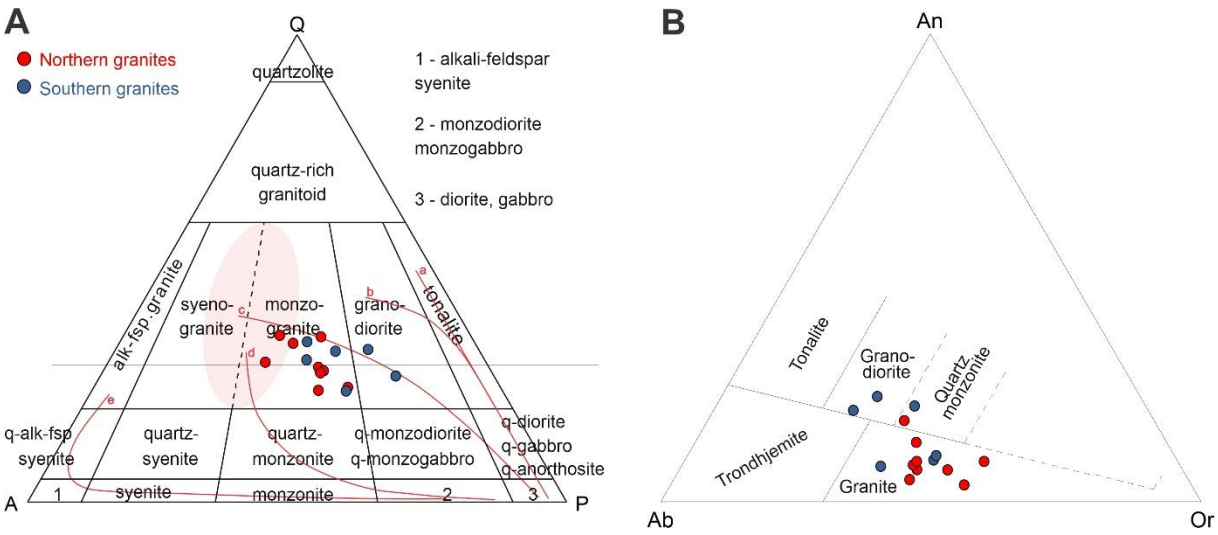

Figure 4.3. Classification of Sunsas belt granites on QAP (modified from Streckeisen, 1974) and feldspar triangle (O'Connor, 1965) diagrams.

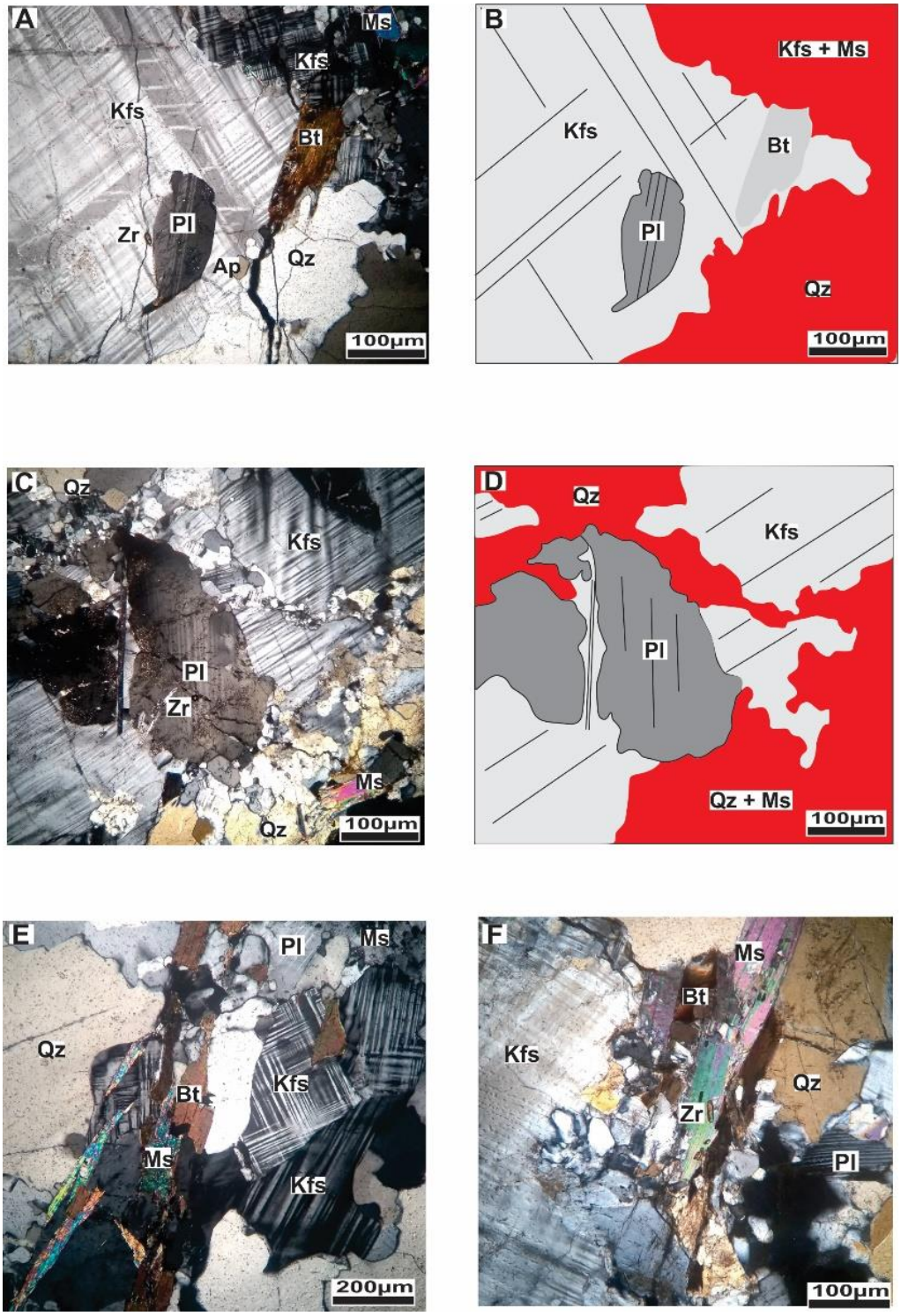

Figure 4.4. Petrographic features and textures of the granitic rocks from Sunsas belt. A and C) Plagioclase enclave included in K-feldspar in equilibrium with biotite. Granitic melt rich in Qz + Kfs + Ms crosscuts the previous two mineral phases. (B and D) Schematic drawing of texture correlations from studied granites. E) Texture of injected granitic melt. F) Coarse-grained K-feldspar reacting with Qz + Kfs + Ms + Bt melt. Bt – biotite, Zr – zircon, Ap – apatite, Kfs – K-feldspar, Pl – plagioclase and Qz – quartz.

4.5.1.1 Biotite composition

Biotite from northern granites domain

Biotite occurs as greenish to brownish subhedral lamellar crystals of dominantly hypidiomorphic shape in the northern granites. Smaller euhedral crystals occur included in plagioclase. Textural features indicate primary biotite in the Nocemano and La Asunta plutons. The Casa de Piedra granite shows secondary biotite occurrences with transformation and/or alteration, such as chloritization, alteration to muscovite, or oxidation. The chloritization reaction took place essentially along the cleavage planes. Also, association with titanite and epidote are common.

Biotite analyses from Nocemano and La Asunta are more Fe-rich end-members (annite) with Mg/(Mg + Fe) values ranging from 0.30 to 0.34, whereas biotite from Casa de Piedra presents one more Mg-rich end-members group (phlogopite) with Mg/(Mg + Fe) values ranging from 0.45 to 0.58 and another group with Mg/(Mg + Fe) values between 0.59 and 0.65 (Table 4.2 and Fig. 4.5A, B). The La Asunta two-mica granite containing both biotite and muscovite.

In the discriminant diagram for primary magmatic, re-equilibrated and neo-formed biotite grains (after Nachit et al., 2005), our analyses of La Asunta and Nocemano plot in the field of primary biotite (Fig. 4.5A). The Casa de Piedra analyses show biotite from a leucocratic portion (sample ID18) plotted in the re-equilibrated field and biotite from Bt-rich schlieren plotted in the re-equilibrated to neo-formed fields (Mg-rich).

Biotite from the southern domain

Petrographic data of Señoritas, Las Tojas, and Nomoca southern granites show greenish to brownish subhedral lamellar crystals of biotite with hypidiomorphic shapes and smaller euhedral crystals included in plagioclase. Biotite from San Pablo monzogranite is reddish brown and subhedral, associated to pyroxene and amphibole. Textural features indicate cogenetic generation with primary minerals. The Tasseoro granite presents late hydrothermal venules of brownish subhedral biotite with plagioclase, quartz, and occasional epidote occurrences.

San Pablo biotite analyses are more Fe-rich end-members (annite) with Mg/(Mg + Fe) values ranging from 0.35 to 0.39 (Table 4.2, Fig. 4.5C, D). Biotite from Señoritas and Las Tojas granites is also of Fe-rich end-members (annite) with Mg/(Mg + Fe)

values ranging from 0.32 to 0.43. Tasseoro and Nomoca plutons present more Mg-rich end-members (phlogopite) with Mg/(Mg + Fe) values ranging from 0.46 to 0.54. Señoritas and Las Tojas record the presence of biotite and muscovite, comprising two-mica granite composition. The discriminant diagram shows primary magmatic biotite for Las Tojas, Señoritas, and San Pablo intrusions whereas Tasseoro and Nomoca present reequilibrated biotite (Fig. 4.5C).

Table 4-2. Biotite composition from Sunsas belt.

Domain	Pluton	Analysis	SiO2	TiO2	Al2O3	FeO	MnO	MgO	CaO	Na2O	K2O	F	Cl	Cr2O3	V2O3	NiO	Total	OH	Cl	F	ΣOH	Si	Al	ΣT	Al	Ti	Cr	V	Mg	Ni	Fe2+	Mn	ΣM	Ca	Na	K	ΣI
Northern	Casa de Piedra	ID-18A_C4_?1	38.93	2.12	16.40	16.86	0.56	8.01	0.06	0.15	8.07	1.19	0.02	0.00	0.09	0.00	92.46	1.70	0.00	0.30	2.00	3.06	0.94	4.00	0.57	0.13	0.00	0.01	0.94	0.00	1.111	0.04	2.79	0.00	0.02	0.81	0.84
		ID-18A_C1_bt6	37.61	1.09	15.64	18.48	0.60	9.42	0.00	0.06	10.03	1.85	0.04	0.07	0.02	0.00	94.91	1.53	0.01	0.47	2.00	3.00	1.00	4.00	0.46	0.07	0.00	0.00	1.12	0.00	1.233	0.04	2.92	0.00	0.01	1.02	1.03
		ID-18A_C4_ms4	38.46	1.76	15.53	19.19	0.57	10.04	0.00	0.02	9.70	1.75	0.03	0.00	0.05	0.00	97.08	1.57	0.00	0.43	2.00	2.98	1.02	4.00	0.40	0.10	0.00	0.00	1.16	0.00	1.224	0.04	2.94	0.00	0.00	0.96	0.96
		ID-18A_C6_bt3	37.91	0.92	15.46	18.51	0.67	10.35	0.05	0.09	9.66	1.95	0.00	0.02	0.06	0.00	95.66	1.51	0.00	0.49	2.00	2.99	1.01	4.00	0.43	0.05	0.00	0.00	1.22	0.00	1.222	0.04	2.98	0.00	0.01	0.97	0.99
		ID-18A_C4_?5	38.51	1.52	15.36	18.77	0.65	8.73	0.06	0.09	8.65	1.48	0.00	0.05	0.05	0.00	93.90	1.63	0.00	0.37	2.00	3.04	0.96	4.00	0.48	0.09	0.00	0.00	1.03	0.00	1.244	0.04	2.88	0.00	0.01	0.87	0.89
		ID-18A_C1_bt13	38.11	1.59	15.15	19.11	0.64	9.67	0.00	0.10	9.86	1.70	0.01	0.06	0.04	0.00	96.02	1.58	0.00	0.42	2.00	2.99	1.01	4.00	0.39	0.09	0.00	0.00	1.13	0.00	1.255	0.04	2.92	0.00	0.01	0.99	1.00
		ID-18A_C5_bt4	37.61	1.22	14.97	19.91	0.73	10.08	0.00	0.05	9.60	2.03	0.03	0.03	0.06	0.10	96.42	1.49	0.00	0.51	2.00	2.98	1.02	4.00	0.37	0.07	0.00	0.00	1.19	0.01	1.322	0.05	3.02	0.00	0.01	0.97	0.98
		ID-18A_C6_bt6	37.54	1.59	14.92	18.01	0.48	10.31	0.03	0.04	9.95	1.88	0.01	0.00	0.07	0.01	94.84	1.52	0.00	0.47	2.00	2.99	1.01	4.00	0.39	0.10	0.00	0.00	1.22	0.00	1.200	0.03	2.94	0.00	0.01	1.01	1.02
		ID-18A_C5_bt3	37.26	1.63	14.91	19.55	0.61	10.00	0.03	0.05	9.77	1.97	0.00	0.00	0.01	0.00	95.81	1.50	0.00	0.50	2.00	2.96	1.04	4.00	0.36	0.10	0.00	0.00	1.19	0.00	1.300	0.04	2.99	0.00	0.01	0.99	1.00
		ID-18A_C6_bt2	37.82	1.18	14.91	19.00	0.69	10.40	0.05	0.04	9.93	2.16	0.00	0.05	0.06	0.01	96.29	1.46	0.00	0.54	2.00	3.00	1.00	4.00	0.39	0.07	0.00	0.00	1.23	0.00	1.266	0.05	3.00	0.00	0.01	1.00	1.01
		ID-18A_C6_pl3	36.48	2.56	14.72	19.40	0.68	9.55	0.00	0.14	9.84	1.63	0.03	0.00	0.00	0.00	95.03	1.58	0.00	0.41	2.00	2.91	1.09	4.00	0.30	0.15	0.00	0.00	1.14	0.00	1.300	0.05	2.93	0.00	0.02	1.00	1.03
		ID-18A_C5_bt5	37.51	1.04	14.68	19.99	0.76	10.04	0.02	0.05	9.79	1.98	0.01	0.00	0.04	0.03	95.94	1.50	0.00	0.50	2.00	2.99	1.01	4.00	0.37	0.06	0.00	0.00	1.19	0.00	1.333	0.05	3.01	0.00	0.01	0.99	1.00
		ID19B_C2 bt 2	41.11	0.62	14.60	13.92	0.65	14.52	0.00	0.07	8.63	2.05	0.00	0.09	0.00	0.00	96.25	1.51	0.00	0.49	2.00	3.11	0.89	4.00	0.42	0.04	0.01	0.00	1.64	0.00	0.888	0.04	3.02	0.00	0.01	0.83	0.84
		ID-18A_C6_bt4	37.73	1.59	14.51	19.11	0.49	10.20	0.01	0.03	9.86	2.15	0.02	0.04	0.04	0.00	95.78	1.46	0.00	0.54	2.00	3.00	1.00	4.00	0.37	0.10	0.00	0.00	1.21	0.00	1.227	0.03	2.98	0.00	0.00	1.00	1.01
		ID-18A_C4_?2	38.27	2.23	14.51	19.16	0.72	9.78	0.03	0.08	9.03	1.77	0.01	0.09	0.00	0.00	95.67	1.56	0.00	0.44	2.00	3.01	0.99	4.00	0.35	0.13	0.01	0.00	1.15	0.00	1.266	0.05	2.94	0.00	0.01	0.91	0.92
		ID-18A_C4_ms2	36.32	2.48	14.50	19.31	0.54	9.35	0.00	0.05	9.56	1.41	0.01	0.00	0.05	0.04	93.62	1.64	0.00	0.36	2.00	2.93	1.07	4.00	0.30	0.15	0.00	0.00	1.12	0.00	1.300	0.04	2.92	0.00	0.01	0.98	0.99
		ID-18A_C6_pl4	37.20	2.48	14.46	19.51	0.68	9.70	0.03	0.05	9.94	1.70	0.01	0.00	0.07	0.00	95.81	1.57	0.00	0.42	2.00	2.95	1.05	4.00	0.30	0.15	0.00	0.00	1.15	0.00	1.229	0.05	2.93	0.00	0.01	1.00	1.01
		ID-18A_C2_bt5	37.22	1.48	14.45	19.33	0.56	10.37	0.00	0.08	9.70	2.19	0.03	0.00	0.05	0.00	95.45	1.44	0.00	0.56	2.00	2.99	1.01	4.00	0.35	0.09	0.00	0.00	1.24	0.00	1.330	0.04	3.02	0.00	0.01	0.99	1.00
		ID19B_C1 bt 2	40.17	0.59	14.41	14.30	0.42	14.03	0.02	0.13	8.54	2.25	0.00	0.00	0.06	0.04	94.95	1.45	0.00	0.55	2.00	3.11	0.89	4.00	0.43	0.03	0.00	0.00	1.62	0.00	0.933	0.03	3.04	0.00	0.02	0.84	0.86
		ID-18A_C4_bt3	37.38	1.73	14.32	19.53	0.63	10.18	0.03	0.03	9.68	2.10	0.00	0.02	0.12	0.06	95.81	1.47	0.00	0.53	2.00	2.98	1.02	4.00	0.33	0.10	0.00	0.01	1.21	0.00	1.330	0.04	3.00	0.00	0.01	0.99	0.99
		ID19B_C3 bt 4	39.71	0.92	13.92	16.20	0.59	12.86	0.02	0.02	8.86	2.55	0.00	0.00	0.01	0.00	95.65	1.37	0.00	0.63	2.00	3.11	0.89	4.00	0.40	0.05	0.00	0.00	1.50	0.00	1.066	0.04	3.06	0.00	0.00	0.89	0.89

Domain	Pluton	Analysis	SiO2	TiO2	Al2O3	FeO	MnO	MgO	CaO	Na2O	K2O	F	Cl	Cr2O3	V2O3	NiO	Total	OH	Cl	F	ΣOH	Si	Al	ΣT	Al	Ti	Cr	V	Mg	Ni	Fe2+	Mn	ΣM	Ca	Na	K	ΣI
		ID-18A_C4_bt2	35.57	2.61	13.90	18.51	0.76	9.37	0.10	0.10	9.11	1.93	0.02	0.10	0.07	0.00	92.15	1.49	0.00	0.50	2.00	2.94	1.06	4.00	0.30	0.16	0.01	0.00	1.16	0.00	1.28	0.05	2.97	0.01	0.02	0.96	0.99
		ID19B_C5 bt 1	40.70	0.78	13.89	14.60	0.38	14.06	0.00	0.06	8.93	2.45	0.02	0.09	0.01	0.04	96.00	1.40	0.00	0.60	2.00	3.14	0.86	4.00	0.40	0.05	0.01	0.00	1.62	0.00	0.94	0.02	3.04	0.00	0.01	0.88	0.89
		ID-18A_C4_bt1	36.75	1.88	13.80	19.22	0.66	9.91	0.03	0.15	9.64	1.86	0.02	0.02	0.06	0.00	93.99	1.52	0.00	0.48	2.00	2.98	1.02	4.00	0.30	0.11	0.00	0.00	1.20	0.00	1.30	0.05	2.97	0.00	0.02	1.00	1.02
		ID19B_C3 bt 3	40.88	0.77	13.66	15.22	0.40	13.80	0.01	0.07	8.99	2.81	0.00	0.04	0.06	0.00	96.72	1.31	0.00	0.69	2.00	3.16	0.84	4.00	0.41	0.05	0.00	0.00	1.59	0.00	0.98	0.03	3.06	0.00	0.01	0.89	0.90
		ID-18A_C2_bt4	34.39	2.10	13.48	19.33	0.63	9.43	0.04	0.19	9.32	2.03	0.01	0.02	0.06	0.00	91.02	1.45	0.00	0.55	2.00	2.92	1.08	4.00	0.27	0.13	0.00	0.00	1.19	0.00	1.37	0.05	3.02	0.00	0.03	1.01	1.04
		ID19B_C1 bt 1	40.13	0.91	13.44	14.88	0.68	14.07	0.01	0.12	8.83	2.55	0.01	0.00	0.07	0.00	95.70	1.37	0.00	0.63	2.00	3.13	0.87	4.00	0.36	0.05	0.00	0.00	1.63	0.00	0.97	0.05	3.07	0.00	0.02	0.88	0.90
		ID19B_C3 bt 5	40.09	0.72	13.21	16.25	0.55	13.33	0.00	0.09	8.83	2.84	0.00	0.05	0.02	0.04	96.00	1.29	0.00	0.71	2.00	3.15	0.85	4.00	0.38	0.04	0.00	0.00	1.56	0.00	1.07	0.04	3.09	0.00	0.01	0.89	0.90
		ID19B_C3 bt 2	40.29	0.58	13.07	15.90	0.57	13.86	0.00	0.06	8.96	2.94	0.00	0.00	0.05	0.03	96.31	1.27	0.00	0.73	2.00	3.16	0.84	4.00	0.37	0.03	0.00	0.00	1.62	0.00	1.04	0.04	3.11	0.00	0.01	0.90	0.91
		ID19C_C1_bt 2	40.84	0.65	13.05	15.96	0.58	14.22	0.00	0.03	9.96	2.47	0.01	0.08	0.01	0.00	97.85	1.40	0.00	0.60	2.00	3.13	0.87	4.00	0.31	0.04	0.01	0.00	1.63	0.00	1.02	0.04	3.05	0.00	0.00	0.98	0.98
		ID19B_C3 bt 1	40.33	1.03	12.99	16.52	0.54	13.22	0.04	0.10	8.78	2.93	0.01	0.00	0.06	0.00	96.56	1.27	0.00	0.73	2.00	3.16	0.84	4.00	0.36	0.06	0.00	0.00	1.55	0.00	1.08	0.04	3.09	0.00	0.01	0.88	0.90
		ID19B_C2 bt 1	39.83	0.97	12.99	16.62	0.59	12.83	0.01	0.03	8.96	2.43	0.00	0.02	0.00	0.00	95.28	1.39	0.00	0.61	2.00	3.14	0.86	4.00	0.35	0.06	0.00	0.00	1.51	0.00	1.10	0.04	3.05	0.00	0.00	0.90	0.91
		ID19A`_C1_bt 1	41.15	0.91	12.98	16.14	0.64	14.27	0.06	0.02	10.14	2.09	0.02	0.06	0.07	0.00	98.54	1.50	0.00	0.50	2.00	3.12	0.88	4.00	0.27	0.05	0.00	0.00	1.61	0.00	1.02	0.04	3.01	0.00	0.00	0.98	0.99
		ID19A_C2_bt 2	40.28	0.66	12.93	16.27	0.56	13.75	0.00	0.08	9.90	2.49	0.00	0.06	0.04	0.02	97.02	1.39	0.00	0.61	2.00	3.13	0.87	4.00	0.31	0.04	0.00	0.00	1.59	0.00	1.06	0.04	3.05	0.00	0.01	0.98	0.99
		ID19C_C1_bt 1	40.29	0.53	12.91	14.45	0.53	14.19	0.01	0.10	9.65	2.00	0.02	0.02	0.01	0.04	94.75	1.50	0.00	0.49	2.00	3.14	0.86	4.00	0.33	0.03	0.00	0.00	1.65	0.00	0.94	0.04	2.99	0.00	0.02	0.96	0.98
		ID19A_C4_bt 1	40.61	0.63	12.84	15.63	0.50	14.00	0.03	0.04	10.04	2.57	0.03	0.08	0.07	0.00	97.07	1.37	0.00	0.63	2.00	3.15	0.85	4.00	0.32	0.04	0.01	0.00	1.62	0.00	1.01	0.03	3.04	0.00	0.01	0.99	1.00
		ID19A`_C5_bt 2	40.36	0.71	12.84	16.08	0.57	13.86	0.01	0.05	9.85	2.44	0.00	0.00	0.00	0.00	96.85	1.40	0.00	0.60	2.00	3.13	0.87	4.00	0.31	0.04	0.00	0.01	1.60	0.00	1.04	0.04	3.04	0.00	0.01	0.98	0.98
		ID19B_C5 bt 1	39.61	0.72	12.84	15.82	0.56	13.49	0.03	0.07	8.78	2.59	0.01	0.02	0.05	0.00	94.59	1.35	0.00	0.65	2.00	3.15	0.85	4.00	0.35	0.04	0.00	0.00	1.60	0.00	1.05	0.04	3.08	0.00	0.01	0.89	0.90
		ID19A_C2_bt 1	40.26	0.79	12.73	16.37	0.50	13.63	0.01	0.11	10.01	2.35	0.02	0.04	0.02	0.00	96.93	1.42	0.00	0.58	2.00	3.13	0.87	4.00	0.29	0.05	0.00	0.01	1.58	0.00	1.06	0.03	3.02	0.00	0.02	0.99	1.01
		ID19A`_C4_bt 1	40.27	1.12	12.72	15.36	0.34	14.40	0.02	0.03	10.08	2.58	0.00	0.03	0.04	0.02	97.02	1.37	0.00	0.63	2.00	3.12	0.88	4.00	0.29	0.07	0.00	0.00	1.66	0.00	1.00	0.02	3.04	0.00	0.01	1.00	1.00
		ID19C_C5_bt 1	39.83	1.05	12.72	15.98	0.57	13.50	0.04	0.06	9.86	2.30	0.01	0.00	0.02	0.00	95.94	1.43	0.00	0.57	2.00	3.12	0.88	4.00	0.29	0.06	0.00	0.00	1.58	0.00	1.05	0.04	3.02	0.00	0.01	0.98	1.00
		ID19A`_C1_bt 3	40.51	0.47	12.66	15.42	0.48	14.56	0.04	0.09	10.01	2.26	0.01	0.00	0.06	0.00	96.57	1.45	0.00	0.55	2.00	3.14	0.86	4.00	0.29	0.03	0.00	0.00	1.68	0.00	1.00	0.03	3.03	0.00	0.01	0.99	1.00
		ID19A`_C5_bt 1	40.21	0.75	12.66	16.69	0.46	13.75	0.02	0.10	9.98	2.47	0.03	0.02	0.00	0.00	97.14	1.39	0.00	0.61	2.00	3.13	0.87	4.00	0.29	0.04	0.00	0.00	1.60	0.00	1.09	0.03	3.05	0.00	0.02	0.99	1.01
		ID19A`_C2_bt 2	40.31	1.47	12.62	16.45	0.84	13.93	0.00	0.04	10.08	2.62	0.02	0.00	0.03	0.02	98.42	1.36	0.00	0.64	2.00	3.11	0.89	4.00	0.25	0.09	0.00	0.00	1.60	0.00	1.06	0.05	3.06	0.00	0.01	0.99	1.00
		ID19A`_C3_bt 1	40.34	1.01	12.43	16.36	0.60	13.97	0.03	0.09	9.86	2.48	0.07	0.09	0.00	0.00	97.34	1.38	0.01	0.61	2.00	3.13	0.87	4.00	0.27	0.06	0.01	0.00	1.62	0.00	1.06	0.04	3.05	0.00	0.01	0.98	0.99
		ID19A`_C2_bt 1	40.62	0.82	12.40	16.75	0.68	13.74	0.00	0.08	9.99	2.65	0.00	0.00	0.02	0.02	97.87	1.35	0.00	0.65	2.00	3.15	0.85	4.00	0.28	0.05	0.00	0.01	1.59	0.00	1.09	0.04	3.06	0.00	0.01	0.99	1.00
		LA-14_C4_bt1	36.23	3.31	16.72	23.49	0.32	6.68	0.01	0.15	9.87	0.82	0.07	0.10	0.09	0.00	97.87	1.79	0.01	0.20	2.00	2.80	1.20	4.00	0.33	0.19	0.01	0.01	0.77	0.00	1.52	0.02	2.84	0.00	0.02	0.97	1.00
	La Asunta	LA-14_C5_bt2	35.54	3.10	16.51	24.06	0.44	7.00	0.00	0.09	9.88	0.88	0.04	0.00	0.01	0.00	97.64	1.78	0.01	0.22	2.00	2.77	1.23	4.00	0.29	0.18	0.00	0.01	0.81	0.00	1.57	0.03	2.89	0.00	0.01	0.98	1.00
		LA-14_C4_bt2	35.81	2.86	16.50	24.61	0.09	6.81	0.00	0.12	9.44	0.89	0.07	0.07	0.02	0.06	97.35	1.77	0.01	0.22	2.00	2.80	1.20	4.00	0.32	0.17	0.00	0.00	0.79	0.00	1.61	0.01	2.90	0.00	0.02	0.94	0.96

Domain	Pluton	Analysis	SiO2	TiO2	Al2O3	FeO	MnO	MgO	CaO	Na2O	K2O	F	Cl	Cr2O3	V2O3	NiO	Total	OH	Cl	F	ΣOH	Si	Al	ΣT	Al	Ti	Cr	V	Mg	Ni	Fe2+	Mn	ΣM	Ca	Na	K	ΣI
		LA-14_C1_bt1	35.95	3.10	16.46	23.47	0.17	6.47	0.02	0.18	9.87	0.64	0.07	0.00	0.06	0.06	96.52	1.83	0.01	0.16	2.00	2.81	1.19	4.00	0.33	0.18	0.00	0.00	0.75	0.00	1.54	0.01	2.82	0.00	0.03	0.99	1.01
		LA-14_C3_bt2	35.63	3.09	16.44	23.26	0.32	6.67	0.00	0.04	9.83	0.71	0.05	0.00	0.08	0.01	96.13	1.82	0.01	0.18	2.00	2.80	1.20	4.00	0.33	0.18	0.00	0.01	0.78	0.00	1.53	0.02	2.85	0.00	0.01	0.99	0.99
		LA-14_C3_bt1	36.48	3.05	16.32	23.60	0.34	7.05	0.02	0.11	9.54	0.85	0.05	0.00	0.04	0.04	97.48	1.78	0.01	0.21	2.00	2.83	1.17	4.00	0.32	0.18	0.00	0.00	0.82	0.00	1.53	0.02	2.87	0.00	0.02	0.94	0.96
		LA-14_C4_bt3	35.76	2.99	16.27	22.88	0.43	6.72	0.01	0.29	9.63	0.88	0.10	0.00	0.04	0.00	96.01	1.77	0.01	0.22	2.00	2.82	1.18	4.00	0.34	0.18	0.00	0.00	0.79	0.00	1.51	0.03	2.85	0.00	0.04	0.97	1.02
		LA-14_C1_bt2	35.89	3.67	16.26	22.92	0.28	6.42	0.00	0.24	9.61	0.82	0.08	0.02	0.06	0.00	96.27	1.79	0.01	0.20	2.00	2.82	1.18	4.00	0.32	0.22	0.00	0.00	0.75	0.00	1.50	0.02	2.82	0.00	0.04	0.96	1.00
		LA-14_C4_bt4	36.05	2.97	16.19	22.85	0.35	6.88	0.00	0.20	9.60	0.92	0.07	0.00	0.06	0.00	96.15	1.76	0.01	0.23	2.00	2.84	1.16	4.00	0.34	0.18	0.00	0.00	0.81	0.00	1.50	0.02	2.85	0.00	0.03	0.96	0.99
		LA-14_C2_bt1	35.68	3.73	16.16	22.97	0.26	6.78	0.00	0.20	9.79	0.79	0.09	0.00	0.09	0.00	96.55	1.79	0.01	0.20	2.00	2.80	1.20	4.00	0.29	0.22	0.00	0.01	0.79	0.00	1.51	0.02	2.83	0.00	0.03	0.98	1.01
		LA-14_C5_bt3	35.62	3.80	16.15	24.45	0.19	6.12	0.03	0.12	9.77	0.78	0.08	0.00	0.03	0.01	97.13	1.80	0.01	0.19	2.00	2.79	1.21	4.00	0.28	0.22	0.00	0.00	0.71	0.00	1.60	0.01	2.84	0.00	0.02	0.98	1.00
		LA-14_C1_bt3	36.36	3.59	16.11	23.05	0.38	6.96	0.00	0.12	9.51	0.90	0.06	0.00	0.07	0.00	97.10	1.77	0.01	0.22	2.00	2.83	1.17	4.00	0.31	0.21	0.00	0.00	0.81	0.00	1.50	0.03	2.85	0.00	0.02	0.94	0.96
		LA-14_C5_bt1	32.53	2.81	15.62	23.69	0.26	7.12	0.02	0.20	9.67	0.88	0.05	0.00	0.06	0.00	92.99	1.76	0.01	0.23	2.00	2.70	1.30	4.00	0.22	0.18	0.01	0.00	0.88	0.00	1.64	0.02	2.95	0.00	0.03	1.02	1.06
	Nocemano	SM07_C5_bt 2	36.81	2.63	15.33	23.25	0.17	7.12	0.04	0.06	9.44	1.24	0.27	0.07	0.11	0.00	96.55	1.65	0.01	0.31	2.00	2.91	1.09	4.00	0.34	0.16	0.00	0.01	0.84	0.00	1.54	0.01	2.90	0.00	0.01	0.95	0.97
		SM07_C3_bt 1	36.43	3.53	15.31	24.12	0.31	6.48	0.02	0.05	9.83	0.96	0.26	0.01	0.14	0.00	97.44	1.73	0.03	0.24	2.00	2.86	1.14	4.00	0.28	0.21	0.01	0.00	0.76	0.00	1.58	0.02	2.86	0.00	0.01	0.98	0.99
		SM07_C4_bt 1	32.95	2.21	15.15	28.12	0.10	6.90	0.06	0.04	6.54	0.52	0.19	0.00	0.11	0.00	93.25	1.84	0.03	0.14	2.00	2.71	1.29	4.00	0.18	0.14	0.01	0.01	0.85	0.00	1.93	0.01	3.12	0.00	0.05	0.69	0.74
		SM07_C1_bt 3	35.98	3.09	14.93	24.23	0.16	6.92	0.05	0.14	9.96	0.90	0.23	0.02	0.12	0.00	96.72	1.74	0.03	0.22	2.00	2.85	1.15	4.00	0.24	0.18	0.00	0.01	0.82	0.00	1.61	0.01	2.87	0.00	0.02	1.01	1.03
		SM07_C2_bt 1	33.22	2.19	14.90	27.92	0.32	7.25	0.09	0.13	6.59	0.54	0.21	0.00	0.11	0.00	93.66	1.83	0.03	0.14	2.00	2.72	1.28	4.00	0.16	0.14	0.00	0.01	0.89	0.00	1.91	0.02	3.13	0.01	0.05	0.69	0.75
		SM07_C1_bt 2	36.85	3.33	14.82	23.59	0.24	6.54	0.03	0.11	9.80	0.90	0.27	0.08	0.12	0.00	96.67	1.74	0.04	0.22	2.00	2.90	1.10	4.00	0.28	0.20	0.00	0.01	0.77	0.00	1.56	0.02	2.83	0.00	0.02	0.99	1.00
		SM07_C5_bt 1	36.62	3.33	14.67	23.89	0.17	6.43	0.05	0.16	9.51	1.15	0.23	0.03	0.12	0.00	96.34	1.68	0.03	0.29	2.00	2.91	1.09	4.00	0.29	0.20	0.00	0.01	0.76	0.00	1.59	0.01	2.86	0.00	0.02	0.96	0.99
		SM07_C5_bt 3	35.97	4.07	14.52	24.41	0.21	6.64	0.04	0.23	9.80	1.06	0.27	0.11	0.18	0.00	97.41	1.70	0.04	0.26	2.00	2.85	1.15	4.00	0.20	0.24	0.01	0.01	0.78	0.00	1.61	0.01	2.86	0.00	0.04	0.99	1.03
		SM07_C1_bt 1	34.51	3.03	14.44	23.61	0.06	6.51	0.13	0.27	9.20	0.84	0.27	0.00	0.08	0.00	93.05	1.74	0.04	0.22	2.00	2.84	1.16	4.00	0.24	0.19	0.00	0.01	0.81	0.00	1.63	0.01	2.88	0.01	0.04	0.97	1.02
		SM07_C3_bt 2	34.12	3.13	14.06	25.13	0.09	6.01	0.02	0.15	9.07	0.64	0.29	0.00	0.07	0.02	92.79	1.79	0.04	0.17	2.00	2.83	1.17	4.00	0.20	0.20	0.00	0.00	0.74	0.00	1.74	0.01	2.90	0.00	0.02	0.96	0.99
Southern	Las Tojas	ID-08_C5_bt4	37.62	3.08	17.74	20.20	0.44	7.45	0.04	0.15	9.75	1.28	0.04	0.04	0.08	0.00	97.99	1.69	0.00	0.31	2.00	2.87	1.13	4.00	0.46	0.18	0.01	0.00	0.85	0.00	1.29	0.03	2.82	0.00	0.02	0.95	0.97
		ID-08_C2_bt8	36.91	3.19	16.11	22.28	0.45	7.00	0.00	0.20	9.45	1.45	0.05	0.00	0.03	0.02	97.12	1.63	0.01	0.36	2.00	2.89	1.11	4.00	0.38	0.19	0.00	0.00	0.82	0.00	1.46	0.03	2.87	0.00	0.03	0.94	0.97
		ID-08_C5_bt5	35.29	2.33	16.08	21.43	0.33	6.69	0.02	0.15	8.76	1.01	0.04	0.00	0.01	0.04	92.25	1.73	0.00	0.26	2.00	2.88	1.12	4.00	0.42	0.14	0.00	0.01	0.81	0.00	1.46	0.02	2.87	0.00	0.02	0.91	0.94
		ID-08_C5_bt8	39.03	1.84	15.86	19.07	0.38	7.97	0.05	0.19	8.39	1.00	0.10	0.00	0.04	0.00	93.93	1.74	0.01	0.25	2.00	3.05	0.95	4.00	0.50	0.11	0.00	0.00	0.93	0.00	1.24	0.03	2.81	0.00	0.03	0.84	0.87
		ID-08_C5_bt1	35.85	2.74	15.78	21.65	0.54	7.09	0.06	0.19	9.14	1.17	0.04	0.00	0.05	0.00	94.30	1.70	0.01	0.30	2.00	2.88	1.12	4.00	0.37	0.17	0.00	0.00	0.85	0.00	1.45	0.04	2.87	0.01	0.03	0.94	0.97
		ID-08_C2_bt3	35.42	2.80	15.25	22.63	0.33	7.70	0.00	0.16	9.60	1.58	0.05	0.00	0.07	0.00	95.65	1.59	0.01	0.40	2.00	2.85	1.15	4.00	0.30	0.17	0.00	0.00	0.92	0.00	1.52	0.02	2.95	0.00	0.03	0.99	1.01
		ID-08_C2_bt7	34.34	2.62	15.22	23.19	0.38	7.11	0.07	0.28	9.47	1.23	0.06	0.00	0.09	0.00	94.18	1.67	0.01	0.32	2.00	2.81	1.19	4.00	0.28	0.16	0.01	0.01	0.87	0.00	1.59	0.03	2.93	0.01	0.04	0.99	1.04
		ID-08_C4_bt2	34.70	3.04	15.11	22.37	0.59	7.23	0.00	0.28	9.64	1.40	0.07	0.00	0.13	0.00	94.58	1.63	0.01	0.36	2.00	2.83	1.17	4.00	0.28	0.19	0.00	0.01	0.88	0.00	1.52	0.04	2.92	0.00	0.04	1.00	1.05
		ID-08_C2_bt2	36.23	2.77	14.74	22.12	0.30	7.25	0.06	0.24	9.19	0.79	0.08	0.02	0.08	0.04	93.91	1.79	0.01	0.20	2.00	2.90	1.10	4.00	0.30	0.17	0.00	0.00	0.87	0.00	1.48	0.02	2.84	0.00	0.04	0.94	0.98

Domain	Pluton	Analysis	SiO2	TiO2	Al2O3	FeO	MnO	MgO	CaO	Na2O	K2O	F	Cl	Cr2O3	V2O3	NiO	Total	OH	Cl	F	ΣOH	Si	Al	ΣT	Al	Ti	Cr	V	Mg	Ni	Fe2+	Mn	ΣM	Ca	Na	K	ΣI
		ID-08_C4_ms2	34.72	3.40	14.72	22.34	0.49	7.48	0.06	0.21	9.53	1.47	0.11	0.07	0.11	0.05	94.76	1.60	0.02	0.38	2.00	2.83	1.17	4.00	0.24	0.21	0.00	0.01	0.91	0.00	1.52	0.03	2.93	0.01	0.03	0.99	1.03
		ID-08_C2_bt4	34.80	1.05	14.53	24.48	0.21	6.49	0.13	0.54	7.41	0.77	0.16	0.06	0.06	0.00	90.69	1.77	0.02	0.20	2.00	2.91	1.09	4.00	0.35	0.07	0.00	0.00	0.81	0.00	1.71	0.01	2.96	0.01	0.09	0.79	0.89
		TAP-02A_C4_bt3	37.16	0.94	15.00	17.58	0.40	11.42	0.02	0.11	9.64	1.16	0.02	0.02	0.07	0.00	93.54	1.71	0.00	0.29	2.00	2.94	1.06	4.00	0.34	0.06	0.00	0.00	1.35	0.00	1.16	0.03	2.95	0.00	0.02	0.97	0.99
		TAP-02A_C4_bt4	38.07	1.39	14.99	17.39	0.26	11.57	0.01	0.13	9.58	1.12	0.02	0.00	0.11	0.01	94.65	1.72	0.00	0.28	2.00	2.96	1.04	4.00	0.34	0.08	0.00	0.01	1.34	0.00	1.13	0.02	2.92	0.00	0.02	0.95	0.97
		TAP-02A_C3_bt1	37.12	1.01	14.96	17.43	0.21	11.49	0.02	0.17	9.29	1.02	0.04	0.00	0.12	0.06	92.93	1.74	0.01	0.26	2.00	2.94	1.06	4.00	0.34	0.06	0.00	0.01	1.36	0.00	1.16	0.01	2.94	0.00	0.03	0.94	0.97
		TAP-02A_C3_bt3	37.15	1.70	14.91	17.55	0.29	11.44	0.01	0.08	9.32	1.18	0.01	0.03	0.04	0.06	93.77	1.71	0.00	0.29	2.00	2.93	1.07	4.00	0.32	0.10	0.00	0.00	1.34	0.00	1.16	0.02	2.95	0.00	0.01	0.94	0.95
		TAP-02A_C4_bt5	37.31	1.39	14.77	18.06	0.23	11.51	0.03	0.21	9.76	1.13	0.02	0.14	0.12	0.04	94.70	1.72	0.00	0.28	2.00	2.93	1.07	4.00	0.29	0.08	0.01	0.01	1.35	0.00	1.18	0.02	2.94	0.00	0.03	0.98	1.01
		TAP-02A_C3_bt2	37.47	2.03	14.74	18.19	0.32	11.34	0.00	0.13	9.55	1.20	0.03	0.00	0.10	0.05	95.15	1.70	0.00	0.30	2.00	2.93	1.07	4.00	0.28	0.12	0.00	0.01	1.32	0.00	1.19	0.02	2.94	0.00	0.02	0.95	0.97
		TAP-02A_C4_bt6	36.96	1.39	14.53	18.05	0.33	11.40	0.00	0.15	9.52	1.13	0.04	0.03	0.06	0.00	93.59	1.71	0.00	0.28	2.00	2.93	1.07	4.00	0.29	0.08	0.00	0.00	1.35	0.00	1.20	0.02	2.95	0.00	0.02	0.96	0.99
		TAP-02A_C4_bt1	37.18	1.30	14.51	18.18	0.36	10.90	0.01	0.24	9.58	1.04	0.06	0.03	0.12	0.00	93.50	1.73	0.01	0.26	2.00	2.95	1.05	4.00	0.31	0.08	0.00	0.01	1.29	0.00	1.21	0.02	2.92	0.00	0.04	0.97	1.01
		TAP-02A_C2_bt3	36.95	1.50	14.50	18.19	0.37	11.08	0.02	0.12	9.50	1.05	0.00	0.08	0.12	0.04	93.50	1.74	0.00	0.26	2.00	2.93	1.07	4.00	0.29	0.09	0.01	0.01	1.31	0.00	1.21	0.02	2.93	0.00	0.02	0.96	0.98
	Nomoca	TAP-02A_C4_bt2	37.57	1.90	14.49	17.32	0.29	11.18	0.44	0.16	9.40	1.09	0.04	0.02	0.07	0.05	94.01	1.73	0.01	0.27	2.00	2.95	1.05	4.00	0.29	0.11	0.00	0.00	1.31	0.00	1.14	0.02	2.88	0.04	0.02	0.94	1.00
		TAP-02A_C3_bt5	36.76	1.06	14.43	17.75	0.35	11.11	0.02	0.27	9.51	1.04	0.07	0.25	0.14	0.00	92.74	1.73	0.01	0.26	2.00	2.94	1.06	4.00	0.30	0.06	0.02	0.01	1.33	0.00	1.19	0.02	2.93	0.00	0.04	0.97	1.01
		TAP-02A_C3_bt4	37.04	1.38	14.41	17.90	0.40	11.31	0.03	0.14	9.54	1.08	0.04	0.11	0.09	0.03	93.51	1.72	0.01	0.27	2.00	2.94	1.06	4.00	0.29	0.08	0.01	0.01	1.34	0.00	1.19	0.03	2.94	0.00	0.02	0.97	0.99
		TAP-02A_C2_bt1	36.09	1.65	14.26	17.36	0.40	11.25	0.00	0.07	9.18	1.31	0.00	0.04	0.13	0.02	91.76	1.66	0.00	0.34	2.00	2.93	1.07	4.00	0.29	0.10	0.00	0.01	1.36	0.00	1.18	0.03	2.97	0.00	0.01	0.95	0.96
		TAP-02A_C2_bt2	36.81	1.48	14.24	17.53	0.35	11.25	0.01	0.12	9.14	1.27	0.03	0.08	0.08	0.00	92.39	1.67	0.00	0.32	2.00	2.96	1.04	4.00	0.31	0.09	0.01	0.01	1.35	0.00	1.18	0.02	2.96	0.00	0.02	0.94	0.96
		TAP-02A_C2_bt4	37.25	1.43	14.14	17.96	0.32	11.40	0.01	0.16	9.25	1.18	0.03	0.26	0.09	0.02	93.48	1.70	0.00	0.30	2.00	2.96	1.04	4.00	0.28	0.09	0.02	0.01	1.35	0.00	1.19	0.02	2.95	0.00	0.02	0.94	0.96
		TAP-02A_C3_bt6	36.49	0.93	14.12	17.47	0.31	11.21	0.03	0.13	9.48	1.18	0.04	0.05	0.08	0.01	91.53	1.69	0.00	0.30	2.00	2.96	1.04	4.00	0.32	0.06	0.00	0.01	1.36	0.00	1.19	0.02	2.95	0.00	0.02	0.98	1.01
		TAP-02A_C1_bt2	36.28	1.26	14.10	18.85	0.43	10.85	0.02	0.12	9.36	1.05	0.00	0.09	0.06	0.00	92.47	1.73	0.00	0.27	2.00	2.93	1.07	4.00	0.27	0.08	0.01	0.00	1.31	0.00	1.27	0.03	2.96	0.00	0.02	0.96	0.98
		TAP-02A_C1_bt1	36.74	1.45	13.96	18.84	0.36	11.27	0.00	0.13	9.37	1.11	0.02	0.08	0.11	0.02	93.45	1.72	0.00	0.28	2.00	2.93	1.07	4.00	0.25	0.09	0.01	0.01	1.34	0.00	1.26	0.02	2.97	0.00	0.02	0.95	0.97
		ID-02_C1_bt1	36.23	4.70	13.31	23.81	0.01	7.89	0.00	0.18	9.36	0.82	0.09	0.00	0.24	0.07	96.69	1.79	0.01	0.20	2.00	2.85	1.15	4.00	0.08	0.28	0.00	0.02	0.92	0.00	1.57	0.00	2.87	0.00	0.03	0.94	0.97
	San Pablo	ID-02_C5_bt4	36.30	4.71	13.14	23.88	0.13	7.72	0.02	0.11	9.60	0.88	0.07	0.00	0.12	0.06	96.75	1.77	0.01	0.22	2.00	2.86	1.14	4.00	0.08	0.28	0.00	0.01	0.91	0.00	1.57	0.01	2.87	0.00	0.02	0.97	0.98

Domain	Pluton	Analysis	SiO2	TiO2	Al2O3	FeO	MnO	MgO	CaO	Na2O	K2O	F	Cl	Cr2O3	V2O3	NiO	Total	OH	Cl	F	ΣOH	Si	Al	ΣT	Al	Ti	Cr	V	Mg	Ni	Fe2+	Mn	ΣM	Ca	Na	K	ΣI
		ID-02_C5_bt3	36.16	5.06	13.09	23.72	0.11	7.50	0.03	0.11	9.50	0.88	0.06	0.03	0.11	0.00	96.36	1.77	0.01	0.22	2.00	2.86	1.14	4.00	0.08	0.30	0.00	0.01	0.88	0.00	1.57	0.01	2.85	0.00	0.02	0.96	0.98
		ID-02_C4_bt2	36.71	5.73	13.07	23.84	0.11	7.78	0.04	0.12	9.43	0.94	0.08	0.07	0.15	0.01	98.07	1.76	0.01	0.23	2.00	2.85	1.15	4.00	0.05	0.33	0.00	0.01	0.90	0.00	1.55	0.01	2.85	0.00	0.02	0.93	0.96
		ID-02_C2_bt1	36.63	4.65	13.01	23.19	0.09	8.05	0.04	0.17	9.37	0.90	0.08	0.00	0.18	0.03	96.38	1.76	0.01	0.22	2.00	2.89	1.11	4.00	0.09	0.28	0.00	0.01	0.95	0.00	1.53	0.01	2.86	0.00	0.03	0.94	0.97
		ID-02_C3_bt4	36.35	5.13	12.98	23.66	0.05	7.31	0.04	0.19	9.47	0.79	0.08	0.00	0.11	0.03	96.19	1.79	0.01	0.20	2.00	2.87	1.13	4.00	0.08	0.31	0.00	0.01	0.86	0.00	1.56	0.00	2.82	0.00	0.03	0.95	0.99
		ID-02_C3_bt3	37.03	4.92	12.95	24.15	0.07	7.55	0.00	0.12	9.65	0.89	0.06	0.00	0.13	0.00	97.53	1.77	0.01	0.22	2.00	2.89	1.11	4.00	0.08	0.29	0.00	0.01	0.88	0.00	1.58	0.00	2.84	0.00	0.02	0.96	0.98
		ID-02_C5_bt1	36.22	5.09	12.88	23.47	0.12	7.67	0.00	0.14	9.78	0.83	0.06	0.03	0.16	0.00	96.45	1.78	0.01	0.21	2.00	2.86	1.14	4.00	0.06	0.30	0.00	0.01	0.90	0.00	1.55	0.01	2.84	0.00	0.02	0.98	1.01
		ID-02_C3_bt2	37.19	5.07	12.85	23.93	0.09	7.49	0.02	0.15	9.40	0.86	0.07	0.01	0.15	0.08	97.36	1.78	0.01	0.21	2.00	2.90	1.10	4.00	0.08	0.30	0.00	0.01	0.87	0.01	1.56	0.01	2.84	0.00	0.02	0.94	0.96
		ID-02_C1_bt3	36.34	5.20	12.82	24.06	0.17	7.41	0.03	0.32	9.39	0.78	0.11	0.03	0.16	0.07	96.89	1.79	0.02	0.19	2.00	2.86	1.14	4.00	0.05	0.31	0.00	0.01	0.87	0.00	1.58	0.01	2.84	0.00	0.05	0.94	0.99
		ID-02_C3_bt1	36.70	4.78	12.81	23.31	0.10	7.56	0.02	0.14	9.20	0.80	0.09	0.01	0.13	0.00	95.67	1.79	0.01	0.20	2.00	2.91	1.09	4.00	0.10	0.28	0.00	0.01	0.89	0.00	1.54	0.01	2.84	0.00	0.02	0.93	0.95
		ID-02_C1_bt2	35.58	5.04	12.64	23.45	0.08	7.52	0.00	0.17	9.26	0.76	0.10	0.00	0.15	0.00	94.74	1.79	0.01	0.19	2.00	2.86	1.14	4.00	0.05	0.30	0.00	0.01	0.90	0.00	1.58	0.01	2.85	0.00	0.03	0.95	0.97
		ID-02_C2_bt2	35.87	4.85	12.57	22.78	0.11	7.95	0.05	0.08	9.46	0.91	0.11	0.00	0.13	0.00	94.87	1.75	0.01	0.23	2.00	2.88	1.12	4.00	0.07	0.29	0.00	0.01	0.95	0.00	1.53	0.01	2.86	0.00	0.01	0.97	0.99
		ID-02_C2_bt3	36.32	4.83	12.50	23.45	0.11	8.27	0.03	0.17	8.90	0.89	0.08	0.04	0.13	0.03	95.75	1.77	0.01	0.22	2.00	2.88	1.12	4.00	0.05	0.29	0.00	0.01	0.98	0.00	1.56	0.01	2.89	0.00	0.03	0.90	0.93
		ID-06A_C1_bt3	35.97	2.93	15.89	21.19	1.33	7.26	0.06	0.17	9.29	1.81	0.11	0.00	0.09	0.05	96.14	1.53	0.01	0.46	2.00	2.88	1.12	4.00	0.38	0.18	0.00	0.01	0.87	0.00	1.42	0.09	2.94	0.01	0.03	0.95	0.98
		ID-06A_C4_bt4	35.20	2.71	15.87	21.65	1.17	7.06	0.00	0.14	9.61	1.87	0.09	0.01	0.05	0.00	95.42	1.51	0.01	0.48	2.00	2.86	1.14	4.00	0.38	0.17	0.00	0.00	0.86	0.00	1.47	0.08	2.95	0.00	0.02	1.00	1.02
		ID-06A_C1_bt2	36.24	2.58	15.76	21.59	1.34	7.57	0.03	0.17	9.77	1.80	0.11	0.09	0.03	0.00	97.08	1.53	0.01	0.45	2.00	2.88	1.12	4.00	0.36	0.15	0.01	0.00	0.90	0.00	1.44	0.09	2.94	0.00	0.03	0.99	1.02
	Señoritas	ID-06A_C4_bt2	34.98	2.57	15.72	21.21	1.33	7.33	0.01	0.14	9.62	1.92	0.09	0.00	0.05	0.06	95.02	1.49	0.01	0.50	2.00	2.86	1.14	4.00	0.37	0.16	0.00	0.00	0.89	0.00	1.45	0.09	2.97	0.00	0.02	1.00	1.03
		ID-06A_C4_bt1	35.27	2.91	15.71	21.10	1.13	7.08	0.03	0.16	9.69	1.80	0.09	0.02	0.05	0.05	95.09	1.52	0.01	0.46	2.00	2.86	1.14	4.00	0.37	0.18	0.00	0.00	0.86	0.00	1.43	0.08	2.92	0.00	0.03	1.00	1.03
		ID-06A_C4_bt3	35.32	3.15	15.48	21.69	1.19	7.55	0.02	0.06	9.92	1.79	0.09	0.00	0.00	0.03	96.36	1.53	0.01	0.45	2.00	2.84	1.16	4.00	0.31	0.19	0.00	0.01	0.90	0.00	1.46	0.08	2.95	0.00	0.01	1.02	1.03
		ID-06A_C1_bt1	35.76	2.76	15.47	21.32	1.47	7.54	0.01	0.21	9.82	1.78	0.08	0.05	0.05	0.00	96.30	1.54	0.01	0.45	2.00	2.87	1.13	4.00	0.33	0.17	0.00	0.00	0.90	0.00	1.43	0.10	2.94	0.00	0.03	1.01	1.04
		TAS-15A_C5_bt1	38.17	1.09	16.45	18.68	0.73	9.84	0.03	0.14	9.18	1.74	0.01	0.18	0.04	0.00	96.27	1.57	0.00	0.43	2.00	2.97	1.03	4.00	0.47	0.06	0.01	0.00	1.14	0.00	1.21	0.05	2.96	0.00	0.02	0.91	0.93
	Tasseoro	TAS-15A_C1_bt1	36.86	1.41	14.70	20.83	0.72	10.02	0.05	0.33	9.85	1.31	0.05	0.00	0.00	0.05	96.19	1.67	0.01	0.33	2.00	2.91	1.09	4.00	0.28	0.08	0.00	0.00	1.18	0.00	1.37	0.05	2.97	0.00	0.05	0.99	1.05
		TAS-15A_C1_bt4	36.85	0.92	14.63	20.18	0.68	10.27	0.04	0.22	9.91	1.42	0.05	0.07	0.02	0.02	95.26	1.64	0.01	0.36	2.00	2.93	1.07	4.00	0.31	0.05	0.00	0.00	1.22	0.00	1.34	0.05	2.98	0.00	0.03	1.01	1.04
		TAS-15A_C1_bt3	36.50	1.15	14.27	20.74	0.50	10.39	0.03	0.15	9.49	1.27	0.04	0.00	0.00	0.08	94.61	1.67	0.01	0.32	2.00	2.92	1.08	4.00	0.27	0.07	0.00	0.00	1.24	0.00	1.39	0.03	3.00	0.00	0.02	0.97	0.99

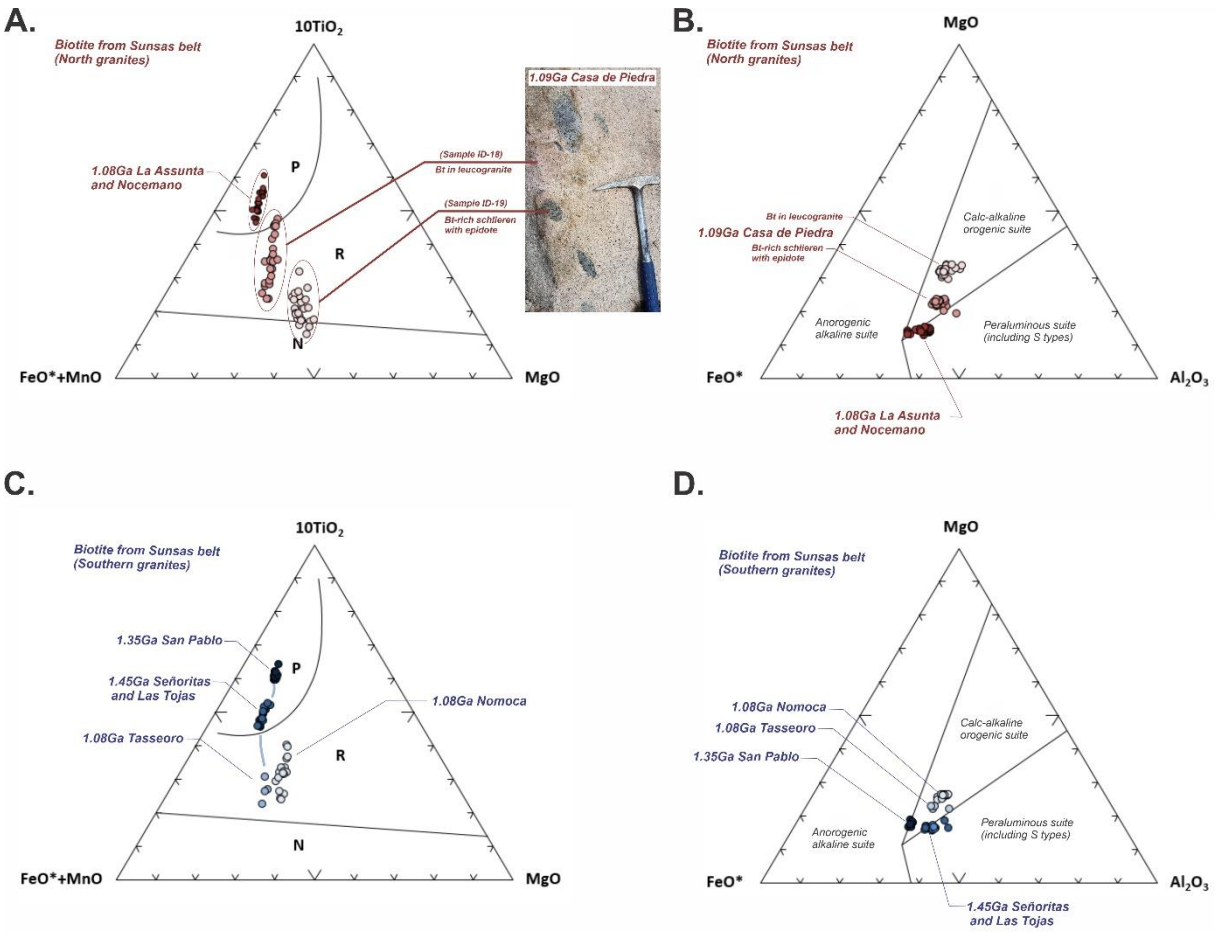

Figure 4.5. Mineral chemistry analyses in biotite from southern and northern granites.

4.5.1.2 Feldspar composition

Plagioclase from northern granites domain

Plagioclase crystals from northern granites (LA14, SM07, and ID18 samples) display hypidiomorphic texture to anhedral shapes. Some crystals exhibit sharply defined polysynthetic twinning occasionally combined with Carlsbad. Less common, myrmekitic texture occurs as vermicular intergrowth of quartz. In addition, most crystals present sericitization reactions in their central portion to form white mica.

Northern plagioclase analyses show composition of albite to andesine. Casa de Piedra Bt-rich schlieren comprises plagioclase with higher Na contents (18.73-19.33 wt.% Na_2O, $An_{94–95}$) (Table 4.3, Fig. 4.6A). Progressive increase in Ca and further decrease in Na contents (14.92-17.63 wt.% CaO and 14.92-17.63 wt.% Na_2O, $An_{74–87}$) marks the oligoclase in the leucocratic portion. Higher Ca contents comprise andesine of the La Asunta (18.73-19.33 wt.% Na_2O, $An_{94–95}$) and Nocemano (18.73-19.33 wt.% Na_2O, $An_{94–95}$).

Plagioclase from southern granites domain

Plagioclase from southern granites occurs as hypidiomorphic to anhedral crystals with exception of the San Pablo granite, which has subhedric phenocrysts. Polysynthetic twinning was not well preserved due to intense sericitization. Tiny inclusions of epidote and zoisite mark calcic portions in plagioclase from the Nomoca granite. Myrmekitic texture is common at the mineral edges as vermicular intergrowth of quartz.

Southern plagioclase analyses show a wide range of chemical compositions. Higher Na contents (18.73-19.33 wt.% Na_2O) characterize albite from the Tasseoro granite (Table 4.3, Fig. 4.6A). Increase of Ca contents differs oligoclase from Señoritas (14.92-17.63 wt.% CaO) and Las Tojas (14.92-17.63 wt.% CaO) granites. San Pablo monzogranite has andesine with highest Ca content (14.92-17.63 wt.% CaO with) and Tauca has andesine with 14.92-17.63 wt.% CaO and 14.92-17.63 wt.% Na_2O.

Table 4-3. Plagiclase composition from Sunsas belt (normalization based on 8 oxygens).

Domain	Pluton	SiO2	TiO2	Al2O3	FeO	MnO	MgO	CaO	Na2O	K2O	Cr2O3	V2O3	NiO	Total	% An	% Ab	% Or
Northern	Casa de Piedra	66.82	0.00	20.10	0.07	0.00	0.00	2.13	10.53	0.23	0.06	0.00	0.00	99.94	9.92	88.81	1.27
		67.76	0.00	20.44	0.13	0.02	0.02	2.25	10.63	0.17	0.01	0.02	0.00	101.44	10.39	88.67	0.94
		67.71	0.00	19.41	0.24	0.06	0.04	1.18	10.73	0.16	0.00	0.00	0.00	99.53	5.70	93.41	0.89
		67.38	0.07	21.50	0.03	0.01	0.00	2.00	9.15	0.16	0.07	0.00	0.04	100.40	10.65	88.37	0.98
		68.49	0.05	21.21	0.06	0.05	0.00	1.46	9.80	0.13	0.00	0.02	0.00	101.27	7.52	91.67	0.81
		67.33	0.00	20.47	0.07	0.01	0.00	2.24	10.93	0.12	0.00	0.04	0.02	101.22	10.09	89.25	0.66
		68.04	0.09	20.66	0.07	0.01	0.01	2.44	10.90	0.11	0.00	0.00	0.00	102.34	10.94	88.45	0.61
		67.25	0.13	21.38	0.08	0.05	0.02	2.01	9.54	0.10	0.00	0.02	0.03	100.62	10.39	89.00	0.61
		68.33	0.09	20.30	0.02	0.01	0.00	1.03	9.80	0.10	0.00	0.00	0.00	99.69	5.44	93.93	0.62
		68.88	0.04	20.53	0.01	0.00	0.03	1.99	10.89	0.10	0.01	0.00	0.00	102.48	9.12	90.35	0.53
		69.23	0.00	19.31	0.00	0.03	0.00	0.97	11.66	0.09	0.00	0.01	0.03	101.32	4.36	95.14	0.50
		67.09	0.07	21.50	0.04	0.07	0.01	1.88	9.56	0.09	0.01	0.01	0.05	100.37	9.74	89.70	0.56
		68.04	0.17	20.64	0.05	0.00	0.01	1.41	9.89	0.09	0.00	0.02	0.00	100.31	7.27	92.20	0.53
		68.29	0.01	19.90	0.01	0.00	0.00	0.84	10.25	0.08	0.01	0.00	0.01	99.41	4.29	95.23	0.48
		66.99	0.09	21.55	0.02	0.00	0.02	2.10	8.89	0.06	0.00	0.00	0.05	99.78	11.51	88.08	0.42
		68.16	0.10	19.99	0.06	0.00	0.00	1.02	9.98	0.06	0.00	0.05	0.00	99.42	5.31	94.30	0.39
		69.09	0.00	20.47	0.00	0.04	0.00	0.77	10.20	0.05	0.04	0.03	0.02	100.70	3.98	95.72	0.30
		67.44	0.00	21.47	0.01	0.00	0.00	2.21	9.18	0.04	0.00	0.00	0.01	100.35	11.70	88.04	0.25
	La Asunta	64.64	0.00	23.28	0.02	0.02	0.00	4.65	8.55	0.20	0.00	0.01	0.03	101.40	22.84	75.97	1.19
		64.39	0.13	22.85	0.01	0.00	0.00	4.20	8.69	0.19	0.06	0.02	0.00	100.55	20.85	78.01	1.15
		64.86	0.00	22.97	0.01	0.02	0.00	4.62	8.65	0.19	0.00	0.06	0.00	101.37	22.53	76.35	1.13
		64.86	0.00	22.92	0.00	0.04	0.00	4.34	8.93	0.18	0.00	0.01	0.02	101.30	20.93	78.05	1.02
		64.59	0.00	23.19	0.00	0.00	0.00	4.67	8.98	0.18	0.06	0.01	0.00	101.68	22.09	76.92	0.99
		64.43	0.00	23.36	0.07	0.06	0.00	4.42	9.18	0.17	0.00	0.00	0.00	101.71	20.82	78.22	0.96
	Nocemano	62.68	0.04	23.17	0.06	0.00	0.01	5.73	8.53	0.40	0.02	0.01	0.00	100.66	26.48	71.33	2.19
		63.77	0.00	23.20	0.10	0.02	0.00	5.39	8.77	0.34	0.01	0.01	0.03	101.65	24.88	73.25	1.87
		63.40	0.00	23.30	0.01	0.00	0.00	5.59	8.62	0.31	0.15	0.04	0.00	101.41	25.93	72.36	1.71
		63.83	0.08	23.17	0.08	0.03	0.00	5.59	8.86	0.29	0.03	0.01	0.00	101.95	25.44	72.97	1.59
		63.04	0.00	23.62	0.05	0.12	0.00	5.54	8.81	0.26	0.00	0.00	0.00	101.44	25.43	73.15	1.42
		63.64	0.00	23.16	0.06	0.00	0.02	5.41	8.81	0.25	0.00	0.00	0.00	101.36	25.00	73.63	1.36
		64.59	0.00	23.36	0.03	0.00	0.00	5.05	9.28	0.12	0.00	0.02	0.05	102.49	22.98	76.38	0.63

Domain	Pluton	SiO2	TiO2	Al2O3	FeO	MnO	MgO	CaO	Na2O	K2O	Cr2O3	V2O3	NiO	Total	% An	% Ab	% Or
		65.65	0.00	21.95	0.07	0.00	0.00	2.79	9.70	0.29	0.00	0.00	0.00	100.45	13.49	84.82	1.69
		64.58	0.00	21.17	0.31	0.08	0.03	1.97	10.25	0.18	0.00	0.00	0.00	98.58	9.51	89.45	1.04
		63.21	0.00	22.14	0.00	0.03	0.00	3.19	9.84	0.16	0.05	0.00	0.00	98.63	15.06	84.05	0.89
		63.52	0.09	21.62	0.05	0.01	0.01	2.97	9.90	0.15	0.04	0.00	0.02	98.39	14.12	85.05	0.83
		63.59	0.04	22.08	0.05	0.07	0.00	3.08	9.79	0.14	0.00	0.00	0.00	98.84	14.68	84.51	0.80
	Casa de Piedra	63.53	0.00	21.86	0.03	0.12	0.00	3.27	9.38	0.13	0.00	0.00	0.00	98.31	16.03	83.20	0.77
		63.03	0.00	21.91	0.02	0.00	0.00	3.27	9.53	0.13	0.00	0.03	0.00	97.92	15.82	83.44	0.74
		63.23	0.00	21.60	0.05	0.02	0.00	3.09	9.94	0.12	0.06	0.03	0.05	98.20	14.57	84.74	0.70
		63.33	0.17	21.84	0.04	0.00	0.02	3.02	9.75	0.12	0.01	0.01	0.00	98.31	14.54	84.79	0.67
		63.77	0.00	21.87	0.01	0.07	0.02	3.03	9.77	0.08	0.08	0.01	0.03	98.74	14.56	84.98	0.45
		66.85	0.00	19.29	0.02	0.00	0.00	0.53	11.96	0.07	0.00	0.05	0.02	98.78	2.37	97.27	0.35
Southern		61.42	0.00	22.81	0.05	0.05	0.01	4.18	8.39	0.37	0.00	0.03	0.00	97.29	21.12	76.68	2.20
		61.66	0.00	22.63	0.04	0.03	0.02	4.26	8.92	0.25	0.06	0.02	0.00	97.90	20.59	77.99	1.42
		62.83	0.02	23.28	0.00	0.00	0.00	4.31	8.76	0.24	0.05	0.04	0.00	99.52	21.07	77.55	1.39
		62.30	0.06	23.03	0.04	0.00	0.00	4.33	8.98	0.23	0.06	0.03	0.00	99.07	20.77	77.90	1.33
		64.48	0.08	23.65	0.04	0.03	0.00	4.43	9.04	0.21	0.07	0.01	0.00	102.03	21.07	77.73	1.21
	Las Tojas	62.39	0.07	23.09	0.01	0.00	0.02	4.26	8.88	0.21	0.07	0.00	0.07	99.06	20.71	78.06	1.22
		62.48	0.00	22.69	0.01	0.00	0.01	4.18	8.77	0.21	0.05	0.04	0.01	98.45	20.60	78.16	1.24
		61.69	0.20	22.36	0.05	0.00	0.00	4.23	8.90	0.20	0.00	0.00	0.03	97.65	20.56	78.30	1.14
		62.54	0.00	22.74	0.11	0.05	0.00	4.27	8.94	0.18	0.54	0.00	0.00	99.36	20.69	78.30	1.01
		65.77	0.00	21.96	0.00	0.06	0.00	2.63	10.23	0.17	0.00	0.02	0.05	100.88	12.34	86.74	0.93
		61.99	0.05	22.21	0.10	0.00	0.04	3.80	8.81	0.15	0.00	0.05	0.05	97.23	19.07	80.05	0.88
		63.37	0.00	22.58	0.09	0.03	0.04	4.00	8.27	0.38	0.04	0.01	0.04	98.86	20.60	77.04	2.35
		62.18	0.03	22.43	0.08	0.04	0.02	4.63	8.05	0.33	0.00	0.02	0.03	97.84	23.63	74.38	1.99
		62.42	0.00	23.05	0.12	0.00	0.01	5.15	8.22	0.23	0.00	0.03	0.00	99.22	25.39	73.28	1.33
	Nomoca	62.57	0.00	22.33	0.05	0.00	0.02	4.63	8.32	0.20	0.02	0.03	0.02	98.18	23.24	75.56	1.20
		62.75	0.00	22.64	0.16	0.00	0.02	4.68	8.09	0.19	0.02	0.02	0.00	98.59	23.96	74.87	1.17
		63.36	0.00	22.37	0.03	0.03	0.00	4.40	8.53	0.16	0.01	0.05	0.00	98.94	21.98	77.09	0.93
		61.71	0.19	22.39	0.10	0.00	0.01	4.86	8.22	0.12	0.00	0.02	0.00	97.62	24.45	74.81	0.74
		63.86	0.00	22.81	0.06	0.00	0.00	4.38	8.41	0.12	0.00	0.00	0.00	99.63	22.20	77.08	0.72
		62.04	0.00	24.37	0.28	0.02	0.00	5.56	7.58	0.37	0.00	0.00	0.00	100.21	28.21	69.57	2.22
	San Pablo	60.39	0.28	24.80	0.14	0.00	0.02	7.02	7.20	0.29	0.08	0.02	0.00	100.22	34.42	63.89	1.69
		62.04	0.08	25.15	0.09	0.00	0.00	6.54	7.50	0.26	0.00	0.00	0.00	101.65	32.03	66.48	1.49

Domain	Pluton	SiO2	TiO2	Al2O3	FeO	MnO	MgO	CaO	Na2O	K2O	Cr2O3	V2O3	NiO	Total	% An	% Ab	% Or
		61.61	0.00	25.23	0.03	0.00	0.00	6.70	7.30	0.25	0.00	0.01	0.03	101.16	33.12	65.39	1.49
		60.77	0.00	24.27	0.62	0.00	0.10	5.99	7.57	0.24	0.06	0.07	0.00	99.67	29.98	68.61	1.41
		60.89	0.00	25.08	0.73	0.07	0.17	6.93	7.16	0.24	0.00	0.02	0.03	101.29	34.36	64.24	1.39
		61.96	0.00	24.02	0.07	0.00	0.00	6.01	7.64	0.23	0.00	0.04	0.00	99.96	29.86	68.78	1.36
		60.43	0.00	24.64	0.06	0.00	0.00	6.62	7.30	0.21	0.00	0.00	0.06	99.31	32.98	65.77	1.25
		60.45	0.06	25.68	0.06	0.03	0.00	7.60	6.64	0.18	0.03	0.00	0.01	100.74	38.31	60.60	1.09
		61.93	0.10	24.15	0.14	0.00	0.00	6.09	7.88	0.18	0.00	0.00	0.07	100.54	29.62	69.34	1.04
		62.48	0.00	24.38	0.16	0.00	0.02	6.30	7.89	0.18	0.00	0.00	0.06	101.46	30.32	68.67	1.02
		61.86	0.02	24.36	0.06	0.06	0.00	6.19	7.68	0.17	0.00	0.02	0.01	100.43	30.50	68.52	0.98
		61.12	0.00	24.75	0.04	0.03	0.00	6.61	7.58	0.17	0.05	0.00	0.00	100.34	32.23	66.81	0.96
		61.66	0.02	24.59	0.05	0.02	0.00	6.39	7.71	0.17	0.05	0.00	0.00	100.65	31.13	67.92	0.96
		62.25	0.00	24.74	0.06	0.03	0.00	6.62	7.16	0.15	0.05	0.06	0.00	101.11	33.51	65.57	0.92
		61.88	0.00	25.15	0.07	0.14	0.00	6.54	7.41	0.14	0.05	0.00	0.06	101.44	32.50	66.66	0.84
		63.73	0.00	20.96	0.01	0.00	0.01	2.98	9.97	0.39	0.06	0.00	0.00	98.11	13.87	83.95	2.18
		63.48	0.00	20.89	0.04	0.04	0.02	2.77	10.33	0.39	0.00	0.00	0.07	98.03	12.63	85.26	2.11
		63.72	0.00	21.22	0.06	0.05	0.00	2.76	10.30	0.38	0.02	0.00	0.05	98.55	12.63	85.32	2.05
		64.17	0.12	21.23	0.01	0.09	0.00	2.68	10.08	0.37	0.05	0.04	0.04	98.89	12.54	85.42	2.04
		64.12	0.07	21.04	0.01	0.03	0.00	2.75	10.09	0.36	0.08	0.00	0.02	98.57	12.83	85.20	1.98
		63.80	0.00	21.11	0.04	0.04	0.03	2.79	10.32	0.34	0.01	0.01	0.00	98.48	12.75	85.39	1.86
		63.57	0.18	21.07	0.00	0.00	0.00	2.67	10.20	0.34	0.00	0.02	0.01	98.07	12.40	85.74	1.86
		63.62	0.00	21.47	0.04	0.02	0.02	3.14	9.52	0.34	0.00	0.01	0.00	98.17	15.13	82.94	1.93
		63.38	0.00	20.93	0.00	0.00	0.03	2.74	10.26	0.33	0.00	0.00	0.00	97.66	12.61	85.60	1.79
	Señoritas	62.62	0.15	22.07	0.09	0.00	0.00	3.43	9.78	0.32	0.03	0.03	0.00	98.51	15.95	82.29	1.75
		64.31	0.00	21.79	0.07	0.00	0.00	2.81	10.06	0.31	0.10	0.00	0.00	99.43	13.16	85.13	1.71
		63.75	0.00	20.87	0.00	0.00	0.00	2.65	10.35	0.29	0.00	0.01	0.00	97.93	12.22	86.19	1.60
		64.32	0.01	21.38	0.05	0.05	0.01	2.78	9.69	0.29	0.00	0.02	0.00	98.59	13.45	84.89	1.66
		62.78	0.00	21.33	0.00	0.00	0.00	3.17	10.06	0.29	0.00	0.00	0.04	97.66	14.61	83.81	1.57
		63.13	0.05	21.07	0.00	0.01	0.00	2.82	10.09	0.27	0.07	0.00	0.00	97.51	13.17	85.33	1.51
		63.18	0.00	21.03	0.03	0.09	0.00	2.73	10.11	0.27	0.07	0.00	0.00	97.50	12.78	85.72	1.50
		63.28	0.06	20.89	0.04	0.09	0.00	2.66	10.46	0.27	0.03	0.00	0.05	97.82	12.14	86.41	1.46
		63.86	0.12	21.19	0.04	0.00	0.02	2.69	10.15	0.27	0.06	0.00	0.00	98.40	12.59	85.92	1.49
		63.91	0.05	21.07	0.01	0.00	0.00	2.86	10.12	0.27	0.00	0.00	0.00	98.29	13.29	85.22	1.48
		65.49	0.02	21.41	0.00	0.00	0.01	2.38	10.16	0.26	0.02	0.00	0.02	99.78	11.29	87.24	1.47

Domain	Pluton	SiO2	TiO2	Al2O3	FeO	MnO	MgO	CaO	Na2O	K2O	Cr2O3	V2O3	NiO	Total	% An	% Ab	% Or
		64.48	0.00	21.24	0.06	0.05	0.00	2.85	10.27	0.26	0.00	0.00	0.02	99.22	13.10	85.48	1.42
		65.22	0.00	21.23	0.08	0.05	0.00	2.38	9.97	0.26	0.00	0.01	0.01	99.21	11.48	87.03	1.49
		64.43	0.00	21.51	0.06	0.00	0.00	2.81	9.65	0.25	0.00	0.04	0.00	98.75	13.68	84.85	1.47
		63.81	0.00	20.90	0.01	0.00	0.00	2.60	10.60	0.24	0.00	0.00	0.04	98.20	11.78	86.93	1.28
		64.85	0.13	21.20	0.03	0.00	0.00	2.60	10.22	0.23	0.04	0.01	0.00	99.30	12.18	86.53	1.29
		64.94	0.00	21.63	0.02	0.00	0.02	2.67	10.05	0.23	0.05	0.00	0.00	99.60	12.66	86.06	1.28
		64.53	0.08	21.32	0.00	0.00	0.00	2.70	9.85	0.22	0.00	0.00	0.01	98.72	13.00	85.74	1.26
		64.94	0.05	21.80	0.03	0.02	0.00	2.82	9.92	0.22	0.00	0.01	0.00	99.81	13.41	85.34	1.25
		63.68	0.12	20.83	0.06	0.06	0.00	2.67	10.32	0.20	0.06	0.00	0.04	98.03	12.37	86.52	1.11
		66.22	0.04	21.96	0.10	0.02	0.03	2.69	10.32	0.20	0.00	0.00	0.00	101.56	12.45	86.44	1.10
		65.15	0.11	21.58	0.07	0.00	0.03	2.83	9.87	0.18	0.00	0.00	0.01	99.84	13.52	85.45	1.03
		65.41	0.00	21.45	0.02	0.00	0.00	2.64	10.04	0.16	0.00	0.00	0.01	99.74	12.56	86.51	0.93
		65.11	0.11	21.28	0.06	0.01	0.00	2.59	10.22	0.16	0.06	0.02	0.07	99.69	12.17	86.96	0.87
		63.25	0.04	21.08	0.06	0.00	0.00	2.79	10.12	0.14	0.04	0.05	0.05	97.63	13.12	86.09	0.79
		66.64	0.00	19.80	0.41	0.08	0.14	0.63	11.33	0.75	0.00	0.00	0.11	99.88	2.86	93.10	4.04
		66.00	0.09	19.34	0.01	0.00	0.03	0.70	11.28	0.20	0.03	0.03	0.02	97.73	3.28	95.63	1.09
		67.17	0.00	19.79	0.00	0.06	0.00	1.17	11.46	0.13	0.04	0.03	0.06	99.92	5.31	93.98	0.71
		67.35	0.03	19.47	0.00	0.09	0.01	0.78	11.22	0.12	0.01	0.01	0.03	99.12	3.66	95.66	0.68
		68.79	0.16	18.94	0.00	0.07	0.00	0.23	12.06	0.12	0.09	0.03	0.00	100.47	1.04	98.32	0.64
		67.89	0.00	19.90	0.01	0.00	0.00	1.05	11.65	0.12	0.00	0.01	0.01	100.62	4.70	94.67	0.63
		67.18	0.00	19.47	0.00	0.04	0.00	0.54	11.62	0.11	0.00	0.02	0.00	98.97	2.47	96.94	0.59
	Tasseoro	68.08	0.04	19.46	0.01	0.07	0.00	0.34	11.76	0.11	0.01	0.00	0.00	99.88	1.57	97.85	0.58
		68.54	0.02	18.83	0.00	0.01	0.03	0.20	12.16	0.10	0.13	0.03	0.06	100.11	0.90	98.55	0.55
		67.13	0.00	19.77	0.00	0.00	0.00	0.96	11.85	0.10	0.00	0.00	0.00	99.80	4.25	95.22	0.52
		69.00	0.21	19.05	0.00	0.00	0.00	0.18	11.87	0.10	0.04	0.00	0.10	100.55	0.83	98.64	0.53
		68.60	0.02	19.04	0.00	0.07	0.01	0.20	11.81	0.09	0.11	0.00	0.00	99.96	0.94	98.54	0.52
		67.98	0.10	19.59	0.04	0.03	0.02	0.85	11.67	0.09	0.00	0.01	0.00	100.38	3.86	95.64	0.50
		68.78	0.00	18.83	0.03	0.00	0.00	0.14	12.00	0.07	0.00	0.00	0.01	99.85	0.63	98.99	0.38
		68.49	0.08	18.94	0.00	0.00	0.00	0.26	12.12	0.07	0.00	0.01	0.03	99.99	1.17	98.48	0.35
		60.50	0.04	24.33	0.02	0.03	0.01	5.48	7.20	0.18	0.01	0.00	0.04	97.83	29.30	69.57	1.14
	Tauca	59.45	0.00	24.93	0.06	0.02	0.00	6.28	6.73	0.15	0.00	0.04	0.00	97.65	33.72	65.34	0.95
		61.98	0.15	23.59	0.04	0.01	0.02	4.53	7.64	0.14	0.00	0.01	0.00	98.11	24.47	74.64	0.89
		61.13	0.00	24.32	0.00	0.01	0.01	5.16	7.15	0.14	0.01	0.00	0.00	97.93	28.24	70.88	0.88

Domain	Pluton	SiO2	TiO2	Al2O3	FeO	MnO	MgO	CaO	Na2O	K2O	Cr2O3	V2O3	NiO	Total	% An	% Ab	% Or
		61.92	0.00	23.79	0.01	0.00	0.00	4.71	7.42	0.13	0.00	0.00	0.00	97.98	25.75	73.42	0.83
		60.15	0.01	25.54	0.04	0.05	0.01	6.22	6.77	0.12	0.00	0.00	0.00	98.90	33.42	65.82	0.76
		59.60	0.00	25.37	0.03	0.00	0.00	6.14	6.63	0.12	0.00	0.04	0.07	98.00	33.60	65.63	0.77
		60.35	0.06	24.45	0.00	0.00	0.01	5.28	7.08	0.11	0.00	0.02	0.00	97.36	28.96	70.29	0.75
		62.16	0.00	23.37	0.00	0.00	0.00	4.20	7.49	0.09	0.05	0.00	0.04	97.40	23.53	75.90	0.57

K-Feldspar

K-feldspar from northern granites are well preserved light reddish grains with euhedral to subhedral shapes of 0.1 mm to phenocrysts of 1 cm. Most crystals exhibit sharply defined tartan twinning and occasionally Carlsbad twinning. Plagioclase, quartz, biotite and apatite inclusions are common. Tauca and Nocemano granites present perthitic exsolution of vermicular plagioclase.

The K-feldspar analyses show 14.08 to 16.66 wt.% K_2O (Or_{88-93}), with 0.17 to 2.45 wt.% Na_2O (Ab_{4-12}), and are classified as K-Sanidine (Table 4.4, Fig. 4.6C). The SiO_2 versus K_2O diagram shows increase of SiO_2 (62.37 to 63.80 wt.%) in K-feldspar grains of Casa de Piedra leucocratic portion. 19B enclave sample shows increase of SiO_2 (65.52 to 66.87 wt.%) and decrease of K_2O (14.50 to 14.08 wt.%). 19A and 19C enclave samples have similar SiO_2 (65.96 to 67.63 wt.%) and K_2O (15.58 to 16.32 wt.%) contents to the other northern granites.

In the southern granites, K-feldspar occurs as euhedral to subhedral light reddish equigranular crystals. Phenocrysts occur in the Tasseoro granite and occasionally in the Señoritas granite. The crystals present well defined tartan twinning and plagioclase and quartz inclusions. Perthitic exsolution texture of vermicular plagioclase is common. The K-feldspar analyses show 13.6 to 14.9 wt.% K_2O (Or_{88-93}), with 0.45 to 1.25 wt.% Na_2O (Ab_{4-12}), and are classified as K-sanidine (Table 4.4, Fig. 4.6C).

Table 4-4. K-feldspar composition from Sunsas belt (normalization based on 8 oxygens).

Domain	Pluton	SiO2	TiO2	Al2O3	FeO	MnO	MgO	CaO	Na2O	K2O	Cr2O3	V2O3	NiO	Total	% An	% Ab	% Or
Northern	Casa de Piedra	62.84	0.23	17.95	0.01	0.00	0.01	0.00	0.58	15.94	0.04	0.02	0.02	97.63	0.00	5.21	94.79
		63.31	0.34	18.20	0.05	0.03	0.01	0.01	1.96	15.66	0.00	0.05	0.00	99.63	0.05	15.94	84.01
		63.54	0.16	17.81	0.04	0.00	0.01	0.01	0.93	15.72	0.05	0.00	0.01	98.27	0.04	8.24	91.72
		63.59	0.04	18.21	0.01	0.03	0.00	0.02	0.68	15.92	0.05	0.05	0.02	98.60	0.09	6.11	93.80
		63.11	0.00	17.83	0.00	0.00	0.00	0.02	1.06	15.68	0.00	0.00	0.06	97.76	0.09	9.27	90.64
		62.37	0.05	18.01	0.00	0.00	0.00	0.00	0.69	16.18	0.00	0.02	0.02	97.33	0.00	6.09	93.91
		63.67	0.00	18.11	0.05	0.00	0.00	0.00	0.73	15.76	0.07	0.08	0.02	98.51	0.00	6.58	93.42
		63.80	0.04	18.04	0.06	0.00	0.01	0.04	0.87	15.99	0.00	0.02	0.04	98.89	0.19	7.62	92.18
		66.31	0.00	17.69	0.06	0.00	0.00	0.01	0.42	16.05	0.00	0.00	0.02	100.55	0.04	3.83	96.13
		66.66	0.01	17.51	0.04	0.02	0.00	0.00	0.73	15.92	0.00	0.00	0.00	100.90	0.00	6.51	93.49
		66.03	0.00	17.43	0.04	0.10	0.00	0.01	0.57	16.32	0.00	0.07	0.00	100.56	0.04	5.01	94.96
		66.84	0.00	17.67	0.03	0.03	0.00	0.00	0.56	15.93	0.00	0.00	0.01	101.07	0.00	5.08	94.92
		66.84	0.00	17.80	0.03	0.00	0.00	0.00	0.89	15.91	0.00	0.00	0.00	101.47	0.00	7.79	92.21
		65.96	0.10	17.26	0.04	0.04	0.00	0.03	0.81	16.01	0.00	0.00	0.00	100.24	0.13	7.16	92.71
		65.52	0.13	18.53	0.02	0.07	0.00	0.00	0.97	14.50	0.01	0.01	0.01	99.76	0.00	9.21	90.79
		66.01	0.16	18.48	0.03	0.02	0.00	0.00	1.29	14.33	0.03	0.00	0.06	100.39	0.01	12.00	87.99
		65.70	0.00	18.39	0.06	0.00	0.00	0.01	1.19	14.42	0.00	0.08	0.03	99.86	0.03	11.14	88.82
		66.27	0.02	18.55	0.03	0.02	0.00	0.00	1.56	14.32	0.00	0.01	0.01	100.78	0.00	14.17	85.83
		66.34	0.01	18.14	0.00	0.00	0.01	0.02	1.23	14.37	0.10	0.01	0.00	100.23	0.09	11.52	88.39
		66.35	0.00	18.53	0.06	0.00	0.00	0.00	0.20	14.08	0.05	0.00	0.00	99.27	0.00	2.10	97.90
		66.87	0.00	18.68	0.04	0.00	0.00	0.00	0.17	14.22	0.00	0.00	0.01	100.00	0.02	1.81	98.17
		65.96	0.00	17.30	0.00	0.00	0.03	0.00	0.59	15.99	0.00	0.01	0.00	99.88	0.00	5.30	94.70
		66.54	0.04	17.41	0.03	0.00	0.00	0.01	2.45	15.58	0.05	0.03	0.00	102.14	0.04	19.30	80.66
		66.27	0.17	17.26	0.01	0.00	0.01	0.02	1.00	15.68	0.02	0.00	0.01	100.47	0.12	8.80	91.08
		67.63	0.04	17.88	0.06	0.07	0.01	0.00	0.46	15.93	0.09	0.08	0.00	102.22	0.00	4.16	95.84
	La Asunta	67.06	0.18	18.41	0.04	0.00	0.00	0.00	0.49	15.93	0.06	0.01	0.01	102.19	0.00	4.45	95.55
		67.23	0.00	18.47	0.02	0.07	0.00	0.01	0.70	15.56	0.00	0.05	0.01	102.12	0.07	6.43	93.50
		66.03	0.07	18.40	0.00	0.04	0.00	0.05	0.99	15.51	0.01	0.01	0.01	101.12	0.23	8.82	90.95
	Nocemano	65.48	0.00	17.49	0.06	0.00	0.01	0.05	0.37	16.44	0.00	0.03	0.00	99.93	0.23	3.33	96.44
		67.03	0.04	18.00	0.12	0.00	0.00	0.04	0.35	16.09	0.18	0.01	0.00	101.87	0.22	3.19	96.60
		67.13	0.05	17.97	0.04	0.03	0.01	0.00	0.87	16.00	0.01	0.03	0.00	102.13	0.00	7.63	92.37

Domain	Pluton	SiO2	TiO2	Al2O3	FeO	MnO	MgO	CaO	Na2O	K2O	Cr2O3	V2O3	NiO	Total	% An	% Ab	% Or
		66.36	0.01	17.93	0.00	0.05	0.00	0.05	0.93	15.72	0.00	0.00	0.00	101.05	0.25	8.19	91.56
		66.65	0.00	17.73	0.01	0.00	0.02	0.00	1.02	15.23	0.00	0.03	0.00	100.69	0.00	9.23	90.77
		67.40	0.00	18.15	0.01	0.00	0.01	0.03	0.57	16.66	0.00	0.00	0.01	102.83	0.12	4.96	94.91
		67.24	0.07	17.93	0.05	0.02	0.00	0.02	0.51	16.32	0.00	0.01	0.00	102.17	0.11	4.52	95.37
	San Ramón	66.70	0.07	18.59	0.02	0.00	0.00	0.00	0.52	16.30	0.06	0.03	0.00	102.29	0.00	4.62	95.38
		66.71	0.02	18.36	0.05	0.06	0.00	0.00	0.54	16.29	0.00	0.01	0.00	102.04	0.00	4.79	95.21
		67.33	0.00	18.25	0.00	0.01	0.00	0.00	0.50	16.13	0.00	0.00	0.02	102.24	0.00	4.47	95.53
		67.60	0.11	18.23	0.00	0.02	0.01	0.00	0.41	16.06	0.06	0.00	0.00	102.49	0.00	3.73	96.27
		64.82	0.10	18.12	0.03	0.04	0.00	0.02	0.63	15.96	0.01	0.00	0.03	99.76	0.09	5.66	94.25
		64.21	0.00	18.07	0.05	0.00	0.01	0.02	0.46	15.93	0.00	0.07	0.00	98.82	0.12	4.21	95.67
		64.30	0.10	18.09	0.00	0.05	0.01	0.01	0.74	15.83	0.00	0.00	0.00	99.13	0.04	6.66	93.31
		65.02	0.16	18.36	0.00	0.07	0.01	0.00	0.81	15.79	0.10	0.00	0.03	100.36	0.00	7.23	92.77
		65.12	0.00	18.10	0.01	0.03	0.00	0.00	0.59	15.77	0.07	0.03	0.02	99.75	0.00	5.41	94.59
		64.54	0.09	18.05	0.00	0.11	0.00	0.01	0.86	15.75	0.00	0.02	0.01	99.44	0.03	7.66	92.31
		64.92	0.01	18.35	0.02	0.00	0.00	0.01	1.09	15.74	0.12	0.00	0.00	100.25	0.04	9.48	90.48
		64.91	0.09	18.48	0.00	0.00	0.00	0.01	1.06	15.71	0.05	0.01	0.00	100.32	0.06	9.32	90.62
		63.91	0.01	17.90	0.01	0.00	0.00	0.00	0.64	15.57	0.01	0.00	0.01	98.07	0.00	5.90	94.10
		64.69	0.05	18.05	0.02	0.01	0.01	0.05	0.83	15.54	0.05	0.00	0.00	99.29	0.25	7.51	92.24
		62.97	0.00	17.80	0.02	0.00	0.00	0.05	1.76	15.50	0.00	0.00	0.01	98.11	0.22	14.70	85.09
		63.92	0.24	17.92	0.02	0.01	0.02	0.00	0.41	15.49	0.12	0.00	0.00	98.14	0.00	3.85	96.15
Southern	Señoritas	65.35	0.18	18.46	0.00	0.06	0.00	0.01	0.29	15.46	0.00	0.06	0.00	99.86	0.04	2.80	97.16
		63.92	0.00	17.52	0.01	0.03	0.01	0.00	0.36	15.42	0.07	0.03	0.00	97.37	0.01	3.42	96.57
		64.83	0.08	17.97	0.03	0.02	0.00	0.06	0.47	15.41	0.05	0.00	0.00	98.91	0.32	4.41	95.28
		64.58	0.00	18.39	0.05	0.04	0.00	0.00	0.66	15.41	0.08	0.04	0.00	99.26	0.02	6.11	93.87
		64.02	0.08	17.80	0.00	0.07	0.02	0.05	0.87	15.38	0.00	0.05	0.00	98.35	0.26	7.89	91.85
		64.34	0.17	17.80	0.00	0.01	0.00	0.02	0.75	15.37	0.00	0.03	0.01	98.48	0.11	6.91	92.98
		63.79	0.00	17.55	0.00	0.02	0.00	0.05	0.91	15.35	0.00	0.04	0.04	97.76	0.24	8.23	91.54
		64.92	0.08	18.32	0.01	0.00	0.00	0.01	0.87	15.34	0.01	0.05	0.00	99.61	0.07	7.94	91.99
		64.13	0.06	18.11	0.03	0.00	0.00	0.06	0.82	15.33	0.00	0.00	0.00	98.54	0.28	7.49	92.23
		64.18	0.02	17.87	0.00	0.00	0.01	0.09	0.96	15.33	0.09	0.01	0.00	98.55	0.46	8.61	90.93
		63.78	0.10	17.83	0.00	0.00	0.00	0.04	0.80	15.33	0.00	0.04	0.00	97.93	0.18	7.36	92.46
		64.35	0.00	17.97	0.00	0.00	0.00	0.05	1.03	15.28	0.08	0.00	0.04	98.79	0.22	9.25	90.53
		65.64	0.14	18.43	0.02	0.10	0.01	0.00	0.94	15.27	0.02	0.00	0.00	100.57	0.00	8.57	91.43

Domain	Pluton	SiO2	TiO2	Al2O3	FeO	MnO	MgO	CaO	Na2O	K2O	Cr2O3	V2O3	NiO	Total	% An	% Ab	% Or
		65.13	0.00	18.21	0.01	0.00	0.02	0.01	0.94	15.25	0.05	0.00	0.03	99.64	0.03	8.55	91.42
		63.93	0.01	17.88	0.03	0.05	0.00	0.06	0.86	15.19	0.07	0.00	0.00	98.09	0.30	7.92	91.78
		64.51	0.01	17.62	0.00	0.02	0.00	0.02	0.93	15.11	0.00	0.01	0.00	98.21	0.08	8.55	91.37
		65.13	0.12	18.05	0.02	0.04	0.00	0.06	1.04	14.84	0.00	0.01	0.00	99.31	0.30	9.57	90.13
		63.89	0.07	17.72	0.00	0.00	0.00	0.05	0.94	14.75	0.00	0.05	0.00	97.47	0.25	8.81	90.94
		64.55	0.02	18.08	0.05	0.04	0.00	0.04	1.00	14.72	0.05	0.01	0.00	98.55	0.21	9.35	90.45
	Tasseoro	64.75	0.00	17.46	0.05	0.03	0.00	0.00	0.50	16.74	0.00	0.00	0.04	99.56	0.00	4.33	95.67
		64.59	0.00	17.76	0.08	0.02	0.00	0.01	0.55	16.73	0.00	0.00	0.00	99.74	0.06	4.77	95.17
		65.00	0.00	17.87	0.06	0.05	0.00	0.00	0.49	16.51	0.03	0.06	0.02	100.08	0.01	4.32	95.66
		63.73	0.21	17.89	0.00	0.00	0.00	0.02	0.48	16.50	0.00	0.00	0.03	98.86	0.10	4.20	95.70
		63.88	0.00	18.18	0.00	0.00	0.01	0.00	0.32	16.11	0.02	0.01	0.00	98.54	0.00	2.89	97.11
		64.90	0.00	17.96	0.12	0.08	0.01	0.01	0.54	15.96	0.00	0.05	0.07	99.68	0.04	4.85	95.12
		65.25	0.07	17.88	0.00	0.00	0.00	0.04	1.03	15.07	0.00	0.00	0.00	99.32	0.18	9.38	90.44
	Tauca	65.17	0.00	18.33	0.06	0.00	0.01	0.00	0.53	13.61	0.08	0.00	0.00	97.80	0.02	5.56	94.43
		65.35	0.00	18.29	0.01	0.00	0.02	0.11	0.60	13.17	0.00	0.00	0.00	97.54	0.64	6.42	92.94
	San Pablo	66.04	0.00	18.26	0.12	0.00	0.00	0.03	1.08	14.54	0.01	0.00	0.00	100.08	0.17	10.13	89.71
		66.35	0.27	18.43	0.11	0.02	0.00	0.09	0.44	14.01	0.08	0.00	0.00	99.81	0.53	4.54	94.93
	Las Tojas	65.84	0.00	18.81	0.00	0.00	0.00	0.06	0.44	16.36	0.04	0.02	0.00	101.56	0.30	3.92	95.78
		65.50	0.00	18.56	0.04	0.00	0.00	0.06	0.50	16.35	0.00	0.00	0.04	101.04	0.28	4.40	95.32
		65.16	0.00	18.33	0.00	0.04	0.00	0.00	0.55	16.22	0.03	0.00	0.00	100.34	0.00	4.89	95.10
		64.98	0.05	18.20	0.05	0.02	0.00	0.04	0.61	16.21	0.04	0.03	0.03	100.24	0.19	5.43	94.37
		63.85	0.14	18.09	0.00	0.08	0.02	0.01	0.51	16.18	0.00	0.02	0.00	98.91	0.07	4.60	95.33
		65.02	0.04	18.50	0.03	0.00	0.01	0.01	0.57	16.14	0.00	0.00	0.04	100.35	0.02	5.13	94.85
		65.99	0.00	18.84	0.01	0.03	0.01	0.03	0.31	16.11	0.00	0.02	0.00	101.35	0.15	2.86	96.99
		64.54	0.00	18.41	0.05	0.05	0.00	0.00	0.32	16.07	0.00	0.04	0.00	99.48	0.00	2.91	97.09
		65.08	0.01	18.46	0.00	0.00	0.03	0.02	0.49	16.01	0.01	0.00	0.00	100.11	0.09	4.45	95.47
		64.99	0.00	18.22	0.02	0.00	0.00	0.00	0.64	15.98	0.09	0.00	0.01	99.94	0.00	5.73	94.27
		65.06	0.16	18.48	0.01	0.02	0.00	0.00	0.82	15.87	0.00	0.01	0.00	100.44	0.02	7.31	92.67
		66.01	0.04	18.98	0.02	0.00	0.00	0.03	0.66	15.78	0.00	0.00	0.00	101.50	0.16	5.93	93.91
		64.50	0.00	18.09	0.02	0.04	0.00	0.04	1.05	15.73	0.00	0.02	0.00	99.49	0.17	9.18	90.65
		66.32	0.00	18.67	0.00	0.04	0.00	0.04	1.35	15.70	0.00	0.00	0.00	102.10	0.18	11.52	88.30
		64.95	0.04	18.57	0.02	0.00	0.01	0.05	1.09	15.62	0.04	0.00	0.00	100.38	0.26	9.56	90.18
		64.31	0.01	18.17	0.12	0.00	0.00	0.02	2.60	15.58	0.06	0.00	0.01	100.89	0.10	20.18	79.72

Domain	Pluton	SiO2	TiO2	Al2O3	FeO	MnO	MgO	CaO	Na2O	K2O	Cr2O3	V2O3	NiO	Total	% An	% Ab	% Or
		64.69	0.08	18.31	0.00	0.00	0.01	0.00	0.35	15.58	0.00	0.00	0.00	99.02	0.00	3.27	96.73
		64.18	0.06	18.06	0.01	0.00	0.01	0.04	1.44	15.51	0.11	0.00	0.00	99.42	0.19	12.37	87.44
		65.03	0.20	18.23	0.00	0.00	0.03	0.01	0.49	15.43	0.00	0.00	0.00	99.42	0.06	4.61	95.33
		66.08	0.04	18.60	0.01	0.00	0.00	0.05	0.49	15.41	0.00	0.00	0.00	100.67	0.24	4.55	95.20
		64.75	0.01	18.08	0.02	0.02	0.00	0.07	0.70	15.39	0.07	0.03	0.05	99.19	0.37	6.42	93.21
		65.14	0.24	18.45	0.02	0.00	0.00	0.01	1.00	15.32	0.00	0.00	0.05	100.22	0.05	9.05	90.90
		62.70	0.00	17.93	0.03	0.00	0.01	0.07	0.82	15.32	0.05	0.07	0.03	97.02	0.34	7.52	92.14
		66.05	0.01	18.87	0.00	0.00	0.00	0.03	0.81	15.25	0.00	0.00	0.00	101.03	0.17	7.48	92.35
		63.10	0.00	17.72	0.06	0.10	0.03	0.11	0.79	15.22	0.33	0.00	0.01	97.46	0.55	7.23	92.22
		64.75	0.00	18.56	0.06	0.02	0.00	0.02	1.10	15.19	0.00	0.00	0.00	99.69	0.09	9.87	90.04
		64.41	0.00	18.32	0.01	0.00	0.00	0.05	0.97	15.01	0.02	0.04	0.00	98.83	0.25	8.91	90.84
		65.27	0.00	18.71	0.01	0.00	0.00	0.05	0.21	14.13	0.01	0.01	0.00	98.42	0.28	2.24	97.47
		61.96	0.12	17.46	4.04	0.00	0.03	0.06	0.33	14.06	0.05	0.01	0.07	98.19	0.32	3.46	96.22
		65.68	0.13	18.54	0.05	0.05	0.02	0.03	1.45	13.35	0.01	0.00	0.01	99.32	0.15	14.16	85.69
		64.46	0.04	18.49	0.08	0.05	0.00	0.07	0.84	13.14	0.00	0.00	0.00	97.18	0.39	8.84	90.77

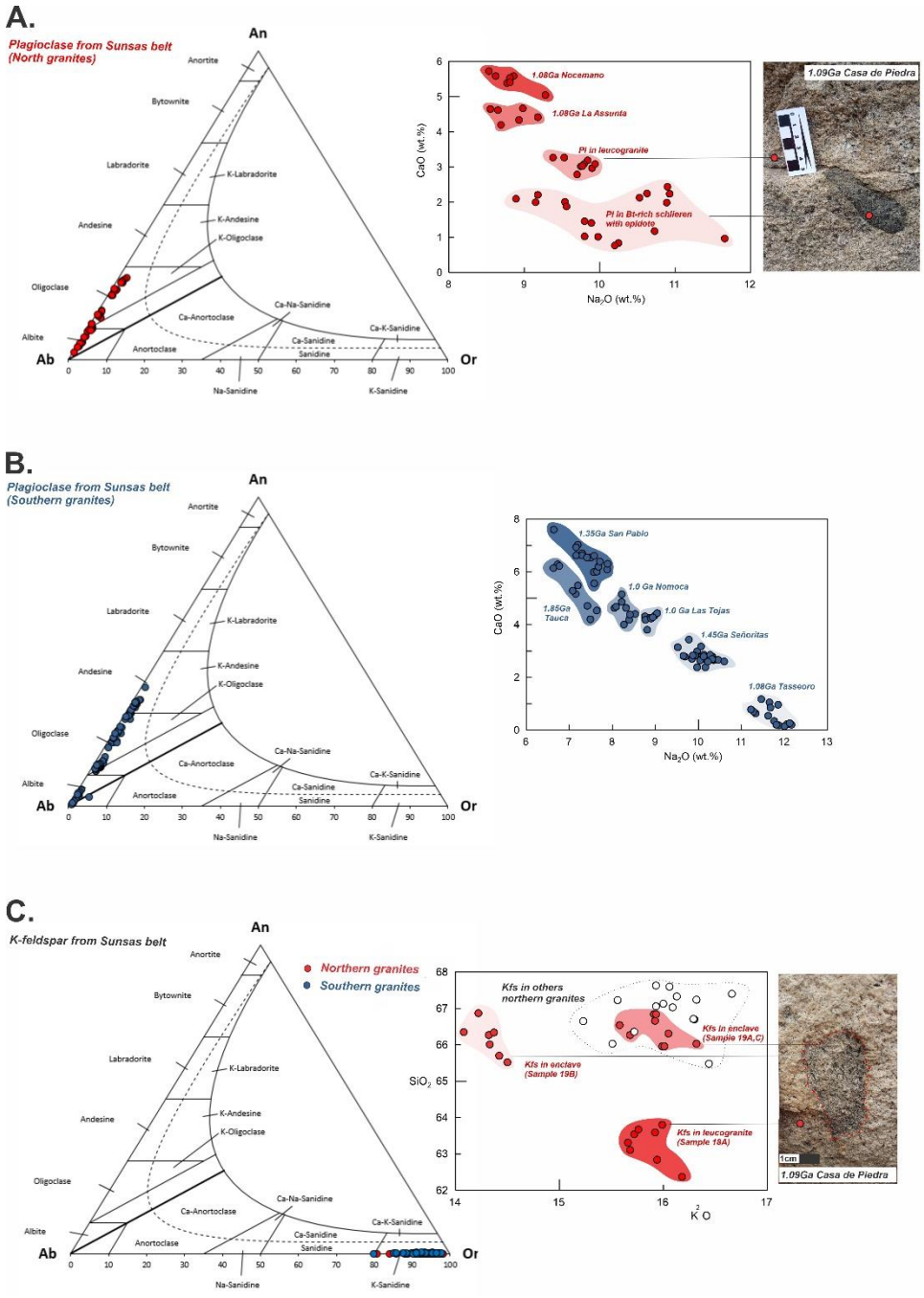

Figure 4.6. Mineral chemistry analyses in plagioclase and K-feldspar from southern and northern granites.

4.5.1.3 Orthopyroxene

The San Pablo monzogranite, Sunsas belt southern portion, is the only intrusion with pyroxene (Table 4.5, Fig. 4.7). The grains are fine-grained subrounded to rectangular in habit, and pleochroic. Mineral chemistry reveals ferrosilite composition with high Al_2O_3 (0.21 to 0.53 wt.%), FeO (36.79 to 37.87 wt.%), MgO (10.02-10.38 wt.%) and low CaO, from 0.65 to 1.21 wt.%, Na_2O (0.00 to 0.04 wt.%), TiO_2 (0.00 to 0.97 wt.%).

Table 4-5. Representative analyses of orthopyroxene from Sunsas belt.

	San Pablo granite - Opx						
SiO_2	50.86	50.45	48.97	49.57	50.32	50.08	49.88
TiO_2	0.03	0.00	0.97	0.24	0.05	0.07	0.05
Al_2O_3	0.44	0.46	0.41	0.32	0.53	0.43	0.50
Cr_2O_3	0.36	0.32	0.09	0.57	0.08	0.00	0.00
MgO	10.02	10.31	10.09	10.38	10.18	10.16	10.14
CaO	1.21	0.70	0.67	0.66	0.73	0.65	0.71
MnO	1.00	1.24	1.49	1.36	1.27	1.06	1.35
FeO	37.05	37.82	37.87	37.85	36.98	37.31	36.79
NiO	0.00	0.00	0.05	0.04	0.00	0.00	0.06
Na2O	0.04	0.00	0.02	0.02	0.00	0.00	0.04
Total	101	101	101	101	100	100	100
Normalization based on 6 oxygens							
Si	2.03	2.02	1.98	2.00	2.03	2.03	2.03
Ti	0.00	0.00	0.03	0.01	0.00	0.00	0.00
Al	0.02	0.02	0.02	0.02	0.03	0.02	0.02
Cr	0.01	0.01	0.00	0.02	0.00	0.00	0.00
Mg	0.63	0.62	0.61	0.62	0.61	0.61	0.61
Ca	0.05	0.03	0.03	0.03	0.03	0.03	0.03
Mn	0.03	0.04	0.05	0.05	0.04	0.04	0.05
Fe^{2+}	1.24	1.27	1.28	1.28	1.25	1.27	1.25
Ni	0.00	0.00	0.00	0.00	0.00	0.00	0.00
Na	0.00	0.00	0.00	0.00	0.00	0.00	0.00
Total	4.01	4.01	4.00	4.02	4.00	4.00	4.00

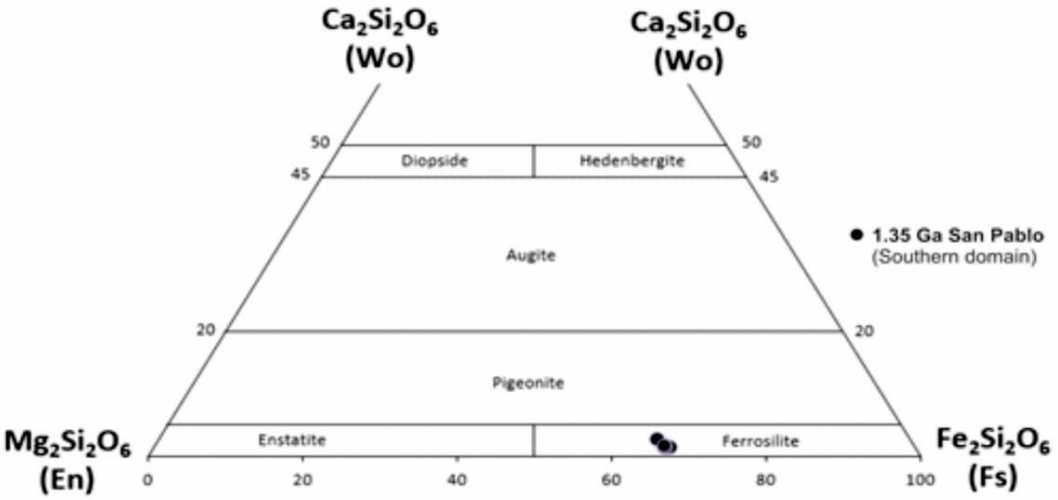

Figure 4.7. Mineral chemistry analyses in orthopyroxenes from San Pablo monzogranite, southern portion of Sunsas belt.

4.5.1.4 Amphibole

Amphibole crystals appear associated to pyroxene in the San Pablo monzogranite (Table 4.6). The hornblende grains occur as anhedral crystals replacing pyroxene and as isolated euhedral crystals. Relationships with plagioclase and biotite with straight contact indicate primary origin. The Hawthorne et al. (2012) scheme was used for classification and nomenclature. Based on chemistry, amphibole grains vary in Fe content. Hornblende presents Al^{+IV} ranging from 1.33 to 1.78 apfu, Mg from 1.43 to 1.72 apfu, Ti from 0.14 to 0.24 apfu, Na from 0.08 to 0.17 apfu, Ca from 1.70 to 1.86 apfu, and Si from 6.22 to 6.67 apfu. Ferro-hornblende shows Fe^{3+} ranging from 0.39 to 0.49 apfu and Fe^{2+} from 2.24 to 2.38 apfu and ferro-ferri-hornblende displays Fe^{3+} ranging from 0.43 to 0.92 apfu and Fe^{2+} from 2.07 to 2.41 apfu. TiO_2 contents vary from 1.23 to 2.01 wt.%, Al_2O_3 from 9.48 to 11.97 wt.%, and MgO from 6.07 to 7.14 wt.%.

Table 4-6. Analyses of the amphiboles from Sunsas belt.

	Sample						San Pablo				
	SiO_2	42.94	42.36	40.49	42.50	42.23	42.63	42.28	42.63	41.46	41.74
	TiO_2	1.23	1.40	1.53	1.76	1.72	1.66	1.50	1.73	2.01	1.75
	Al_2O_3	9.90	9.93	11.97	10.24	10.33	9.96	10.03	9.68	9.72	9.48
	FeO	21.63	21.60	21.95	22.76	22.66	22.55	22.63	22.03	21.69	21.90
	MnO	0.24	0.34	0.13	0.19	0.26	0.35	0.24	0.33	0.35	0.26
general formula $AB_2C_5T_8O_{22}W_2$	MgO	7.14	6.78	6.07	6.68	6.66	6.69	6.59	6.84	7.11	7.01
	CaO	10.18	10.56	10.25	10.52	10.56	10.44	10.29	10.22	10.67	10.52
	Na_2O	1.41	1.37	1.49	1.51	1.40	1.51	1.47	1.45	1.51	1.59
	Cr_2O_3	0.00	0.04	0.01	0.09	0.12	0.00	0.04	0.05	0.01	0.07
	V_2O_3	0.10	0.12	0.11	0.12	0.06	0.10	0.09	0.12	0.09	0.08
	NiO	0.00	0.01	0.02	0.07	0.02	0.00	0.01	0.05	0.06	0.00
	Total	94.77	94.51	94.00	96.41	96.01	95.88	95.17	95.11	94.69	94.39
	Si	6.67	6.63	6.38	6.54	6.52	6.60	6.59	6.63	6.50	6.22
T (8 apfu)	Al^{+IV}	1.33	1.37	1.62	1.46	1.48	1.40	1.41	1.37	1.50	1.78
	T subtotal	8.00	8.00	8.00	8.00	8.00	8.00	8.00	8.00	8.00	8.00
	Ti	0.14	0.16	0.18	0.20	0.20	0.19	0.18	0.20	0.24	0.22
	Al	0.48	0.46	0.60	0.40	0.40	0.41	0.43	0.41	0.29	0.06
	V	0.01	0.02	0.01	0.01	0.01	0.01	0.01	0.01	0.01	0.01
	Cr		0.01	0.00	0.01	0.02		0.01	0.01	0.00	0.01
C (5 apfu)	Fe^{3+}	0.47	0.39	0.49	0.46	0.51	0.43	0.47	0.44	0.49	0.92
	Ni		0.00	0.00	0.01	0.00		0.00	0.01	0.01	
	Fe^{2+}	2.24	2.38	2.30	2.37	2.34	2.41	2.38	2.34	2.30	2.07
	Mg	1.65	1.58	1.43	1.53	1.53	1.54	1.53	1.59	1.66	1.72
	C subtotal	5.00	5.00	5.00	5.00	5.00	5.00	5.00	5.00	5.00	5.00
AB (2	Mn^{2+}	0.03	0.05	0.02	0.02	0.03	0.05	0.03	0.04	0.05	0.04

apfu)											
	Fe^{2+}	0.10	0.06	0.11	0.10	0.09	0.08	0.10	0.08	0.05	0.03
	Ca	1.70	1.77	1.73	1.74	1.75	1.73	1.72	1.70	1.79	1.86
	Na	0.17	0.12	0.14	0.14	0.14	0.15	0.15	0.17	0.11	0.08
	Total	2.00	2.00	2.00	2.00	2.00	2.00	2.00	2.00	2.00	2.00
	Species	ferro-hornblende	ferro-hornblende	ferro-hornblende	ferro-ferri-hornblende	ferro-ferri-hornblende	ferro-ferri-hornblende	ferro-ferri-hornblende	ferro-ferri-hornblende	ferro-ferri-hornblende	ferro-ferri-hornblende

4.5.2 Whole-rock geochemical composition

4.5.2.1 Major elements

The Harker diagrams of major elements taking SiO_2 as fractionation factor show more primitive magmas in the southern Sunsas belt and more fractioned granites in the north (Table 4.7, Fig. 4.8). Northern granites show increase of CaO (0.17 to 2.61 wt.%), MgO (0.05 to 1.63 wt.%), TiO_2 (0.05 to 0.63 wt.%), and FeO (0.64 to 4.17 wt.%) with decreasing SiO_2 (76.40 to 67.40 wt.%) (Fig. 4.8). Fe_2O and TiO_2 show negative correlation indicating fractionation of biotite. The Salinas monzogranite presents the highest contents of Ca (2.61 wt.%), Mg (1.63 wt.%), Fe (4.17 wt.%), and Ti (0.63 wt.%) (Fig. 4.8) indicating the more primitive composition in the northern portion. The progressive decrease in concentrations of FeO (7.72 to 0.64 wt.%) and TiO_2 (1.15 to 0.05 wt.%) of the northern granite samples show a regular trend (Fig. 4.8C, D), indicating a more homogeneous geochemical path compared to the southern portion magmatism.

For southern granites, the Harker diagrams of CaO and MgO versus SiO_2 show two compositional groups, one more primitive with CaO contents ranging from 2.86 to 3.45 wt.% and MgO from 1.23 to 1.63 wt.%, and the second group of higher differentiated granites that form a progressively decreasing trend in CaO (1.07 to 1.32 wt. %) and MgO (0.25 to 0.45 wt. %) with increasing SiO_2 (71.90 to 74.10 wt.%) (Fig. 4.8A, B). Fe and Ti present positive correlation to SiO_2, forming a trend from more primitive (Fe of 7.72 wt.%; Ti of 1.15 wt.%) to fractionated granites (Fe 1.33 wt.%; Ti 0.14 wt.%).

The diagram of Na_2O versus SiO_2 shows that the Na concentration is not controlled by silica increase (Fig. 4.8E). Na-rich northern granites (Na from 3.93 to 4.09 wt.%) indicate crystallization of plagioclase whereas granites with Na contents between 2.68 to 3.61 wt.% have lower plagioclase concentration**.** Southern granites present the same distribution pattern, with Na contents ranging from 4.21 to 4.22 in plagioclase-rich granites and from 3.18 to 3.44 for granites with lower plagioclase concentration. On the other hand, K_2O concentrations are strongly compatible with increasing SiO_2 (Fig. 4.8), also reflecting K-feldspar crystallization, higher in northern granites (4.08 to 5.94 wt.% K_2O; e.g. Nocemano granite) compared to southern granites (2.83 to 4.79 wt.% K_2O; e.g. Tauca granodiorite).

Table 4-7. Geochemistry analyses of Sunsas belt magmatism.

Granite	Nocemano	La Asunta	Casa de Piedra				Salinas	San Ramón		Sujalito	San Pablo	Tasseoro	Señoritas	Las Tojas	Tauca	Nomoca
Terrane/Block			Sunsas north domain								Sunsas south domain					
Sample	SM-07A	LA14	ID18	ID19	ID20	ID21	SM-10	ID11	ID11B	SR20	ID02	TAS15	ID06	ID08	ID09	TAP02
SiO2	70.40	74.90	73.50	70.90	73.60	72.40	67.40	76.40	77.30	72.70	64.30	74.10	73.70	71.90	66.70	67.30
Al2O3	14.00	13.85	14.40	14.15	14.45	13.60	14.70	13.00	12.65	13.50	14.20	13.05	13.95	14.15	14.95	16.45
Fe2O3	3.31	2.26	2.03	2.74	2.07	1.97	4.17	1.31	0.64	1.92	7.72	2.17	1.33	1.81	4.69	3.81
MnO	0.03	0.03	0.04	0.05	0.03	0.04	0.07	0.01	<0.01	0.05	0.14	0.06	0.04	0.02	0.08	0.06
MgO	0.56	0.34	0.44	0.73	0.41	0.41	1.63	0.17	0.05	0.72	1.63	0.45	0.25	0.37	1.23	1.61
CaO	1.30	0.92	1.22	1.36	1.32	0.76	2.61	0.17	0.48	1.62	3.45	1.25	1.07	1.32	2.86	2.88
Na2O	2.68	3.16	4.01	4.09	3.93	3.99	3.61	3.32	3.07	3.25	3.18	3.24	4.22	3.44	3.29	4.21
K2O	5.94	5.14	4.92	5.18	4.98	4.82	4.04	5.44	5.65	4.08	3.91	4.78	4.03	5.09	2.83	2.88
P2O5	0.15	0.05	0.10	0.21	0.09	0.09	0.21	0.01	<0.01	0.08	0.32	0.11	0.08	0.04	0.19	0.21
TiO2	0.50	0.24	0.30	0.42	0.29	0.27	0.63	0.13	0.05	0.32	1.15	0.39	0.14	0.26	0.63	0.54
Cr2O3	<0.01	<0.01	<0.002	<0.002	<0.002	<0.002	0.01	<0.002	<0.002	<0.01	0.01	<0.01	<0.002	<0.002	<0.002	0.01
LOI	1.06	0.72	0.67	0.48	0.58	0.70	1.43	1.08	0.34	1.44	0.25	1.46	0.44	0.48	2.13	1.41
TOTAL	99.93	101.61	101.63	100.31	101.75	99.05	100.51	101.04	100.23	99.68	100.26	101.06	99.25	98.88	99.58	101.37
Mg#	23.17	21.15	27.87	32.20	26.09	27.06	41.06	18.79	12.22	40.06	27.35	26.99	25.10	26.71	31.86	42.96
Sc	5.00	4.00	3.00	4.00	3.00	3.00	11.00	<1	<1	7.00	18.00	6.00	2.00	2.00	11.00	7.00
V	33.00	16.00	20.00	29.00	26.00	20.00	64.00	14.00	5.00	18.00	89.00	29.00	6.00	16.00	56.00	80.00
Cr	10.00	10.00	30.00	30.00	30.00	30.00	40.00	30.00	30.00	20.00	60.00	10.00	20.00	30.00	40.00	90.00
Co	4.00	2.00	3.00	3.00	2.00	2.00	10.00	2.00	<1	132.00	12.00	3.00	1.00	2.00	7.00	9.00
Ni	2.00	1.00	2.00	8.00	<1	<1	18.00	<1	1.00	3.00	13.00	2.00	<1	1.00	8.00	26.00
Cu	3.00	5.00	2.00	7.00	10.00	3.00	40.00	1.00	2.00	1.00	24.00	8.00	27.00	12.00	16.00	378.00
Zn	85.00	48.00	53.00	67.00	55.00	47.00	77.00	16.00	3.00	28.00	115.00	35.00	48.00	45.00	55.00	98.00
Ga	22.60	20.10	27.30	28.20	27.20	24.80	22.10	16.20	16.60	18.00	24.00	21.10	23.60	25.50	20.70	25.90
Rb	305.00	214.00	302.00	305.00	275.00	228.00	162.00	74.70	70.20	204.00	137.50	410.00	357.00	286.00	121.00	164.00

Granite	Nocemano	La Asunta	Casa de Piedra				Salinas	San Ramón		Sujalito	San Pablo	Tasseoro	Señoritas	Las Tojas	Tauca	Nomoca
Terrane/Block			Sunsas north domain								Sunsas south domain					
Sr	139.00	167.00	401.00	697.00	364.00	566.00	577.00	231.00	307.00	109.00	220.00	156.50	122.00	375.00	347.00	395.00
Y	22.20	15.70	19.90	21.20	13.60	17.50	35.90	3.40	0.40	41.40	49.10	27.30	9.00	8.50	31.30	17.90
Zr	447.00	267.00	193.00	342.00	254.00	239.00	243.00	63.00	10.00	252.00	402.00	267.00	105.00	217.00	253.00	383.00
Nb	14.70	12.70	18.80	16.80	16.00	16.30	14.40	1.00	0.20	14.70	25.30	21.80	15.20	9.60	9.20	12.50
Cs	1.34	3.09	8.74	9.09	5.34	3.54	6.89	0.16	0.11	2.85	0.94	6.26	8.55	6.38	3.54	2.78
Ba	784.00	733.00	1220.00	2030.00	1215.00	1700.00	1470.00	1315.00	1110.00	827.00	1315.00	646.00	396.00	1335.00	1065.00	542.00
Hf	13.40	8.10	5.40	8.70	6.90	6.60	6.70	1.60	0.30	6.70	9.90	8.70	3.30	5.90	6.70	9.40
Ta	0.30	0.60	1.50	1.30	1.50	1.40	1.50	<0.1	<0.1	2.40	1.50	1.40	2.10	1.00	0.80	1.30
Pb	38.00	29.00	65.00	93.00	56.00	81.00	21.00	12.00	18.00	22.00	11.00	44.00	45.00	56.00	12.00	19.00
Th	83.60	59.90	45.80	45.50	37.90	51.60	13.15	1.52	0.41	24.60	5.79	67.90	32.70	54.60	10.25	33.60
U	1.71	5.71	6.23	12.60	7.67	5.09	5.01	0.35	0.10	4.71	0.78	12.15	3.86	6.68	1.83	4.58
La	171.50	115.00	117.00	116.50	86.90	106.50	53.80	34.20	8.40	48.90	53.50	100.50	39.10	90.60	49.10	74.30
Ce	397.00	242.00	152.50	232.00	161.00	184.00	122.00	24.80	8.20	102.00	108.50	170.50	67.60	158.00	99.70	141.00
Pr	41.70	24.50	18.40	21.40	15.60	17.75	13.60	4.26	0.66	11.85	12.75	15.25	6.18	14.65	11.00	12.95
Nd	141.50	81.40	64.60	74.00	53.20	59.60	52.90	13.50	1.90	44.20	53.60	48.00	21.20	49.70	44.00	43.00
Sm	22.80	13.20	8.03	10.85	7.39	7.13	9.20	1.59	0.20	8.64	11.25	6.96	3.43	6.23	8.61	6.61
Eu	1.42	1.06	1.41	2.08	1.13	1.45	1.73	1.17	0.88	1.44	2.81	1.08	0.55	0.99	1.56	1.38
Gd	11.15	7.92	5.14	6.11	3.97	4.77	7.22	1.03	0.15	7.80	9.78	5.44	1.97	3.23	6.67	4.28
Tb	1.39	0.98	0.61	0.79	0.57	0.54	1.06	0.14	0.04	1.18	1.57	0.78	0.32	0.36	1.07	0.59
Dy	5.90	4.45	3.10	4.27	2.51	3.18	6.18	0.52	<0.05	7.68	8.84	4.52	1.71	1.70	6.11	3.46
Ho	0.91	0.60	0.57	0.67	0.41	0.56	1.32	0.09	<0.01	1.49	1.76	0.93	0.26	0.29	1.10	0.58
Er	2.01	1.34	1.60	1.90	1.05	1.56	3.51	0.38	0.09	4.39	5.22	3.12	0.88	0.74	3.22	1.77
Tm	0.23	0.17	0.23	0.26	0.19	0.29	0.52	0.05	0.05	0.71	0.75	0.47	0.18	0.14	0.46	0.23
Yb	1.30	1.04	1.27	1.41	1.11	1.70	3.05	0.24	0.03	4.11	4.53	3.43	0.91	0.60	3.02	1.65
Lu	0.20	0.22	0.22	0.22	0.17	0.27	0.53	0.06	0.01	0.63	0.70	0.64	0.14	0.10	0.44	0.25

Granite	Nocemano	La Asunta	Casa de Piedra				Salinas	San Ramón		Sujalito	San Pablo	Tasseoro	Señoritas	Las Tojas	Tauca	Nomoca
Terrane/Block					Sunsas north domain								Sunsas south domain			
Eu/Eu*	0.14	0.16	0.35	0.40	0.33	0.39	0.34	1.45	8.04	0.28	0.42	0.28	0.33	0.35	0.33	0.41

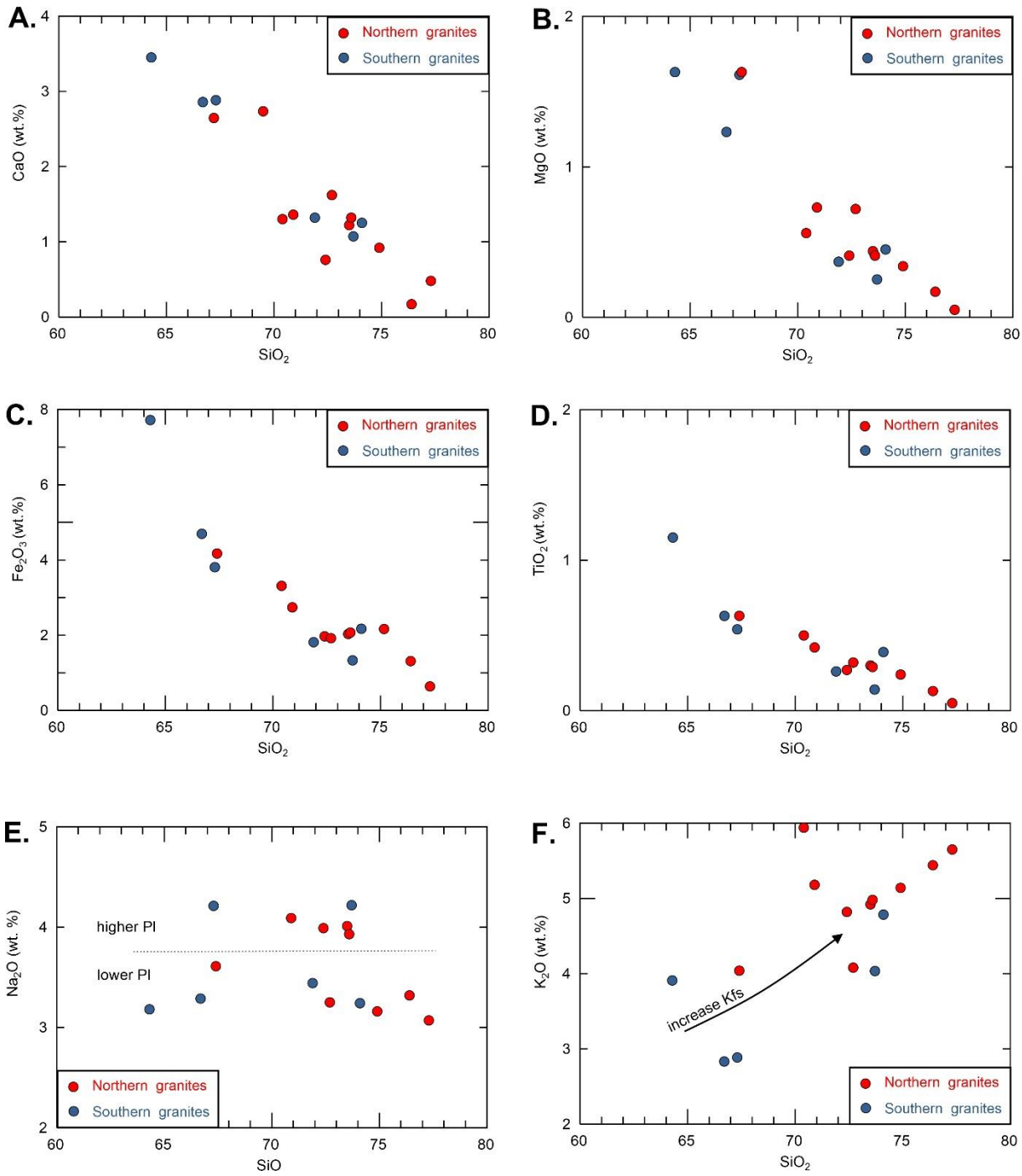

Figure 4.8. Harker diagrams of major elements versus Si02 of the southern and northern granites in the Sunsas belt.

In the AFM diagram (Irvine and Baragar, 1971), the studied plutons show calc-alkaline geochemical affinity, with a well-defined alkali enrichment trend from the northern (e.g. San Ramón granite) to southern granites (e.g. San Pablo monzogranite), that show more affinity with the tholeiitic series (Fig. 4.9A). The Na_2O+K_2O-CaO diagram versus SiO_2 (Frost et al., 2001) shows the fractionation of northern granites in relation to southern plutons. The Casa de Piedra monzogranite,

and San Ramón and Nocemano granites present a compatible pattern with more fractionated alkali-calcium (K_2O ~5.5 wt.%) evolution, although the calc-alkaline series is the main evolutionary trend recorded in the studied rocks (Fig. 4.9B). The Salinas monzogranite (K_2O ~4.04 wt.%), despite being in the northern portion, presents a less fractionated pattern (Fig. 4.9B).

In the Al/(Na+K) per Al/(Ca+Na+ K) diagram (Shand, 1943), the granitic bodies show metalluminous to peraluminous character (Fig. 4.9C), recording the fractionation of the San Pablo monzogranite compared to the San Ramón granite in both depletion of aluminum (16.45 to 12.65 wt.%) and calcium (3.45 to 0.17 wt. %). Granites from the southern portion show a group of three plutons with higher contents of Al_2O_3 (14.2 to 16.45 wt.%) and CaO (2.86 to 3.45 wt.%), and less K_2O (2.83 to 3.91 wt.%) that result in a high Al/(Na+K) ratio (Fig. 4.9C). The compositional transition from magnesian to ferrous magma in Harker diagrams is also evident in the $FeO_t/(FeO_t+MgO)$ versus SiO_2 diagram (Frost et al., 2001). The $FeO_t/(FeO_t+MgO)$ ratio ranges from 0.6 to 1 (Fig. 4.9D), reflecting decreasing MgO contents from 1.63 wt.% (Nomoca granodiorite, Salinas monzogranite) to only 0.05 wt.% (San Ramón granite). The three south plutons detached in the Al/(Na+K) per Al/(Ca+Na+ K) diagram due to the higher Al contents, also present a pattern compatible with more primitive magmas in the $FeO_t/(FeO_t+MgO)$ versus SiO_2 diagram, with higher MgO (1.23 to 1.63 wt.%) and FeO (3.81 to 7.72 wt.%) contents (Fig. 4.9D).

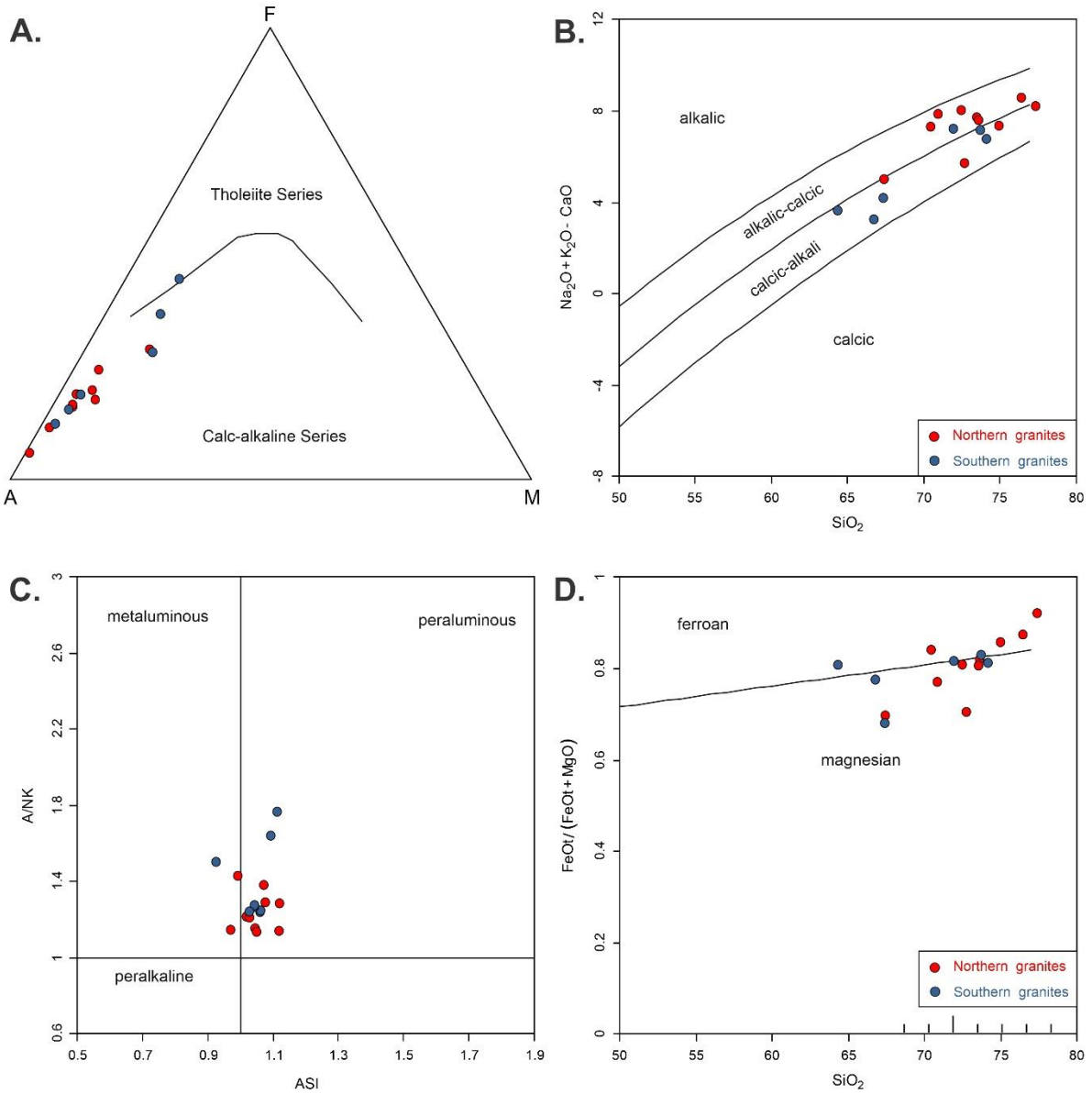

Figure 4.9. Discriminant diagrams of the studied Sunsas granitoids. (A) AFM diagram from Irvine and Baragar (1971); (B) Na2O+K2O-CaO versus SiO2 (Frost et al., 2001); (C) A/NK [= (Al/Na+K)] versus A/CNK [= (Al+Na+K)] (Shand, 1943); (D) FeOt/(FeOt-MgO) versus SiO2 (Frost et al., 2001).

4.5.2.2 Trace and rare-earth elements

The trace elements as barium and thorium, despite having a large compositional range (398 to 2030 ppm Ba, and 0.4 to 83 ppm Th) do not define an enrichment or depletion trend due to silicon content. However, the Rb diagram (Fig. 4.10K) shows enrichment in the southern granites (121 ppm in the Tauca granodiorite, to 410 ppm in the Tasseoro granite), while for the northern granites the concentrations of Rb decrease (305 ppm in the the Casa de Piedra, to 70 ppm in the San Ramón) as SiO_2 increases. Therefore, although the southern and northern granites have similar

mineralogy, they present different chemical paths (Fig. 4.10A-F). The Sr diagram suggests a high complexity in the chemical evolution of the granitic magmatism in the Sunsas Belt, indicating at least three trends of Sr fractionation as a function of the SiO_2 contents at 65 wt.%, 70 wt.% 75 wt.% (Fig. 4.10L).

The REE primitive mantle-normalized discriminant diagram (Sun and McDonough, 1989) defines the slight enrichment of the heavy REE in south granites (Tb/Yb)N=1.03 to 2.73, and higher fractionation of light rare earth elements (LREE), (La/Sm)N=3.07 to 9.39, with a discrete negative Eu anomaly (Eu/Eu*=~0.60) (Fig. 4.10G-J). The Señoritas two-mica granite shows higher HREE fractionation (Tb/Yb)N=2.73, and lesser LREE enrichment, (La/Sm)N= 9.39. The northern granites show a higher LREE enrichment, (La/Sm)N=3.65 to 9.64, and higher fractionation of HREE, (Tb/Yb)N=1.31 to 4.86, with a pronounced negative Eu anomaly (Eu/Eu*=~0.60) (Fig. 4.10A). The Salinas and Sujalito granites show smaller LREE enrichment, (La/Sm)N=3.78 and 3.65, respectively, and low fractionation of HREE, (Tb/Yb)N=1.58 and 1.31 (Fig. 4.10C). The San Ramón granite defines an incompatible pattern in relation to the other plutons with higher LREE enrichment, (La/Sm)N=13.89 to 27.11, higher fractionation of HREE, (Tb/Yb)N=2.65 to 6.06, and positive Eu anomaly (Eu/Eu*=~15). The primitive mantle-normalized multielement diagram (McDonough and Sun, 1995) shows significant negative anomalies of Ti, P, Nb, Ta and less significative of Ba and positive anomalies of Th, Pb and U (Fig. 4.10B). The northern plutons also present Sm and Nd positive anomalies. The San Ramón granite shows a different pattern, with more pronounced anomalies and depletion of Yb, P, Pr, Ce, Nb, Th and Cs, besides being more enriched in Eu, Sr, Pb, K and Ba (Fig. 4.10B).

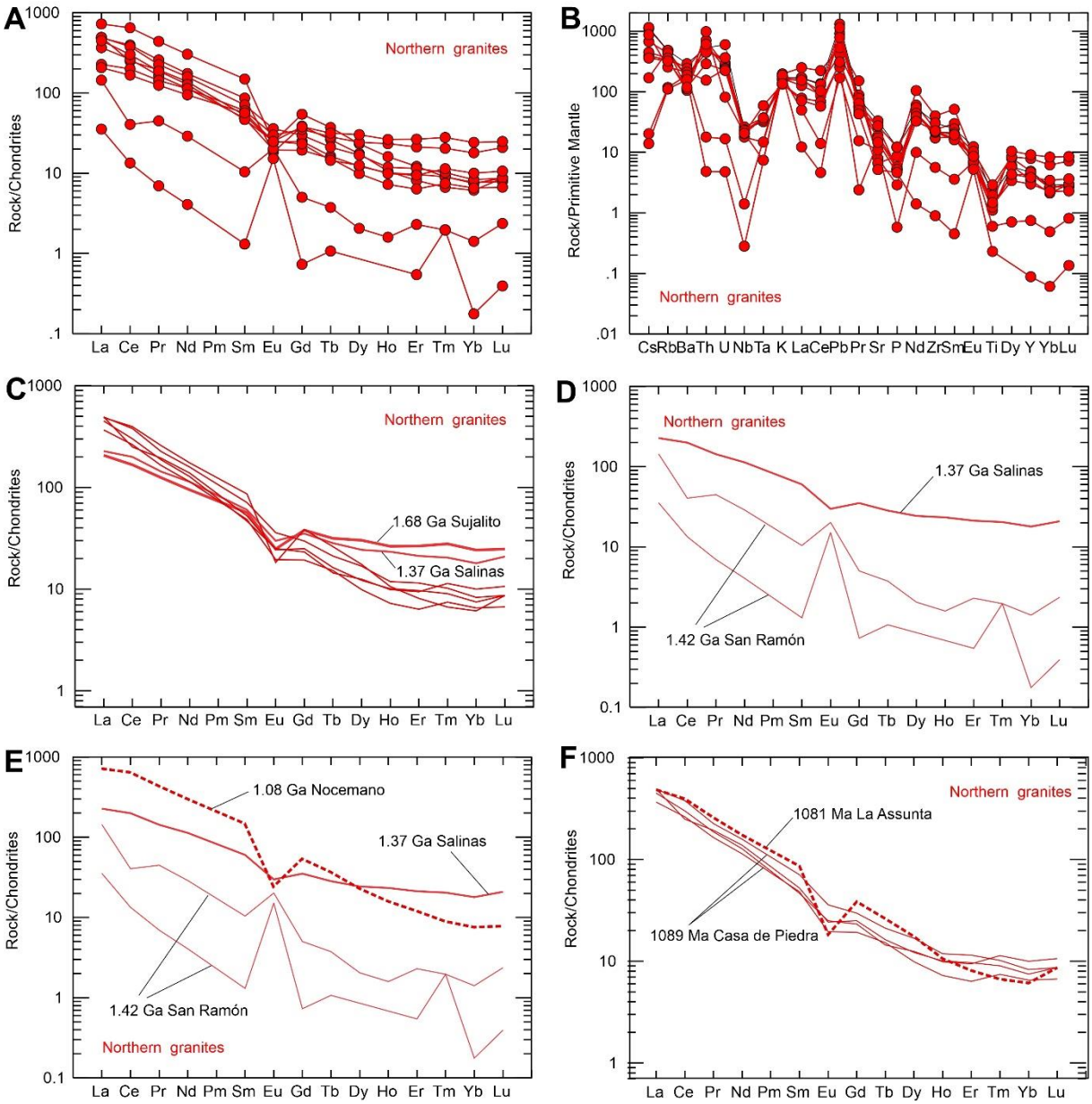
A
Rock/Chondrites
Northern granites
La Ce Pr Nd Pm Sm Eu Gd Tb Dy Ho Er Tm Yb Lu
B
Rock/Primitive Mantle
Northern granites
Cs Rb Ba Th U Nb Ta K La Ce Pb Pr Sr P Nd Zr Sm Eu Ti Dy Y Yb Lu
C
Rock/Chondrites
Northern granites
1.68 Ga Sujalito
1.37 Ga Salinas
D
Rock/Chondrites
Northern granites
1.37 Ga Salinas
1.42 Ga San Ramón
E
Rock/Chondrites
1.08 Ga Nocemano
1.37 Ga Salinas
1.42 Ga San Ramón
Northern granites
F
Rock/Chondrites
Northern granites
1081 Ma La Assunta
1089 Ma Casa de Piedra

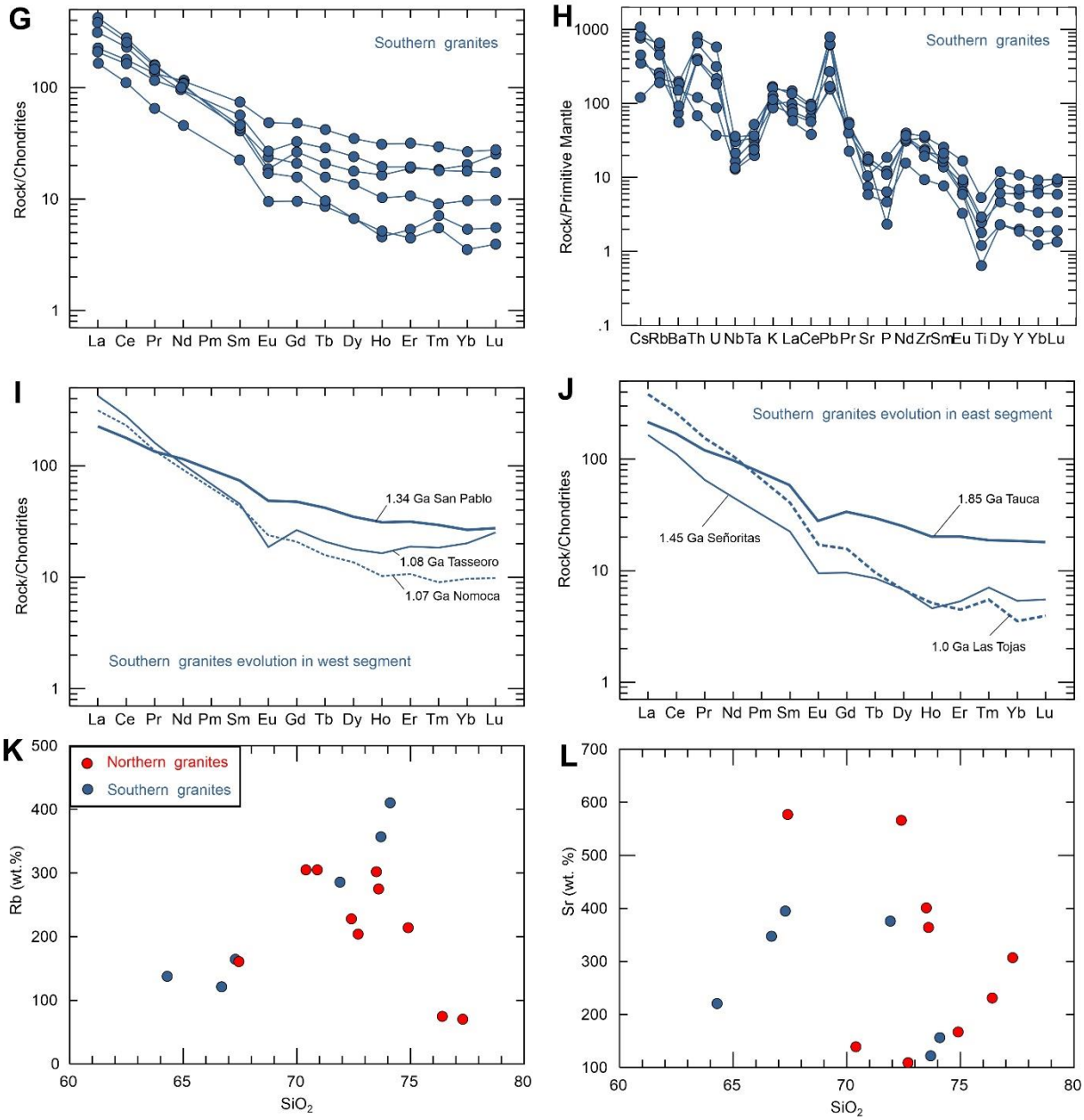

Figure 4.10. (A-F) Primitive mantle-normalized REE fractionation diagrams for the northern granites from the Sunsas Belt according to Sun and McDonough (1989); (G-J) Primitive mantle-normalized REE fractionation diagrams for the southern granites from the Sunsas Belt according to Sun and McDonough (1989); (K) Rb vs. SiO2 diagram of northern and southern granites; (L) Sr vs. SiO2 diagram of northern and southern granites.

4.5.3 Sr and Nd isotopic compositions

The Sr-Nd isotopic signatures of the sixteen studied granites were calculated on the basis of their zircon U-Pb ages and are presented in Table 4.8. The northern granites have $^{143}Nd/^{144}Nd_{(t)}$ ratios between 0.510488 and 0.511124 and $^{87}Sr/^{86}Sr_{(t)}$ between 0.69685 and 0.84081, with positive to negative $\varepsilon Nd_{(t)}$ values ranging from -4.60 to 2.26. The southern granites show $^{143}Nd/^{144}Nd_{(t)}$ between 0.510470 and 0.511021, $^{87}Sr/^{86}Sr_{(t)}$ ranging from 0.69668 to 0.78307, and $\varepsilon Nd_{(t)}$ values between -6.52 and

0.43. All initial $^{87}Sr/^{86}Sr_{(t)}$ isotopic ratios less than the primitive Earth value of <0.700 cannot be real and must be considered as artefacts produced from the long extrapolation from very radiogenic data. However, the $^{143}Nd/^{144}Nd$ values are similar in north and south Sunsas Belt. The $^{87}Sr/^{86}Sr_{(t)}$ reaches the highest value in the northern Sujalito granite (0.84081), typical of high-K calc-alkaline magmas, and the lowest value in the southern Tauca granodiorite (0.70146), compatible with mantle derived magma signature. The $\varepsilon Nd_{(t)}$ values (Table 4.8) show larger negative to positive variation in northern granites, consistent with fractionation of mantle sources, and negative values in the southern granites, characteristic of granitic magmas from reworked crustal sources.

Furthermore, the $^{87}Sr/^{86}Sr_{(i)}$ vs. Ages (Ga) diagram (Fig. 4.11A) shows a pattern of increasing Sr in southern plutons as the magmatism becomes younger, resulting of increasing crustal reworking. The northern granites show high concentration of $^{87}Sr/^{86}Sr_{(i)}$ values around 0.700 that indicate the rebalance of magmatic source systems at 1.1 Ga. The Sujalito granite differs from the others by the more fractionated pattern with highest levels of $^{87}Sr/^{86}Sr_{(i)}$ (0.84081) and lowest of $^{143}Nd/^{144}Nd_{(i)}$ (0.510559) (Fig. 4.11B). The $^{143}Nd/^{144}Nd_{(i)}$ vs. ages diagram (Fig. 4.11C) shows a better-defined pattern for the studied plutons of increasing Nd as magmatism becomes younger. The Colmena and Tasseoro granites, situated in the central shear zone part of the San Diablo Front, accompanied by the Nocemano granite, present mixing isotopic signatures with average ratios between both patterns, probably resultant of system reopening at 1.1 and 1.3 Ga (Fig. 4.11C).

Table 4-8. Sm-Nd and Sr analyses of Sunsas belt granites.

Sample	Granite		Sm (ppm)	Nd (ppm)	$^{147}Sm/^{144}Nd$	$^{143}Nd/^{144}Nd_m$	$^{143}Nd/^{144}Nd_i$	$\varepsilon_{Nd(0)}$	$\varepsilon_{Nd(t)}$	T_{DM}(Ga)	$^{87}Sr/^{86}Sr_m$	$^{87}Sr/^{86}Sr_i$	U-Pb age (Ga)					
													Protoliths			*Crustal reworking*		
ID 18	Casa de Piedra	Northern granites	8.10	61.05	0.0802	0.511698	0.511124	-18.33	-2.09	1.53	0.73848	0.70439			1.76		1.28	1.09
SR 20	Sujalito		20.28	101.12	0.1212	0.511898	0.510559	-14.43	1.84	1.87	0.97496	0.84081			1.68			
ID 11	San Ramón		2.08	17.47	0.0719	0.511589	0.510918	-20.47	2.26	1.55	0.71592	0.69685				1.42		
SM 07	Nocemano		23.44	159.87	0.0886	0.511637	0.511009	-19.52	-4.60	1.70	0.8078	0.70873			1.69	1.41	1.37	1.10
IM 11	Miraflores		2.75	20.15	0.0824	0.511430	0.510520	-23.55	1.07	1.86					1.68			
IM 32	Santo Rosário		11.37	60.25	0.1141	0.511749	0.510488	-17.34	0.46	1.97					1.68			
LA 14	La Asunta		–	–	–	–	–	–	–		0.76562	0.70800			1.60		1.28	1.08
ID 06	Señoritas	Southern granites	1.42	8.75	0.0984	0.511608	0.510910	-20.10	-6.52	1.89	0.91658	0.78307	1.95			1.45		1.00
ID 08	Las Tojas		2.84	20.93	0.0820	0.511592	0.511011	-20.40	-5.74	1.67	0.74024	0.70858	1.94					0.99
ID 09	Tauca		8.76	46.91	0.1128	0.511523	0.510470	-21.75	-1.84	2.29	0.72837	0.70146		1.85				
ID 02(A)	San Pablo		9.45	47.26	0.1209	0.511832	0.510768	-15.72	-2.72	1.97	0.7471	0.71223					1.34	
ID 02(B)	San Pablo		9.50	47.52	0.1209	0.511786	0.510722	-16.61	-3.61	2.05	0.74716	0.71229					1.34	
TAS 15	Tasseoro		5.55	34.29	0.0978	0.511721	0.511021	-17.89	-4.23	1.73	0.81505	0.69668						1.08
IM 33	Colmena		10.62	56.97	0.1127	0.511813	0.510814	-16.09	-2.11	1.84	–	–					1.34	
IM 34	Colmena		4.24	20.664	0.1241	0.512040	0.510939	-11.67	0.43	1.69	–	–					1.34	
IM 35	Colmena		0.75	4.009	0.1130	0.511801	0.510799	-16.32	-2.39	1.86	–	–					1.34	
TAP 02	Nomoca		8.42	53.89	0.0944	0.51195	0.511281	-13.42	0.72	1.39	0.72527	0.70667	2.05	1.83	1.76	1.44	1.35	1.08

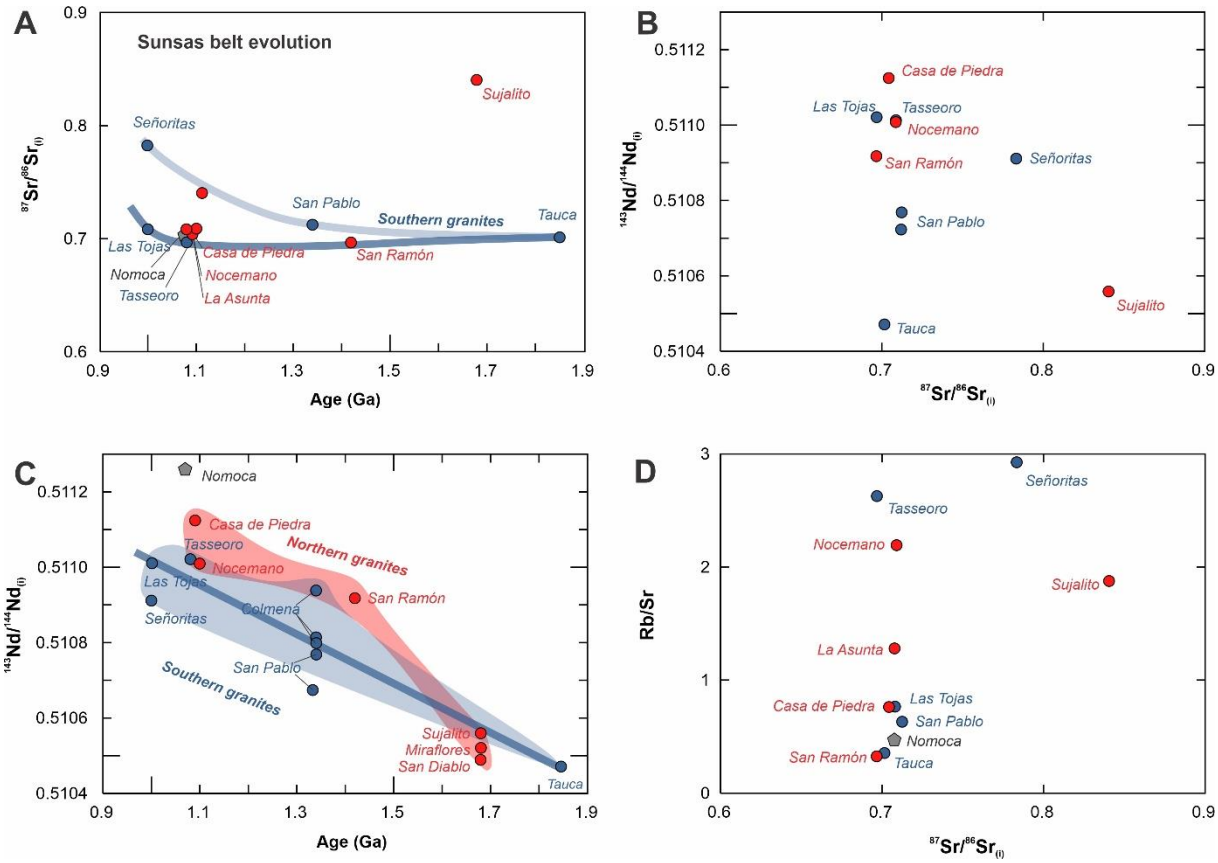

Figure 4.11. Isotopes diagrams of tectonic evolution and fractionation patterns for the Sunsas belt magmatism. (A) 87Sr/86Sr(i) vs. Ages (Ga); (B) 143Nd/144Nd(i) vs. 87Sr/86Sr(i); (C) 143Nd/144Nd(i) vs. Ages (Ga); (D) Rb/Sr vs. 87Sr/86Sr(i).

The depleted mantle model ages (T_{DM}) yielded in the analyzed whole-rock samples reflected the different sources signatures in southern and northern domains and can be divided in four groups. The oldest depleted mantle model (T_{DM}) age is 2.21 Ga of the Tauca granodiorite, with $\varepsilon Nd_{(t)}$ value at 1.8 Ga of -1.84 (Fig. 4.12A). These data imply that Tauca originated from Rhyacian protoliths with a short crustal residence and some crustal contribution by partial melting. The T_{DM} ages from 1.99 to 1.81 Ga are dominantly from southern granites, with the exception of Sujalito, recorded in plutons of 1.6 Ga (Chiquitania Complex) and 1.45-1.3 Ga (San Ignacio magmatism). The $\varepsilon Nd_{(t)}$ values at 1.6 Ga vary from 0.46 to 1.07 and at 1.45-1.3 Ga between -3.61 and -2.11. The $\varepsilon Nd_{(t)}$ value in the Sujalito granite is 1.84.

The southern basement isotopic data show positive $\varepsilon Nd_{(t)}$ values for poorly differentiated sources compared with the San Ignacio magmatism (1.3 Ga) that presents negative $\varepsilon Nd_{(t)}$, compatible with evolution from crustal melting. Part of the Sunsas magmatism preserved the isotopic signatures from sources with T_{DM} ages from 1.71 to 1.65 Ga and $\varepsilon Nd_{(t)}$ at 1.08 Ga between -4.23 and -5.74. These data are

consistent with evolution from partial melting of the Chiquitania-Lomas Manechis complexes, with strong crustal contribution, also evident in inherited zircon crystals presented previously (Fig. 4.12B). The Colmena granite yielded a T_{DM} age of 1.67 Ga with $\varepsilon Nd_{(t)}$ at 1.3 Ga of 0.43, indicating crustal sources with subordinate juvenile input. The youngest T_{DM} ages of 1.39 to 1.55 Ga, with $\varepsilon Nd_{(t)}$ at 1.45 Ga of 2.26 and at 1.08 Ga between -2.09 and 0.72, show a reopening of the isotopic systems compatible with San Ignacio orogenic times, that homogenized the isotopic signatures of the original sources.

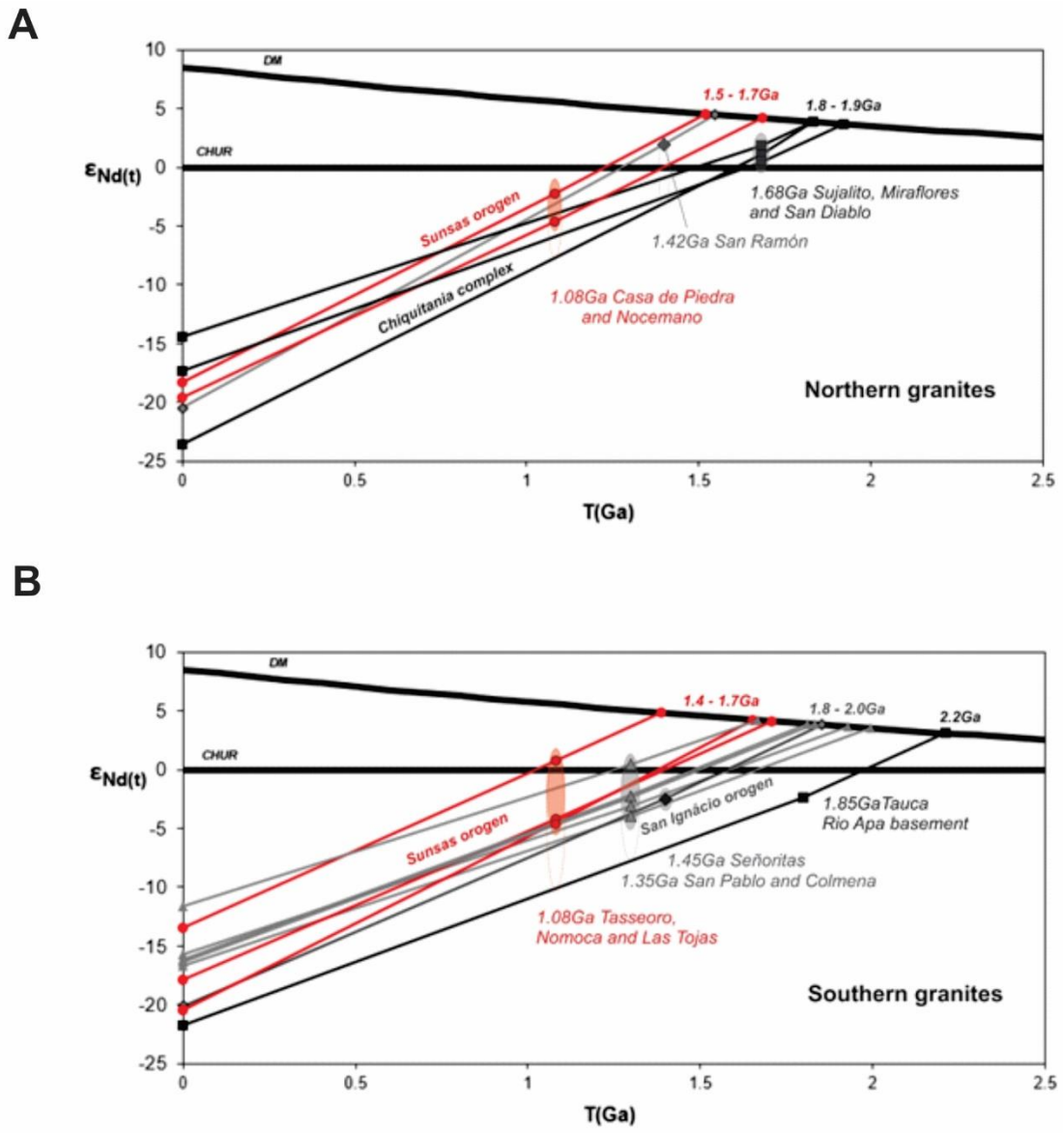

Figure 4.12. Nd isotope evolution of Sunsas belt granites. (A) Nd isotopes of northern granites; (B) Nd isotopes of southern granites.

4.6 Discussion

All granite samples studied in this work were previously dated by U-Pb on zircon and monazite (Nedel et al., 2020a, b). The data revealed that the Sunsas belt record several Proterozoic magmatic events from 1.95 to 0.95 Ga. The crystallization and metamorphic ages (Table 4.1) were used to integrate the mineral composition, geochemical and isotopic data from the studied granites.

4.6.1 Geochemical evolution

The geochemical compositions of igneous rocks reflect their source characteristics (e.g., Zhou et al., 2006; Condie and Kröner, 2013; Hagen-Peter and Cottle, 2018; Brown et al., 2020; Nedel et al., 2020a). For the northern granites, the lower LREE/HREE ratios and stronger negative Eu, Nb, and Ti anomalies of the 1.68 Ga old Sujalito granite, suggest that it represents the less evolved protolith (Fig. 4.10A, C). The 1.37 Ga Salinas granite is more fractionated in LREE, with minor negative anomalies of Eu, Nb, and Ti compared to the Sujalito granite (Fig. 4.10D, E). It corroborates the hypothesis that the 1.68 Ga granitic protolith was reworked during c. 1.37 Ga partial melting events (Nedel et al., 2020a, b). The younger 1.08 Ga old La Asunta, Nocemano and Casa de Piedra granites have lower HREE contents and are mostly enriched in LREE when compared to older granites (Fig. 4.10F). Therefore, the incompatible element compositions are controlled by minerals in the source or crystallized during melting fractionation processes. That is, the REE and trace element patterns reflect more the presence and amount of minerals of the melting source than those that are actually in the crystallized rock. Thus, the REE compositions show a progressive fractionation likely from the same 1.68 (Sujalito) source to 1.08 Ga (Nocemano) granitic magmatism episodes in the northern domain of the Sunsas belt. On the other hand, the 1.42 Ga old San Ramón granite presents a different geochemical composition even when compared to the nearest granite in age (1.37 Ga Salinas). The lower HREE contents, higher $(La/Lu)_N$ ratios (up to 100) and positive Eu anomaly (Fig. 4.10D, E) suggest that the San Ramón was derived from a different and plagioclase-garnet-bearing source. Thus, combined geochronology and geochemical results for the northern portion suggest that the Sunsas belt evolved from a 1.68 Ga old felsic protolith with minor ~1.42 Ga old mafic contribution.

For the Sunsas belt south domain, the geochemical composition shows more homogenous trace element patterns, with stronger negative Nb, Ta and Ti anomalies (Fig. 4.10C, D). However, in the west segment, the 1.34 Ga old San Pablo granite has higher HREE contents and shows less a fractionated LREE/HREE ratio when compared to the younger Tasseoro and Nomoca granites. It may suggest diachronic and progressive crustal reworking. For the east segment in the south domain, the 1.85 Ga Tauca granodiorite displays higher HREE content and lower LREE/HREE ratio, reflecting the most primitive composition (Fig. 4.10G, I). In contrast, the Las Tojas granite, dated at 1.95 Ga by U-Pb zircon and 1.0 Ga by U-Pb monazite, presents lower HREE content and higher LREE/HREE ratio, representing the most evolved composition. Lastly, the 1.45 Ga Señoritas granite has similar REE compositions and patterns to the Las Tojas granite (Fig. 4.10G, J). U-Pb monazite ages from the Señoritas granite also indicate an isotopic system opening at 1.0 Ga similar to that recorded in the Las Tojas granite (Nedel et al., 2020b). Thus, in the southern domain, the 1.85 Ga Tauca granite may represent the felsic protolith that was reworked at c. 1.45 Ga and c. 1.08 Ga, whereas the San Pablo granodiorite may reflect a mafic episode at 1.34 Ga with juvenile contributions.

4.6.2 Isotope constraints

In the northern domain of the Sunsas belt, the 1.42 Ga old San Ramón granite presents a lower initial $^{87}Sr/^{86}Sr$ value of 0.696 and positive $\varepsilon Nd_{(t)}$ of 2.26. It confirms that the San Ramón intrusion was generated from mantle-derived magmas with minor continental crust contribution. In contrast, the 1.68 Ga old Sujalito granite has a higher initial $^{87}Sr/^{86}Sr$ value of 0.840, supporting a crustal source. However, positive $\varepsilon Nd_{(t)}$ of 1.87 also recorded in the Sujalito granite suggests a juvenile source for the ~1.68 Ga magmatism. Lastly, c. 1.08 Ga Stenian granites have negative $\varepsilon Nd_{(t)}$ values and intermediary initial $^{87}Sr/^{86}Sr$ values (0.704 to 0.708), close to the San Ramón pluton (Fig. 4.12A). Therefore, Sr and Nd isotopic data support a crucial crustal reworking of the Paleoproterozoic protoliths with T_{DM} model ages between 1.53 and 1.97 Ga during the evolution of the northern domain. Moreover, mantle-derived sources also played an important role mainly for the 1.68 and 1.44 Ga magmatism.

In the Sunsas belt southern domain, the 1.85 Ga Tauca granodiorite shows low initial $^{87}Sr/^{86}Sr$ value (0.701) and negative $\varepsilon Nd_{(t)}$ (-1.84) with lower initial $^{143}Nd/^{144}Nd$ (0.5104). The initial $^{143}Nd/^{144}Nd$ ratios (Fig. 4.11C) and $\varepsilon Nd_{(t)}$ values (Fig. 4.11C,

12B) from the older Tauca granodiorite to the younger granites define a linear fractionation trend. It indicates a progressive crustal reworking at c. 1.42–1.35 Ga and c. 1.08 Ga from felsic protolith similar to the 1.85 Ga old Tauca granodiorite (Fig. 4.11C, 12B). Moreover, the Señoritas ($^{87}Sr/^{86}Sr_i$=0.783) and Nomoca ($^{143}Nd/^{144}Nd_i$ = 0.5112) granites can be interpreted as more fractionated end-members (Fig. 4.11C, D, 4.12B). Therefore, Nd and Sr isotopic data of the southern granites reveal pervasive crustal reworking of Paleoproterozoic protoliths with T_{DM} model ages between 1.8 and 2.2 Ga.

4.6.3 Petrogenesis and crustal reworking

The magmatic rock composition is a result of the mineral assemblage crystallized during melting fractionation processes (e.g., Gardien et al., 2000; Watkins et al., 2007; Rubatto et al., 2009; Ferreira et al., 2020). However, magmatic rock compositions reflect the mineral phases in the residue (or cumulates) that did not retain the incompatible elements in their crystalline structures (e.g., Gardien et al., 2000; Rubatto et al., 2009). The mineral compositions are controlled by partition coefficients ($D = c_{mineral}/c_{melt} < 0.1$) in the source or previous mineral phases, not by minerals in the crystallized melt composition. In this matter, biotite analyses from the northern granites corroborate similar sources and fractionation processes for the 1.08 Ga Nocemano and La Asunta granites (Fig. 4.5A, B). On the other hand, the 1.09 Ga Casa de Piedra granite reveals at least two distinct sources for the biotite composition (Fig. 4.5A, B). The biotite analyses from the schlieren enclaves are Mg-rich, whereas biotite compositions in the granitic leucosome portions are Fe-rich. In the southern domain, the mineral chemistry of biotite shows a progressive enrichment in Fe and Mg contents from older to younger granites (Fig. 4.5C, D). It suggests recrystallization and element mobilization during subsequent crustal anatexis. Moreover, the contemporaneous c. 1.08 Ga old Tasseoro and Nomoca granites likely derived from different sources.

The feldspar analyses also reflect the heterogeneous sources and multiple partial melting processes recorded in the Sunsas belt (Fig. 4.6A to D). In the northern domain, plagioclase analyses show a progressive increase in Na from Nocemano to schlieren enclave of the Casa de Piedra monzogranite (Fig. 4.6A). Even the K-feldspar compositions show distinct granites (Fig. 4.6C). Moreover, the K-feldspar crystals from enclaves have the same K_2O contents (15-17wt. %) compared to other

granites from the northern domain (Fig. 4.6C). It may suggest mixing of protoliths during c. 1.0 Ga old continental crust reworking. The composition of plagioclase from southern granites, such as observed for the biotite fractionation, clearly illustrate the multiple recrystallization processes with progressive enrichment in Na from 1.85 Ga to 1.0 Ga granites (Fig. 4.6B). In addition, the Ca-rich plagioclase from the 1.35 Ga San Pablo granite indicates a less evolved source for this pluton. Therefore, the multiple and progressive anatexis events recorded in the Sunsas belt can be observed in the mineral composition scale. Thus, crystallization of Ca- to Na-rich plagioclase, K-feldspar and biotite (and accessory minerals such as zircon, apatite, monazite and titanite) played a crucial role in the crustal reworking processes.

4.6.4 Tectonic setting

The geochemical characteristics of the Sunsas granitic rocks vary between fractionated I-type granites and hybrid A-type granites (Barbarin, 1990; Castro et al., 1991; Zhou et al., 2006; Murphy et al., 2017). In addition, presence of magnetite (e.g., La Asunta granite) and titanite (e.g., Casa de Piedra monzogranite) in some plutons corroborates the I-type granite classification of Chappell and White (1974) and Ishihara (1977), formed after igneous reworking processes. The strongly negative Nd, Ta and Ti anomalies indicate sources related to subduction processes (Baier et al., 2008; Nedel et al., 2020a). Complementarily, negative Ba, Sr, and Eu anomalies reflect felsic minerals as feldspar in the parental magma (Baier et al., 2008). Likewise, all biotite analyses plot in the calc-alkaline orogenic peraluminous field (Fig. 4.5B, D). The Sr and Nd isotopic data also suggest that the Sunsas granitic magmatism was built from a mixing of heterogeneous and different parental magmas and sources. Therefore, the geochemical, isotope and mineral chemistry data indicate that the Stenian Sunsas magmatism was generated in a magmatic arc setting likely during the transition of orogenic to post-orogenic crustal anatexis (Nedel et al., 2020a).

4.6.5 Geodynamic correlations

The c. 1.0 Ga final configuration of the Sunsas belt is associated with the Rodinia supercontinent assembly (e.g., Hoffman, 1991; Sadowski and Bettencourt, 1996; Kröner and Cordani, 2003). Likewise, geochronology data of the Sunsas Province are near coeval with continental accretion and magmatic episodes recorded in the

Grenville Province (Tohver et al., 2002, 2004; Boger et al., 2005; Li et al., 2008; McLelland et al., 2010). The Sunsas and Grenville orogenies share multiple crustal reworking processes with collisional and extensional episodes with minor mantle-derived sources (Rizzotto et al., 2001, 2013; Boger et al., 2005; Santos et al., 2008; Teixeira et al., 2010; Lima et al., 2019; Quadros et al., 2020; Nedel et al., 2020a, b). These correlations allow to propose a genetic link between the Amazonia and Laurentia paleocontinents (Hoffman, 1991, 1992; Dalziel, 1997; Tohver et al., 2002; 2004; Li et al., 2008).

The evolution of Sunsas belt protoliths started with the deposition of supracrustal rocks and granitic magmatism between 1.9 and 1.7 Ga (Teixeira et al., 2010, 2020; Nedel et al., 2020a, b). In the Sunsas northern portion, the 1.68 Ga Sujalito granite represents the less evolved rock and it is coeval with the emplacement of the Lomas Manechis granitoid suite between 1.69 and 1.66 Ga (Boger et al., 2005; Nedel et al., 2020a, b). In the Sunsas southern portion, the 1.85 Ga Tauca granodiorite represents felsic protolith possibly correlated to the Alumiador Suite (1.95–1.85 Ga) of the Rio Apa Terrane (Cordani et al., 2010; Faleiros et al., 2016; Teixeira et al., 2020; Nedel et al., 2020b).

The Sunsas Province records important magmatic activity between 1.45 and 1.35 Ga related to Rondonian-San Ignacio orogeny that yielded granites with T_{DM} model ages of 1.7 and 2.0 Ga (Fig. 4.12A, B). It was followed by 1.2 to 1.1 Ga extension episodes and rift sequences depositions (e.g. Sunsas-Vibosi, Huanchaca-Aguapeí and Nova Brasilândia groups; Teixeira et al., 2010). Lastly, the 1.1-1.0 Ga orogenic magmatic events are related to the Rodinia assembly.

The Grenville Province evolved over an extended period (c. 2.0–1.3 Ga; McLelland et al., 2010) that included long-lived continental margin magmatic arcs located along the southeast margin of Laurentia (McLelland et al., 2010), whereas the Sunsas Province represents multiple crustal reworking from to 1.9 to 1.0 Ga in the southwestern Amazonian Craton (Litherland et al., 1986; Cordani and Teixeira, 2007; Teixeira et al., 2010; Nedel et al., 2020a, b). The Grenvillian Orogeny, as well as the Sunsas Orogeny, developed between 1.2 and 0.9 Ga, comprised at least three distinct magmatic pulses at ~1.19-1.14, 1.08-1.02 and 1.00-0.85 Ga separated by continental extension events (Tollo et al., 2004; Rivers, 1997, 2008). These large, hot, long-lived orogenic processes can be similar to the Himalayan orogen

(McLelland et al., 2010). Moreover, the crustal extension episodes were coeval with the emplacement of ultramafic and anorthite complexes (McLelland et al., 2010). It suggests mantle-derived sources likely related to orogenic collapse due to higher crust thickness (McLelland et al., 2010).

Moreover, the 1.08-1.02 Ga Grenvillian magmatic pulse is correlated with the Amazonian and Laurentia collision climax (Nedel et al., 2020a). It is supported by the 1.08 Ga magmatic peak related to magmatic arc setting in the Sunsas belt (Boger et al., 2005; Nedel et al., 2020a, b). The previous granite emplacements in Laurentia, from 1.1 to 0.9 Ga, comprised alkaline intrusions and syenite-monzonite-granite plutons and small potassic to shoshonitic monzonite-diorite syenite-granite plutons, similar to the magmatism observed in the Sunsas belt shortly after (Rivers, 1997; Corriveau, 1990; Lumbers et al., 1990; Boger et al., 2005; Nedel et al., 2020a, b).

Lastly, the present results confirm the geotectonic model by Li et al. (2008) that proposed a longer geodynamic interaction and continental accretions between southwestern Amazonian and eastern Laurentia. The intense crustal reworking process of Paleoproterozoic protoliths with minor ~1.4 to 1.6 Ga mantle-derived contributions, related to continental rift or orogenic collapse, are main characteristics shared by the 1.2 to 0.9 Ga Sunsas and Grenvillian provinces.

4.7 Conclusion

The mineral chemistry, geochemical and Nd-Sr isotopic data reveal that the Sunsas belt was generated from heterogeneous crustal and juvenile sources. Likewise, combined results support that the crustal reworkings related to 1.4–1.3 Ga Rondonian-San Ignacio and 1.1–0.95 Ga Sunsas orogenies were the crucial process for the continental differentiation. Specifically, the main contributions are:

1. The Chiquitania and Lomas Manechis complexes in the northern part and Rio Apa terrane in the southern extension likely are the major crustal protoliths for the Sunsas belt.

2. Contributions from minor 1.42 and 1.35 Ga mantle-derived plagioclase-garnet-bearing sources were also recognized.

3. Plagioclase and biotite composition show progressive anatexis events, crustal differentiation, and mixing between different protoliths.

4. The crustal reworking events are related to 1.4–1.3 Ga and 1.1–0.95 Ga continental accretions, the latter associated with the magmatic arc developed by the Amazonian and Laurentia collision during Rodinia assembly.

4.8 Acknowledgements

This study was financed in part by the Coordenação de Aperfeiçoamento de Pessoal de Nível Superior - Brasil (CAPES) - Finance Code 001. The authors acknowledge the support of the Laboratório de Geocronologia (Universidade de Brasília) and the Grupo de Pesquisa em Evolução Crustal e Tectônica (Guaporé). The authors also acknowledge Fundação de Apoio à Pesquisa do Distrito Federal (FAPDF) and INCT Estudos Tectônicos (CNPq-CAPES-FAPDF) for financial support. IMN thanks CAPES and Programa de Excelência Acadêmica (PROEX, Edital - 0487) for granting the Doctorate scholarship. RAF and ASR acknowledge CNPq for research fellowship.

5. ARTIGO CIENTÍFICO 4: CRUSTAL EVOLUTION OF THE SUNSAS BELT, SW AMAZONIAN CRATON: IMPLICATIONS FOR RODINIA ASSEMBLY

Ingrid M. Nedel[1], Reinhardt A. Fuck[1], Alanielson C. D. Ferreira[2], Amarildo S. Ruiz[3], Gerardo R. Matos-Salinas[4]

[1]Instituto de Geociências, Universidade de Brasília (UnB), 70910-900 Brasília-DF, Brazil.

[2]Instituto de Geociências, Universidade Federal do Rio Grande do Sul, Porto Alegre - RS, Brazil.

[3]Faculdade de Geociências, Universidade Federal de Mato Grosso, Cuiabá-MT, Brazil.

[4]Instituto de Investigaciones Geológicas y del Medio Ambiente, Universidad Mayor de San Andrés (UMSA), Pabellón Geología, Calle 27, Campus Universitario Cota Cota, La Paz, Bolivia.

Author correspondence: Ingrid M. Nedel (ingrid_mn@hotmail.com)

5.1 Abstract

The Sunsas belt records Paleo- to Neoproterozoic crustal evolution events of the SW Amazonian Craton. 1.95-1.85 Ga granitic rocks represent the early protolith in the southern domain of the Sunsas Belt, whereas in the northern domain c. 1.68 Ga granitic complex rocks make up the main protoliths. Both Paleoproterozoic north and south protoliths were reworked at 1.42-1.35 Ga with minor juvenile sources contributions during the San Ignacio orogeny. All these precursors underwent reworking again between 1.17 and 1.04 Ga with magmatic generation climax at 1.08 Ga related to the Sunsas orogeny. U-Pb monazite, K-Ar biotite and Rb-Sr isochron ages suggest a long period of tectonic-thermal activity between c. 1005 and 935 Ma in the Sunsas Belt. The geochronological events recorded in the Sunsas Belt are similar to those recorded in the Grenville Province (Southern Laurentia), Sveconorwegian Province (Baltic Shield) and Rio Apa Terrane, indicating that these crustal fragments may have shared the same evolution during Mesoproterozoic

times. Therefore, it appears that the Sunsas belt records important geological information to understand configurations and models proposed for Rodinia assembly.

5.2 Introduction

The continental crust is the archive of Earth's history and records the multiple processes of crustal reworking and differentiation as well as its PT path (e.g., Condie et al., 2012; Cawood et al., 2013; Hawkesworth et al., 2017; Ferreira et al., 2020). The preservation of continental crust is related to terrane accretion mechanisms (e.g., Condie et al., 2012; Nance et al., 2014; Cawood et al., 2013; Hawkesworth et al., 2020). Understanding the role of tectonics in Earth's continental growth allows to recognize the mechanisms of the ongoing generation of calc-alkaline andesite crust as well as its destruction and recycling on short and long-term time scales through active margins (e.g., Armstrong, 1981; Cawood et al., 2013; Hawkesworth et al., 2020).

The major tectonic effects and magmatic records of the Sunsas orogeny (1.2-0.9 Ga) is mainly registered along the Sunsas belt, SW Amazonian Craton (Litherland et al., 1986; Teixeira et al., 2010; Nedel et al., 2020a, b). The orogeny is related to the late Mesoproterozoic collision of the Amazonian Craton with south Laurentia for the Rodinia assembly at ~0.9 Ga (e.g., Hoffman, 1991; Sadowski and Bettencourt, 1996; Kröner and Cordani, 2003). The 1.1-1.0 Ga associated magmatism reflects a variety of crustal and mantle sources reworked during 1.4–1.3 Ga and 1.1–0.95 Ga continental accretions (Boger et al., 2005; Teixeira et al., 2010; Nedel et al., 2020a, b). Precisely dated magmatic events can provide an age 'barcode' of tectonic events that affected a crustal fragment during its evolution (Bleeker and Ernst, 2006; Ernst and Bleeker, 2010; Ernst et al., 2016). When compared, these age 'barcodes' allow to recognize the possible crustal fragments related to simultaneous orogenic collages responsible for the supercontinent architecture (e.g., Hawkesworth et al., 2009, 2020; Brown et al., 2020). Furthermore, the evidence of magmatic generation peaks has been linked to the development of supercontinents (e.g., Condie, 1998, 2000, 2004, 2005; Hawkesworth et al., 2020). Therefore, combined isotopic systems such as Pb-Nd-Hf and whole-rock and mineral composition of igneous rocks can support time-integrated correlations of tectonic settings during magmatic episodes (Spencer et al., 2015).

The integration of recently published isotopic and chemical data from the Sunsas belt established the most important tectonic events that reworked the sources of the 1.1-1.0 Ga magmatic rocks in the SW Amazonian Craton (Nedel et al., 2020a, b, c). The results provide new insights on the Laurentia-Baltica-Amazonia configuration and geotectonic correlations for the Rodinia supercontinent (Fig. 5.1A).

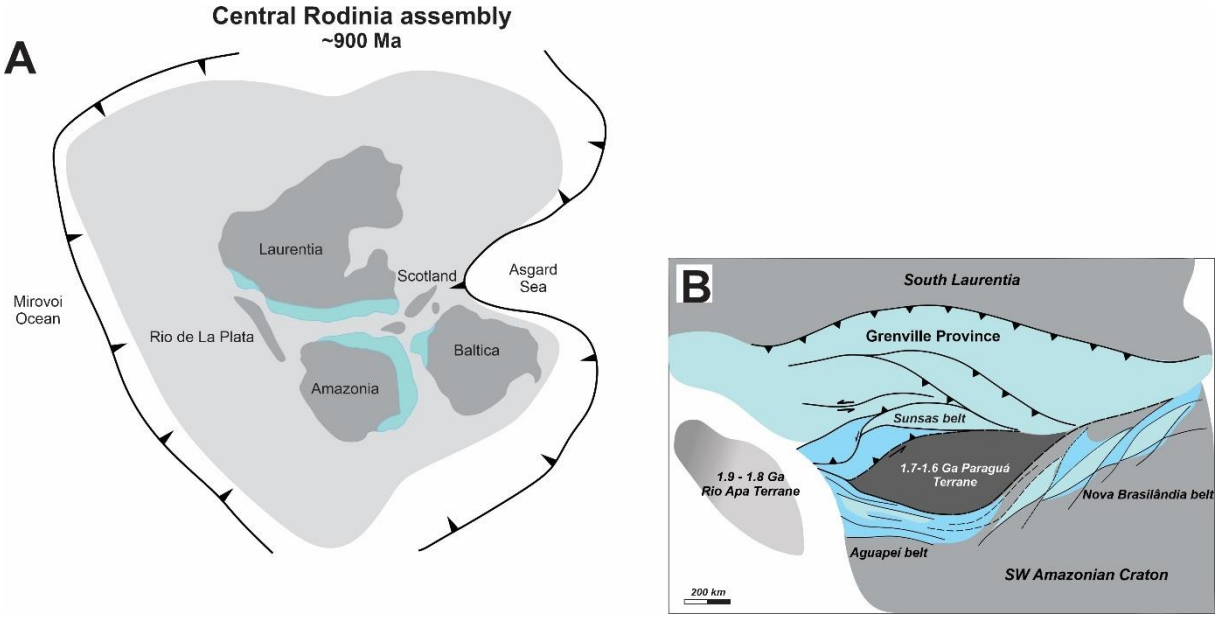

Figure 5.1. (A) Geodynamic configuration for the ~900 Ma Rodinia assembly (Spencer et al., 2015); (B) Geological setting of the Sunsas belt during its collision with the Grenville Province in Laurentia.

5.3 Geologic setting

The Sunsas Province (Fig. 5.1B) corresponds to the last crustal accretion at the southwestern Amazonian Craton before its final tectonic stabilization (e.g., Tassinari and Macambira, 2004; Cordani and Teixeira, 2007; Nedel et al., 2020). It comprises igneous and supracrustal rocks affected by the Sunsas orogeny, the counterpart of the Grenville Orogeny in Laurentia (e.g., Hoffman, 1992; Sadowski and Bettencourt, 1996; Kröner and Cordani, 2003). The collisional-type event was restricted to the Sunsas, Nova Brasilândia and Aguapeí belts in the Amazonian Craton, associated with low- to medium-grade metamorphism near-coeval with 1.1–1.0 Ga syn-tectonic granite emplacement (e.g., Litherland et al., 1989; Tassinari et al., 2000; Tassinari and Macambira, 2004; Cordani and Teixeira, 2007; Teixeira et al., 2010; 2020).

5.4 Results and Discussion

The detailed description of analytical methods and procedures used in the previous papers for results discussed here, are presented in the 2, 3, and 4 chapters of this thesis.

5.4.1 Geochronological evolution

The geochronological results revealed four magmatic events in the Sunsas belt (Table 5.1). They indicate a complex magmatic history with multiple crustal reworking processes at the SW Amazonian Craton. The oldest magmatism is recorded in the Sunsas southern domain by the 1.9-1.8 Ga granitic crust. The geological configuration of the Amazonian Craton at ~0.9 Ga (Fig. 5.1) suggests a previous petrogenetic link with the western domain of the Rio Apa Terrane (Cordani et al., 2010; Faleiros et al., 2016; Redes et al., 2016, 2018; Plens, 2018; Nedel et al., 2020; Teixeira et al., 2020). The Paraguá Terrane (1.7-1.6 Ga) represents the oldest basement from the Sunsas northern domain and marks the second magmatic event at c. 1.68 Ga (Litherland et al., 1986; Boger et al., 2005; Santos et al., 2008; Nedel et al., 2020a, b).

The Mesoproterozoic 1.42–1.35 Ga Calymmian to Ectasian transition records the main magmatic generation in the central portion of the Sunsas belt (Nedel et al., 2020a, b) (Fig. 5.1; Table 5.1). Specifically, the 1.37-1.34 Ga granitogenesis can be related to the amalgamation of the Paraguá Terrane to the SW Amazonian Craton during the Rondonian-San Ignacio orogeny (Matos et al., 2009; Bettencourt et al., 2010). Moreover, 1.9-1.8 Ga and 1.6 Ga old inherited zircon cores present in 1.4-1.3 Ga old granitic intrusions indicate the crustal reworking of Paleoproterozoic basement during the San Ignacio collision (Nedel et al., 2020b) (Table 5.1). The older 1.45-1.42 Ga granitic pulses reflect the Santa Helena Orogen effects recorded in the Jauru and Paraguá terranes (Santos et al., 2000; Matos et al., 2009; Bettencourt et al., 2010).

Lastly, the magmatism associated to the Sunsas orogeny took place between 1.1 and 1.04 Ga. The 1.76 Ga, 1.62 Ga, and 1.38 Ga inherited zircon cores in the Sunsas belt granitoids corroborate the Paraguá and Rio Apa terranes as the main sources for the Sunsas magmatism and their reworking during the San Ignacio and Sunsas orogenies (Nedel et al., 2020b, c; Teixeira et al., 2020). These ages also

indicate the important relation of the Sunsas granites with the Pensamiento Suite (1.37-1.34 Ga), during their emplacement at the final stages of the Sunsas Orogeny. Furthermore, the 1000±9.8 Ma and 992±41 Ma monazite ages can reflect lower temperature melt pulses in the post-collision setting and the 1.9 Ga and 1.4 Ga protolith sources reworking (Table 5.1). These monazite ages are coeval with Rb-Sr (1005 ± 12 Ma) and K-Ar (1008 ± 22 to 935 ± 21 Ma) ages in biotite from the Sunsas belt (Litherland et al., 1986). Thus, the monazite results are relevant and can contribute to unravel a complex tectonic history for igneous rocks dated only by U-Pb zircon (e.g., Ondrejka et al., 2012; Piechocka et al., 2017).

Table 5.1. Geochronological evolution for the Sunsas Province.

Granitoid	Reference	*U-Pb zircon ages*			*Tardi-magmatic to metamorphic ages*				Isotopic patterns		
		Protolith	*San-Ignácio*	*Sunsas*	*U-Pb monazite*	*Rb-Sr isochron*	*K-Ar biotite*	*U-Pb titanite*	$^{87}Sr/^{86}Sr_i$	$\varepsilon_{Nd(t)}$	T_{DM} *Model (Ga)*
Tasseoro	Litherland et al. (1986)						991 ± 27				
Taperas	Litherland et al. (1986)						935 ± 21				
Taperas	Boger et al. (2005)			1076 ± 18						-5.81	
Taperas	Vargas-Mattos (2010)			1047 ± 24						-4.74	1.71
Casa de Piedra	Litherland et al. (1986)					1005 ± 12	958 ± 27				
Casa de Piedra	Darbyshire et al. (2000)			1089						-4	1.92
Casa de Piedra	Vargas-Mattos (2010)			1089						-4.94	
Casa de Piedra	Vargas-Mattos (2010)			1030						-3.52	
San Pedro (injected vein)	Litherland et al. (1986)						1008 ± 22				
San Javier (injected vein)	Litherland et al. (1986)						948 ± 21				
El Carmem (injected vein)	Litherland et al. (1986)						972 ± 21				
El Carmem	Vargas-Mattos (2010)			1071 ± 34						-3.05	1.8
Naranjito	Vargas-Mattos (2010)			1048 ± 19						-3.17	1.75
Primavera	Vargas-Mattos (2010)			1080						-0.59	1.66
São Domingos	Ruiz (2005)			1086 ± 4				886 ± 9			
Señoritas	Nedel (2020)	1954 ± 51	1454 ± 20	1004 ± 1	1006 ± 8				0.78307	-6.52	1.89
La Asunta	Nedel (2020)			1081 ± 6					0.70800	-5.74	1.67
Tasseoro	Nedel (2020)			1086 ± 20					0.69668	-4.23	1.73
Nocemano	Nedel (2020)	1690 ± 37	1386 ± 18	1107 ± 11					0.70873	-4.60	1.70
Nomoca	Nedel (2020)	1781 ± 160	1354	1086 ± 9					0.70667	0.72	1.39
Colmena	Nedel (2020)		1348 ± 8							-2.11	1.84
Salinas	Nedel (2020)		1372 ± 36								
Marimonos	Nedel (2020)			1060 ± 8							
San Pablo	Nedel (2020)		1344 ± 6.8						0.71223	-2.72	1.97
Señoritas	Nedel (2020)	1976 ± 24									
Las Tojas	Nedel (2020)	1918 ± 22			991 ± 41						
Tauca	Nedel (2020)	1855 ± 4							0.70146	-1.84	2.29

San Ramón	Nedel (2020)		1417 ± 10			0.69685	2.26	1.55
Casa de Piedra	Nedel (2020)	1763 ± 35	1278 ± 96	1077 ± 22		0.70439	-2.09	1.53
Sujalito	Nedel (2020)	1682 ± 2				0.84081	1.84	1.87
Miraflores	Nedel et al. (2017)	1685 ± 5					1.07	1.86
Santo Rosário	Nedel et al. (2017)	1686 ± 5					0.46	1.97

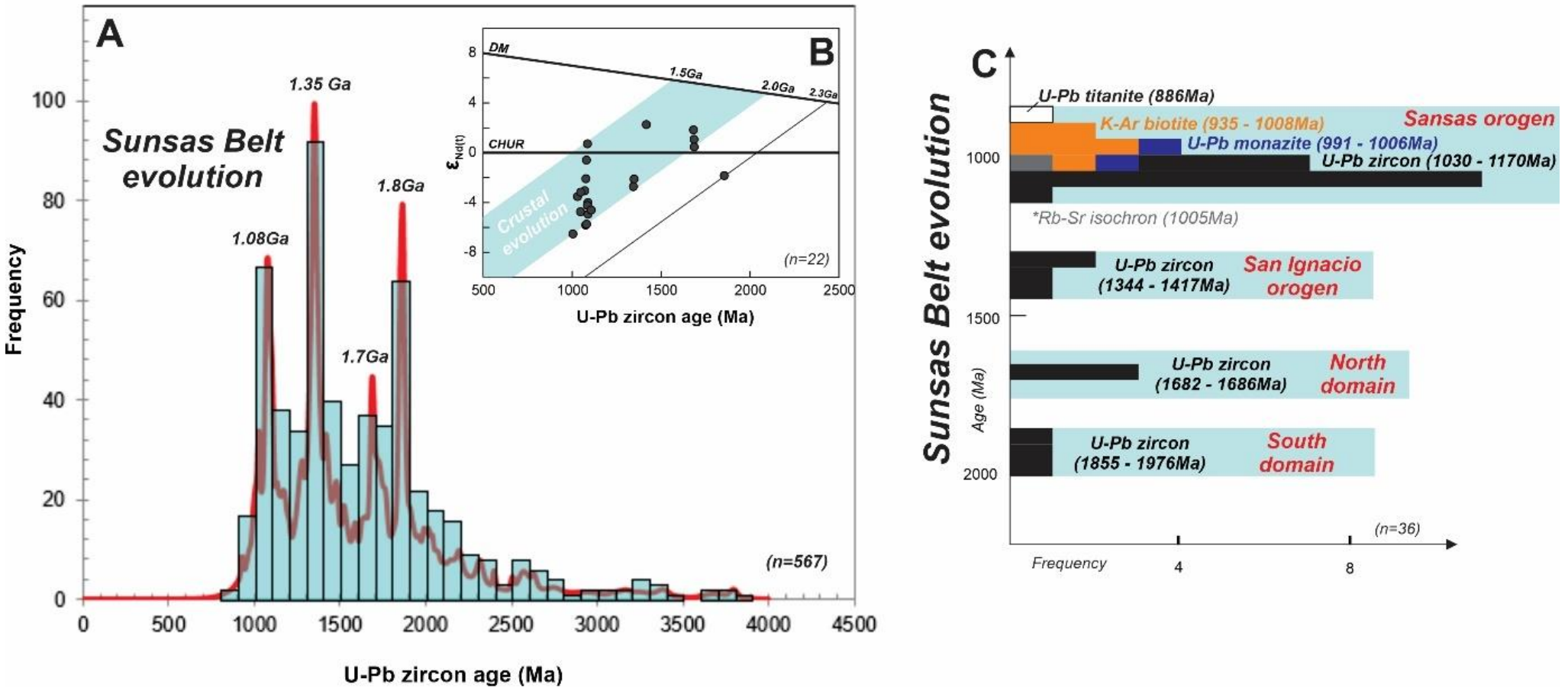

Figure 5.2. (A) Histogram of U-Pb zircon ages from the Sunsas belt magmatism; (B) $\varepsilon Nd^{(t)}$ data showing the crustal evolution of the Sunsas belt; (C) Geochronological evolution for the Sunsas belt (Nedel et al., 2020a, b, c). Data from Table 5.1.

5.4.2 Geochemical and isotopes constraints

The 1.68 Ga basement from the Sunsas northern domain represents the less evolved protolith, with lower LREE/HREE ratios, stronger negative Nb, Ta and Ti anomalies and higher initial 87Sr/86Sr (0.840), compatible with crustal sources patterns. Furthermore, a record of positive 1.87 εNd(t) suggests a juvenile contribution for the ~1.68 Ga magmatism. The younger 1.37 Ga magmatic pulse related to the Pensamiento Suite presents more fractionated LREE patterns, with minor negative anomalies of Eu, Nb, and Ti compared to the older basement. It indicates the reworking of 1.68 Ga granitic protolith during c. 1.37 Ga partial melting events of the San Ignacio Orogeny. Moreover, 1.42 Ga old granite with positive 2.26 εNd(t), lower initial 87Sr/86Sr (0.696) and lower HREE contents with positive Eu anomalies supports mantle-derived sources with minor continental crust contribution for Mesoproterozoic magmatism. It suggests mixing of felsic crust and juvenile magmas during the c. 1.35 and c. 1.0 Ga orogenies in the northern domain.

In contrast to the north, the Sunsas belt southern domain is formed of 1.95 and 1.85 Ga old granitic crust with minor 1.34 Ga juvenile contribution, that provide the main sources for 1.1-1.0 Ga old magmatism. The older crust presents homogenous trace element patterns, with stronger negative Nb, Ta and Ti anomalies and positive εNd(t) values likely suggesting poorly differentiated sources. In the eastern segment of the southern domain, a 1.85 Ga older crust with higher HREE content and lower LREE/HREE ratio reflects the most primitive composition of the Sunsas belt magmatism. To the west segment, the 1.95 Ga crust, with 1.0 Ga U-Pb monazite age, presents lower HREE content and higher LREE/HREE ratio, representing the most evolved composition. The 1.34 Ga magmatic record with higher HREE contents and less fractionated LREE/HREE ratios compared to younger granitoids (1.08 Ga) suggests diachronic and progressive crustal reworking. The negative εNd(t) values are also compatible with evolution from crustal melting.

The 1.08 Ga old Stenian granites present negative εNd(t) values and intermediary initial 87Sr/86Sr values (0.704 to 0.708). The Sr and Nd isotopic data support crustal reworking of the Paleoproterozoic protoliths with TDM model ages between 1.53 and 1.97 Ga during the evolution of the northern domain. Moreover, mantle-derived sources also played an important role mainly for the 1.68 and 1.44 Ga magmatism. In

both domains, the 1.1-1.0 Ga Sunsas orogeny promoted a new partial melting of Paleo- and early Mesoproterozoic felsic crust. This is also evident in the U-Pb monazite ages of 992±41 Ma and 1006±8 Ma from 1.95 Ga and 1.45 Ga granites, respectively, that indicate isotopic system opening at 1.0 Ga during the Rodinia assembly.

5.4.3 Implications for Rodinia assembly

The c. 1.0 Ga final configuration of the Sunsas belt is associated with the Rodinia supercontinent assembly (e.g., Hoffman, 1991; Sadowski and Bettencourt, 1996; Kröner and Cordani, 2003). The most important magmatic events recorded in the provinces related to the central Rodinia configuration are shown in Figure 5.3.

The Sunsas and Grenville Provinces share multiple magmatic pulses with the same age as from 1.18 Ga, associated to their collision (Fig. 5.3) (Rizzotto et al., 2001, 2013; Tollo et al., 2004; Boger et al., 2005; Santos et al., 2008; Rivers, 1997, 2008; Teixeira et al., 2010; Nedel et al., 2020a, b, c). The different ages from Paleoproterozoic crustal sources for Grenvillian magmatism indicate distinct tectonic evolution for Amazonia and Laurentia until ~1.1 Ga. The Sveconorwegian Province in eastern Baltica presents Grenvillian-age collision-related magmatism correlated to Laurentia and Amazonia. The longevity of the inherited or captured zircon isotopic signature since ~1,8 Ga can be associated with the collisional phases of previous orogenic cycles for the same plate tectonic interaction (Spencer et al., 2015).

On the other hand, the Rio Apa Terrane is formed of a Paleorpoterozoic crust that matches with inherited or captured zircon ages recorded in the southern domain of the Sunsas belt. The absence of younger 1.4 and 1.3 Ga magmatism and records of Ar-Ar 1.30-1.27 Ga ages correlate with the San Ignacio Orogeny can indicate the proximity of the Rio Apa and Paraguá terrains at 1.3 Ga, but not sufficient for crustal reworking and magmatic generation. Furthermore, the fissural magmatism restricted to the Paraguá and Rio Apa terrains at ~1.11 Ga resulted from an attempted continental break-up and suggests the juxtaposition of these terrains and is likely associated with the setting-up of the Aguapeí Aulacogen (Teixeira et al., 2015, 2020).

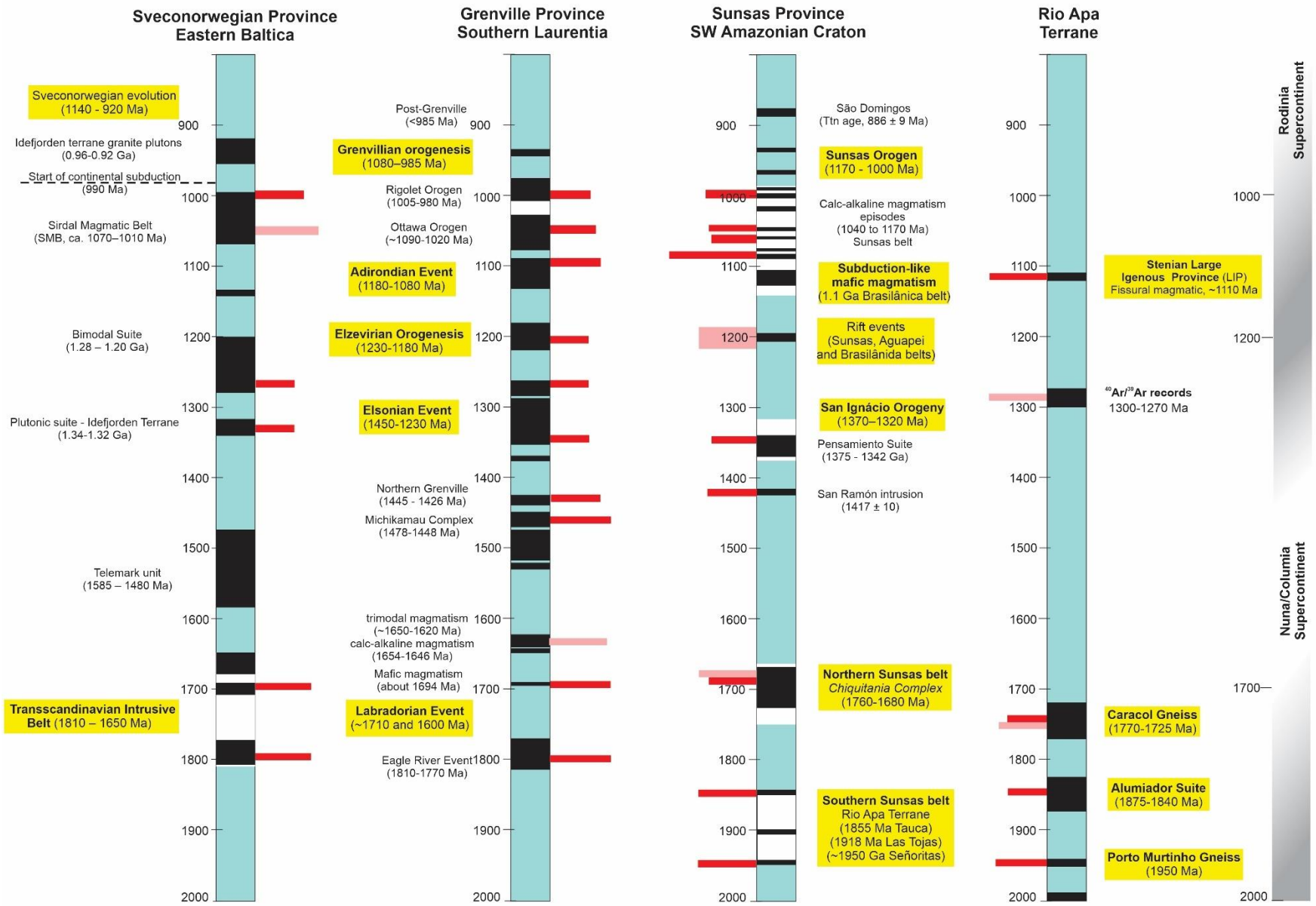

Figure 5.3. Magmatic event barcodes for Eastern Baltica, Southern Laurentia, SW Amazonian Craton and Rio Apa Terrane (Gower and Krogh, 2002; Högdahl et al., 2004; Bingen et al., 2005; Li et al., 2008; Spencer et al., 2015; Redes et al., 2020; Teixeira et al., 2020).

Moreover, the 1.08-1.02 Ga Grenvillian magmatic pulse is correlated with the Amazonian and Laurentia collision climax (Nedel et al., 2020a). It is supported by the 1.08 Ga magmatic peak related to magmatic arc setting in the Sunsas belt (Boger et al., 2005; Nedel et al., 2020a, b). Therefore, Amazonia, Baltica, Laurentia and the Rio Apa Terrane show near-coeval magmatic and crustal reworking events from Paleo to Neoproterozoic, which reflects a long-lived tectonic plate interaction in its geodynamic evolution.

5.5 Conclusion

The integration of geochemical, Nd and Sr isotopic and petrological data with several geochronological methods allowed the establishment of geological correlations among the heterogeneous crustal fragments that built the Sunsas belt. For the Sunsas northern domain, the sources are represented by 1.68 Ga felsic protoliths with 1.42 Ga juvenile sources. For the southern domain of the Sunsas belt, the 1.95 and 1.85 Ga granitic crust with minor 1.34 Ga juvenile contributions represent the main sources. The north and south protoliths were reworked between 1.17 and 1.04 Ga related to Sunsas-Grenville orogenic collages. A long period of tectonic-thermal activity remained (1005 to 935 Ma) associated with metamorphic conditions related to the post-collision setting. The Sunsas belt has a similar evolution to the Grenville Province, Sveconorwegian Province e Rio Apa Terrane. It indicates that these crustal fragments may have shared a previous Mesoproterozoic evolution before being amalgamated during Rodinia assembly.

5.6 Acknowledgements

This study was financed in part by the Coordenação de Aperfeiçoamento de Pessoal de Nível Superior - Brasil (CAPES) - Finance Code 001. The authors acknowledge the support of the Laboratório de Geocronologia (Universidade de Brasília) and the Grupo de Pesquisa em Evolução Crustal e Tectônica (Guaporé). The authors also acknowledge Fundação de Apoio à Pesquisa do Distrito Federal (FAPDF) and INCT Estudos Tectônicos (CNPq-CAPES-FAPDF) for financial support. IMN thanks CAPES and Programa de Excelência Acadêmica (PROEX, Edital - 0487) for granting the Doctorate scholarship. RAF and ASR acknowledge CNPq for research fellowship.

6. CONCLUSÃO

O volume e a sistematização de dados petrológicos, geoquímicos, isotópicos e geocronológicos produzidos durente a realização desta tese trouxe novas pespectivas para a evolução da Faixa Sunsas no sudoeste do Craton Amazônico, principalmente se considerado que os trabalhos disponíveis para essa região da Bolívia eram escassos e pouco representativos em relação à extensão da faixa. A integração de diferentes metodologias possibilitou a identificação de, no mínimo, dois diferentes protólitos paleoproterozoicos, um de 1,9–1,8 Ga na porção sul da faixa, possivelmente relacionado ao Terreno Rio Apa, e outro de 1,68 Ga na porção norte da faixa, correlacionado aos complexos Lomas Manechis e Chiquitania. Além desses protólitos continentais, dados isotópicos e geoquímicos sugerem contribuições restritas de fontes juvenis em 1,4 Ga. Todos esses precusores foram amalgamados e retrabalhados durante a Orogenia San Ignácio em ~ 1.35 Ga. Após episódios extensionais em ~1,2 Ga, novo processo de retrabalhamento e fusão parcial ocorreu entre 1,17 e 1,04 Ga, associado às colagens orogênicas Sunsas-Grenville, principalmente ao longo de estruturas herdadas das colagens anteriores. Por um perído de c. 100 Ma o sistema termal tardi a pós-orogênico ainda permaneceu ativo até ~935 Ma (K-Ar em biotita) ou mesmo até 886 (U-Pb em titanita). Portanto, a Faixa Sunsas apresenta longa e complexa história, com distintos protólitos e fontes, além de múltiplos processos de anatexia crustal de 1.9 a 0.9 Ga. Estudos futuros que espeficiquem as características das fontes, bem como descrevam as condições termobarométricas dos processos de fusão parcial serão necessários para correlacionar a evolução da Faixa Sunsas com a estabilização do supercontinente Rodínia. Por fim, a Faixa Sunsas configura-se uma área promissora para o estudo dos mecanismos de diferenciação crustal atuantes do final do Paleoproterozoico ao início do Neoproterozoico.

7. REFERÊNCIAS

Adamek, P.M., Troeng, B., Landivar, G., Llanos, A., Matos, R. 1996. Evaluación del los recursos minerales del Distrito San Ramón. Boletín del Servicio Geológico de Bolivia 10, 77.

Albarède, F., Telouk, P., Blichert-Toft, J., Boyet, M., Agranier, A., Nelson, B. 2004. Precise and accurate isotopic measurements using multiple collector ICPMS. Geochimica et Cosmochimica Acta 68, 2725–2744.

Aleinikoff, J.N., Schenk, W.S., Plank, M.O., Srogi, L.A., Fanning, C.M., Kamo, S.L., Bosbyshell, H. 2006. Deciphering igneous and metamorphic events in high-grade rocks of the Wilmington complex, Delaware: morphology, cathodoluminescence and backscattered electron zoning, and SHRIMP U–Pb geochronology of zircon and monazite. Geological Society of America Bulletin, 118, 39–64.

Armstrong, R. L. (1981). Radiogenic isotopes: the case for crustal recycling on a near-steady-state no-continental-growth Earth. Philos. Trans. R. Soc. Lond. Seri. Math. Phys. Eng. Sci. 301, 443–472. doi: 10.1098/rsta.1981.0122

Baier, J., Audétat, A., Keppler, K., 2008. The origin of the negative niobium tantalum anomaly in subduction zone magmas. Earth and Planetary Science Letters 267, 290-300.

Barbarin, B. 1990. Granitoids: main petrogenetic classifications in relation to origin and tectonic setting. Geological Journal 25, 227-238.

Barbarin, B. 1996. Genesis of the two main types of peraluminous granitoids. Geology 24(4), 295-298.

Barbarin, B. 1999. A review of the relationships between granitoid types, their origins and their geodynamic environments. Lithos 46, 605–626.

Batchelor, R. A., bowden, P. 1985. Petrogenetic interpretation of granitoids series using multicationic parameters. Chemical Geology, n. 48, p. 43-55.

Best, M.G. 2013. Igneous and Metamorphic Petrology. John Wiley and Sons (752 pp.).

Bettencourt, J.S., Leite Jr, W.B., Ruiz, A.S., Matos, R., Payolla, B.L., Tosdal, R.M. 2010. The Rondonian-San Ignacio Province in the SW Amazonian Craton: an overview. Journal of South American Earth Science, 29, 28–46.

Bickford, M.E., Wooden, J.L., and Bauer, R.L., 2006. SHRIMP study of zircons from Early Archean rocks in the Minnesota River Valley: Implications for the tectonic history of the Superior Province: Geological Society of America Bulletin, v. 118, p. 94–108, doi:10.1130/B25741.1.

Bingen, B., Skår, Ø.,Marker, M., Sigmond, E. M.O.,Nordgulen, Ø., Ragnhildstveit, J.,Mansfeld, J., Tucker, R. D. & Liégeois, J.-P. 2005. Timing of continental building in the Sveconorwegian orogen, SW Scandinavia.Norwegian Journal of Geology,Vol. 85, pp. 87-116. Trondheim. ISSN 029-196X.

Bleeker, W., Ernst, R.E. 2006. Short-lived mantle generated magmatic events and their dyke swarms: The key unlocking earth's paleogeographic record back to 2.6 Ga. In: Hanski E, Mertanen S, Rämö T, Vuollo J (eds) Dyke Swarms -Time Markers of Crustal Evolution, Taylor & Francis Group, London: 3–26

Boger, S.D., Raetz, M., Giles, D., Etchart, E., Fanning, C.M. 2005. U–Pb age from the Sunsás region of Eastern Bolivia, evidence for allochtonous origin of the Paragua Block. Precambrian Research, 139(2005), 121–146.

Bonin, B. 1990. From orogenic to anorogenic settings: evolution of granitoid suites after a major orogenesis. Geological Journal 25, 261–270.

Brito Neves, B.B., Fuck, R.A. 2014. The basement of the South American Platform: half Laurentian (N-NW) + half Gondwanan (E-SE) domains. Precambrian Research 244, 75-86.

Brown, M., Johnson, T., Gardiner, N.J., 2020. Plate Tectonics and the Archean Earth. Annu. Rev. Earth Planet. Sci. 48, 1–12.

Bucher, K., Grapes, M. 2011. Petrogenesis of Metamorphic Rocks. Springer-Verlag, 8th Edition.

Bühn, B.M., Pimentel, M, M., Matteini, M., Dantas, E.L., 2009. High spatial resolution analyses of Pb and U isotopes for geochronology by laser ablation multi-collector

inductively coupled plasma mass spectrometry LA-MC-ICP-MS. Anais da Academia Brasileira de Ciências 81, 1-16.

Carlson, W. D., Anderson, S. D., Mosher, S., Davidow, J. S., Crawford, W. D., and Lane, E. D. 2007. High pressure metamorphism in the Texas Grenville Orogen: Mesoproterozoic subduction of the Southern Laurentian continental margin: International Geology Review, v. 49, in press.

Castro, A., Moreno-Ventas, I., de la Rosa, J.D. 1991. H-type (hybrid) granitoids: a proposed revision of the granite-type classification and nomenclature. Earth-Science Reviews 31, 237–253.

Casquet, C., Rapela, C.W., Pankhurst, R.J., Baldo, E.G., Galindo, C., Fanning, C.M., Dahlquist, J.A., Saavedra, J., 2012. A history of Proterozoic terranes in southern South America: from Rodinia to Gondwana. Geosci. Front. 3, 137–145.

Cawood, P.A., Hawkesworth, C.J., Dhuime, B. 2013. The continental record and the generation of continental crust. Geological Society of America Bulletin, 125, 14-32.

Chapman, J.B., Ducea, M.N., DeCelles, P.G., Profeta, L. 2015. Tracking changes in crustal thickness during orogenic evolution with Sr/Y: an example from the North American Cordillera. Geology 43, 919–922.

Chappell, B.W., White, A.J.R. 1974. Two contrasting granite types. Pacific Geology 8, 173–174.

Chappell B.W., White A.J.R. 1992. I-and S-type granites in the Lachlan Fold Belt. Trans R Soc Edinb Earth Sci 83:1–26.

Chappell, B. W., Bryant, C. J., Wyborn D., White A. J. R. & Williams I. S. 1998. High- and low-temperature I-type granites. Resource Geology, 48, 225–236.

Chaves, M. L. S. C., Brandão, P. R. G., Buhn, B. 2010. Monazita em veios de quartzo da Serra do Espinhaço Meridional (MG): mineralogia, idades LA-ICP-MS e implicações geológicas. Revista Brasileira de Geociências, v. 40, 506-515.

Chiarenzelli, J., Kratzmann, D., Selleck, B., deLorraine, W. 2015. Age and provenance of Grenville supergroup rocks, Trans-Adirondack Basin, constrained by detrital zircons. Geology 43, 183–186.

Collins, W.J., Beams, S.D., White, A.J.R., Chappell, B.W. 1982. Nature and origin of A-type granites with particular reference to southeastern Australia. Contrib. Mineral. Petrol. 80, 189– 200.

Collins, W.J., Huang, H.Q., Bowden, P., 2019. Repeated S-I-A-type Granite Trilogy in the Lachlan Orogen, and Geochemical Contrasts with A-type Granites in Nigeria: Implications for Petrogenesis and Tectonic Discrimination. Geological Society, London, Special Publications, 491.

Condie, K.C., 2000, Episodic continental growth models: Afterthoughts and extensions: Tectonophysics, v. 322, p. 153–162. doi:10.1016/S0040-1951(00)00061-5

Condie, K.C. 2004. Supercontinents and superplume events: distinguishing signals in the geologic record. Physics of the Earth and Planetary Interiors, 146, 319–332.

Condie, K., Kröner, A., 2013. The building blocks of continental crust: Evidence for a major change in the tectonic setting of continental growth at the end of the Archean. Gondwana Research 23, 394-402.

Condie, K.C., Bickford, M.E., Aster, R.C., Belousova, E., Scholl, D.W., 2011. Episodic zircon ages, Hf isotopic composition, and the preservation rate of continental crust. Geological Society of America Bulletin 123, 951-957.

Condie, K., Kröner, A., 2013. The building blocks of continental crust: Evidence for a major change in the tectonic setting of continental growth at the end of the Archean. Gondwana Research 23, 394-402.

Cordani, U.G., Tassinari, C.C.G., Teixeira, W., Basei, M.A.S., and Kawashita, K. 1979. Evolução tectônica da Amazônia com base nos dados geocronológicos: Actas, II Congresso Geologico Chileno, p. 137–148.

Cordani, U.G., Sato, K., Teixeira, W., Tassinari, C.C.G., and Basei, M.A.S. 2000, Crustal evolution of the South American platform, in Cordani, U.G., Milani, E.J., Thomaz-Filho, A., and Campos, D.A., eds., Tectonic evolution of South America: Rio de Janeiro, Brazil, 31st International Geological Congress, p. 19–40.

Cordani, U.G., Teixeira, W. 2007. Proterozoic accretionary belts in the Amazonian Craton. The Geological Society of America (GSA), Memoir 200, 297–320.

Cordani, U.G., Teixeira, W., D'Agrella-Filho, M.S., Trindade, R.I. 2009. The position of the Amazonian Craton in supercontinents. Gondwana Research, 15, pp. 396-407

Cordani, U.G., Teixeira, W., Tassinari, C.C.G., Coutinho, J.M.V., Ruiz, A.S. 2010. The Rio Apa Craton in Mato Grosso do Sul (Brazil) and northern Paraguay: Geochronological evolution, correlations and tectonic implications for Rodinia and Gondwana. Gondwana Research 15, 396–407.

Corrigan, D., Hanmer, S., 1995. Arc accretion, thickening, post-collisional extension and plutonism in the Grenville orogen; constraints from the Mauricie region, south-central Quebec. In: Precambrian '95, International Conference on Tectonics and Metallogeny of Early/Mid Precambrian orogenic Belts, Program and Abstracts, Montreal, p. 106.

Corriveau, L., Heaman, L. M., Marcantonio, F., Breemen, O. 1990. 1.1 Ga K-rich alkaline plutonism in the SW Grenville Province. Contrib. Mineral. Petrol. 105, 473. doi:10.1007/BF00286834

Dalziel, I.W.D., 1997. Neoproterozoic–Paleozoic geography and tectonics: review, hypothesis, environmental speculation. Geol. Soc. Am. Bull. 109, 16–42.

Darbyshire, D.P.F. 2000. The Precambrian of Eastern Bolívia−Sm-Nd isotope study. The 31st Int. Geol. Congress, Rio de Janeiro, Brazil, Abstr. Vol. Rio de Janeiro, Geol. Surv. Brazil [CD-ROM].

Davidson, A. 1995. A review of the Grenville orogen in its North American type area. J. Aust. Geol. Geophys. 16, 3–24.

Davis, D.W., Amelin, Y., Nowell, G.M., and Parrish, R.R., 2005. Hf isotopes in zircon from the western Superior province, Canada: Implications for Archean crustal development and evolution of the depleted mantle reservoir: Precambrian Research, v. 140, p. 132–156, doi: 10.1016/j.precamres.2005.07.005.

DePaolo, D. J. 1981. A neodymium and strontium isotopic study of the Mesozoic calc-alkaline granitic batholithys of the Sierra Nevada and Peninsular Ranges, California. J. of Geophys. Res., 86, 10470-10488.

Dhuime, B., Hawkesworth, C.J., Cawood, P.A., Storey, C.D., 2012. A change in the geodynamics of continental growth 3 billion years ago. Science 335:1334–36

Dragone, G.N., Ussami, N., Gimenez, M.E., Lince Klinger, F.G., Chaves, C.A.M. 2017. Western Paraná suture/shear zone and the limits of Rio Apa, Rio Tebicuary and Rio de la Plata cratons from gravity data. Precambrian Research, 291, 162-177.

Draut, A.E., Clift, P.D., Amato, J.M., Blusztajn, J., Schouten, H., 2009. Arc-continent collision and the formation of continental crust: a new geochemical and isotopic record from the Ordovician Tyrone Igneous Complex, Ireland. Journal of the Geological Society of London 166, 485–500.

Droop, G.T.R., 1987. A general equation for estimating Fe3+ concentrations in ferromagnesian silicates and oxides from microprobe analyses, using stoichiometric criteria. Mineralogical Magazine 51, 431-435.

Eby, G.N. 1992. Chemical subdivision of the A-type granitoids: petrogenetic and tectonic implications. Geology 20, 641– 644.

Ernst, R. E. & Bleeker, W. 2010. Large igneous provinces (LIPs), giant dyke swarms, and mantle plumes: significance for breakup events within Canada and adjacent regions from 2.5 Ga to the present. Can. J. Earth Science 47, 695739.

Ernst, R.E., Hamilton, M.A., Söderlund, U., Hanes, J.A., Gladkochub, D.P., Okrugin, A.V., Kolotilina, T., Mekhonoshin, A.S., Bleeker, W., LeCheminant, A.N., Buchan, K.L. 2016. Long-lived connection between southern Siberia and northern Laurentia in the Proterozoic. Nature Geoscience 9 (6), 464–469.

Evans, D. A. D. & Mitchell, R. N. Assembly and breakup of the core of Paleoproterozoic-Mesoproterozoic supercontinent Nuna. Geology 39, 443-446 (2011).

Faleiros, F.M., Pavan, M., Remédio, M.J., Rodrigues, J.B., Almeida, V.V., Caltabeloti, F.P., Pinto, L.G.R., Oliveira, A.A., Pinto de Azevedo, E.J., Costa, V.S., 2016. Zircon U-Pb ages of rocks from the Rio Apa Cratonic Terrane (Mato Grosso do Sul, Brazil): new insights for its connection with the Amazonian Craton in pre-Gondwana times. Gondwana Research. 34, 187–204.

Faria, D. A., Ruiz, A.S., Matos, J.B., Sousa, M.Z.A., Lima, G.A., Macambira, J.B.M. 2014. Geology, Geochemistry, and Geochronology (U-Pb) of the Rio Fortuna Gneiss

– Serra do Baú Intrusive Suite – Paraguá Terrane – SW Amazonian Craton. Brazilian Journal of Geology, 44(1): 139-154.

Fernandes, C. J., Ruiz, A. S., Pinho, F. E. C., Kuyumjian, R. M. 2005. Compartimentação Tectônica da deformação Na Faixa Móvel Aguapeí, Sudoeste Do Cráton Amazônico, E As Mineralizações Auríferas Associadas. Revista Brasileira de Geociências, 35(1):1-12.

Fernandes, C.J., Kuyumjian, R.M., Pulz, G.M., Geraldes, M.C., Pinho, F.E.C. 2006. Geologia estrutural e idade 40Ar/39Ar do depósito de ouro Pau-a-Pique, Faixa Móvel Aguapeí, sudoeste do Estado do Mato Grosso. Revista Brasileira de Geociências, 36, 3–15.

Ferreira, A.C.D., Dantas, E.L., Fuck, R.A., Nedel, I.M. 2020. Arc accretion and crustal reworking from late Archean to Neoproterozoic in Northeast Brazil. Scientific Reports, 10, 7855.

Ferreira, A.C.D., Dantas, E.L.; Fuck, R.A.; Nedel, I.M.; Reimold, W.U., 2020. Multiple stages of migmatite generation during the Archean to Proterozoic crustal evolution in the Borborema Province, Northeast Brazil. Gondwana Research, doi.org/10.1016/j.gr.2020.09.005.

Fioretti, A.M., Black, L.P., Foden, J., Visona, D., 2005. Grenville-age magmatism at the South Tasman Rise (Australia): a new piercing point for the reconstruction of Rodinia. Geology 33, 769–772.

Fitzsimons, I.C.W., 2000. Grenville-age basement provinces in East Antarctica: evidence for three separate collisional orogens. Geology 28, 879–882.

Fuck, R.A., Brito Neves, B.B., Schobbenhaus, C. 2008. Rodinia descendants in South America. Precambrian Research 160, 108-126.

Frost, B.R., Barnes, C.G., Collins, W.J., Arculus, R.J., Ellis, D.J., Frost, C.D. 2001. A geochemical classification for granitic rocks. Journal of Petrology 42, 2033–2048.

Gao, L.-E., Zeng, L.-S. 2014. Fluxed melting of metapelite and the formation of Miocene high-CaO two-mica granites in the Malashan gneiss dome, southern Tibet. Geochimica et Cosmochimica Acta 130, 136–155.

Gardien, V., Thompson, A.B., Ulmer, P., 2000. Melting of biotite + plagioclase + quartz gneisses: the role of H2O in the stability of amphibole. Journal of Petrology 41, 651–666.

Gaucher, C., Frei, R., Chemale Jr, F., Frei, D., Bossi, J., Martínez, G., Chiglino, L., Cernuschi, F. 2011. Mesoproterozoic evolution of the Río de la Plata Craton in Uruguay: at the heart of Rodinia? International Journal of Earth Sciences, v. 100, 273–288.

Geraldes M.C. 2000 Geoquímica e Geocronologia do Plutonismo Mesoproterzóico do SW do Cráton Amazônico, SW do Estado de Mato Grosso. Doctored Dissertation. Universidade de São Paulo. São Paulo. 196p.

Geraldes, M.C., Teixeira, W., Van Schmus, W.R., 2000. Isotopic and chemical evidence for three accretioary magmatic arcs (1.79–1.42 Ga) in SW Amazon craton, Mato Grosso state, Brazil. Revista Brasileira de Geociências 30, 99–101.

Geraldes, M.C., Van Schmus, W.R., Condie, K.C., Bell, S., Teixeira, W., Babinski, M. 2001. Proterozoic geologic evolution of the SW part of the Amazonian Craton in Mato Grosso state, Brazil. Precambrian Research 111, 91–128.

Gill, R. 2010. Igneous Rocks and Processes – A Pratical Guide, Wiley-Blackwell.

Gioia, S.M.C. L. and Pimentel, M.M., 2000. The Sm-Nd isotopic method in the Geochronology Laboratory of the University of Brasília. Anais Academia Brasileira de Ciências 72, 219-245.

Gower, C. F., Krogh, T. E. 2002. A U–Pb geochronological review of the Proterozoic history of the eastern Grenville Province. Canadian Journal of Earth Sciences, volume 39, number 5. https://doi.org/10.1139/e01-090

Hagen-Peter, G., Cottle, J., 2018. Evaluating the relative roles of crustal growth versus reworking through continental arc magmatism: A case study from the Ross orogen, Antarctica. Gondwana Research 55, 153-166.

Hawkesworth, C. J., Cawood, P. A., Kemp, A. I. S., Storey, C. D., Dhuime, B. 2009. A matter of preservation. Science 323, 49–50.

Hawkesworth, C. J., Dhuime, B., Pietranik, A. B., Cawood, P. A., Kemp, A. I. S., Storey, C. D. 2010. The generation and evolution of the continental crust. Journal of the Geological Society, London, 167, 229–248.

Hawkesworth, C. J., Cawood, P. A., Dhuime, B. & Kemp, A. I. S. 2017. Earth's continental lithosphere through time. Annu. Rev. Earth. Sci 45, 169–198.

Hawkesworth, C.J., Cawood, P. A., Dhuime, B. 2020. The Evolution of the Continental Crust and the Onset of Plate Tectonics. Front. Earth Sci. 8:326. doi: 10.3389/feart.2020.00326

Hawthorne F.C., Oberti R., Harlow G.E., Maresch W.V., Martin, R.F., Schumacher J.C., Welch, M.D. 2012. Nomenclature of the amphibole supergroup. American Mineralogist, 97:2031-2048. DOI: 10.2138/am.2012.4276

Hodych, J.P., Cox, R.A., Košler, J., 2004. An equatorial Laurentia at 550 Ma confirmed by Grenvillian inherited zircons dated by LAM ICP-MS in the Skinner Cove volcanics of western Newfoundland: implications for inertial interchange true polar wander. Precambrian Research. 129, 93–113.

Hoffman, P.F., 1991. Did the breakout of Laurentia turn Gondwanaland inside-out? Science 252, 1409–1412.

Hoffman, P.F., 1992. Global Grenvillian kinematics and fusion of the Neoproterozoic Supercontinent Rodinia. Geological Association of Canada, Prog. Abstr., 17: 49.

Högdahl, K., Andersson, U. B., & Eklund, O. (2004). The Transscandinavian Igneous Belt (TIB) in Sweden: A review of its character and evolution. Espoo: Geological Survey of Finland.

Holder, R.M., Viete, D.R., Brown, M., Johnson, T.E. 2019. Metamorphism and the evolution of plate tectonics. Nature, 572, 378–381.

Hugh, R. 1993. Using geochemical data: evaluation, presentation, interpretation. Longman Geochemistry Series.

Irvine, T. N. and Baragar, W. R. A. 1971. A guide to the chemical classification of the common 1088 volcanic rocks. Canadian Journal of Earth Sciences, 8(5), 523-548.

Ishihara, S. 1977. The magnetite-series and ilmenite-series granitic rocks. Mining Geology 27, 293–305.

Isla-Moreno, L. 2009. Distrito Don Mario, un deposito de Au-Cu hidrotermal asociado a zonas de cizalla. XVIII Congreso Geológico de Bolivia, Potosi, Bolívia. Memorias del Colegio de Geólogos, 85–92.

Jackson, S.E., Pearson, N. J., Griffin, W.L., Belousova, E.A., 2004. The application of laser ablation-inductively coupled plasma-mass spectrometry to in situ U-Pb zircon geochronology. Chemical Geology 211, 47-69.

Jaffey, A. H., Flynn, K. F., Glendenin, L. E., Bentley, W. C., Essling, A. M. 1971. Precision measurement of the half-lives and specific activities of 235U and 238U. Physical Review C, 4, 1889-1906.

Keppie, J.D., Dostal, J., Cameron, K.L., Solari, L.A., Ortega-Gutierrez, F., Lopez, R., 2003. Geochronology and geochemistry of Grenvillian igneous suites in the northern Oaxacan Complex, southern Mexico: tectonic implications. Precambrian Res. 120, 365–389.

Košler, J., Fonneland, H., Sylvester, P., Tubrett, M., Pedersen, R.b., 2002. U-Pb dating of detrital zircons for sediment provenance studies – a comparison of laser ablation ICMPS and SIMS techniques. Chem Geol 182: 605–618.

Kröner, A., and Cordani, U.G., 2003, African, southern Indian and South American cratons were not part of the Rodinia supercontinent: Evidence from field relationships and geochronology: Tectonophysics, v. 375, p. 325–352, doi: 10.1016/S0040-1951(03)00344-5.

Lacerda-Filho, J.V., Brito, R.S.C., Silva, M.G., Oliveira, C.C. De., Moreton, L.C., Martins, E.G., Lopes, R.C., Lima, T.M., Larizzatti, J.H., Valente, C.R., 2006. Geologia e Recursos Minerais do Estado de Mato Grosso do Sul. Programa integração, atualização e difusão de dados de geologia do Brasil. Convênio CPRM/SICME - MS, MME. 10 - 28.

Lacerda-Filho, J.V., Fuck, R.A., Ruiz, A.S., Dantas, E.L., Scandolara, J.E., Rodrigues, J.B., Nascimento, N.D.C., 2016. Palaeoproterozoic tectonic evolution of

the Alto Tererê Group, southernmost Amazonian Craton, based on field mapping, zircon dating and rock geochemistry. J. S. Am. Earth Sci. 65, 122–141.

Li, Z.X., Li, X., Zhou, H., Kinny, P.D. 2002. Grenvillian continental collision in South China: new SHRIMP U–Pb zircon results and implications for the configuration of Rodinia. Geology 30, 163–166.

Li, Z.X., Bogdanova, S.V., Collins, A.S., Davidson, A., De Waele, B., Ernst, R.E., Fitzsimons, I.C.W., Fuck, R.A., Gladkochub, D.P., Jacobs, J., Karlstrom, K.E., Lu, S., Natapov, L.M., Pease, V., Pisarevskya, S.A., Thrane, K., Vernikovsky, V., 2008. Assembly, configuration and break-up history of Rodinia: A synthesis. Precambrian Research 1-2, 179-210.

Lima, G.A., 2016. Soleiras e enxames de diques máficos do sul-sudoeste do Cráton Amazônico. Instituto de Geociências, Universidade Federal do Pará, Brazil, Tese de Doutorado, pp. 130p.

Lima, G.A., Sousa, M.Z.A., Ruiz, A.S., D'agrella Filho, M.S., Vasconcelos, P., 2012. Sills máficos da Suíte Intrusiva Huanchaca - SW do Cráton Amazônico: registro de magmatismo fissural relacionado à ruptura do Supercontinente Rodínia. Rev. Bras. Geociencias 42, 111–129.

Lima, G.A., Macambira, M.J.B., Sousa, M.Z.A., Ruiz, A.S., D'Agrella-Filho, M.S., 2019. Fissural mafic magmatism on southwestern Amazonian Craton: Petrogenesis and 40Ar-39Ar geochronology. Journal of South American Earth Sciences 93, 214–231.

Litherland, M., Bloomfield, K. 1981. The Proterozoic history of eastern Bolivia. Precambrian Research 15, 157–179.

Litherland, M., Power, P.E.J., 1989. The geologic and geomorphologic evolution of Serrania Huanchaca, eastern Bolivia: the legendary ‘‘Lost World”. Journal of South American Earth Sciences 2(1), 1–17.

Litherland, M., Annells, R.N., Appleton, J.D., Berrange, J.P., Bloomfield, K., Burton, C.C.I., Darbyshire, D.P.F., Fletcher, C.J.N., Hawkins, M.P., Klinck, B.A., Llanos, A., Mitchell, W.I., O'Connor, E.A., Pitfield, P.E.J., Power, G., Webb, B.C. (1986). The

Geology and Mineral Resources of the Bolivian Precambrian Shield. British Geological Survey, Overseas Memoir 9, p.153.

Litherland, M., Annels, R.N., Hawkins, M.P., Klinck, B.A., O'Connor, E.A., Pitfield, P.E.J., Power, G., Darbyshire, D.P.F., Fletcher, C.N.J., Mitchell, W.I., Webb, B.C. 1989. The Proterozoic of eastern Bolivia and its relationships to the Andean mobile belt. Precambrian Research 43, 157–174.

Loewy, S. L., Connelly, J. N., Dalziel, I. W. D. 2004. An orphaned basement block: the Arequipa-Antofalla Basement of the central Andean margin of South America. Geological Society of America Bulletin, 116, 171-187.

Ludwig, K.R., 1991. ISOPLOT – A Plotting and Regression Program for Radiogenic Isotope Data, Version 2.70. U.S. Geological Survey Open/File Report, 91-445, 42pp.

Ludwig, K. R. 2008. User's Manual for Isoplot 3.70. A geochronological Toolkit for Microsoft Excel. Berkeley Geochronology Center, 4(4), 76.

Luft, J.L.J., Rizzotto, G., Chemale Jr., F., Lima, E.F. 2000. Análise geológica-estrutural do Cinturão Sunsás na Região de Nova Brasilândia, Sudeste de Rondônia. Revista Pesquisas Geociências 2, 65–78.

Lumbers, S.B., Heaman, L.M., Vertolli, V.M., Wu, T-W., 1990. Nature and timing of Middle Proterozoic magmatism in the Central Metasedimentary Belt, Grenville Province, Ontario. In: Gower, C.F., Rivers, T., Ryan, A.B. (Eds.), Mid-Proterozoic Laurentia-Baltica, Geological Association of Canada Special Paper 38. Geological Association of Canada, St. John's, NF, Canada, pp. 243-276.

Matos, J.B., Schorscher J.H.D., Geraldes M.C., Sousa M.Z.A., Ruiz A.S. 2004. Petrografia, geoquímica e geocronologia das rochas do Orógeno Rio Alegre, Mato Grosso: um registro de crosta oceânica mesoproterozóica no SW do Cráton Amazônico. Geologia USP. Série Científica 4:75-90.

Matos, R., Teixeira W., Geraldes M.C., Bettencourt J.S. 2009. Geochemistry and Nd–Sr isotopic signatures of the Pensamiento Granitoid Complex, Rondonian- San Ignacio Province, Eastern Precambrian Shield of Bolivia: Petrogenetic constraints for a Mesoproterozoic magmatic arc settting. Geologia USP, Série Científica 9, 89–117.

McLelland, J., Daly, J.S., McLelland, J.M. 1996. The Grenville orogenic cycle (ca. 1350–1000 Ma): An Adirondack perspective. Tectonophysics 265:1–28.

Meert, J.G., 2001. Growing Gondwana and refining Rodinia: a paleomagnetic perspective. Gondwana Research, 4, 279–288.

Merdith, A.S., Collins, A. S., Williams, S. E., Pisarevsky, S., Fodenc, J. D., Archibald, D. B., Blades, M. L., Alessio, B. L., Armistead, S., Plavsa, D., Clark C., Müller R. D. (2017). A full-plate global reconstruction of the Neoproterozoic. Gondwana Research. http://dx.doi.org/10.1016/j.gr.2017.04.001

Moyen J.F. 2020. Archean granitoids: classification, petrology, geochemistry and origin. Geological Society, London, Special Publications, 489, https://doi.org/10.1144/SP489-2018-34

Murphy, J.B., Shellnutt, J.G., Collins, W.J. 2017. Late Neoproterozoic to Carboniferous genesis of A-type magmas in Avalonia of northern Nova Scotia: repeated partial melting of anhydrous lower crust in contrasting tectonic environments. International Journal of Earth Sciences https://doi.org/10.1007/s00531-017-1512-7.

Nachit, H., Ibhi, A., El Hassan, A., Bem, M. O. 2005. Discrimination between primary magmatic biotites,reequilibrated biotites and neoformed biotites. Comptes. Rendus Géoscience, 337, 1415-1420.

Nance, D. R., Murphy, B. J., Santosh, M. 2014. The supercontinent cycle: A retrospective essay. Gondwana Research, 25, 4–29.

296-299, 129-141.

Nebel, O., Scherer, E.E., Mezger, K., 2011. Evaluation of the 87Rb decay-constant by age-comparison against the U–Pb system. Earth and Planetary Science Letters 301, 1-8.

Nedel, I. M., Ruiz, A. S., Matos-Salinas, G. R., Sousa, M. Z. A., Pimentel, M. M., Pavanetto, P. 2017. Front San Diablo na região de Miraflores, Faixa Sunsás, Bolívia: implicações tectônicas e estratigráficas. Geologia USP Série científica, São Paulo, v. 17, n. 3, p. 12-147.

Nedel, I. M., Fuck, R. A., Ruiz, A. S., Matos-Salinas, G. R., Ferreira, A. C. D. 2020a. U-Pb Geochronology and Geochemistry of Grenville-age Plutons in the Sunsás Belt - Bolivia, SW Amazonian Craton: Tectonic and Magmatic Implications. Submitted to Journal of South American Earth Sciences.

Nedel, I. M., Fuck, R. A., Ruiz, A. S., Matos-Salinas, G. R., Ferreira, A. C. D. 2020b. Long-lived Proterozoic magmatism in the Bolivian Precambrian Sunsas belt. Submitted to Geoscience Frontiers (GSF-D-20-00698).

O'Connor, J.T. 1965. A classification for quartz-rich igneous rocks based on feldspar ratios. US Geological Survey Professional Papers, B525, 79–84.

Oliveira, F. V., 2016. Chronus: Um novo suplemento para a redução de dados U-Pb obtidos por LAMC-ICPMS. Universidade de Brasília. Instituto de Geociências. Dissertação de Mestrado N°348.

Oliveira, J. R., Sousa, M. Z. A., Ruiz, A. S., Matos, G. R. S. 2017. Granulito Uyarani – uma janela estrutural Pré-Cambriana no Altiplano Boliviano: petrogênese e significado tectônico. Geol. USP, Sér. cient., São Paulo, v. 17, n. 2, p. 22-245.

Ondrejka, M., Uher, P., Putiš, M., Broska, I., Bačík P., Konečný, P., Schmiedt, I. 2012. Two stage breakdown of monazite by post-magmatic andmetamorphic fluids: an example from the Veporic orthogneiss, Western Carpathians, Slovakia. Lithos 142–143:245–255.

Parrish, R.R. 1990. U-Pb dating of monazite and its application to geological problems. Canadian Journal of Earth Sciences, 27, 1431-1450.

Patiño Douce, A.E. 1997. Generation of metaluminous A-type granites by low-pressure melting of calc-alkaline granitoids. Geology 25, 743–746.

Pearce, J.A. 1996. Source and setting of granitic rocks. Episodes 19, 120–125.

Pearce, J.A, 2008. Geochemical fingerprinting of oceanic basalts with applications to ophiolite classification and the search for Archean oceanic crust. Lithos 100, 14–48.

Pearce, J.A., Harris N.B.W., Tindle, A.G. 1984. Trace elements discrimination diagrams for the tectonic interpretation of granitic rocks. Journal of Petrology, 25 (4): 956-983.

Peck, W., Selleck, B., Wong, M., Chiarenzelli, J., Harpp, K., Hollocher, K., Lackey, J., Catalano, J., Regan, S., Stocker, A. 2013. Orogenic to post-orogenic (1.20-1.15 Ga) magmatism in the Adirondack lowlands and Frontenac terrane, southern Grenville Province, USA and Canada. Geosphere 9, 1637-1663.

Piechocka, A. M., Gregory, C. J., Zi, J. W., Sheppard, S., Wingate, M. T. D., Rasmussen, B. 2017. Monazite trumps zircon: applying SHRIMP U–Pb geochronology to systematically evaluate emplacement ages of leucocratic, low-temperature granites in a complex Precambrian orogen. Contributions to Mineralogy and Petrology, 172, 63.

Pitcher, W.S. 1982. Granite type and tectonic environment. In: Hsu, K.J. (Ed.), Mountain Building Processes. Academic Press, London, pp. 19–40.

Plens, D.P. 2018. Petrogênese e análise estrutural da Suíte Caracol: implicações para a evolução geodinâmica do Bloco Rio Apa, sul do Cráton Amazônico. xiii, 117 f., il. Tese (Doutorado em Geologia) — Universidade de Brasília, Brasília, 2018.

Quadros, M. L., Della Giustina, M. E., Souza, V. S., Scandolara, J. E. 2020. Geology, geochemistry and Sr-Nd isotopes of the Rio Branco Suite, Nova Brasilândia belt in southwest of the Amazonian Craton: Evidence of a Rodinia pre-assembly accretionary phase (ca. 1137 and 1106 Ma) during the evolution of the Nova Brasilândia orogeny. Lithos, 372–373.

Ramos, V.A., Vujovich, G., Martino, R., Otamendi, J. 2010. Pampia: a large cratonic block missing in the Rodinia Supercontinent. Journal of Geodynamics, 50:243-255.

Reddy, S.M. and Evans, D.A.D, 2009, in Reddy, S.M., Mazumder, R., Collins, A.S., and Evans, D.A.D, eds., Palaeoproterozoic supercontinents and global evolution: Correlations from core to atmosphere: Palaeoproterozoic Supercontinents and Global Evolution, Geological Society of London Special Publication 323, p. 1–26, doi:10.1144/SP323.1

Redes, L. A., Sousa, M. Z. A., Ruiz, A. S., Lafon, J. 2015. Petrogenesis and U-Pb and Sm-Nd geochronology of the Taquaral granite: record of an orosirian continental magmatic arc in the region of Corumba - MS. Brazilian Journal of Geology, 45(3), 431-451.

Redes, L. A., Pimentel, M. M., Ruiz, A. S., Matos, G. R. S., 2016. Granito Correreca - um registro magmático orosiriano no oriente boliviano: implicações tectônicas e estratigráficas. In: Anais do 48 Congresso Brasileiro de Geologia – Porto Alegre – Brazil.

Redes, L.A., Pimentel, M.M., Ruiz, A.S., Matos, G. R.S., Nedel, I. M. 2018. Granito Santa Terezita – Magmatismo do Bloco Rio Apa a Sul do Aulacógeno Tucavaca - Oriente Boliviano. In: Anais do 49 Congresso Brasileiro de Geologia – Rio de Janeiro – Brazil.

Redes, L. A., Hauser, N., Ruiz, A. S., Matos, R. S., Reimold, W. U., Dantas, E. L., Schmitt, R. T., Lima, B. A. F., Zacchi, E. N. P., Chaves, J. G. S., Osorio, L. F. B., Pimentel, M. M. 2020. U-Pb and Hf Isotopes in Granitoids from the eastern Bolivian Basement: insights into the Paleoproterozoic evolution of the western part of South America. Submitted to Journal of South American Earth Sciences.

Rivers, T., Martignole, J., Gower, CF. and Davidson, A., 1989. New tectonic divisions of the Grenville Province, southeast Canadian shield. Tectonics, 8(1): 63-84.

Rivers, T., 1997, Lithotectonic elements of the Grenville Province: Review and tectonic implications: Precambrian Research, v. 86, p. 117–154.

Rivers, T., 2008, Assembly and preservation of upper, middle, and lower orogenic crust in the Grenville Province—Implications for the evolution of large, hot, long-duration orogens: Precambrian Research, v. 167, p. 237–259, doi: 10.1016/j.precamres.2008.08.005.

Rizzotto, G.J. 1999. Petrologia e Ambiente Tectônico do Grupo Nova Brasilândia-RO. Dissertação de Mestrado, Universidade Federal do Rio Grande do Sul, Porto Alegre, 136 p.

Rizzotto G.J., Hartmann L.A. 2012. Geological and geochemical evolution of the Trincheira Complex, a Mesoproterozoic ophiolite in the southwestern Amazon craton, Brazil. Lithos, 148, 277-295.

Rizzotto, G. J. 2001. Reavaliação do Ciclo Orogênico Sunsas/Aguapeí no Sudoeste do Amazonian 1150 Craton. Abstracts Workshop on Geology of the SW Amazonian Craton: state of the art, IGC 1151 Project 426 (pp. 66-67).

Rizzotto, G. J., Bettencourt, J. S., Teixeira, W., Pacca, I. I. G., D'Agrella-Filho, M. S., Vasconcelos, P., Basei, M. A. S., Anoe, A. T., Passarelli, C. R. 2002. Geologia e Geocronologia da Suíte Metamórfica Colorado e suas Encaixantes, SE de Rondônia: Implicações para a Evolução Mesoproterozóica do SW do Cráton Amazônico. Geologia USP Série Científica, São Paulo, v. 2, p. 41-55.

Rizzotto G.J., Santos J.O.S., Hartmann L.A., Tohver E., Pimentel, M.M., Mcnaughton N.J. 2013. The Mesoproterozoic Guaporé suture in the SW Amazonian Craton: Geotectonic implications based on field geology, zircon geochronology and Nd-Sr isotope geochemistry. Journal of South American Earth Sciences, 48, 271-295.

Rizzotto, G.J., Hartmann, L.A., Santos, J.O.S., McNaughton N.J. 2014. Tectonic evolution of the southern margin of the Amazonian craton in the late Mesoproterozoic based on field relationships and zircon U-Pb geochronology. Anais da Academia Brasileira de Ciências, 86, 57-84.

Roberts, N.M.W., Slagstad, T., 2014. Continental growth and reworking on the edge of the Columbia and Rodinia supercontinents; 1.86–0.9 Ga accretionary orogeny in southwest Fennoscandia. International Geology Review 57, 11-12.

Rubatto, D., Hermann, J., Berger, A., Engi, M., 2009. Protracted fluid-induced melting during Barrovian metamorphism in the Central Alps. Contributions to Mineralogy and Petrology 158, 703–722.

Rubatto, D., Chakraborty, S., Dasgupta, S., 2013. Timescales of crustal melting in the Higher Himalayan Crystallines (Sikkim, Eastern Himalaya) inferred from trace element-constrained monazite and zircon chronology. Contributions to Mineral Petrology, 165, 349-372.

Ruiz, A.S. 2005. Evolução geológica do sudoeste do Cráton Amazônico, região limítrofe Brasil-Bolívia-Mato Grosso. Tese (Doutorado). Rio Claro: UNESP, p. 260.

Ruiz, A.S. 2009. Compartimentação Tectônica (Pré-) do SW do Cráton Amazônico: ênfase em Mato Grosso – Brasil. Congreso Geológico Boliviano, Acta 18, p.159-163. Potosi-BO.

Ruiz A.S., Sousa M.Z.A., Matos J.B., Lima G.A. 2007. Geologia do Domínio Tectônico Paraguá, SW do Cráton Amazônico – Fronteira Brasil-Bolívia. In: X Simpósio de Geologia do Centro-Oeste, Anais, Pirenópolis, Brasil, CD-ROM.

Ruiz A.S., Sousa M.Z.A., Macambira M.B., Lima G.A., Santos F. 2009. Evidências geológicas e geocronológicas (Pb-Pb e U-Pb) dos episódios magmáticos Lomas Manechis e San Ignácio no Terreno Paraguá - SW do Craton Amazônico - Vila Bela (MT). In: Simpósio 45 Anos de Geocronologia no Brasil, São Paulo, Anais, p. 304-306.

Ruiz A.S., D'Agrella Filho M.S., Sousa M.Z.A., Lima G.A. 2010. Tonian sills and mafic dike swarms of S-SW Amazonian Craton: records of Rodinia Supercontinent break-up? In: The Meeting of the Americas, 1, Abstracts, p. 3.

Ruiz A.S., Sousa M Z.A., Matos J.B., Macambira M.B., Lima G.A., Faria D.A. 2011. Craton ou Terreno Paraguá? Uma discussão baseada em novos dados geológicos e geocronológicos do SW do Craton Amazônico em território brasileiro [Craton or Paraguá Terrane? A discussion based on new geological and geochronological data of the SW Amazonian Craton in Brazilian territory]. In: XIII Simpósio Nacional de Estudos Tectônicos, Campinas, Anais, p. 239-242.

Sadowski, G.R., Bettencourt J.S., 1996. Mesoproterozoic tectonic correlations between eastern Laurentia and the western border of the Amazon Craton. Precambrian Research 76, 213-227.

Saes, G.S., and Leite, J.A.D. 1993. Evolução tectono-sedimentar do Grupo Aguapeí, Proterozóico Medio na porção meridional do Craton Amazonico: Mato Grosso e oriente boliviano. Revista Brasileira de Geociências, 23:31-38.

Sang, L.K., Ma, C.Q., 2012. Petrology. Geological Publishing House, 1-620 (in

Chinese).

Santos, J.O.S., Hartmann, L.A., Gaudette, H.E., Groves, D.I., McNaughton, N. J., Fletcher, I. R. 2000. A new understanding of the Amazon Craton provinces based on integration of field mapping and U-Pb and Sm-Nd geochronology. Gondwana Research 3, 453-488.

Santos, J.O.S, Rizzotto, G.J., Potter, P.E., McNaughton, N.J., Matos, R.S., Hartmann, L.A., Chemale Jr., F., Quadros, M.S. 2008. Age and autochthonous evolution of the Sunsás Orogen in West Amazon Craton based on mapping and U-Pb geochronology. Precambrian Research 165, 120-152.

Shand, S.J. 1943. The eruptive rocks. John Wiley, New York, second edition. 444p.

Siqueira, L.H. 2015. Granito São Domingos: Registro de Magmatismo Pós-Tectônico do Orógeno Intracontinental Aguapeí, SW do Cráton Amazônico. Universidade Federal de Mato Grosso. Instituto de Ciências Exatas e da Terra. Departamento de Recursos Minerais. Dissertação de Mestrado, 64p.

Smith, H.A., Giletti, B.J. 1997. Pb diffusion in monazite. Geochimica et Cosmochimica Acta, 51, 1047-1055.

Spencer, C. J., Cawood, P. A., Hawkesworth, C. J., Prave, A. R., Roberts, N. M. W., Horstwood, M. S. A., et al. (2015). Generation and preservation of continental crust in the Grenville Orogeny. Geosci. Front. 6, 357–372. doi: 10.1016/j.gsf.2014.12.001

Spencer, C. J., Kirkland, C. L., Prave, A. R., Strachan, R. A., Pease, V., 2019. Crustal reworking and orogenic styles inferred from zircon Hf isotopes: Proterozoic examples from the North Atlantic region. Geoscience Frontiers 10, 417–424.

Streckeisen, A. 1974. Classification and nomenclature of plutonic rocks: Recommendations of the IUGS subcommission on the systematics of igneous rocks. Geologische Rundschau, 63, 773-786.

Sun, S.S., and McDonough, W.F. 1989. Chemical and isotopic systematics of oceanic basalts: implications for mantle composition and processes. In Magmatism in the Ocean Basins (eds. A. D. Saunders and M. J. Norry, vol. 42.). The Geological Society, pp. 313–345.

Tassinari, C.C.G., Bettencourt, J.S., Geraldes, M.C., Macambira, M.J.B., Lafon, J.M. 2000. The Amazonian Craton. In: Cordani, U.G., Miliani, E.J., Thomaz-Filho, A., Campos, D.A. (Coord.), Tectonic Evolution of South America. 31st International Geological Congress, Rio de Janeiro, Brazil, pp. 41–95.

Tassinari, C.C.G., Munhá, J.M.U., Teixeira, W., Palácios, T., Nutman, A.P., and Sosa, S.C., Santos, A.P., and Calado, B.O. 2004. The Imataca Complex, NW

Amazonian Craton, Venezuela: Crustal evolution and integration of geochronological and petrological cooling histories: Episodes, v. 27, no. 1, p. 3–12.

Tassinari C.C.G., Macambira M.J.B. 1999. Geochronological provinces of the Amazonian Craton. Episodes 38, 174-182.

Tassinari, C.C.G., Macambira M.J.B. 2004. A evolução tectônica do Cráton Amazônico. In: Mantesso-Neto, V., Bartorelli, A., Carneiro, C.R., Brito-Neves, B.B. (Eds.), Geologia do Continente Sul-Americano. São Paulo, Beca, pp. 471–485.

Teixeira, W., Tassinari, C.C.G. 1984. Caracterização geocronológica da Província Rondoniana e suas implicações geotectônicas. 2 Symposium Amazônico, Actas, p. 87-102.

Teixeira, W., Tassinari, C.C.G., Cordani, U.G., Kawashita, K., 1989. A review of the geochronology of the Amazonian Craton: tectonic implications. Precambrian Research 42, 213–227.

Teixeira, W., Geraldes M.C., Matos R., Ruiz A.S., Saes G., Vargas-Mattos G. 2010. A review of the tectonic evolution of the Sunsás belt, SW Amazonian Craton. Journal of South American Earth Sciences 29, 47–60.

Teixeira, W., Hamilton, M.A., Lima G.A., Ruiz A.S., Matos R., Ernst, R.E. 2015. Precise ID-TIMS U–Pb baddeleyite ages (1110–1112 Ma) for the Rincón del Tigre–Huanchaca large igneous province (LIP) of the Amazonian Craton: Implications for the Rodinia supercontinent. Precambrian Research 265, 273–285.

Teixeira, W., Hamilton, M. A., Girardi, V. A. V., Faleiros, F. M., Ernst, R. E., 2018. U-Pb baddeleyite ages of key dyke swarms in the Amazonian craton (Carajás/Rio Maria and Rio Apa areas): tectonic implications for 1880, 1110 Ma, 535 Ma and 200 Ma events. Precambr Res (in press). http://doi-org.ez54.periodicos.capes.gov.br/10.1016/j.precamres.2018.02.008

Teixeira, W., Cordani, U.G., Faleiros, F.M., Sato, K., Maurer, V.C., Ruiz, A.S., Azevedo, E.J.P. 2020. The Rio Apa Terrane reviewed: U-Pb zircon geochronology and provenance studies provide paleotectonic links with a growing Proterozoic Amazonia. Earth-Science Reviews, 202, 1-35.

Thirlwall, M.F., 1991. Long-term reproducibility of multicollector Sr and Nd isotope ratio analysis. Chemical Geology 94, 85-104.

Tohver, E., Van der Pluijm, B.A., Van der Voo, R., Rizzotto, G.J., Scandolara, J.E., 2002. Paleogeography of the Amazon Craton at 1.2 Ga: early Grenvillian collision with the Llano segment of Laurentia. Earth and Planetary Science Letters 199, 185 – 200.

Tohver, E., Van der Pluijm, B.A., Mezger, K., Essene, E., Scandorala, J.E., Rizzotto, G.J., 2004. Significance of the Nova Brasilândia metasedimentary belt in western Brazil: redefining the mesoproterozoic boundary of the Amazon Craton. Tectonics. doi:10.1029/2003TC001563 (TC6004).

Tohver, E., van der Pluijm, B.A., Scandolara, J.E., Essene, E.J., 2005. Grenville-aged deformation of Amazonia (Rondônia, Brazil): evidence for collision with southern Laurentia. Journal of Geology, 113, 309–323.

Tohver, E., Teixeira, W., Van der Pluijm, B.A., Geraldes, M.C., Bettencourt, J.S., Rizzotto, G. 2006. A restored transect across the exhumed Grenville orogen of Laurentia and Amazonia, with implications for crustal architecture. Geology 34, 669–672.

Tollo, R., Aleinikoff, J., Borduas, E., Hackley, P., and Fanning, M., 2004, Petrologic and geochronologic evolution of the Grenville orogen, northern Blue Ridge Province, Virginia, in Tollo, R.P., Corriveau, L., McLelland, J., and Bartholomew, M.J., eds., 2004, Proterozoic Tectonic Evolution of the Grenville Orogen in North America: Geological Society of America Memoir 197, p. 647–677.

Trompette, R., Alvarenga, C.J.S., and de Walde, D. 1998. Geological evolution of the Neoproterozoic Corumbá graben system (Brazil): Depositional context of the stratified Fe and Mn ores of the Jacadigo Group: Journal of South America Earth Sciences, v. 11, p. 587−597.

Vance, D., Harris, N. 1999. The timing of prograde metamorphism in the Zanskar Himalaya. Geology, 27, 395-398.

Vargas-Mattos, G.L. 2006. Geocronologia U/Pb en granitos post y sin-tectónicos de la Orogenia Sunsás en el Cratón Amazonico de Bolivia. Msc Dissertation, Universidade do Estado do Rio de Janeiro, Rio de Janeiro, Brazil.

Vargas-Mattos G.L. 2010. Caracterização geocronológica e geoquímica dos granitos proterozoicos: implicação para a evolução crustal da borda SW do Cráton Amazônico na Bolívia. Tese de Doutorado, Faculdade de Geologia, Universidade do Estado do Rio de Janeiro, p. 164.

Walde, D.H.G., do Carmo D.A., Guimararaes E.M., Vieira L.C., Erdtmann B-D, Sanchez E.A.M., Adorno R.R., Tobias T.C. 2015. New aspects of Neoproterozoic – Cambrian transition in the Corumbá region (state of Mato Grosso do Sul, Brazil). Ann. Paléontol. 101, 213–224. (doi: 10.1016/j.annpal.2015.07.002)

Wang, H.L., Chung, S.L., O'Reilly, S.Y., Sun, S.S, Shinjo, R., Chen, C.H., 2004. Geochemical Constraints for the Genesis of Post-collisional Magmatism and the Geodynamic Evolution of the Northern Taiwan Region. Journal of Petrology 45, 975–1011.

Wang, Y.J., Zhu, W.G., Huang, H.Q., Zhong, H., Bai, Z.-J., Fan, H.P., Yang, Y.J., 2019. Ca. 1.04 Ga hot Grenville granites in the western Yangtze Block, southwest China. Precambrian Research 328, 217-234.

Watkins, J.M., Clemens, J.D., Treloar, P.J., 2007. Archaean TTGs as sources of younger granitic magmas: melting of sodic metatonalites at 0.6–1.2 GPa. Contributions to Mineralogy and Petrology 154, 91–110.

Weinberg, R.F., Hasalová, P., 2015. Water-fluxed melting of the continental crust: a review. Lithos 212, 158–188.

Wiedenbeck, M., Hanchar, J.M., Peck, W.H., Sylvester, P., Valley, J.W., Whitehouse, M.J., Kronz, A., Morishita, Y., Nasdala, L., Fiebig, J., Franchi, I., Girard, J.P., Greenwood, R.C., Hinton, R., Kita, N., Mason, P.R.D., Norman, M., Ogasawara, M., Piccoli, R., Rhede, D., Satoh, H., Schulz-Dobrick, B., Skar, O., Spicuzza, M.J., Terada, K., Tindle, A., Togashi, S., Vennemann, T., Xie, Q., Zheng, Y.F. 2004. Further characterisation of the 91500-zircon crystal. Geostandards and Geoanalytical Research, 28, 9-39.

Whalen, J.B., Currie, K.L., Chappell, B.W. 1987. A-type granites: geochemical characteristics, discrimination and petrogenesis. Contributions to Mineralogy and Petrology 95, 407– 419.

Wilson, M. 1991. Igneous Petrogenesis: a global tectonic approach. London, Harper Collins Academic, 466 p.

Windley, B.F. 1989. Anorogenic magmatism and the Grenvillian Orogeny. Canadian Journal Earth Sciences, 26: 479-489.

Windley, B.F. 1993. Proterozoic anorogenic magmatism and its erogenic connections. Journal of the Geological Society, London 150: 39-50.

Winter, J.D. 2010. Principles of igneous and metamorphic petrology. 2a edição. New York, Prentice Hall, 702 p.

Wyllie, P.J. 1981. Plate tectonics and magma Genesis. Geologische Rundschau, 70:128-153.

Zeng, L., Gao, L.-E., Xie, K., Liu, Z.-J. 2011. Mid-Eocene high Sr/Y granites in the Northern Himalayan Gneiss Domes: melting thickened lower continental crust. Earth and Planetary Science Letters 303, 251–266.

Zhang, H., Li, S.-Q., Fang, B.-W., He, J.-F., Xue, Y.-Y., Siebel, W., Chen, F. 2018. Zircon U-Pb ages and geochemistry of migmatites and granites in the Foping dome: Evidence for Late Triassic crustal evolution in South Qinling, China. Lithos, volumes 296–299, 129-141 p. doi.org/10.1016/j.lithos.2017.10.024

Zhou, M.F., Ma, Y.X., Yan D.P. 2006. The Yanbian Terrane (Southern Sichuan Province, SW China): A Neoproterozoic arc assemblage in the western margin of the Yangtze Block. Precambrian Research, 144:19－38.